Fermi National Accelerator Laboratory

CP and CPT Symmetry Tests from the Two-Pion Decays of the Neutral Kaon with the FNAL E731 Detector

L.K. Gibbons et al.

The E731 Collaboration

Fermi National Accelerator Laboratory
P.O. Box 500, Batavia, Illinois 60510

January 1996

Disclaimer

This report was prepared as an account of work sponsored by an agency of the United States Government. Neither the United States Government nor any agency thereof, nor any of their employees, makes any warranty, expressed or implied, or assumes any legal liability or responsibility for the accuracy, completeness, or usefulness of any information, apparatus, product, or process disclosed, or represents that its use would not infringe privately owned rights. Reference herein to any specific commercial product, process, or service by trade name, trademark, manufacturer, or otherwise, does not necessarily constitute or imply its endorsement, recommendation, or favoring by the United States Government or any agency thereof. The views and opinions of authors expressed herein do not necessarily state or reflect those of the United States Government or any agency thereof.

CP AND CPT SYMMETRY TESTS FROM THE TWO-PION DECAYS OF THE NEUTRAL KAON WITH THE FNAL E731 DETECTOR

L.K. Gibbons, A.R. Barker, R.A. Briere, G. Makoff, V. Papadimitriou,
J.R. Patterson, B. Schwingenheuer, S.V. Somalwar, Y.W. Wah, B. Winstein,
R. Winston, M. Woods, H. Yamamoto
G.J. Bock, R. Coleman, J. Enagonio, Y.B. Hsiung,
E.J. Ramberg, K. Stanfield, R. Tschirhart, T. Yamanaka
E.C. Swallow
G.D. Gollin, M. Karlsson, J.K. Okamitsu
P. Debu, B. Peyaud, R. Turlay, and B. Vallage
(FNAL E731 Collaboration)

December 28, 1995

CP AND CPT SYMMETRY TESTS FROM THE TWO-PION DECAYS OF THE NEUTRAL KAON WITH THE FNAL E731 DETECTOR

L.K. Gibbons[*], A.R. Barker[†], R.A. Briere[‡], G. Makoff[§], V. Papadimitriou[||],
J.R. Patterson[¶], B. Schwingenheuer[**], S.V. Somalwar[††], Y.W. Wah, B. Winstein,
R. Winston, M. Woods[‡‡] and H. Yamamoto[‡]

The Enrico Fermi Institute and the Department of Physics,
The University of Chicago, Chicago, Illinois, 60637

G.J. Bock, R. Coleman, J. Enagonio[§§], Y.B. Hsiung,
E.J. Ramberg, K. Stanfield, R. Tschirhart and T. Yamanaka[¶¶]

Fermi National Accelerator Laboratory, Batavia, Illinois 60510

E.C. Swallow
Department of Physics, Elmhurst College, Elmhurst, Illinois 60126 and
The Enrico Fermi Institute, The University of Chicago, Chicago, Illinois, 60637

G.D. Gollin[***], M. Karlsson[†††], and J.K. Okamitsu[‡‡‡]
Department of Physics, Princeton University, Princeton, New Jersey 08544

P. Debu, B. Peyaud, R. Turlay, and B. Vallage
Department d'Astrophysique, de Physique des Particules,
de Physique Nucleaire et de l'Instrumentation Associee,
Centre d'Etudes de Saclay, 91191 Gif-sur-Yvette CEDEX, France
(December 29, 1995)

We present a comprehensive treatment of the precise determinations of the parameters $Re(\varepsilon'/\varepsilon)$, τ_S, Δm, ϕ_{+-} and $\Delta\phi$ in the neutral kaon system with the FNAL E731 detector. Together, these determinations allow accurate studies of both CP and CPT symmetry. Details of the detector and its performance and the data analysis are given. The extensive Monte Carlo simulation of the detector and comparison with data are also presented.

PACS number(s): 13.25.Es, 11.30.Er, 14.40.Aq

[*] Present address: Rochester University, Rochester, NY 14627.
[†] Present address: University of Colorado, Boulder, CO 80309.
[‡] Present address: Harvard University, Cambridge, MA 02138.
[§] Present address: Solomon Brothers, New York, NY 10048.
[||] Present address: Fermi National Accelerator Laboratory, Batavia, IL 60510.

¶ Present address: Cornell University, Ithaca, NY 14853.

** Present address: Max-Planck Institute for Nuclear Physics, P.O. Box 103980, 69029 Heidel-berg, Germany

†† Present address: Rutgers University, P.O. Box 849, Piscataway, NJ 08855.

‡‡ Present address: SLAC, P.O. Box 4349, Stanford, CA 94305.

§§ Present address: Department of Atomospheric Science, Colorado State University, Fort Collins, CO 80523.

¶¶ Present address: Physics Department, Osaka University, Toyonaka, Osaka 560, Japan.

*** Present address: Department of Physics, U. of Illinois, Urbana, IL 61801.

††† Present address: CERN, CH-1211, Geneva 23, Switzerland.

‡‡‡ Present address: Princeton Combustion Research Laboratories, Monmouth Junction, NJ 08852.

<div align="center">

Contents

</div>

I. INTRODUCTION

This article presents a full description of Fermilab experiment 731, focussing upon the determination of the CP violation parameter $Re(\varepsilon'/\varepsilon)$ in the decay of the K_L and K_S meson into two pions. It is largely based on the Ph.D. thesis of L. K. Gibbons [1]. After a brief review of the relevant phenomenology in the neutral kaon system, we describe the detector, beam and the analysis of the data. The Monte-Carlo simulation reflecting the degree of understanding of the apparatus is presented in detail. As well, calibration of the detector elements is fully treated. As a byproduct, this experiment is sensitive to many of the fundamental parameters of the neutral kaon system, which also allows us to probe the validity of CPT symmetry. These parameters include the K_S lifetime (τ_S) and the difference in mass between the K_L and K_S $(\Delta m \equiv m_L - m_S)$. We also present the values of the phase ϕ_{+-} and the phase difference $\Delta\phi \equiv \phi_{00} - \phi_{+-}$, where ϕ_{+-} and ϕ_{00} are the phases of η_{+-} and η_{00}, respectively.

A. Kaon Phenomenology and CP Violation

This section gives the essentials of the phenomenology of the neutral kaon system, primarily as needed for the determination of $Re(\varepsilon'/\varepsilon)$. We assume that CPT symmetry holds in this section. The implications of CPT symmetry violation are treated in the next section. The formalism of kaon phenomenology has been extensively treated in the literature [2–8]. The experimental status is also briefly summarized.

To study CP violation and CPT symmetry in the $K^0 - \bar{K}^0$ complex, it has been traditional to describe the system by an effective 2×2 Hamiltonian [2]

$$\mathbf{H}_{eff} = \mathbf{M} - i\mathbf{\Gamma}/2, \tag{1}$$

where both the mass matrix $\mathbf{M}$ and the decay matrix $\mathbf{\Gamma}$ are Hermitian.

The physical eigenstates $|K_{L,S}\rangle$ with definite masses $m_{L,S}$ and lifetimes $\tau_{L,S} = 1/\Gamma_{L,S}$, have time dependences

$$|K_{L,S}(t)\rangle = e^{-im_{L,S}t}e^{-\Gamma_{L,S}t/2}|K_{L,S}(0)\rangle. \tag{2}$$

The two states with definite CP are

$$
\begin{aligned}
|K_1\rangle &\sim |K^0\rangle + \left|\bar{K}^0\right\rangle \qquad (CP = +1) \\
|K_2\rangle &\sim |K^0\rangle - \left|\bar{K}^0\right\rangle \qquad (CP = -1).
\end{aligned}
\tag{3}
$$

These would be the weak eigenstates if CP symmetry were not violated.

Allowing for CP violation, the eigenstates become asymmetric mixtures of the K^0 and $\bar{K}^0$:

$$
\begin{aligned}
|K_S\rangle &= \frac{1}{\sqrt{2(1+|\varepsilon|^2)}}\left((1+\varepsilon)|K^0\rangle + (1-\varepsilon)\left|\bar{K}^0\right\rangle\right) \\
|K_L\rangle &= \frac{1}{\sqrt{2(1+|\varepsilon|^2)}}\left((1+\varepsilon)|K^0\rangle - (1-\varepsilon)\left|\bar{K}^0\right\rangle\right).
\end{aligned}
\tag{4}
$$

In the above expression, ε is given by

$$\varepsilon = \frac{ImM_{12} - \frac{1}{2}\imath Im\Gamma_{12}}{\imath\Delta m - \frac{1}{2}(\Gamma_S - \Gamma_L)}, \tag{5}$$

where $M_{12} = \langle K^0 | \mathbf{M} | \bar{K}^0 \rangle$ and $\Gamma_{12} = \langle K^0 | \mathbf{\Gamma} | \bar{K}^0 \rangle$. This expression is valid in the Wu-Yang phase convention [9]. Here Δm is the mass difference between the long and short lived weak eigenstates,

$$\Delta m \equiv m_L - m_S. \tag{6}$$

There are two classes of CP violating effects. In one, the K^0 and the $\bar{K}^0$ mix asymmetrically, resulting in small admixtures of the "wrong" CP states, described as ε in Eqs. (4) and (5). In the other, the K^0 and the $\bar{K}^0$ *decay* asymmetrically, from a CP violating amplitude directly in the decay. The latter effect has been appropriately dubbed "*direct*" CP violation. Over 30 years of effort have gone into establishing whether the observed CP violation arises solely from *mixing* in the mass matrix, or whether *direct* CP violation also occurs in the decay amplitude.

1. CP Violation from Mixing

For decay modes where the final state has a definite CP, it is interesting to consider the ratio of CP violating to CP conserving amplitudes for the decay modes. In the traditional notation, we have for the charged decay mode

$$\eta_{+-} \equiv \frac{\langle \pi^+\pi^- | \mathbf{H}_W | K_L \rangle}{\langle \pi^+\pi^- | \mathbf{H}_W | K_S \rangle}, \tag{7}$$

and for the neutral mode

$$\eta_{00} \equiv \frac{\langle \pi^0\pi^0 | \mathbf{H}_W | K_L \rangle}{\langle \pi^0\pi^0 | \mathbf{H}_W | K_S \rangle}. \tag{8}$$

If only the asymmetric $K^0 - \bar{K}^0$ mixing in the mass matrix contributes to the CP violating amplitudes, then

$$\eta_{+-} = \eta_{00} = \varepsilon. \tag{9}$$

Experimentally, both the phases and the magnitudes of η_{+-} and η_{00} are accessible. The "natural" phase for ε is then,

$$\phi_\varepsilon = \tan^{-1}\left(\frac{2\Delta m}{\Gamma_S - \Gamma_L}\right), \tag{10}$$

which follows from Eq. (5) as one can phenomenologically limit $Im\Gamma_{12}$. This natural phase is often referred to as the "superweak" phase. Obviously, Eq. (9) implies that experiments should be consistent with both

$$|\eta_{+-}| = |\eta_{00}|, \tag{11}$$

2

and

$$\phi_{+-} = \phi_{00} = \tan^{-1}\left(\frac{2\Delta m}{\Gamma_S - \Gamma_L}\right), \tag{12}$$

where ϕ_{+-} and ϕ_{00} are the phases of η_{+-} and η_{00}, respectively. The best fit values for $|\eta_{+-}|$ and $|\eta_{00}|$ were calculated by the Particle Data Group [10],

$$\begin{aligned}|\eta_{+-}| &= (2.269 \pm 0.023) \times 10^{-3} \\ |\eta_{00}| &= (2.259 \pm 0.023) \times 10^{-3},\end{aligned} \tag{13}$$

which were consistent with the prediction of Eq. (11), that is, with the hypothesis that the observed CP violation in K_L decays was due to mixing alone.

When experiment 731 was begun in 1983, $|\eta_{+-}|$ and $|\eta_{00}|$ were consistent with each other. The phase, ϕ_{+-}, was accurately known and a little more than two standard deviations away from the superweak phase ϕ_ε. The phase difference, $\Delta\phi \equiv \phi_{00} - \phi_{+-}$, was known only to about 6° and its value differed by two standard deviations from zero. In the remainder of this article, we describe how these quantities were measured in E731.

2. Direct CP Violation in $\pi\pi$ Decays

One way of isolating the mixing and decay contributions is to compare the level of CP violation in two different CP-violating final states. The two CP-violating decays $K_L \to \pi^+\pi^-$ and $K_L \to \pi^0\pi^0$ allow such a comparison. Another way is to search for CP-violating decays, such as the rare $K_L \to \pi^0\nu\bar{\nu}$ decay, where the CP-conserving as well as indirect CP-violating decay amplitudes are highly suppressed. An observation of such a decay mode would then essentially be a signal of direct CP violation. In this experiment, we use the first approach. Since this approach involved the use of an intense K_L beam, we were also able to obtain limits on some rare decay modes of the K_L relating to CP violation [11–15].

As is customary, we define

$$\langle I | \mathbf{H}_W | K^0 \rangle = a_I \equiv A_I e^{i\delta_I}, \tag{14}$$

where I denotes the isospin ($I = 0, 2$) of the $\pi\pi$ final state. The overall amplitude has been separated into an amplitude A_I corresponding to the weak decay process itself, and a phase shift δ_I from the final state interactions. From the assumption of CPT symmetry, one also has (see, for example, reference [6])

$$\langle I | \mathbf{H}_W | \bar{K}^0 \rangle = \bar{a}_I \equiv A_I^* e^{i\delta_I}. \tag{15}$$

One can now explicitly adopt the Wu–Yang phase convention [9] and take A_0 to be real. This fixes the relative phase between the $|S| = 1$ and the $S = 0$ sectors, which are not connected by the strong and electromagnetic interactions. Of course all physical observables are independent of the choice of phase.

Allowing for direct CP violation, then, yields the following:

$$\varepsilon' \equiv \frac{i}{\sqrt{2}} e^{i(\delta_2 - \delta_0)} \frac{Im A_2}{A_0}, \tag{16}$$

3
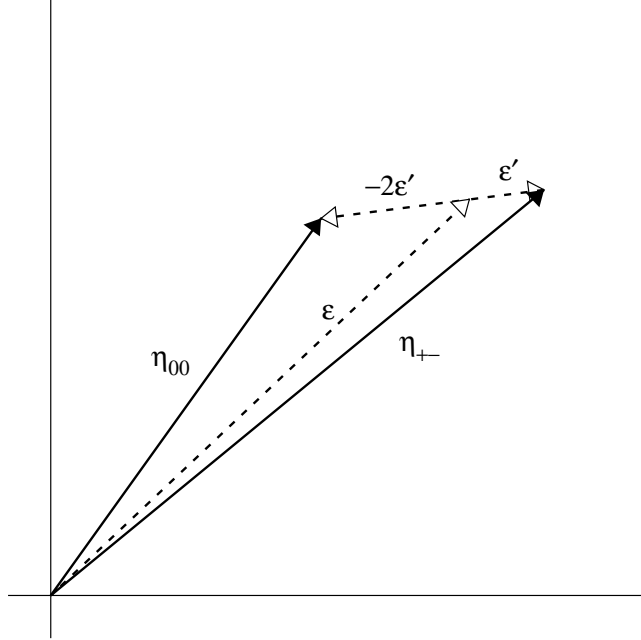
FIG. 1. The Wu-Yang phase diagram for $K \to \pi\pi$ decays. The phase and magnitude of ε' relative to ε have been greatly exaggerated for the sake of clarity.

$$\eta_{+-} \approx \varepsilon + \varepsilon', \tag{17}$$

and

$$\eta_{00} \approx \varepsilon - 2\varepsilon'. \tag{18}$$

If there is direct CP violation in the $\pi\pi$ decay of the neutral kaon, then the ratio of CP-violating to CP-conserving amplitudes are different for the $\pi^+\pi^-$ and $2\pi^0$ final states. The geometrical relation between the different CP-violating amplitudes is illustrated in the Wu-Yang diagram in Fig. 1.

The phase of ε' follows from its definition:

$$\phi_{\varepsilon'} = \delta_2 - \delta_0 + \frac{\pi}{2}. \tag{19}$$

The $I = 0$ and $I = 2$ final state phase shifts have been measured in other experiments, and in a recent compilation, Ochs [16] obtains $\delta_2 - \delta_0 = -43° \pm 6°$. This implies that the phase of ε' is $\phi_{\varepsilon'} = 47° \pm 6°$. Comparing this phase to the phase of ε obtained above, we see that ε' and ε are almost parallel, a convenient but accidental coincidence. To a good approximation then, we have CP violation parametrized by $Re(\varepsilon'/\varepsilon)$, and CPT violation parametrized by $Im\varepsilon'/\varepsilon$. The latter would result if, for example, the $K^0 - \bar{K}^0$ mixing asymmetry were different for the K_L and K_S.

In an experiment, one can only directly measure the decay rates for the different $K \to \pi\pi$ decays. Expressed in terms of the decay rates, a signal for direct CP violation in $K \to \pi\pi$ decays is a deviation of the double ratio of rates away from unity,

$$\frac{\Gamma(K_L \to \pi^+\pi^-)/\Gamma(K_S \to \pi^+\pi^-)}{\Gamma(K_L \to \pi^0\pi^0)/\Gamma(K_S \to \pi^0\pi^0)} = \frac{|\eta_{+-}|^2}{|\eta_{00}|^2} \approx 1 + 6Re(\varepsilon'/\varepsilon). \tag{20}$$

4

TABLE I. Recently published measurements of $Re(\varepsilon'/\varepsilon)$. Errors listed are statistical error first and the systematic error second, otherwise the combined error.

Collaboration	Year	$Re(\varepsilon'/\varepsilon)\ (10^{-4})$
Yale–BNL [29]	1985	17 ± 82
Chicago–Saclay (FNAL E617) [30]	1985	$-46 \pm 53 \pm 24$
Chicago–Elmhurst–FNAL–Princeton–Saclay (FNAL E731A) [31]	1988	$32 \pm 28 \pm 12$
CERN–Dortmund–Edinburgh–Mainz–Orsay– Pisa–Siegen (CERN NA31) [17]	1988	$33 \pm 7 \pm 8$
Chicago–Elmhurst–FNAL–Princeton–Saclay (FNAL E731 20%) [18]	1990	$-4 \pm 14 \pm 6$
Chicago–Elmhurst–FNAL–Princeton–Saclay (FNAL E731 final result) [19]	1993	$7.4 \pm 5.2 \pm 2.9$
CERN–Edinburgh–Mainz–Orsay–Pisa–Siegen (CERN NA31 final result) [20]	1993	23 ± 6.5

Since $Re(\varepsilon'/\varepsilon)$ is expected to be small, this deviation is approximately $6Re(\varepsilon'/\varepsilon)$.

There has been quite an industry measuring $Re(\varepsilon'/\varepsilon)$ over the past 30 years, and the recently published results are presented in Table I. In 1988, the NA31 group published evidence [17] for direct CP violation at the 3 standard deviation level. An initial result [18] from our group based upon 20% of the data collected here was, however, consistent with no direct CP violation. The analysis of the complete E731 data set, which is the focus of this article, has been published [19]; this result together with the final one from NA31 [20], are also shown in the Table I for comparison. There is approximately a two standard deviation discrepancy between the NA31 publication and our initial result. The analysis presented here also reanalyzes the data used in reference [18], so this result supersedes the previous one.

There has been considerable theoretical effort placed on the evaluation of $Re(\varepsilon'/\varepsilon)$ over the last few years, with results ranging from as small as 10^{-4} up to several 10^{-3}. Perhaps the only hard conclusion one can draw from these calculations is that, from an experimentalist's point of view, $Re(\varepsilon'/\varepsilon)$ is expected to be *small* in the Standard Model! The theoretical situation has greatly improved very recently with two new calculations of $Re(\varepsilon'/\varepsilon)$ at next-to–leading order. We, however, defer further discussion of these results until Section XI.

B. Tests of CPT Invariance

In the phenomenological analysis of CP violation in the $\pi\pi$ decays of neutral kaons given above, many of the results we obtained rested on the assumption that the weak hamiltonian underlying $\mathbf{H}_{eff}$ was invariant under CPT. CPT invariance is a very general property, arising in any local field theory which incorporates proper Lorentz transformations. However, there have been several issues recently raised which question the validity of assuming CPT.

For example, Kobayashi and Sanda [21] question the applicability of the CPT theorem to QCD because the proof of the CPT theorem used the properties of asymptotically free states, while the quarks and gluons are confined and do not appear in such states. Furthermore, one might question the validity of the assumption that the world is described by a local field theory. We may well be seeing the low-energy effective interactions of some more fundamental process. If, for example, a string theory turns out to be a valid description of nature, then the nonlocal nature of such a theory could lead to CPT-violating phenomena. Indeed, there have even been recent speculations that such phenomena could lead to observable effects in the $K^0 - \bar{K}^0$ system [22].

We now briefly discuss some of the tests of CPT symmetry open to the kaon system and accessible by our experiment.

The phases ϕ_{+-} and ϕ_{00} can be used to test CPT symmetry. Eq. (12) can be divided into two different tests, and different assumptions enter each. In the first, one wishes to compare the phases ϕ_{+-} and ϕ_{00} directly, that is, to measure the phase difference $\Delta\phi \equiv \phi_{00} - \phi_{+-}$. To make such comparisons in Eq. (12), we need measurements of the mass difference (Δm), of the K_S and K_L lifetimes (τ_S and τ_L), and of the phases themselves. Using Eqs. (17) and (18), one finds that the effect of ε' on the phase difference is given approximately by

$$\Delta\phi \approx 3 Re(\varepsilon'/\varepsilon) \tan(\phi_\varepsilon - \phi_{\varepsilon'}). \tag{21}$$

Using the uncertainties in the previous measurements of $Re(\varepsilon'/\varepsilon)$ and in the $\pi\pi$ final state phase shifts, one can limit the contribution from direct CP violation to the phase difference to be under $0.2°$. There were two measurements of the phase difference $\Delta\phi$, one based on a subset of the data used in this experiment [23], and another from the NA31 experiment [24] at CERN. The values obtained for $\Delta\phi$ were

$$-0.3° \pm 2.4° \pm 1.2° \quad \text{(E731 20\%, partial data set)},$$
$$+0.2° \pm 2.6° \pm 1.2° \quad \text{(NA31)}.$$

In both cases, the first errors are statistical and the second are systematic. Together, these measurements imply $\Delta\phi = -0.1° \pm 1.9°$. The experimental values for the phase above are consistent with CPT, but further accuracy is desired.

The other phase comparison we can make is the agreement between ϕ_{+-} and the superweak phase $\tan^{-1}(2\Delta m/[\Gamma_S - \Gamma_L])$. Here, we neglect the contribution of Γ_{12} in Eq. (5) to the phase. If one assumes that the $\Delta S = \Delta Q$ law is not significantly violated, and that CP violation in the 3π decays is not anomalously large, then the $\pi\pi$ contribution is expected to dominate by a factor of $\Gamma_S/\Gamma_L \approx 580$. The $\pi\pi$ contribution to $Im\Gamma_{12}/\Gamma_S$ is of order $\frac{1}{22}|\varepsilon'/\varepsilon|$, so the contribution of Γ_{12} to the phase of ε is expected to be extremely small. The phase ϕ_ε (and therefore the phase ϕ_{+-}) should thus be very close to the superweak phase. The experimental data was not in the best agreement with this assertion. The phase ϕ_{+-} of η_{+-} has been measured previously by studying the interference in $\pi^+\pi^-$ decays [24–26]. The world average [27] at the time we obtained our data was $\phi_{+-} = 46.6° \pm 1.2°$, over 2 standard deviations away from the superweak phase $43.68° \pm 0.14°$.

The latter test is, unfortunately, a somewhat model dependent one since the assumption that the semileptonic and 3π contributions to Γ_{12} are small could be questioned. If one is questioning the validity of CPT, it is not clear that it is fair to make model-dependent

assumptions about these rates. Since the $\Delta S = -\Delta Q$ amplitude is only limited at the 2% level, and CP violation in 3π decays is only limited at the 10% level, a completely model independent estimate of ϕ_ε is actually much poorer. Recent estimates [21], strictly using only the actual experimental information, have placed the value of ϕ_ε within the 39.5° to 47.4° range at the 90% confidence level. It is still interesting to probe the experimental discrepancy between ϕ_{+-} and the superweak phase. If the discrepancy is not an artifact of the measurements, then it *is* an indication of some new physics, even if not CPT violation.

A new result for $\Delta\phi$ that supersedes our previous measurement listed above has been published [28], along with a new determination of ϕ_{+-}. These measurements are also part of the results on neutral kaon physics presented here.

C. Overview

We have discussed many of the basic issues relevant to the measurements we can perform in this experiment. The rest of the article describes the measurement technique, data analysis and results. In the next section, the issues affecting a measurement of $Re(\varepsilon'/\varepsilon)$ and how these issues affected the design of our experiment, are discussed. Following this, we examine the detector itself and give a brief description of the data collection. Sections IV through VI presents the analysis of the data, covering the calibration techniques, and the different reconstruction and background subtraction techniques in the $\pi^+\pi^-$ and $2\pi^0$ decay modes.

Our experimental method requires understanding the acceptance of the detector at a precise level. Section VII details the Monte Carlo simulation of our experiment that we used to determine the acceptance. The fitting techniques used in extracting the physical parameters are covered in Section VIII. Many of the issues treated are quite important as considerations for future experiments using this technique. The results of the fits for $Re(\varepsilon'/\varepsilon)$ and the other parameters of the kaon system are presented separately in Section IX.

The final part of the analysis involved the determination of the systematic uncertainty on each of the particular measurements. In Section X, we focus on the systematic checks and the final systematic uncertainty for our measurement of $Re(\varepsilon'/\varepsilon)$, with contributions to the uncertainty in the other parameters noted where important. With our measured parameters and systematic uncertainties all in hand, we conclude in Section XI by relating our findings back to the issues presented in this section.

II. EXPERIMENT TECHNIQUE

A precise determination of $Re(\varepsilon'/\varepsilon)$ to better than 0.001 requires measuring the double ratio of rates (Eq. (20)) to better than 0.6%. This means collecting a large number of $K \to \pi\pi$ decays in each of the four modes, and requires strict controls of biases in extracting the double ratio of rates. Here we outline the issues in measuring this double ratio and discuss how E731 techniques reduce the systematic sensitivity. Finally, we outline how these techniques allow the extraction of other parameters in the neutral kaon system. The detector itself is described in the next section.

The origins of this technique are as follows. During the mid 1970's, some of the authors of this paper made the first successful measurement of the charge radius of the neutral kaon [32]. One needed to measure the coherent regeneration (where the contribution from atomic electrons adds to that of the nuclei) and the diffractive regeneration (where the electron contribution is incoherent); comparing the two allows isolation of the electron contribution. The problem is that the former requires a *thick* regenerator for the signal and background suppression, while the latter requires a *thin* regenerator to suppress multiple scattering effects. Previous attempts used a compromise in the regenerator size; the choice in [32] was to use two regenerators simultaneously in two distinct kaon beams derived from the same target. By frequent alternation of the regenerators, one could assure that each saw the same incident flux.

One of the early papers on the phenomenology of CP violation in the standard model was by Ellis, Gaillard, and Nanopoulos [33]. In [33], they calculated the value of $Re(\varepsilon'/\varepsilon)$, saying that it would be in the neighborhood of $\frac{1}{450}$ and that this "would remain outside the reach of experiments for some time to come." The subject of *direct* CP violation had not been pursued for a number of years as there was no compelling indications as to its size. Now, with a possible model for the effect, it appeared at least possible to say whether the 6-quark CKM model definitively accounted for CP violation. With our double beam technique, one could see an effect of this size. This led to Fermilab experiment 617. For this effort, it was required that one photon converts in a thin conversion plane in the middle of the decay region so that the resultant e^+e^- pair could be tracked, reducing background by providing a means of giving the decay vertex. The result (Bernstein *et al.* [30]) was consistent with zero with a precision of 0.006, not quite at the level predicted. (Interestingly, a BNL–YALE group [29] also performed a measurement at about the same time, with an error of 0.008.)

In 1983, we proposed a new double beam and experiment 731, to make the measurement with a precision of 0.001. E731 had a brief test run (E731A) in 1985, where again a photon conversion was required, with the result $Re(\varepsilon'/\varepsilon) = 0.0032 \pm 0.0030$ (Woods *et al.* [31]). An extensive upgrade followed the 1985 run which permitted the use of events with no conversion and thus much higher statistics. This paper treats the upgraded detector and the data it collected.

A. Measurement

The instantaneous rate for K^0 decays downstream of a target is:

$$\frac{d\Gamma(2\pi)}{d\tau} \propto |e^{-\tau/2\tau_S + i\Delta m\tau} + \eta e^{-\tau/2\tau_L}|^2, \tag{22}$$

where τ_S and τ_L are the K_S and K_L lifetimes, Δm is the $K_L - K_S$ mass difference, and τ is the kaon proper time. Since $|\eta|$ is small, a 2π event sample from a detector close to a target would be dominated by decays of K_S. In the interference region where the K_S and interference terms in Eq. (22) are comparable ($\tau \approx 12\tau_S$), η_{+-} and η_{00} could be extracted but this requires the relative numbers of K^0 and $\bar{K}^0$ be accurately known. Using separate sources for K_L and K_S decays, one far from the decay volume to give a K_L sample, and the other close for the K_S sample, is the method of choice.

Care must be taken that biases in the relative collection efficiencies of the two samples are minimized. Detector performance can change over time, but the ratio of K_S and K_L in either the $\pi^+\pi^-$ (charged) or $2\pi^0$ (neutral) decay mode should be robust against such changes. Differences in the relative loss of K_S and K_L because of spurious ("accidental") activity in the detector needs to be minimized. Such activity arises from noise in the detector and readout electronics, muons from target and beam dump, neutral beam halo and interactions in detector material, and from decays. Hence the number of decays collected depends non-linearly on primary beam intensity. Biases from changes in accidental losses need to be controlled.

The detector acceptance is a function of the decay position and energy of the kaon. The lifetime difference between the K_L and K_S leads to different distributions of decays and hence different acceptances. The design must provide strict control of biases in these acceptance corrections.

Other K_L decay modes present backgrounds. Detection of $\pi^+\pi^-$ decays compete with $\pi^+\pi^-\pi^0$ and semileptonic ($\pi^\pm \ell^\mp \nu$) decays with branching ratios from 60 to 200 times larger. Similarly, the $2\pi^0$ mode has to compete with the more prodigious $3\pi^0$ mode. The $\pi\pi$ decays must be filtered from these more common K_L decays without trigger bias. For example, in the test run for this experiment [31] we discovered that rejecting $\pi^\pm e^\mp \nu_e$ (K_{e3}) decays at the trigger level from eletron showers in a lead curtain in front of trigger hodoscopes introduced an uncontrollable bias in the relative loss of $\pi^+\pi^-$ decays in the K_L beam relative to the K_S beam. We chose to accept the K_{e3} decays, eliminating them only off-line.

Finally, to extract $Re(\varepsilon'/\varepsilon)$, one measures charged and neutral decays within specified fiducial regions in the center of mass. Since this requires (un)boosting the reconstructed kaons back to their rest frames, the relative energy scale between the charged and neutral modes must be very well understood.

We now describe the principles we used to control these effects.

B. Double Beams and the Regenerator

Two nearly parallel beams were produced by collimating the products of an 800 GeV/c proton beam striking a beryllium target. The detector was located over 100 m downstream, giving ample room for sweeping away charged particles and sufficient time for neutral hyperons to decay. Essentially all of the K_S component of the K^0s and $\bar{K}^0$s produced in the target decayed, leaving two neutral K_L beams (with neutron contamination).

At the upstream end of the decay volume, one of the K_L beams passed through two interaction lengths of boron carbide (B_4C), providing coherently regenerated K_S. Downstream, the $\pi\pi$ decay rate at momentum p is given by

$$\frac{d\Gamma_R}{dz} \propto aF(p)\{|\rho(p)|^2 e^{-z/\gamma\beta c\tau_S} + |\eta|^2 e^{-z/\gamma\beta c\tau_L}$$

$$+ 2|\rho||\eta|cos(\Delta mz/\gamma\beta c + \phi_\rho - \phi_\eta)e^{-z(1/\tau_S+1/\tau_L)/2\gamma\beta c}\}, \tag{23}$$

where z is the distance from the downstream end of the regenerator, ρ is the coherent regeneration amplitude, and a is the beam attenuation. The ratio, $|\rho/\eta|$, was chosen in the 10-20 range (due to the momentum dependence of ρ), so the K_S decay term dominated. In the other (vacuum) beam, the rate is given by

$$\frac{d\Gamma_V}{dz} \propto F(p)|\eta|^2 e^{-z/\gamma\beta c\tau_L}. \tag{24}$$

In both Eqs. (23) and (24), $F(p)$ is the K_L flux. The regenerator alternated between the two K_L beams making $F(p)$ nearly identical and rendering biases from detector asymmetries negligible.

Decays from both beams to a common decay mode, either $\pi^+\pi^-$ or $2\pi^0$, were detected simultaneously. (In the last 20% of the data set, all four of the $K \to \pi\pi$ modes were collected simultaneously. While collecting the $2\pi^0$ and $\pi^+\pi^-$ decays simultaneously is not crucial for the success of our technique, it does allow several more systematic cross checks.) It is particularly important that biases in the collection and reconstruction efficiencies were kept to a minimum by keeping all triggering, reconstruction and analysis cuts strictly independent of the beam in which a decay occurred.

Many of the advantages of simultaneously collecting the K_L and K_S decays to a common mode are clear. Changes in the detector response affect the K_L and K_S decays identically and cancel in the ratio of K_L/K_S (the "single" ratio). Losses due to accidental activity cancel to first order. Intensity fluctuations in the primary proton beam also cancel in each of the single ratios.

A regenerator to produce the K_S decays, rather than using a second target far downstream of the first, was chosen for the following reasons. A closer target generates backgrounds difficult to sweep away. Coherent regeneration produces a sample of K_S decays with an angular spread identical to that of the K_L sample. Also, the momentum distributions of the K_S and K_L samples are quite similar.

The use of the regenerator makes the single ratios physically meaningful. Comparing Eqs. (23) and (24), the incident kaon flux cancels in the K_S/K_L ratio, leaving a measure of $|\rho/\eta|$. Since the same regenerator was used throughout the run, we have a powerful physical check (we should always measure the same regeneration amplitude) to apply to different subsets of the $\pi\pi$ decays.

The regeneration amplitude ρ is related to the difference in the forward scattering amplitudes $f(0) - \bar{f}(0)$ of the K^0 and $\bar{K}^0$ by

$$\rho \approx \imath\pi\frac{f(0) - \bar{f}(0)}{k}Ng(L, p), \tag{25}$$

where $k = p/\hbar$ is the kaon wavenumber, N is the density of scatterers, and $g(L, p)$ (close to unity) is a function of the length L of the regenerator and the kaon momentum. Regge theory predicts [34] that the difference in the forward amplitudes is dominated by the exchange of a single trajectory, the ω. This leads to the particularly simple form for the amplitude difference:

$$\frac{f(0) - \bar{f}(0)}{k} = A p^\alpha e^{-i\frac{\pi}{2}(2+\alpha)}. \tag{26}$$

Analyticity leads to the constraint between the power α and the phase of $f(0) - \bar{f}(0)$, $\phi_{f-\bar{f}} = -\pi(2+\alpha)/2$. In the high momentum region, deviations from this power-law dependence are very small [35].

The expected power-law behavior adds one more physical constraint for controlling biases in the measurement of $Re(\varepsilon'/\varepsilon)$. From the charged and neutral single ratios we obtain a measure of ρ/η_{+-} and ρ/η_{00} whose magnitudes will be identical only if ε' is zero. However, the momentum dependences (power-law) should be the same. Since essentially orthogonal elements of the detector are used for the two modes which have quite different backgrounds, a physical parameter which can be independently extracted and compared gives a powerful systematic check. This is useful in limiting biases due to nonlinear differences in the two energy scales.

There are disadvantages associated with this technique. The most serious one is additional background due to scattering in the regenerator. Diffractive regeneration, where there is a finite momentum transfer between the kaon and a particular nucleus, is present. There are also inelastic processes where a nucleus breaks up or is excited.

Another disadvantage arises from the difference in the K_S and K_L lifetimes leading to different average acceptances. We use a Monte Carlo simulation to determine the corrections needed in the two modes. The acceptance function $\epsilon(p, z)$ is *identical* for the vacuum and regenerator beams. By using large bins (in p and z) relative to the inherent detector resolution, we reduce our sensitivity to smearing effects, generally the hardest aspect of a detector to be simulated accurately.

C. Detector Design

We focus on three aspects in the design of the detector to use the double beams: (a) acceptance corrections, (b) detection of the $K \to 2\pi^0$ decays and background elimination in this mode, and (c) detection of the $K \to \pi^+\pi^-$ and elimination of the background. In both modes we need to reconstruct the momentum and decay position to compare the observed distributions to Eqs. (23) and (24) above.

1. Acceptance Corrections

It was important to make the acceptance calculation as simple as possible. All of the limiting geometrical apertures of the detector were defined by active veto elements. This effectively reduced the problem of determining the acceptance to measuring the edges of several planar counters at known distances from the target.

To study the detector performance and determine the acceptance, we collected high statistics samples in the $3\pi^0$, $\pi^+\pi^-\pi^0$, and K_{e3} decay modes. None of the important parameters of the detector performance, as input to the Monte Carlo, was determined with the $\pi\pi$ event samples used to calculate $Re(\varepsilon'/\varepsilon)$.

2. $K \to 2\pi^0$ Decays

For $2\pi^0$ decays, measuring the energies and positions of the four photons required a high resolution, segmented, electromagnetic calorimeter. The calorimeter had to be sufficiently radiation hard and have a good time response. An array of lead glass crystals, measuring Čerenkov light produced by electromagnetic showers, had been used in FNAL E617 and was reused for this effort.

The largest background at the trigger level came from $K_L \to 3\pi^0$ decays. These could be reduced by requiring four energy clusters in the calorimeter. Because of photons escaping the detector or landing near each other ("fusing") in the calorimeter, background remained. Many planes of veto counters to detect photons escaping the lead glass aperture helped further to reduce the background.

3. $K \to \pi^+\pi^-$ Decays

The $\pi^+\pi^-$ decay required detecting two charged particles. For triggering, we used two hodoscope planes. The trajectories and momenta of the particles were measured using two pairs of drift chambers and a dipole analyzing magnet. The decay position of the kaon was determined by extrapolating the trajectories in the upstream chambers to a common point.

The major backgrounds to $\pi^+\pi^-$ decays, such as $\pi^+\pi^-\pi^0$ and $\pi^\pm\ell^\mp\nu$ were reduced by requiring two symmetric up-down and right-left signatures in hodoscope hits at the trigger level.

With a muon filter, the $\pi^\pm\mu^\mp\nu_\mu$ decays were vetoed at the trigger level. The K_{e3} background was rejected off-line using the ratio of energy from the lead glass to momentum.

Finally, the relative charged and neutral energy scales had to be well known. This was accomplished by calibrating the lead glass with tracks from electron and positron samples measured in the charged spectrometer. The samples came both from special electron calibration runs and from the K_{e3} sample collected simultaneously with the $\pi^+\pi^-$ decays.

D. Sensitivity to Other Kaon Parameters

Examining Eq. (23) shows there is sensitivity to other important parameters of neutral kaon decay. Using the vacuum beam for normalization, we can obtain the incident flux on the regenerator. Then from the shape of the decay distribution immediately downstream, we have good sensitivity to the K_S lifetime, as well as the $K_L - K_S$ interference term, allowing us to probe both the $K_L - K_S$ mass difference, Δm, and the relative phase $\phi_\rho - \phi_\eta$.

III. APPARATUS AND DATA RUN

Here we give a description of the kaon beam, the detector, and special features of the data run. Earlier descriptions and illustrations of various detector elements can be found in references [1,37–39].

A. Kaon Beams

The experiment was located in the Fermilab Meson Center beam line. The two kaon beams were formed by collimating secondaries produced by 800 GeV primary protons hitting a beryllium target. The primary beam was delivered in a 20 second "spill" once every minute, with intensity between 3×10^{11} and 2×10^{12} protons per spill. The protons arrived in ~ 1.8 ns "buckets" at 53 MHz; the instantaneous intensity varied by about a factor of 2 from bucket to bucket. The radiofrequency (RF) timing signal, provided by the proton accelerator, provided the basic timing used in the trigger.

The target was a beryllium rod 36 cm long and 3.2 mm on a side; the proton beam profile was roughly Gaussian with a width of 0.4 mm. The beam position on the target was monitored and read out throughout each spill with a wire chamber.

The neutral beams each subtended a solid angle of 300 nstr were produced using the collimation scheme shown in Fig. 2a. First, there was a 5.8 m long two-hole copper collimator; it began 9 m downstream of the target and contained two tapered channels 5 mrad away from the proton beam horizontally. At the upstream end, the channels each measured 6.65×6.65 mm^2, centered 5.8 mm above and below the target location. The edges of neutral beams were further defined by sets of steel collimators ranging in length from 1.2 m to 1.8 m. Two slab collimators defining the inner beam edges were located at 25 m and 49 m. The outer beam edges were defined by sets of horizontal and vertical collimators at 52 m and 83 m. Charged particles were swept out of the beams with several magnets behind the target and between the collimators.

The neutron production spectrum peaks more strongly in the forward direction than the kaon spectrum, so the 5 mrad "targetting angle" served to decrease the n/K ratio without greatly sacrificing kaon beam intensity. The ratio was further reduced by an absorber of 50.8 cm of beryllium and 7.6 cm of lead positioned just downstream of the copper collimator. This "common" absorber also converted photons, eliminating them from the beams. A second 45.7 cm beryllium "shadow absorber" only in the regenerator beam reduced the rate of interactions in the regenerator.

The entire beam path and decay volume from 17 m to 160 m was held at a vacuum under 0.015 torr. The downstream end of the vacuum was sealed by a 1.22 m diameter window, made from 0.127 mm thick mylar and 0.584 mm thick Kevlar-29 mesh.

The decay region began 110 m downstream of the target. At the entrance to the decay volume, there were roughly equal numbers of K_L and neutrons, and the number of Λ particles was about 0.05% of the number of K_L in the energy range (20 GeV/c to 160 GeV/c) of interest. At the mean energy of 70 GeV/c, the residual K_S component from the target was under 10^{-6}.

A beam intensity of 3×10^{11} protons per spill resulted in roughly 25 million K_L entering the decay volume in the vacuum beam with about 2% K_L decaying in the decay volume.

13
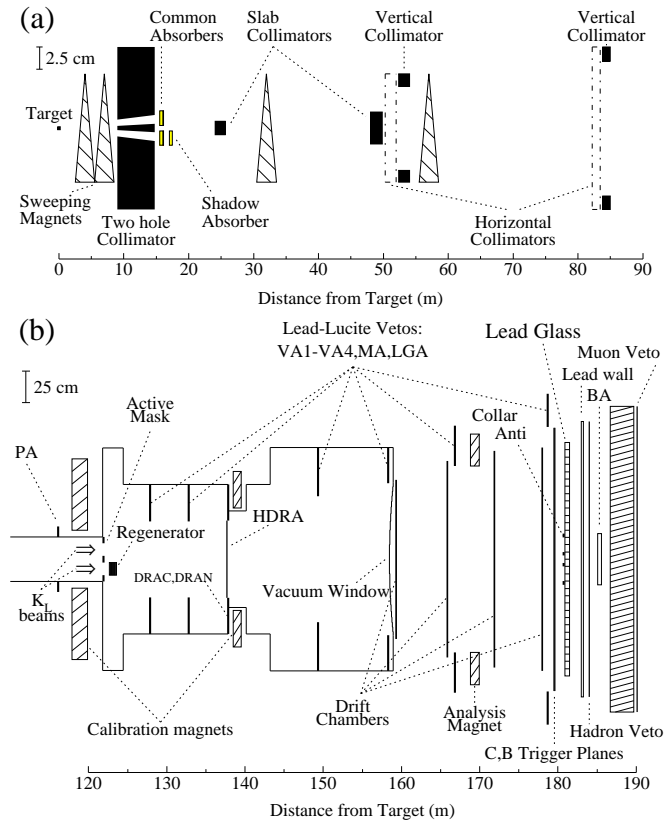
FIG. 2. Illustration of the apparatus used in this experiment. (a) is an elevation view of the layout of the collimation and sweeping system used to produce the two neutral beams. (b) shows the apparatus used to detect the kaon decay products.

TABLE II. The detector elements and their positions from target.

Detector Element	z-location (meter)	Detector Element	z-location (meter)
Pinching Anti (PA)	116.118	Drift Chamber 1	159.292
Sweeper Anti (SA)	119.59	Drift Chamber 2	165.867
Sweeper Magnet	119.59	Magnet Anti (MA)	166.836
Active Mask (AM)	121.893	Analyzing Magnet	168.865
Regenerator	123.550	Drift Chamber 3	171.857
Vacuum Anti 1 (VA1)	127.855	Drift Chamber 4	178.004
Vacuum Anti 2 (VA2)	132.819	Lead Glass Anti (LGA)	178.710
V hodoscope	137.792	C Hodoscope	179.502
Lead sheet	137.804	B Hodoscope	179.520
T hodoscope	137.815	Collar Anti (CA)	180.700
DRAC veto counter	137.826	Lead Glass Array	181.809
DRAN veto counter	137.866	Lead Wall	182.7
Separator Magnet	139.008	Mu1 Hadron Veto	183.996
Vacuum Anti 3 (VA3)	149.309	Back Anti (BA)	185.047
Vacuum Anti 4 (VA4)	158.291	3.2m Steel Muon Filter	186.7
Vacuum Window	158.965	Mu2 Muon Veto	189.914

B. Detector

The apparatus used in this experiment is illustrated in Fig. 2b. A list of the detector elements and their locations is given in Table II. The coordinate system used defines a z axis along the beam direction. The x and y axes are the horizontal and vertical directions transverse to the beam, respectively. Those components which play a role common to both the $\pi^+\pi^-$ and $2\pi^0$ decay modes are described first.

1. Common Elements

a. Regenerator The regenerator, depicted in Fig. 3, consisted of four blocks of boron carbide (B_4C), each $19.0 \times 8.9 \times 8.9$ cm^3. It totalled two interaction lengths which maximizes coherent regeneration. Within each 3.5 cm gap between the B_4C blocks were six $8.90 \times 1.74 \times 0.63$ cm^3 overlapping strips of scintillator. These veto counters reduced backgrounds from inelastic interactions and vetoed kaon decays within the regenerator. A 1.25 cm thick lead piece at the very end of the regenerator converted photons from $2\pi^0$ decays within the regenerator, defining a sharp boundary for the start of the $2\pi^0$ decays in the regenerator beam. The last set of veto counters 1.75 cm downstream of the lead detected conversion products and vetoed $\pi^+\pi^-$ decays. The face of the downstream scintillator defined the start of the decay region for the $\pi^+\pi^-$ mode.

b. Upstream Mask The behavior of the acceptance in the farthest upstream region of the vacuum beam was defined by a precision veto counter (the "active mask" or AM) located

15
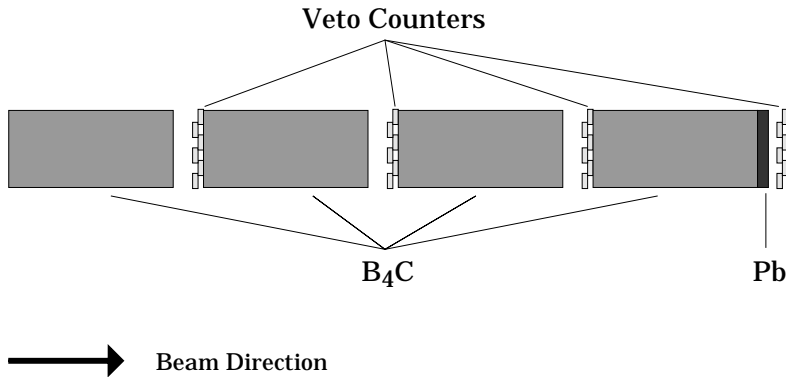
FIG. 3. The makeup of the regenerator.
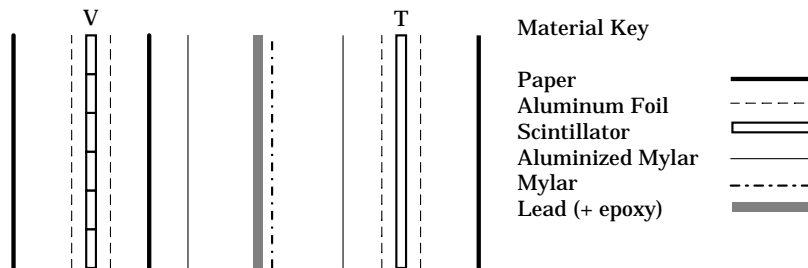
FIG. 4. An exploded view of the material contained within the HDRA. The 0.5 mm lead-sheet, bonded to a mylar sheet for support, was only in place for the neutral mode lead-sheet data subsets.

at 121.9 m from the target. The mask consisted of two layers of 2.54 cm thick lead with scintillator behind each layer. Precise beam holes were milled in the lead and scintillator. The holes were sized and positioned such that (a) decay products from the regenerator beam occurring upstream of the regenerator would miss the regenerator (and its anticounters) and hit the AM; and (b) wide-angle decay products from upstream of the mask in the vacuum beam were detected by the mask and could not hit the "dead" material (such as the box enclosing the regenerator). The locations of the mask edges were determined with electrons from K_{e3} decays.

  c. HDRA   The Hodoscope and Decay Region Anticounter (HDRA) was a trigger and veto system used in both charged and neutral modes. The makeup of HDRA is given in Fig. 4 and Table III. The hodoscopes were originally intended to flag a photon conversion. A 0.5 mm lead sheet converted one and only one photon 25% of the time, leaving a signal in the trigger (T) counters downstream of the lead and none in the veto (V) counters upstream. Both the T and V hodoscopes consisted of six 1 mm thick staves of NE110 scintillator. A more detailed description of this conversion techinique can be found elsewhere [40]. The $\pi^+\pi^-$ running used T and V for triggering (without the lead sheet).

  Initially the $2\pi^0$ and $\pi^+\pi^-$ events were thus collected separately. During the run we found that $2\pi^0$ events with no photon conversion would yield a more accurate result. This allowed the removal of the lead sheet and the extension of the decay volume for $2\pi^0$. Using

16

TABLE III. A list of the materials in the HDRA and their physical properties. The thicknesses are averaged over the beam region, while the radiation lengths are averaged over the illuminated region. The lead sheet was not always present (see text). $(f - \bar{f})/k$ is given at 70 GeV/c.

Material	Thickness (mm)	Density (gm/cm^3)	Atomic Weight	$\frac{f-\bar{f}}{k}$ (mb)	$\frac{f+\bar{f}}{k}$ (mb)	Radiation Length (%)
Scintillator	2.17	1.03	13.0	1.15	33.10	0.497
Mylar	0.11	1.39	96.1	8.29	239.57	0.044
Aluminum	0.05	2.70	27.0	2.07	59.21	0.058
Paper	0.38	0.63	94.1	10.89	229.51	0.066
Lead	0.515	11.35	207.2	9.71	326.28	8.9

the downstream events does, however, require careful measurement of the materials listed in Table III to treat regeneration and conversions.

2. Neutral Detection

a. Lead Glass Calorimeter   The heart of $2\pi^0$ detection was the electromagnetic calorimeter located at 181 m. It has been detailed previously in reference [37]. Fig. 5 illustrates an event in the calorimeter. It consisted of 804 blocks of Schott F-2 lead glass arranged in a circular array with two beam holes. The blocks were 5.82×5.82 cm^2 by 60.17 cm long, about 18.74 radiation lengths. The radius of the array was about 0.93 m.

Ten-stage Amperex 2202 photomultiplier tubes (PMT) with bialkali photocathodes were pressure mounted to the back of each block. The tube gains were roughly 1.2×10^5. Their voltage settings were stable to within a few tenth of a volt throughout the run. A xenon flash lamp system was pulsed every two seconds throughout the run to monitor the combined effects of block transmission and PMT gain; this system worked at the 0.2% level.

Each PMT signal was delayed by 83.8 m of RG58 cable to allow time for the formation of the trigger before digitization. The signals were integrated for 150 ns and digitized in LeCroy 2280 ADCs. (The long gate was necessary because of pulse broadening in the cables and the scintillation component in the lead glass.) The ADC had 12-bit accuracy but operated in dual range mode, extending the dynamic range to 15 bits. The crossover point of the dual range corresponded to roughly 16 GeV, and the gain ratio (nominally 8) was measured for each channel to 0.1% with the K_{e3} sample. When neutral triggers were collected, the readout threshold was 5 ADC counts (about 25 MeV); when only charged events were collected, the threshold was 20 counts.

The light transmission response of the lead glass blocks was non-linear because of absorption of the Čerenkov light. Electromagnetic showers have shower maximum increasing as the energy increases; this results in less attenuation as the light travels to the photomultiplier tube. This attenuation was the most severe and varied most rapidly for the shorter wavelength Čerenkov light, so Wratten 2A filters were placed before the PMTs to block light with wavelengths under 430 nm [41]. These filters (while reducing the total light by a factor
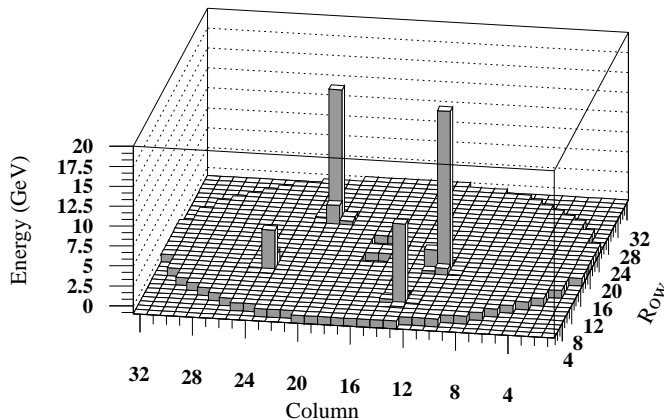
FIG. 5. The lead glass calorimeter with a typical $2\pi^0$ event. The two holes to pass the kaon beam can be seen in the center of the array.

of 2) improved the resolution and simplified the calibration of the glass. Typical absorptions resulted in nonlinearities of $E_{\text{true}} \propto E_{\text{measured}}^{0.97}$.

During the run, the light absorption increased because of radiation damage, particularly for blocks near the center of the array. Transmission decreased by 5% per week in the worst case. To avoid serious degradations in resolution, much of the damage was cured with ultraviolet light supplied by 400 W mercury vapor lamps. Curings were done about once a month and took about 2 days.

For each block, the absorption and gain were determined several times during the run (see Section IV B) from electron samples obtained from special calibration runs and from K_{e3} decays.

The EM shower from an incoming electron develops across several blocks. To reconstruct the total energy in a shower, the energies from a 3×3 array of blocks (a "cluster") centered on the block of maximum energy were summed. This sum was then corrected as described in reference [37] for threshold effects, pedestal shifts, leakage into blocks outside of the 3×3 array, and the nonlinearity described above. These corrections were extensively studied using both EGS simulations and the electron samples.

Photon shower response is somewhat different from that for electrons because of the variation in conversion depth. A photon shower gives a response effectively as the sum of an electron and positron shower in a block shortened by the photon conversion depth t_0. A correction for the photon conversion depth was made on an average, but the variation added an additional contribution to the photon resolution.

The average energy resolution for electrons was described by

$$1.5\% \oplus 5\%/\sqrt{E}, \tag{27}$$

where the energy E is measured in GeV, though it varied from block to block because of variations in attenuation and quantum efficiencies. The overall photon energy resolution

was

$$2.5\% \oplus 5\%/\sqrt{E}. \tag{28}$$

The position of a photon or electron can be extracted from the pattern of energy in the 3×3 cluster. By summing the energies in each column (row) of the cluster and comparing the ratio of the edge sums to the center sum, the x (y) position was obtained. Small corrections to the positions were made using the measured variations of the individual block dimensions from the average. This method gave an average resolution of 2.8 mm; varied from 1.5 mm for a particle near a block's edge to 4.0 mm for a particle in a block's center.

The signals from the lead glass were used for triggering purposes as well as being integrated and digitized. For this purpose, the signals from the array were viewed by two devices in addition to the ADCs.

For fast triggering, the lead glass array was subdivided into 3×3 groups of blocks, and the signals from the blocks in each 3×3 group were sent to an "adder". Each sum was integrated with a 30 ns gate. The short gate helped to identify out of time clusters. The adder outputs were summed together to give the total energy of the calorimeter.

A hardware cluster finder (HCF) counted the number of clusters in the lead glass calorimeter. A cluster refers to a contiguous island of blocks all above the HCF threshold. This led to a factor of ten reduction in the neutral trigger rate. The signal from each block was viewed capacitively, and digitized by a 30 MHz 6-bit flash ADC. A block registered a hit if its energy content was above about 1 GeV, low enough to allow high efficiency and high enough to reduce losses from photon fusions or accidental activity. Details of the HCF construction and the cluster-finding algorithm have been published elsewhere [38,42].

b. Neutral Veto Systems A photon veto counter (the "collar anti" or CA) covered the inner halves of the sixteen blocks around the two beam holes. The counter consisted of 8 radiation lengths (4.45 cm of copper and 2.8 cm of lead) followed by scintillation counters. Its main purpose was to provide a clean and easily determined edge to the detector's photon acceptance.

The remaining photon veto counters rejected $3\pi^0$ decays, and to a lesser degree other charged decays. The counters in most of these veto banks consisted of a scintillator plane followed by two lead-lucite sandwiches, each with 5 layers of lead and of lucite, totalling 3 radiation lengths. Four sets (the "vacuum antis", VA1 - VA4) were arranged in rings inside the decay pipes, two on either side of the HDRA. Another set (MA), in a square ring, surrounded the aperture of the analysis magnet. A final ring was just upstream of the lead glass (LGA).

At the far upstream end there were two sets of counters used to detect photons from $3\pi^0$'s that decayed in the beam pipe preceding the decay volume. The most upstream "pinch anti" (PA) consisted of a layer of lead followed by a layer of scintillator collaring the beam pipe. The "sweeper anti" (SA) consisted of scintillator panels which lined the outside surface of the beam pipe from 117.8 m to 121.4 m. Photons that converted in this pipe section, missing the VAs, were vetoed by these scintillator panels.

A scintillator plane (DRAC) followed by five radiation lengths of 5-layer lead and scintillator sandwich counter (DRAN) filled the area between the T and V hodoscope planes and the vacuum pipe. Decay products outside the T and V hodoscopes struck these and vetoed the event.
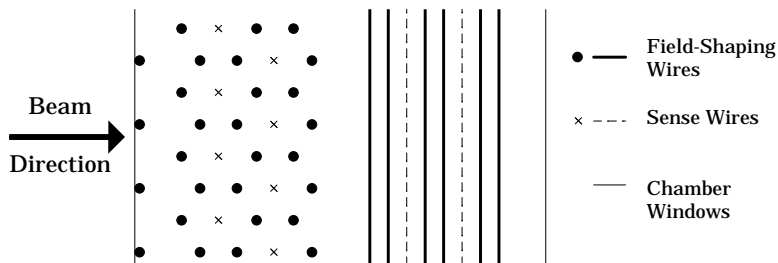
FIG. 6. Layout of the field shaping and sense wires used in all drift chambers. This is the view looking down on the chambers, with the vertical wires which measure x positions in the front (left) and the horizontal wires which measure y positions in the rear of the chamber.

Photons remaining in the beams were detected with the 28.1 radiation length "back anti" (BA) counter, made from 48 layers of 0.33 cm lead sandwiched with lucite. Hadronic showers from neutrons in the beam characteristically deposited energy deep into the BA. By comparing the energy deposit in the last one-third relative to the first two-third of BA, events with photons could be vetoed with tolerable loss from accidental beam neutrons.

Finally, a hodoscope plane (Mu1) downstream of the lead glass helped reject $\pi^+\pi^-\pi^0$ decays in neutral trigger that mimicked the four photon $2\pi^0$ decays. A 21 radiation length lead wall behind the glass, but immediately upstream of Mu1, together with a lead collar around the beam region prevented particles from an electromagnetic shower registering in Mu1. Hadronic showers, however, would light up Mu1 with reasonable efficiency.

3. Charged Detection

a. Drift Chamber Spectrometer   The charged spectrometer consisted of two pairs of drift chambers to measure particle trajectories upstream and downstream of a momentum analyzing magnet. Helium bags were placed between the chambers to reduce the effects of multiple scattering.

As shown in Fig. 6, the cells of the drift chamber consisted of a sense wire located at the center of a hexagon defined by six field shaping wires. The wires in a sense plane were separated by 12.7 mm, and both the x- and y-views of each chamber had two sense planes offset by half that distance. This yielded a maximum drift distance of 6.35 mm perpendicular to a wire and an unambiguous determination of the side of the wire on which a particle passed. The chamber farthest upstream was the smallest, measuring 1.26×1.26 m^2 with 101 sense wires in each plane. The last chamber was the largest being 1.77×1.77 m^2 with 140 sense wires per plane.

The field shaping wires were 100μm gold-plated copper-beryllium and the sense wires were 25μm gold-plated tungsten. The tolerance on wire placement was about 25μm. More details on the construction can be found in reference [40].

The chambers used 50% Argon and 50% Ethane. The drift velocity was of the order of 50μm/ns at $-2650V$.

The applied high voltage was ramped down to 80% of its nominal value during the 40
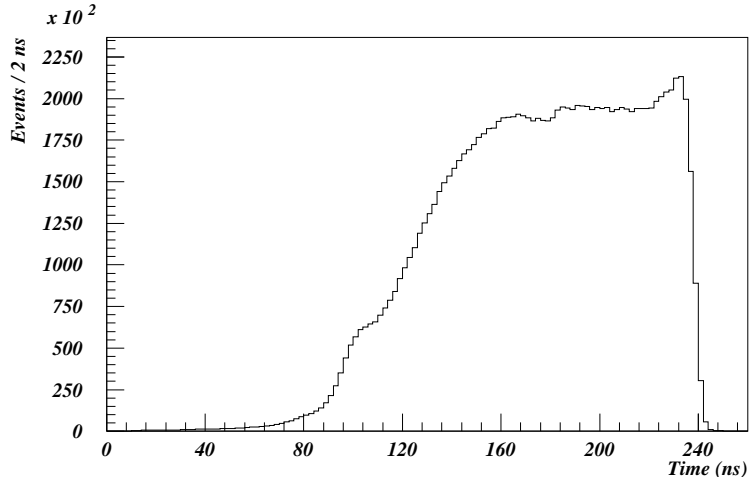
FIG. 7. The distribution of chamber drift times for in-time two track events.

seconds between spills when the dark currents were typically 0.1–0.2 μamps. Also, a small amount of alcohol (about 1%) was added to the argon-ethane as a quenching agent to help prevent breakdown and slow the chamber aging process. Ethanol was initially used, but was replaced later in the run with isopropanol.

The chamber pulses were amplified and discriminated in cards mounted on the chambers. LeCroy 4291B TDCs with a resolution of 1 ns were used. They were operated in *common stop* mode, where an incoming pulse would trigger a channel and a later pulse from the first level trigger would stop all triggered channels from counting further. The resulting inverted time distribution is shown in Fig. 7. The sharp edge near 240 nsec corresponds to tracks hitting a sense wire. A TDC channel was dead for 250 ns after registering a hit. As described in reference [39], the time distribution can be inverted to obtain a conversion from TDC time to a distance from the sense wire. The time to distance conversion assumed that the first drift electrons to arrive at the sense wire were those in the plane of the sense wires.

A 6 kG analysis magnet, with a 1.46 m gap, was situated between the second and third drift chambers. The transverse momentum "kick", $\Delta p_t = (q/c) \int B \, dz$, was typically 200 MeV. Values of $\int B \, dz$ were measured on a 2 inch square grid and were interpolated between grid points. The field map is shown in Fig. 8. There was a very small horizontal field; its effect was negligible, though it did introduce a small bend in a particle's vertical trajectory.

The dipole field was negligible at the chambers, so particles followed straight line trajectories between the upstream and downstream two chambers, greatly simplifying the track finding.

b. Charged Particle Tracking The tracking algorithm used to reconstruct the charged particle trajectories was fairly straightforward. Tracks in the x and y views were found independently. An x track segment candidate, either upstream or downstream, had to have at least 3 of the 4 possible planes hit. A y track was accepted if it had hits on at least 5 of the 8 possible planes. No track segments were allowed to share hits. The drift distance information from the TDCs was used to refine the location of the particle's passage. A least squares fit to the measured points yielded direction tangents and intercepts for each of the

21
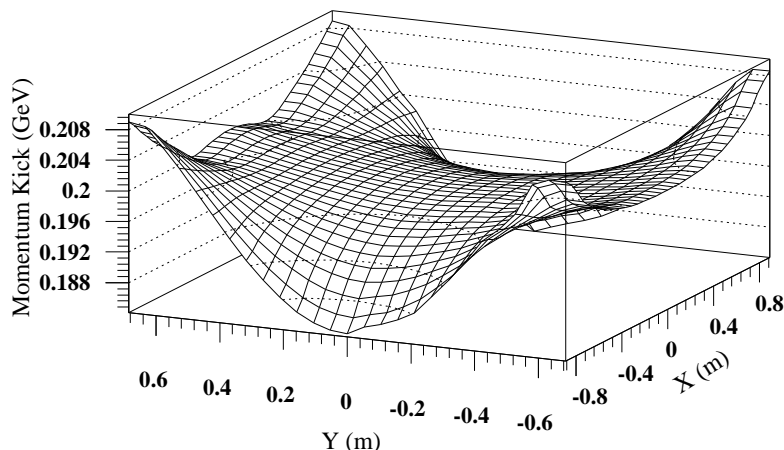
FIG. 8. Transverse momentum kick of the analysis magnet as a function of the x and y position of a charged particle at the "bend plane" of the magnet.

candidate segments. The upstream and downstream segments were projected to the bend plane, and segments were paired if their projections were separated by less than 1.5 cm.

The x and y segments were matched by pairing the tracks using the lead glass cluster positions. After matching, the hit positions were refined once more to correct for small (of order mrad) chamber rotations and differences in signal propagation time along the sense wires (a 6 ns maximum difference). In addition, the upstream and downstream y track segments were refit separately.

An inefficiency in one plane (of order 1%) meant that the "ambiguity" could not be resolved directly. In the x view, the best match of the two candidate track segments (passing on either side of the unpaired wire) with a downstream segment was kept. In the y view, the track fit to the other chambers was used to resolve the ambiguity.

It was useful to examine the sum of the two measured drift distances in one view of a chamber. This sum should equal the 6.35 mm separation in x (or y) of the two wires, though a small angle correction was needed because of the 1.1 cm z separation of the two planes. The deviation of the measured sum from this cell size is shown in the solid histogram in Fig. 9 for events with two valid in-time tracks (see below). The resolution of each plane can be deduced from the width of the central peak. We achieved resolutions in the 95–105 (105–115) μm range for the smaller (larger) chambers.

The low side tail agrees very well with the expected delta ray production. The TDCs were dead immediately after a hit so only delta rays producing ionization arriving *earlier* than that from the primary particle were seen, making the drift distance (hence the sum of distances) appear too small. There was roughly a 0.5% chance per plane per track for a delta ray to cause a mismeasurement of the drift distance by 500μm (5 sigma) or more. The high side tail came almost exclusively from tracks passing very close to the sense wire so that the ionization is drifting longitudinally rather than transversely.

The sum-of-distances provides a means for identifying and throwing away out-of-time tracks. An x or y segment was flagged as out-of-time when 2 or more of the chambers have a sum-of-distance that deviates from 6.35 mm by more than 1 mm (7 sigma). The
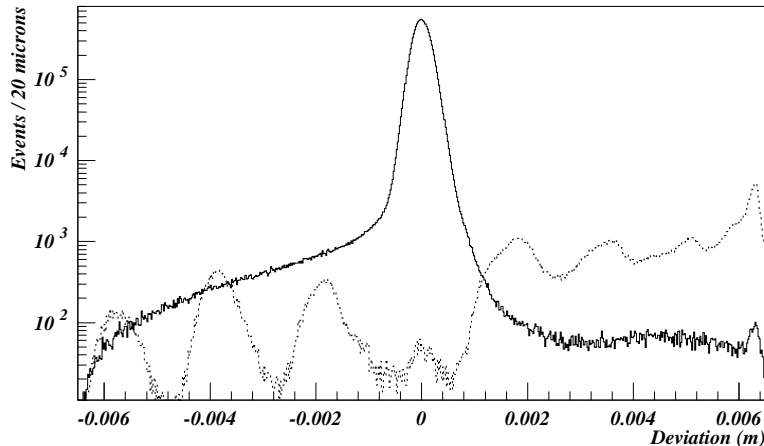
FIG. 9. The deviation of the sum of drift distances from the nominal cell size of 6.35 mm. The solid histogram is the distribution for in-time two track events. The dot-dash histogram is the distribution for tracks that have been identified as out-of-time (see text) in events with two other in-time tracks.

distribution of the sum of distances for out-of-time tracks identified in events with two other in-time tracks is shown as the dot-dashed histogram in Fig. 9. The expected 1.8 mm shift between the peaks can be clearly seen. The pile-up and dilution of the peak structure on the high side (late buckets) is an artifact of the time-to-distance conversion which assigns a maximum drift distance of 6.35 mm to any given hit. The small central peak in the out-of-time distribution results from the small chance to have *very* early false TDC times from δ rays in two separate chambers which each cause a 1 mm mismeasurement of the sum of distance in both of the chambers. The delta rays cause this algorithm to flag in-time segments as out-of-time with a probability of 0.07%, resulting in a 0.28% event loss. By ridding events of the out-of-time tracks, however, there is an 8% recovery of 2 track events, far outweighing the small loss.

Once the particle trajectories were determined, their momenta were deduced by comparing the measured upstream (up) and downstream (dn) direction tangents $\theta_{x,y}$ of each measured track. Since $\theta_{x,y} = p_{x,y}/p_z$, we obtain

$$\left| \frac{\theta_x^{up}}{\sqrt{1 + (\theta_x^{up})^2 + (\theta_y^{up})^2}} - \frac{\theta_x^{dn}}{\sqrt{1 + (\theta_x^{dn})^2 + (\theta_y^{dn})^2}} \right| = \frac{|\Delta p_t|}{|p|},$$

where Δp_t is the transverse momentum kick of the analysis magnet. The average momentum resolution was under 1%, with a dependence given by

$$\frac{\sigma_p}{p} = 0.45[1 \oplus p/(37.5 GeV/c)]\%, \tag{29}$$

where the momentum p is measured in GeV/c. The constant term results from multiple scattering within the spectrometer.

c. Trigger Hodoscopes and Veto Banks   Several planes of scintillation trigger hodoscopes were installed to provide a fast trigger. The downstream end of the charged decay volume

23

was defined by the T and V hodoscopes, described earlier. Two more scintillation planes, the B and C hodoscopes, were located 1.5 m downstream of the last drift chamber. These were made of 1 cm thick scintillator staves which did not overlap.

There was also a bank of scintillator counters (the Mu2 bank) located behind a 3.2 m thick steel wall. This identified muons, both for triggering purposes in special chamber alignment runs (see Section IV A 2) and for rejecting $K_{\mu3}$ ($\pi\mu\nu$) decays in normal data taking runs.

C. Event Triggers

The event triggers were kept independent of the regenerator position and of the beam from which the particle decayed. This approach resulted in triggers with minimal biases and no preference between decays from the vacuum or regenerator beam.

The first level triggers were based on information which could be obtained very quickly, such as the hit patterns in the trigger hodoscopes, the veto counter signals, and the total energy in the lead glass calorimeter. These were formed within about 450 ns of the actual decay. A successful trigger initiated the TDC counting and gated the ADC. The timing for all first level triggers was defined by the 53 MHz RF signal synchronized to the proton bucket structure. A failure at the second level trigger aborted an event before reading it out for event building.

1. Neutral Triggering

The neutral trigger was designed to accept 4 photon ($2\pi^0$) decays as well as some 6 photon ($3\pi^0$) decays, while simultaneously minimizing false triggers from $3\pi^0$ decays with missing and/or fused photons and accidental activity. The heart of the first level neutral trigger required the total energy in the calorimeter to satisfy $E_t > 28$ GeV, greatly reducing accidental triggers. The event was vetoed with a signal in the AM, PA, SA, VA2-VA4, DRAN, MA or LGA. Here VA1 was not used because of the activity in that counter induced by interactions in the regenerator. A BA signal vetoed events with more than 5 GeV in the first two-thirds of that counter and under 10 GeV in the last one-third. Also 25 times minimum ionizing particles (MIPs) or more in the CA vetoed events, well above the level from nearby photon showers in the calorimeter.

Hadronic events (such as $K_L \rightarrow \pi^+\pi^-\pi^0$ decays) were rejected with an energy deposit of 5 MIPs or more in Mu1. Finally, any activity in the regenerator anticounters (RAs) with an energy deposit above 0.8 MIPs vetoed the event.

A factor of ten reduction in the neutral trigger rate within 20 μsec after the event, was obtained by counting isolated clusters in the lead glass with the HCF, as described above. Events with four clusters were accepted as candidate $2\pi^0$ events. We also accepted 0.05% of all first level triggers independent of the HCF information in order to monitor its operation. Some events with 6 HCF clusters were accepted to obtain $3\pi^0$ decays for detector and systematic studies. These were mostly prescaled by 8 except for the last 20% of the run (accepted them all).

24

2. Charged Triggering

A pulse height greater than 1.5 MIPs in the sum of signals from *either* the T *or* the V counters was required.

The B and C hodoscope banks defined a topological trigger which took advantage of symmetry in $\pi^+\pi^-$ decays. In the B bank, at least two distinct paddles had to be hit, with one in the left and the other in the right half. A central counter could satisfy either the left or right trigger requirement. In the C bank, it was required that hits be seen in top and bottom "halves", but again with substantial overlap.

Unwanted $K_{\mu3}$ decays were rejected with the Mu2 scintillator bank. Vetos from signals in the lead lucite counters of the VA4 and LGA banks helped reduce the trigger rate from $\pi^+\pi^-\pi^0$ decays. Studies at the beginning of the run and experience during the test run [40] showed it would be difficult to reject K_{e3} decays in the trigger without bias in $\pi^+\pi^-$ decays.

As in the neutral trigger, the regenerator anti counters vetoed inelastic kaon scatters. Activity in the MA or PA also vetoed an event.

The rate was reduced 30% by a second level trigger requiring hits in the (non-overlapping) left and right halves of the second drift chamber.

3. Other Triggers

There were a number of special purpose triggers collected simultaneously with the $\pi\pi$ triggers. The most important were:

- "Accidental" triggers, to study the effects of random activity in the detector. A scintillation telescope aimed at the target pile, out of the line of sight of the detector, provided a trigger proportional to the instantaneous beam intensity, and independent of activity in the detector.

- The "pedestal" trigger, which randomly triggered the readout of the lead glass with no readout threshold.

- The "flasher" trigger, which flashed the xenon lamp used to monitor the lead-glass photomultiplier tube gains throughout the run.

- The $K_{\mu3}$ trigger, identical to the $\pi^+\pi^-$ trigger, but with Mu2 bank in coincidence.

The special purpose triggers constituted 7% of the recorded triggers. The pedestal and flasher triggers were collected between spills as well as during the spill.

D. Data Collection

The data were obtained between August, 1987 and February, 1988. The sample occupied approximately 5000 9-track data tapes. The details of the data-taking run and of the first data analysis pass are described in detail in references [37] and [38].

The data collection was initially divided into periods with either $2\pi^0$ or $\pi^+\pi^-$ triggers. We alternated collection between charged and neutral running to ensure that we obtained

25

TABLE IV. The characteristics of the $\pi^+\pi^-$ and $2\pi^0$ data subsets.

Subset	Proton Beam Intensity (10^{12} per spill)	Pb Sheet Installed	$2\pi^0$ Triggers to Tape (10^6)	$\pi^+\pi^-$ Triggers to Tape (10^6)
C1	0.3	No	–	16
N1	2.0	Yes	44	–
C2	0.3	No	–	70
N2	2.0	Yes	36	–
C3	0.3	No	–	82
N3	2.0	Yes	22	–
N4	2.0	No	8	–
C4	0.3	No	–	75
NC	0.8	No	61	61

an adequate sample of each mode. The proton beam intensity, the number of raw triggers recorded on tape, and the lead sheet status are summarized for each of these sets in Table IV.

At the end of neutral subset N3, one of the drift chambers had to be temporarily brought off-line. Since the neutral conversion trigger (and the charged trigger) was of no use without all chambers operating, it was decided to study $2\pi^0$ collection without lead sheet (the N4 subset) and with the nonconversion trigger described above. The success of this test lead us to abandon the conversion trigger in favor of collecting $2\pi^0$ and $\pi^+\pi^-$ events simultaneously in subset NC. This was the first time in any experiment that all four of the $K \to \pi\pi$ decay modes were collected simultaneously.

Our first published result [18] was based on 80% of the data in the NC sample, which we call the NCa subset. The results of analyses of each subset are given later.

Special data samples were collected in short runs interspersed throughout the entire run. The most important ones were for calibrating the lead glass and aligning the chamber system. These are discussed in the next section.

The analysis of the data occurred in two stages. A first pass was made through all of the raw data tapes using preliminary calibrations of detector elements and analysis cuts loose enough so that minor changes to the calibrations would not change the final event sample. Candidate event types were split onto smaller sets of data summary tapes (DSTs). The samples obtained included very large samples of K_{e3}, $3\pi^0$ $\pi^+\pi^-\pi^0$ decays, along with samples useful for searching for rare kaon decays.

26

IV. CALIBRATION AND DETECTOR PERFORMANCE

A large effort went into calibrating the lead glass calorimeter and the drift chamber system. The most difficult challenge was to understand the energy scale for $2\pi^0$ relative to $\pi^+\pi^-$ to better than 0.1%. We discuss the use of K_{e3} electrons for the final set of calibrations.

For the acceptance, the positions of the defining apertures had to be tracked accurately over time. A large sample of electrons, again from K_{e3} decays, was used to measure the position of each aperture edge throughout the run. Since one of the apertures was almost 50 m upstream of the first chamber, the best possible resolution was required of the drift chamber system. The alignment of the drift chambers relative to each other and to fixed reference points in the detector was tracked.

A. Drift Chamber Calibration and Alignment

1. Review of Time to Distance Conversion

The time to distance calibration was based on the assumption that the illumination across a cell is uniform. This is a good assumption when averaging over all the cells in a single plane. After correcting for effects like nonuniformities in the response across a drift cell [39], the time distribution (Fig. 7) can be inverted and a signal arriving n nanoseconds after the earliest time corresponds to a distance d_n given by

$$d_n = 0.00635 \left(\sum_{i=1}^{n} t_i / \sum_{i=1}^{N} t_i \right), \tag{30}$$

where t_i is the total number of events arriving in the bin corresponding to i nanoseconds after the earliest time, and N is the total number of bins. This was done separately for each of the 16 wire planes once every several days of running to prevent drifts in the calibration from seriously degrading the resolution. A plot of the resolution as a function of time for the smallest (#1) and largest (#4) chambers in the x view is shown in Fig. 10. When operating conditions were optimal, several planes had better than 100μm resolution.

2. Chamber Alignment

The alignment of the drift chamber system was performed in two steps. The first was internal, where the positions of the chambers were determined relative to each other. The second was an external alignment, where the positions were measured relative to the lead glass calorimeter and the production target, both taken as fixed reference points. The goal was to locate the chambers with a transverse accuracy of 10μm.

The internal alignment involved two procedures: (1) to fix positions of the inner chambers in a coordinate system defined by the two outer chambers, and (2) to remove any residual rotation (about the z axis) between the outer chambers. The external alignment involved the measurement of, and correction for, the apparent "motion" of the production target and the calorimeter.
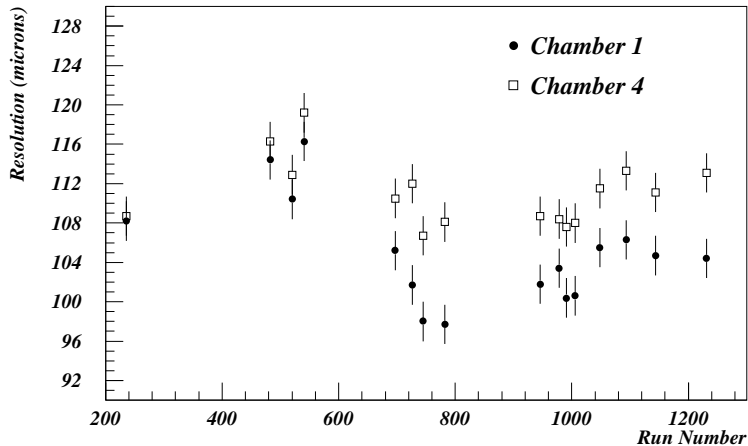
FIG. 10. The average resolution in the smallest (dots) and largest (squares) drift chamber as a function of run number.

TABLE V. Rotation of the horizontal y view sense wires away from the perpendicular x view wires in each drift chamber. For a positive rotation, the horizontal y wires are high on the $+x$ side of the chamber and low on the $-x$ side.

Chamber	Rotation (μrad)
1	0
2	47
3	198
4	-150

The important alignment constants were the transverse offsets for each chamber and the rotation of the chamber about the z axis. The complete set of constants were updated for every day of running in the $\pi^+\pi^-$ data set; the transverse offsets were adjusted two to three times a day.

The relative angles between the x and y planes were taken from a survey of the wires during chamber construction. The deviations from a 90° angle are listed in Table V. These values were verified for consistency with the data, but were difficult to extract. The accuracy on the survey measurements varied from 30 μrad in the smallest chamber (#1) to 20 μrad in the largest chamber (#4).

For the rest of the discussion, we assume these corrections have been made, and hence that the x and y measurements from a given chamber are in an orthogonal coordinate system.

a. Internal Alignment 1: Muon Samples The first step in alignment was to orient the second and third chambers in a system defined by the two outer chambers. The procedure used muons collected with the analysis magnet off. The sample of muons illuminated each chamber fully. Roughly 50,000 muon triggers, accumulated in a few spills, provided an adequate sample for alignment.

Events with out-of-time tracks or accidental coincidences were removed. In addition,
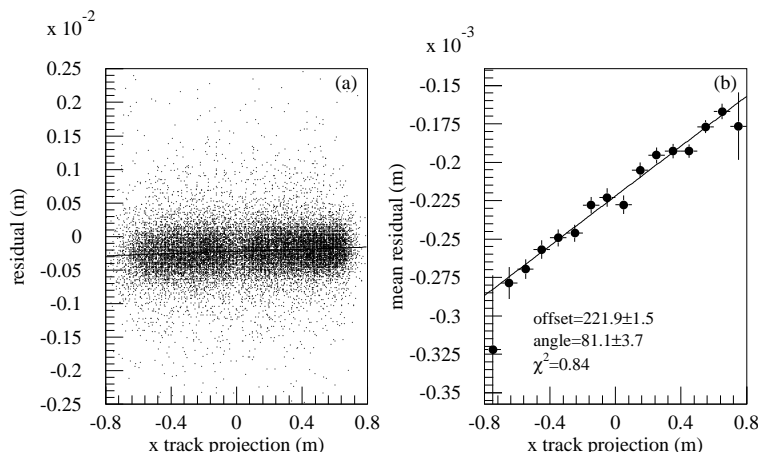
28

FIG. 11. The residual between the measured and predicted position of a muon track in the downstream y plane of chamber-2. (a) The residual versus the x track projection. (b) The variation of the mean y residual with the x position, and the best fit line.

only high quality tracks were accepted: all 8 planes in each view had to have hits, and every sum-of-distance (which uses only drift times and hence is *independent* of the chamber offsets) had to be within 450μm of the nominal cell size. This minimized biases from δ-rays in the offsets.

A line segment in each view was defined by fitting to the x and y track positions measured in the first and fourth chamber. For each plane in chambers 2 and 3, the residual between the fit and the measured hit is plotted versus the track projection in the orthogonal view. Such a plot is shown in Fig. 11a. A linear fit to the mean residual versus position, as in Fig. 11b, yields the offset and rotation for each plane.

In systematic studies, the reproducibility of these measurements was about 5 μm for the offsets and 10 μrad for the rotations.

For each pair of planes in one view of a chamber, the effective separation (relative to the nominal separation of 6.35 mm) can be obtained from the distribution of the difference of the offsets measured in each plane. The measured separation can have contributions both from a true separation and from a chamber rotation about the x (or y) axis. The x view distributions from the alignment data are shown in Fig. 12. The different histograms for chamber 1 correspond to time periods between work on that chamber, where changes in the y chamber rotation shifted the effective offset. To refine the alignment, the two offsets for one view of a chamber were averaged, keeping the separation between the two planes at the average separation in a time period between work on that chamber.

The difference in the rotations between a plane pair can also be measured this way. There are no contributions to the measured difference aside from a true physical rotation of one plane relative to the other. The measured differences were within 8 μrad for all plane pairs, well within our desired tolerance.

b. Internal Alignment 2: Removing Screw Rotations While the above method aligns the inner chambers in a coordinate system defined by the outer ones, possible misalignments of the outer two chambers must be considered. If there is a rotation ϕ around the z axis between the outer chambers, then the coordinate system they define leaves a "screw rotation", where
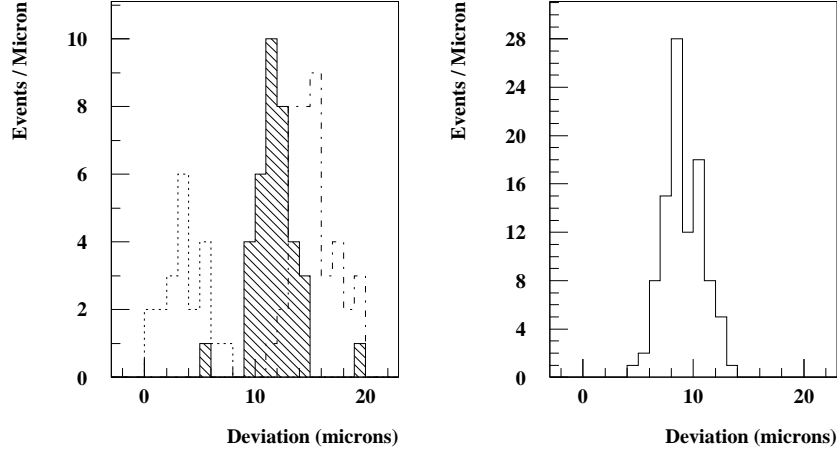
29

FIG. 12. The deviation of the effective separation between two x-planes within a chamber. (a) Chamber-1 – the three different histograms correspond to groups of alignment data between major chamber repair work. (b) Chamber-4 – little work was done on this chamber during the run.

the ith chamber is rotated out of true alignment by an angle $\phi_i = \phi(z_i - z_4)/(z_1 - z_4)$, with z_i the location of the ith chamber. This rotation cannot be removed with single-track events. This effect also prevents the absolute measurement of the angle between the x and y planes mentioned above.

Decays with two charged particles defining a plane in the final state provide the sample for determining the screw rotations.

The trajectories of the tracks coming from the vertex were measured in the two chambers upstream of the magnet. Let us consider the effect due to a rotation between these chambers. Let $\vec{t}_a = (\theta_{x_a}, \theta_{y_a}, 1)$ and $\vec{t}_b = (\theta_{x_b}, \theta_{y_b}, 1)$ be the direction tangents for the two charged particles a and b, respectively. Also let $\vec{x}_{a_i} = (x_{a_i}, y_{a_i}, z_i)$ and $\vec{x}_{b_i} = (x_{b_i}, y_{b_i}, z_i)$ be the positions of the two particles in chamber i ($i = 1, 2$), and let $\vec{r}_i = \vec{x}_{b_i} - \vec{x}_{a_i}$ be the separation vector of the two particles in the plane of chamber i. For the true trajectories, the triple product

$$d_s = \vec{t}_a \times \vec{t}_b \cdot \vec{r}_1 = 0$$

because $\vec{r}_1$ lies in the plane defined by $\vec{t}_a$ and $\vec{t}_b$.

If chamber 2 is rotated by an angle ϕ relative to chamber 1 and this rotation is not corrected, then measured direction tangents become

$$
\begin{pmatrix} \theta_{x_\alpha}^m \\ \theta_{y_\alpha}^m \end{pmatrix} = \begin{pmatrix} (x'_{\alpha_2} - x_{\alpha_1})/z_{21} \\ (y'_{\alpha_2} - y_{\alpha_1})/z_{21} \end{pmatrix}
$$
$$
= \begin{pmatrix} \theta_{x_\alpha} \\ \theta_{y_\alpha} \end{pmatrix} + \begin{pmatrix} 2\sin^2\frac{\phi}{2} & \sin\phi \\ -\sin\phi & 2\sin^2\frac{\phi}{2} \end{pmatrix} \begin{pmatrix} x_{\alpha_2}/z_{21} \\ y_{\alpha_2}/z_{21} \end{pmatrix}
$$
$$
\equiv \begin{pmatrix} \theta_{x_\alpha} \\ \theta_{y_\alpha} \end{pmatrix} + \begin{pmatrix} \delta\theta_{x_\alpha} \\ \delta\theta_{y_\alpha} \end{pmatrix} \tag{31}
$$

for each of the tracks $\alpha = \{a, b\}$. Here $z_{21} \equiv z_2 - z_1$ is the separation between the two
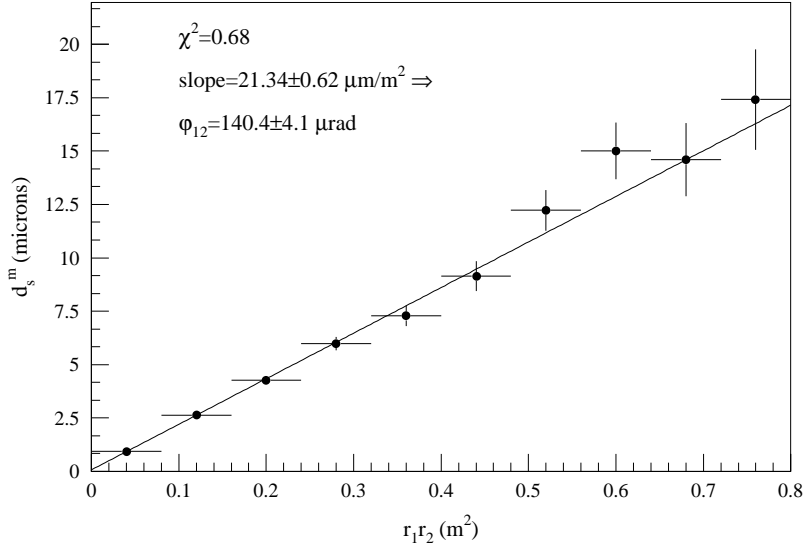
FIG. 13. The variation of the mean of d_s^m with $|\vec{r}_1||\vec{r}_2|$ for one subset of K_{e3} decays. The slope of the fit line is the rotation angle scaled by the separation between the first and second chambers.

drift chambers. The track tangent vectors are distorted by $\vec{t}_\alpha^m = \vec{t}_\alpha + \Delta\vec{t}_\alpha$, with $\Delta\vec{t}_\alpha = (\delta\theta_{x\alpha}, \delta\theta_{y\alpha}, 0)$. This in turn changes the triple product d_s to

$$
\begin{aligned}
d_s^m &= \vec{t}_a^m \times \vec{t}_b^m \cdot \vec{r}_1 \\
&= (\vec{t}_a \times \Delta\vec{t}_b + \Delta\vec{t}_a \times \vec{t}_b) \cdot \vec{r}_1 \\
&= \frac{\vec{r}_2 \cdot \vec{r}_1}{z_{21}} \sin\phi + 2\frac{(\vec{r}_2 \times \vec{r}_1)_z}{z_{21}} \sin^2\frac{\phi}{2}
\end{aligned}
\tag{32}
$$

where we have used the fact that the true triple product vanishes and that

$$
(\Delta\vec{t}_a \times \Delta\vec{t}_b) \perp \vec{r}_1.
$$

The chambers were surveyed into position to limit the size of ϕ to a few hundred μrad, so in our sample $d_s^m \approx |\vec{r}_1||\vec{r}_2|\phi/z_{21}$. We measured the variation of d_s^m with $|\vec{r}_1||\vec{r}_2|$ in the charged mode using samples of K_{e3} decays obtained near the time of each muon alignment. Fig. 13 shows a plot of this dependence for one of the alignments. Since z_{21} is known to better than 0.02%, ϕ can be extracted from the slope ϕ/z_{12} with accuracies in the range of 5 to 10 μrad. Fig. 14 is a plot of ϕ as a function of time throughout the $\pi^+\pi^-$ running. The variation is quite smooth, with occasional breaks or isolated points associated with repair work on the chambers.

A much smaller $\pi^+\pi^-\pi^0$ sample obtained during $2\pi^0$ running was used to measure ϕ for the remaining alignments. These measurements are also shown in Fig. 14. The chambers are not used extensively in the neutral mode, so the poorer accuracy of the $\pi^+\pi^-\pi^0$ measurements does not pose a problem.

Once the absolute rotation ϕ between chambers 1 and 2 was known, the screw rotation was then removed from the entire chamber system. In principle, the measurement of the angle between the x and y views of a chamber could have been refined by studying the
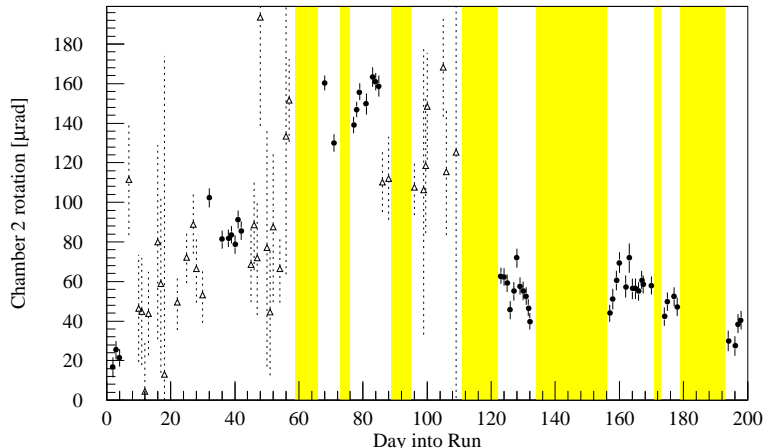
31

FIG. 14. The rotation of chamber-2 about the z axis relative to chamber-1. The solid circles are measurements obtained with K_{e3} decays accumulated in charged mode running. The open diamonds are measurements made with $\pi^+\pi^-\pi^0$ decays collected during neutral running. The gaps correspond to periods when no $\pi\pi$ data was collected due to accelerator shutdowns, etc.

variation in ϕ as the decay plane varied from horizontal through vertical, but the values from the survey were sufficiently accurate for our purposes.

c. *External Alignment* Both the lead glass calorimeter and the target provided fixed points in x and y, giving a line of sight for aligning the chamber centers. The lead glass also provided a reference for the chamber rotation angle about the line of sight.

The electrons from the K_{e3} decays gave the position of the chamber system relative to the lead glass from the comparison of the track projection with the cluster position in the calorimeter. The average difference of the track and cluster positions integrated over the entire calorimeter gave a very good measurement of the average offset between the chamber system and the calorimeter. The resolution on the cluster position measurement was 2.5 mm, and there were ample statistics to obtain the mean positions to better than 10μm.

To obtain the rotation of the chamber system relative to the lead glass, the x (y) difference was studied as a function of the row (column) of the central block. There is a bias in the reconstructed cluster position as a function of the angle of the incoming particle of order 70 μm/mrad; averaging the x (y) track-cluster difference over a row (column) reduces this bias. From uncertainties in the true positions of the blocks, there were nonstatistical fluctuations in the measured difference from row to row and column to column of the order of 50μm. The average trend in the x and y views both imply a rotation of order 300 μrad, with an estimated systematic uncertainty of 50 μrad. The variation in the rotation from alignment to alignment was determined quite accurately.

A large sample of $\Lambda \to p\pi$ decays in the vacuum beam was used to align the chamber system with the target. At our energy, the Λ's could be identified cleanly by requiring $p_p/p_\pi > 3$, and $E_\Lambda > 130$ GeV. Track quality cuts similar to those in the muon samples as well as cuts to eliminate K decays were made.

The average target position measured with the Λ's for one alignment is shown in Fig. 15. The single event resolution was about 3 mm, and there were about 75,000 Λ events in each alignment. The apparent horizontal and vertical motions of the target are shown in
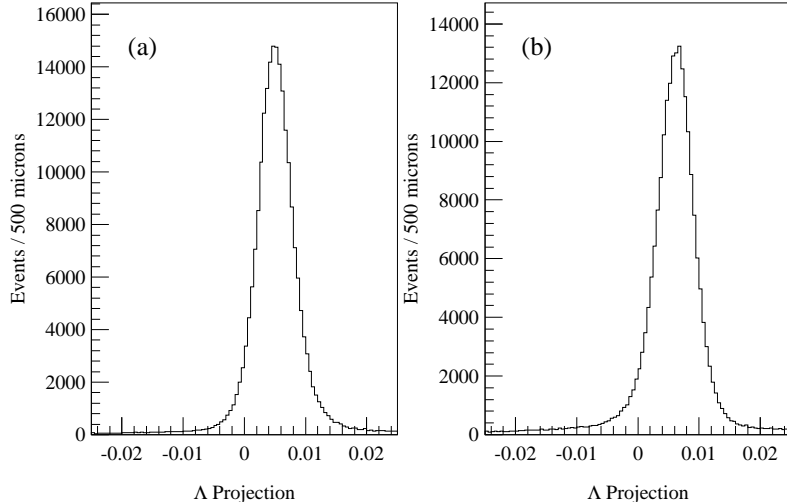
32

FIG. 15. The projected location of reconstructed Λ decays from the $p\pi$ decay mode back to the plane of the target. (a) x projection. (b) y projection.

Fig. 16. The structure is real, corresponding to a shifting of the chambers. A 1 mm shift in the target position corresponds to only a 120μm motion of the upstream chamber. During neutral mode running, the target positions were measured with $K_L \rightarrow \pi^+\pi^-\pi^0$ decays; these are also plotted in Fig. 16. There were sufficient statistics in the Λ sample to track the motion of the chamber system on a much finer time scale than the time between muon runs.

We thus corrected the chamber system alignment once every run, roughly every eight hours of data taking. These adjustments made a small but noticeable improvement in the measurement of the transverse momentum of coherent kaons in $K \rightarrow \pi^+\pi^-$ decays.

This completes the discussion of chamber alignment. Because of the numerous large data samples that we collected using a simple, unbiased, two track trigger, we have been able to successfully track the chamber motion versus time at the 20μm level, where most of the uncertainty comes from the motion of the chambers between alignments. This was beneficial for determining the positions of the critical limiting apertures.

3. Chamber Efficiencies

Many planes had efficiencies of 99% or greater throughout the run. Spot checks of the average efficiency for several planes during charged mode running are shown in Fig. 17.

The inner y plane of chamber 1 was problematic. As seen in the figure, its efficiency degraded as the run progressed. We believe the mechanism for this was the following. This plane became increasingly sensitive to late arriving drift hits as the rate of outgassing within the chamber decreased. The late hits originate in the dead region between the x and the y high voltage planes. As the outgassing subsided, particularly in the smallest first chamber, there were fewer impurities to trap these slowly drifting electrons. Shifting the TDC distribution to view the tail of the distribution for this plane shows a marked difference from an efficient plane (see Fig. 18). There were almost no late times in the efficient plane, while in the inefficient plane there is a broad distribution of late arrival times which reset the

33
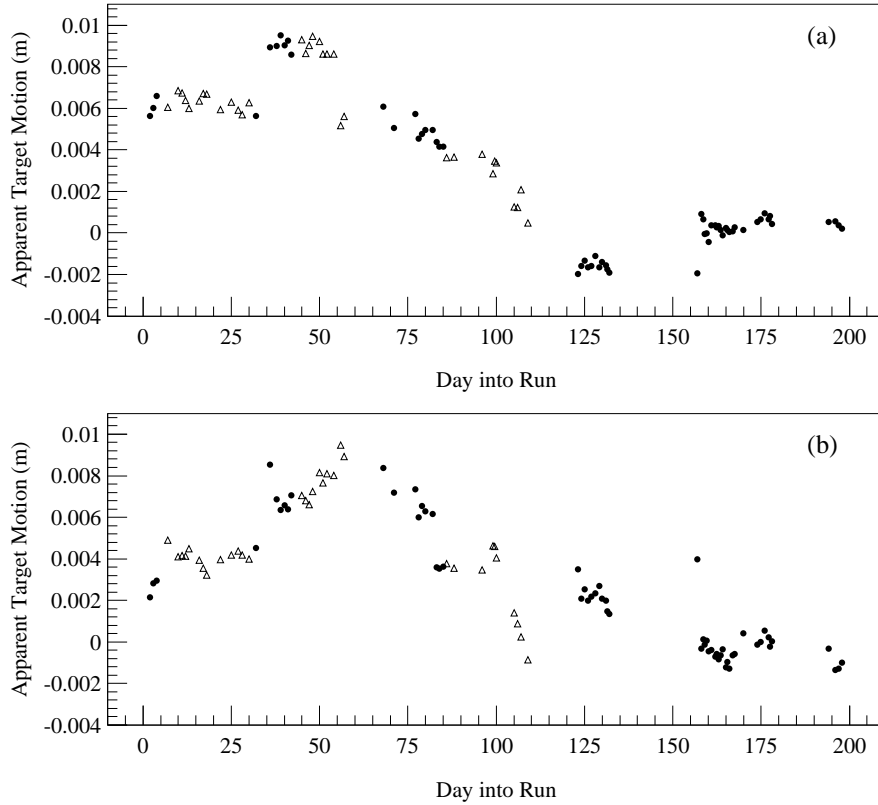
FIG. 16. The apparent motion of the target position due to the motion of the drift chamber system as a function of time into the run. The motion has been tracked with $\Lambda \to p\pi$ decays (solid circles) and $K_L \to \pi^+\pi^-\pi^0$ decays (triangles). (a) Horizontal (x) motion. (b) Vertical (y) motion.
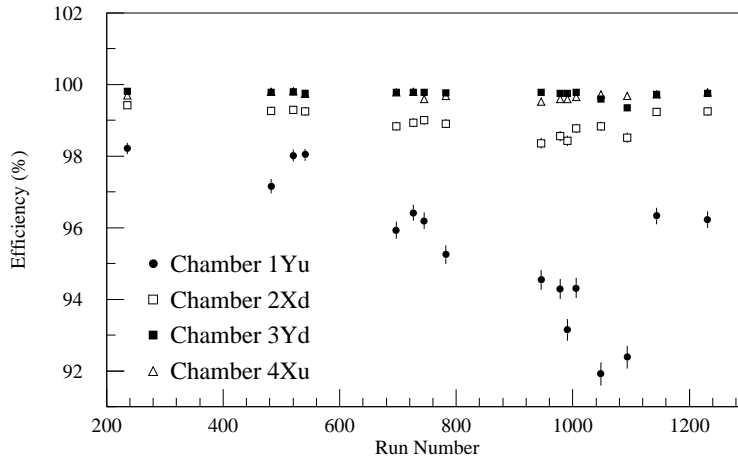
FIG. 17. Chamber efficiencies during several of the $\pi^+\pi^-$ runs. One of the four planes from each chamber has been plotted. These efficiencies were measured using pions. The layers shown for chamber 1 and 2 were the *most* inefficient layers (see text). The other layers in those chambers had efficiencies closer to those shown for chambers 3 and 4.
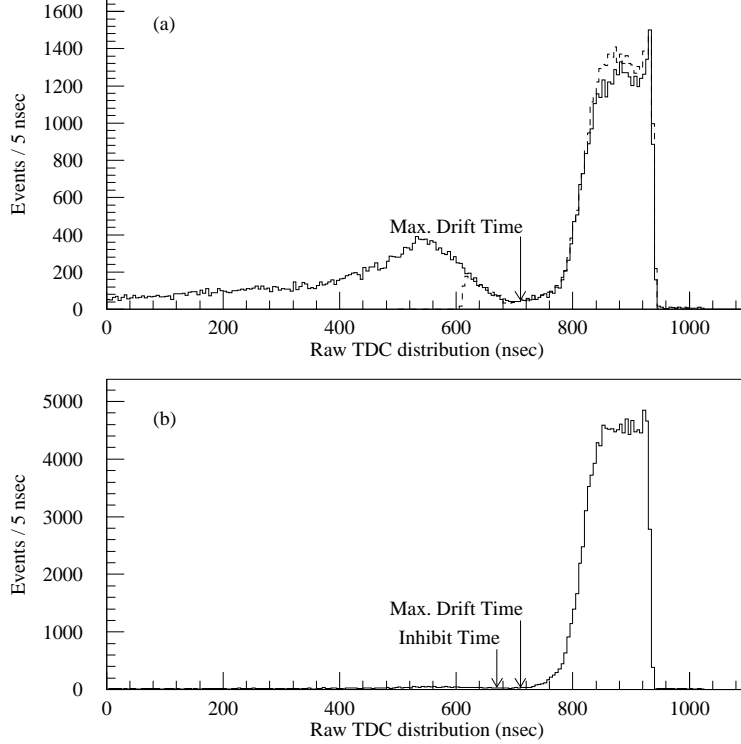
FIG. 18. Raw chamber TDC times measured using a delayed common stop. (a) Inner Y plane of chamber-1. The solid histogram was collected using no inhibit. The dashed histogram was collected with the standard inhibit time relative to the common stop for that chamber. The arrow indicates the position of the maximum drift time used for tracking. (b) Outer Y plane of chamber-4. The small arrow indicates the standard inhibit timing for this plane, and the large arrow indicates the maximum drift time used for tracking. Note the shift of this inhibit time relative to the inhibit timing in (a).

TDC, making the wire inefficient in normal operation. The area under this late arrival peak relative to the area under the signal region is very close to the observed chamber inefficiency.

This problem was alleviated somewhat by bringing inhibit signals to the TDCs as fast as possible. The change in the inhibit timing resulted in the abrupt increase in efficiency in this plane. Because of the distant location of the TDCs from the trigger electronics, it was not possible to inhibit all of the late arrivals, and we were therefore left with a residual inefficiency in this plane. The tendencies are also visible in the inner planes of chamber 2, such as the X plane plotted in Fig. 17, but have disappeared in the two chambers farthest downstream where accidental activity was lower and the inhibit timing more favorable.

The other planes in chamber 1 were not seriously affected by these late hits. The inner x plane had efficiencies similar to the x plane shown for chamber 2, while the outer x and y planes had efficiencies better than 99.5%.

The effect of this inefficiency on $Re(\varepsilon'/\varepsilon)$ turns out to be negligible. On one hand, the tracking efficiency was not seriously affected since the only seriously degraded plane was a y plane in which the tracks do not bend. Since the y track finding requires only at least 5 out of the 8 planes and all of the other planes are very efficient, the change in the probability

35
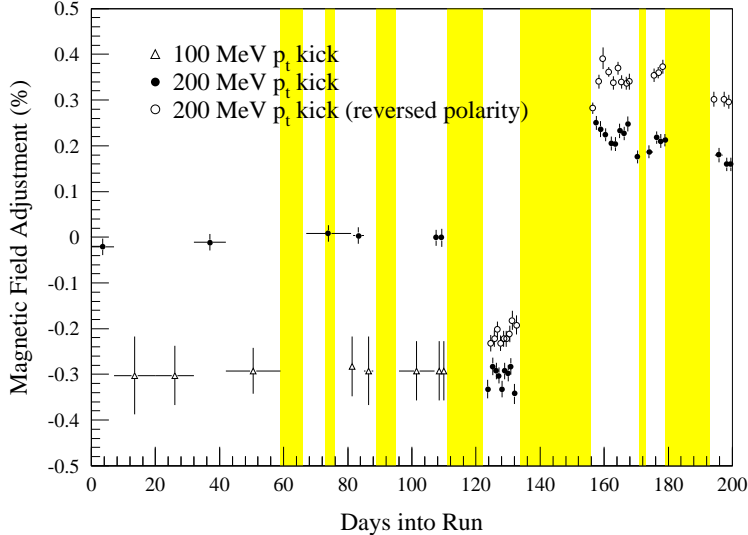
FIG. 19. The magnetic field correction factors. The corrections are grouped into three magnet configurations: "normal" polarity with a 200 MeV p_t kick (solid circles), normal polarity with a 100 MeV p_t kick (hollow triangles), and reversed polarity with a 200 MeV p_t kick.

that we lose a track is small (on the order 10^{-4}). On the other hand, since we collect the decays from the vacuum and regenerator beams simultaneously and the problem occured roughly uniformly across the chamber, the inefficiency affects the K_S and K_L samples almost identically.

4. Momentum Scale

The last component of the chamber calibration and alignment was the tuning of the momentum scale. While a survey of the magnetic field was able to map the shape and obtain the scale at the 0.2% level, the overall scale of the field would change slightly when the magnet polarity was reversed. During the last two charged data sets (C4 and NC), the polarity was reversed about twice per day to allow a possible measurement of the charge asymmetry in K_{e3} decays.

The $\pi^+\pi^-$ mass is given, to a very good approximation, by

$$
m_{\pi^+\pi^-}^2 - 2m_\pi^2 = p_1 p_2 \left(\theta^2 + \frac{2m_\pi^2}{p_1 p_2} \frac{p_1^2 + p_2^2}{p_1 p_2} \right).
\tag{33}
$$

If the scale of the magnetic field shifted by a factor β, then each of the momenta would also be shifted by β. For small β, the dominant effect on the mass is to have $\Delta m_{\pi^+\pi^-}/m_K \approx$ const $\times \beta$. Hence by monitoring the reconstructed $\pi^+\pi^-$ mass, we were able to improve the average accuracy of the momentum measurements, and map the shifts in the magnetic field strength as a function of time, as shown in Fig. 19. A clear shift of 0.1% was seen between the field strengths for the two polarities. A small correction to the assumed ratio between high field strengths and low field strengths was also necessary. Another step about 150 days into the run occurred after work was done on the power supplies for the magnet.

FIG. 20. Mean value of the ratio of cluster energy to track momentum (E/p) versus momentum for electrons and positrons in one of the e^+e^- calibration sets.

B. Lead Glass Calibration

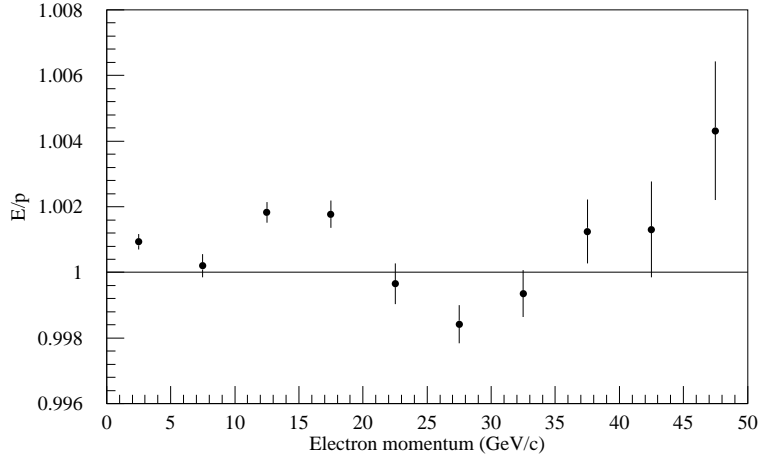The lead glass was calibrated by comparing the momentum of an electron measured in the charged spectrometer to the energy of its shower in the calorimeter. The goal of the calibration was to understand the mean response of the calorimeter at the 0.1% level. The calibration ultimately yielded a measurement of the nonlinearity and the gain for each of the 804 blocks.

There were two types of electrons used for this calibration. The first was obtained from special runs where e^+e^- pairs were created by converting photons in the beam with a copper foil. Calibration magnets upstream of the chamber system (see Fig. 2b) separated the e^+e^- pairs vertically and horizontally so that each particle could be separately tracked in the chamber system. By adjusting the magnet settings, the electrons could be swept to illuminate the entire lead glass array.

The calibration program using these special calibration electrons allowed us to understand the overall calorimeter response within ±0.2% over a 50 GeV range (Fig. 20). The drawback was a lack of statistics, particularly in the few outermost rings of blocks in the array. The outer blocks also suffered because of an insufficient momentum spread needed for the calibration to determine the block nonlinearities.

To probe the calorimeter response further, we turned to an electron sample with much higher statistics. Using the calibration electron gains, it was very simple to isolate the second sample of electrons: those from K_{e3} decays in the data. Almost 40% of charged triggers were K_{e3}'s, leading to a total sample of 120×10^6 electrons potentially available for calibration. For the same calibration shown in Fig. 20, the electron response versus energy reveals a structure (Fig. 21) only hinted at by the calibration electron sample.

Aside from different cuts to clean up the electron samples, the procedure to extract the two calibration constants for each block was essentially identical in both the calibration and K_{e3} electron samples. The calibration procedure and the calibration electron sample are described in detail in reference [37]. A brief review of the model of the lead glass response and its impact on the calibration procedure is given here.
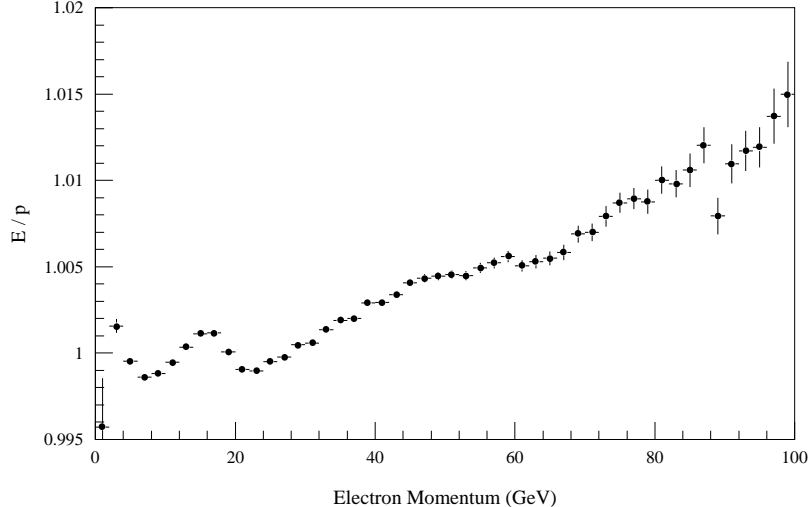
FIG. 21. Mean value of the ratio of cluster-energy to track-momentum (E/p) versus momentum for electrons and positrons from K_{e3} decays using the gains from the e^+e^- calibration set of Fig. 20.

1. Model of Lead Glass Response and Calibration Procedure

Absorption of Čerenkov radiation as it propagates through the lead glass leads to an intrinsic nonlinear response of the calorimeter. This essentially breaks the shower reconstruction algorithm into two pieces: (1) to determine the number of Čerenkov photons present at the back of a block given the observed number n_i of ADC counts in that block, and (2) to determine the energy of the original showering particle given the measured number of photons present in the 3×3 cluster of blocks for that shower. The first step requires the measurement of an effective "gain" for each block. This "gain" is the result of several effects, including the quantum efficiency of the photocathode, the fraction of area of the block covered by the tube, the actual phototube gain, and the conversion constant for that ADC channel. The second step relies on knowledge of the absorption parameter, denoted α, describing the block's absorption per radiation length, and of the variation of the response function, $C(E, \alpha)$, in the Čerenkov light present at the back of the block for an incoming particle of energy E. Here we outline the procedure used to predict the response function $C(E, \alpha)$, and then describe the e^+e^- calibration procedure.

Čerenkov light is produced at an angle $\cos \theta_C = 1/\beta n$, where n is the index of refraction. In the lead glass, with $n = 1.6$, the production angle is 51°, so most of the light produced has to be reflected at least once before reaching the back. Because neighbouring blocks are optically isolated, light not reflected is lost. For particles with $\beta \approx 1$, θ_C is equal to the critical angle for total internal reflection, so the light from shower particles travelling parallel to the longitudinal axis of the block is completely contained within the block. For shower particles produced off-axis, a small amount of light is lost, but we neglect this in our model.

Assuming a uniform absorption parameter α' within a block, the number of Čerenkov photons present at the back of the block for an electron of incident energy E is

$$N(E, \alpha) = \tilde{g} E \int_0^L \tilde{f}(E, \ell) e^{-\alpha'(L-\ell)/\cos\theta_C} \, d\ell, \tag{34}$$

where L is the length of the block, and $\tilde{g}$ is the number of photons produced per GeV. The

function $\tilde{f}(E, \ell)$ is the fractional amount of light produced at a depth ℓ radiation lengths into the block, normalized such that $\int_0^\infty \tilde{f}(E, \ell) d\ell = 1$. Its shape as a function of ℓ is similar to that of a gamma distribution [43]. A block's absorption is always scaled by the same factor $1/\cos\theta_C$, so throughout the analysis we use an effective absorption parameter $\alpha = \alpha'/\cos\theta_C$.

Large number of electron showers were generated using the EGS [44] simulation program to study the longitudinal shower distributions $\tilde{f}(E, \ell)$ and to provide a correction table to map observed signals to true energies. The 18 energies at which showers were generated ranged from 0.25 GeV to 90.51 GeV and were evenly spaced in $\ln E$. We found [37] that the position ℓ_{max} of the longitudinal shower distribution maximum varied with the energy of the incoming particle according to

$$\ell_{max} = 1.022 ln(E) + 3.15 \tag{35}$$

with E measured in GeV and ℓ_{max} in units of radiation length (3.21 cm) of the lead glass.

To obtain the response function $C(E, \alpha)$, $N(E, \alpha)$ was normalized to the total number of photons $(\tilde{g}E)$ produced in a shower and averaged over the ensemble of EGS showers generated at the energy E. The response function was then defined as

$$C(E, \alpha) = \left\langle \frac{N(E, \alpha)}{\tilde{g}E} \right\rangle / c_1(\alpha), \tag{36}$$

where $<>$ denotes the average over the ensemble of showers at energy E. The function $c_1(\alpha) \equiv \exp(-(L - 5.157)\alpha)$ is very close to the response of a lead glass block with absorption parameter α to a 1 GeV electron. This response is also folded into our definition of the "gain", that is, the gain becomes the correction needed to map the ADC counts directly to the true energy for a 1 GeV shower. The function $C(E, \alpha)$ then corrects for the different response at other energies. Most values of α were in the range of 3% to 4% corresponding to corrections in the 1% - 2% range for a typical shower.

The response function $C(E, \alpha)$ was fit reasonably well by a power-law behavior $E = (\sum n_i/g_i)^\beta$, with the power β given by

$$\beta = 1.0053 - 0.9106\alpha. \tag{37}$$

Deviations of the power-law from the proper correction $C(E, \alpha)$ were under 1% [37]. While the deviations were too large to allow simply using a straight power law behavior for the cluster energy reconstruction, the near power-law behavior was still convenient to resolve the conundrum that the final nonlinearity correction depended on the energy E of the original particle, while E is what we need to extract! The response function $C(E, \alpha)$ tends to vary as $\ln E$, so the approximate power-law prediction sufficed to provide an energy prediction E_p that we used to obtain the proper correction $C(E_p, \alpha)$. The calibration procedures also made use of this approximate behavior.

a. Photon Calibration The ultimate goal of the lead glass calibration procedure is to reconstruct the energies of photons from $2\pi^0$ decays. Unfortunately, electrons begin to emit Čerenkov radiation as soon as they enter the glass, while photons do not emit radiation until after an initial conversion. If the photon converts at ℓ_0 radiation lengths into the block, then the photon behaves effectively as the sum of an electron shower with energy $E_{e^-} = \kappa E$ and

a positron shower with energy $E_{e^+} = (1 - \kappa)E$, but in a "foreshortened" block of length $L - \ell_0$.

We can generalize the definition of $N(E, \alpha)$ given in Eq. (34) to depend on the conversion depth, that is,

$$N(E, \alpha, \ell_0) = \tilde{g}E \int_0^{L-\ell_0} \tilde{f}(E, \ell)e^{-\alpha'(L-\ell)/\cos\theta_C} d\ell. \tag{38}$$

After defining $C(E, \alpha, \ell_0)$ analogously to $C(E, \alpha)$, the average electron photon correction $R(E, \alpha)$ can then be calculated as

$$R(E, \alpha) = \int_0^L d\ell_0 \int_0^1 d\kappa P(\ell_0, \kappa)[\kappa C(\kappa E, \alpha, \ell_0) + (1 - \kappa)C((1 - \kappa)E, \alpha, \ell_0)], \tag{39}$$

The probability function $P(\ell_0, \kappa)$ is given by the Bethe-Heitler spectrum,

$$P(\ell_0, \kappa) = (1 + \frac{1}{42\zeta})^{-1} e^{-7/9\,\ell_0}(\kappa^2 + (1 - \kappa)^2 + (\frac{2}{3} - \frac{1}{9\zeta})\kappa(1 - \kappa)), \tag{40}$$

where ζ is the zeta-function. For an absorption parameter α of 4%, the electron-photon difference R has values from 2% to 3% over the energy range of the photons we consider. Understanding this difference between the electron and photon response is very important for the success of the experiment. We evaluate our understanding of the photon response in later sections.

b. e^+e^- electron calibration The procedure used to obtain the first set of calibration constants (g_i, α_i) for each block with the e^+e^- calibration samples utilized the near power-law behavior of the lead glass response. The procedure was an iterative one, where one first corrected the "measured energy"

$$E_m = \sum_{3 \times 3} n_i / g_i \tag{41}$$

(also correcting for thresholds, etc. [37]) to a quantity E'_m that should behave like a true power-law, $E_{true} = E'^\beta_m$.

The momentum p of the electron was measured in the charged spectrometer, and from Eqs. (34) and (36) we see that we should have $E_m/p = C(p, \alpha_i)$, where α_i is the current best guess for the absorption of the central block of the cluster. Using α_i and Eq. (37) to give the best power-law approximation, a correction factor given by

$$d = \left(\frac{C(p, \alpha_i)}{p^{1/\beta - 1}}\right)^{-1/\beta} \tag{42}$$

was applied to E_m to give $E'_m = dE_m$.

A least squares fit to $\ln E'_m$ versus $\ln p$ was then done on an event by event basis – one fit for each block. Each event was weighted with the expected smearing both from the momentum measurement and the cluster energy measurement (see Eqs. (29) and (27)). The slope of the fit gave a corrected power-law β' from which a new absorption for the central block, α'_i was inferred using Eq. (37). The intercept of the plot was taken as the correction to the gain of the central block.

For the final adjustment of the glass calibration we turned to the K_{e3} sample in the vacuum beam. The K_{e3} sample was initially identified by requiring that the ratio of cluster energy to track momentum satisfied $E/p > 0.85$. This left a sample of 120 million events in 5 different data subsets. However, hadronic showers by pions or protons satisfied this requirement several percent of the time, leading to a contamination of several percent. Here we describe the isolation of the electron sample, the study of a structure in the glass response seen at 16 GeV, and the final calibration.

a. K_{e3} isolation The largest backgrounds in the K_{e3} sample came from $\Lambda \to p\pi$ and $K_L \to \pi^+\pi^-\pi^0$ decays. The Λ decays were quite easy to eliminate. For the energies that we are interested, the proton to pion momentum ratio satisfied $p_p/p_\pi > 3$. The Λ's also had to be very energetic in order to live long enough to decay in our decay volume. We are more concerned with rejecting background than preserving signal for this sample, so we reject any event with $E_\Lambda > 100$ GeV and with a $p\pi$ mass within 15 MeV of the nominal Λ mass, minimizing contamination from nongaussian tails on the $p\pi$ mass distribution.

There were several cuts applied to remove $\pi^+\pi^-\pi^0$ decays from the sample. The most powerful was to look at the kinematics of the two tracks, assuming they were associated with charged pions. We could then examine the kinematics of these two tracks assuming that the π^0 was missing [1,45]. The majority of the K_{e3} decays have an unphysical negative value for k_{+-0}, where

$$k_{+-0} = \frac{\left[(M_K^2 - M_{\pi^0}^2 - M_c^2)^2 - 4M_{\pi^0}^2 M_c^2 - 4M_K^2 (P_T^2)_c\right]}{4M_K^2 \left[(P_T^2)_c + M_c^2\right]} = \frac{p_{0_\parallel}^{*2}}{(p_T^2)_c + M_c^2}. \tag{43}$$

Here M_c is the invariant mass of the two charged tracks, $(P_T^2)_c$ is their transverse momentum with respect to the parent kaon, and $p_{0_\parallel}^{*2}$ is the longitudinal π^0 momentum in the kaon rest frame. The $\pi^+\pi^-\pi^0$ was effectively eliminated by removing events that simultaneously satisfied $m_{\pi\pi} < 373$ MeV and $k_{+-0} > -0.04$.

Cuts were also applied to the electron cluster shape. These included cuts on the size of the shower originally designed to eliminate two merged showers, and on the relative track and cluster positions. These reduced contamination of bremsstrahlung and were also effective at eliminating showering pions. Those K_{e3} decays where one track is cleanly identified as an electron were used to show that only about 10% to 15% of showering pions survived the shape cuts.

No cuts were specifically applied to reduce backgrounds from $\pi^+\pi^-$ or $K_{\mu3}$ decays. A $K_{\mu3}$ decay has to be doubly misidentified to make it into the final sample: the pion has to shower and be identified as an electron, and the muon has to fail firing the Mu2 veto. Pions were required to have a momentum greater than 4 GeV/c, and the probability of this double misidentification was of order 10^{-4}. For the $\pi^+\pi^-$ sample there is a several percent chance for one of the two pions to shower and be identified as an electron. When combined with the difference in branching ratios, the background is again expected to be only of order 10^{-4} in the K_{e3} sample. After the electron shape cuts, both these modes had residual contributions at the several 10^{-5} level.

The sample was also required to satisfy K_{e3} kinematics, with $m_{\pi e} < m_{K^0}$ and $p_{\nu_\parallel}^{*2} > -0.005$ (GeV/c)^2, where
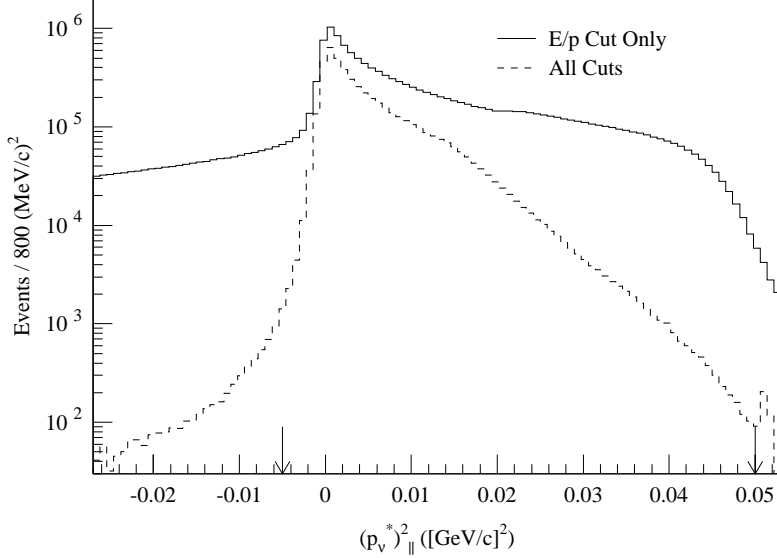
FIG. 22. The K_{e3} kinematic variable $p_{\nu_\parallel}^{*2}$ for K_{e3} candidate calibration events after a loose E/p cut only (solid histogram), and after all but the kinematic cut (dashed histogram). The arrows indicate the analysis cut locations.

$$p_{\nu_\parallel}^{*2} = \frac{\left[(M_K^2 - M_c^2)^2 - 4M_K^2 (P_T^2)_c \right]}{4M_K^2}, \qquad (44)$$

which is the square of the longitudinal neutrino momentum in the kaon center-of-mass. Some resolution smearing is allowed in the latter quantity, which is plotted in Fig. 22 before and after all of the background and misreconstruction rejection cuts (except the cut on $p_{\nu_\parallel}^{*2}$).

Finally, to avoid biases in the momentum and energy measurements, cuts were applied to ensure that the electron track was cleanly reconstructed, and additional cuts were applied on the track projections to keep the electron and pion well separated.

The final distribution of E/p before and after all cuts for the K_{e3} sample from the NC set is shown in Fig. 23. The studies of the lead glass that follow relied most heavily on this set of electrons. From the reduction in the size of the tail on the high side of the distribution, we can see that the background from overlaps has been greatly reduced. The remaining tail on the low side of the E/p distribution is mostly due to electrons that travel some distance down a small gap at the corner of the blocks (caused by a 2 mm bevel along each long edge of each block) before showering, and it could be reduced by rejecting tracks that project near the corners.

b. The 16 GeV structure Since 16 GeV is near the low range to high range crossover point for the ADC modules, there was always the suspicion that a relative high range to low range gain mismatch was responsible for the behavior in E/p versus p in this region (see Fig. reffig:oldKe3Calib). The relative high to low range gain for each ADC channel was measured with a bench test and with the flasher, but it was difficult to get measurements more accurate than several tenths of a percent.

The illustration in Fig. 24 helps clarify the effect. In the ideal case, with the correct high to low range ratio, proper absorptions, etc., the distribution of E/p versus p would be flat. If the absorption was known properly, but there was a gain mismatch between high and
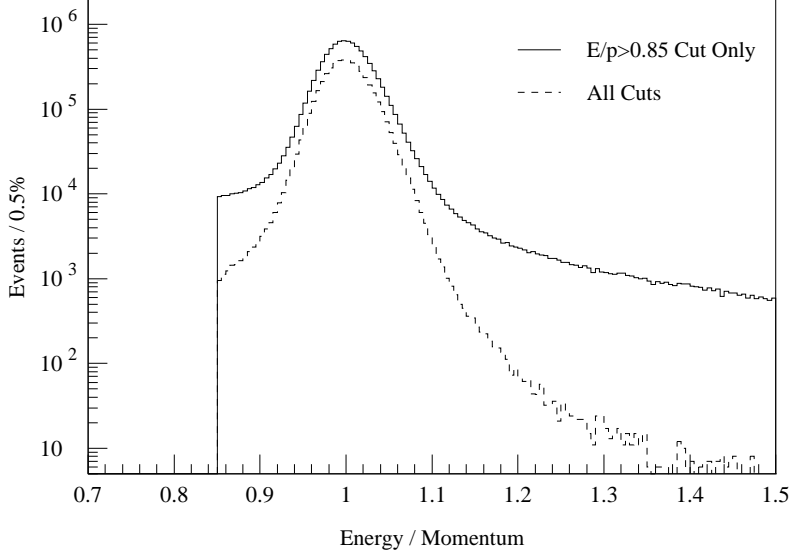
42

FIG. 23. The E/p distribution for electrons in K_{e3} decays with only the initial $E/p > 0.85$ selection criterion and (solid histogram) and with all other cuts (dashed histogram).

low ranges, a step would be introduced in E/p versus p, as in part (a) of the figure. If one tried to find the best nonlinearity, it would partially compensate for the step, fitting a curve similar to the line in Fig. 24a. When we use this new nonlinearity, a measurement of E/p versus p would give the residual between the measured E/p and the fit curve in Fig. 24a, yielding the tilted distributions in Fig. 24b.

This is essentially the structure we see in Fig. 21, except that the structure is blurred by differences in the crossover region and step mismatch from block to block. Using the clean electron sample identified above, we have studied the variation of E/p versus ADC counts for all blocks with electrons extending into the ADC high range. An example is shown in Fig. 25a, with a linear fit to E/p in both the high range and the low range. It is straightforward to show that the necessary fractional correction to the high range gain is simply the difference in E/p measured at the crossover point in the high and low range. We obtained this correction by extrapolating the high and low range fits to the crossover point in that block. After several iterations, the process converged. The distribution of corrections is shown in Fig. 25b. The corrections were reproducible within 0.1% in more than one data sample of K_{e3} decays.

c. K_{e3} Calibration After the above improved measurement of the relative high range to low range gain, and improved measurements of the rate-dependence of pedestal shifts within the ADC modules, each sample of K_{e3} electrons was used to recalibrate. Since the calibration constants from the e^+e^- samples were already quite good, we did not try to make an absolute measurement of the block absorptions as described above. Instead, we assumed any residual between the electron momentum p and the energy prediction $E = E_m/C(p, \alpha)$ would be very close to a residual power-law $p = E^{\Delta\beta}$. The new absorptions were then given by

$$\alpha_{new} = \frac{1.0053}{0.9106} - \Delta\beta \left(\frac{1.0053}{0.9106} - \alpha_{old} \right).$$ (45)

Possible bias still existed from electron bremsstrahlung upstream of the analysis magnet
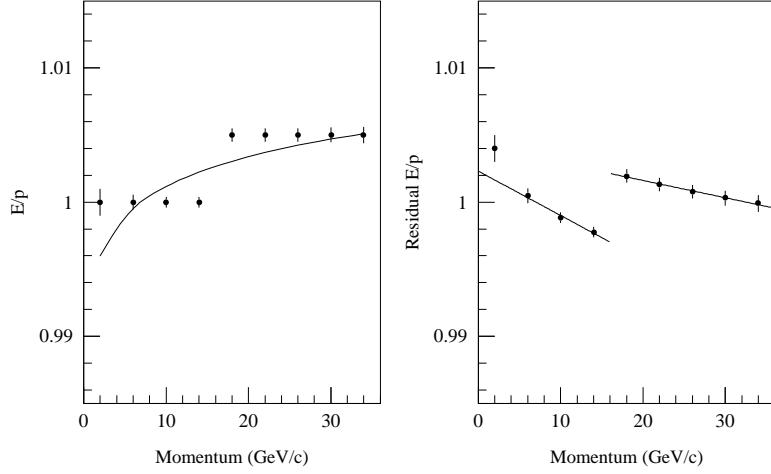
FIG. 24. The distortion introduced into E/p by a 0.5% gain mismatch between the high and low ADC ranges. *Left:* E/p versus p with a gain mismatch, and the best fit nonlinearity which tries to compensate. The errors are representative of those available for an individual block. *Right:* The difference between the distorted E/p and the best fit nonlinearity. The linear fits in the high and low range regions yield a $0.51\% \pm 0.07\%$ measurement of the mismatch.
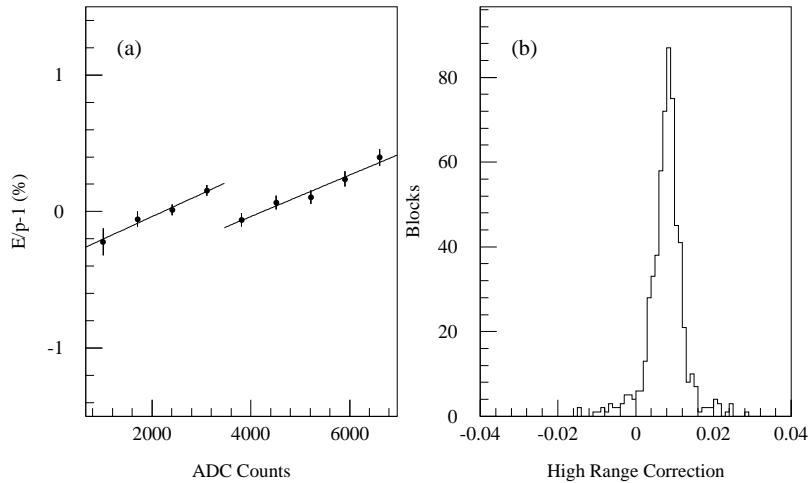
FIG. 25. (a) E/p versus ADC counts for an individual block. The effect of the high range gain mismatch relative to the low range gain, coupled with the nonlinearity fit, clearly stands out. The high range gain was mismatched by 0.6% of itself. (b) The fractional high range gain corrections for each corrected block.
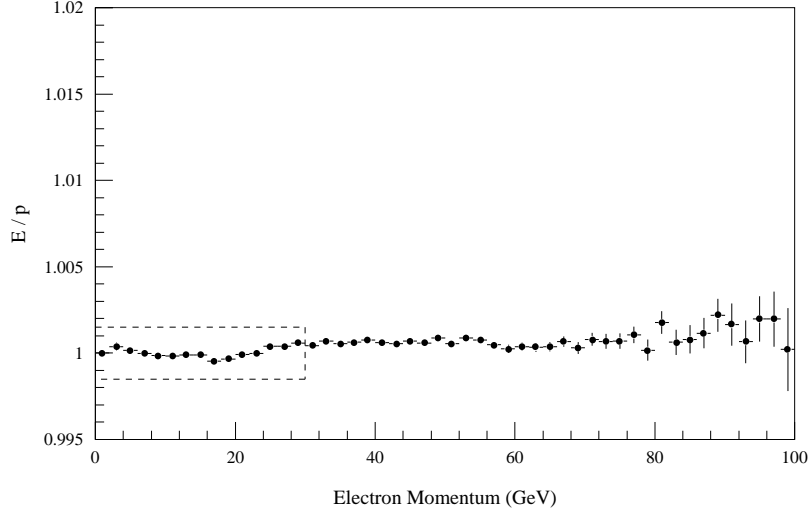
FIG. 26. Mean value of the ratio of cluster energy to track momentum (E/p) versus momentum for electrons and positrons from K_{e3} decays using the K_{e3} calibration gains. The dashed box shows the momentum range used for the calibration.

and from radiative K_{e3} decays. In both of these cases, when the electron momentum is above 40 GeV, the analysis magnet did not bend the electron far enough away from the photon trajectory, resulting in a merging of the photon and electron clusters in the calorimeter. Thus the cluster energy would appear higher than the measured track momentum. While the electron cluster shape cuts should largely eliminate such events, we decided to limit the maximum electron momentum for the NC set calibration to 30 GeV. The minimum momentum accepted was 2 GeV.

After calibration, the resulting distribution of the mean of E/p vs p in the NC set over a 100 GeV range is shown in Fig. 26. The average electron response appears to be understood within 0.1% well beyond the 30 GeV maximum electron energy used in the calibration.

In charged mode sets earlier than the NC set, the readout threshold on the lead glass was 20 counts rather than 5 counts. This made reliable calibration with the lowest energy electrons more difficult. From studies on the NC set with a 20-count threshold simulated in software, the calibration results could be reproduced quite reliably in the inner portions of the array by changing the allowed electron momentum range to be 10 GeV to 60 GeV. In addition, the higher threshold degrades the energy resolution, so an extra resolution term was added to compensate for this when weighting the events. For the outer three rings, where radiation damage was expected to be minimal, the absorptions obtained in the NC set were simply scaled as a group. The measured scale factors were almost flat in time, increasing only slightly as the run progressed.

For neutral mode sets earlier than the NC set, we tried to make the best use of all the calibrations available to obtain the most reliable photon reconstruction. For the inner 10×10 subsection of the array, the e^+e^- samples had sufficient statistics to provide calibration constants. Because the beam intensity was highest during the $2\pi^0$ data taking, this inner portion of the array tended to suffer most from radiation damage in these sets. The e^+e^- calibrations were taken during each set, so they provide the best measure of the absorptions at those times. For the rest of the array, the K_{e3} constants were extrapolated to the neutral sets using the flasher data. The constants from the two sets agreed very well on the boundary

of the 10×10 subsection.

This concludes the discussion of the calibration of the components of the detector needed to reconstruct $\pi\pi$ decays. We now turn to the discussions of reconstruction and background subtraction in the $\pi^+\pi^-$ and $2\pi^0$ decays.

V. $\pi^+\pi^-$ ANALYSIS

In this section we describe the analysis and background subtraction for $\pi^+\pi^-$ decays. For both the $\pi^+\pi^-$ and $2\pi^0$ decay modes, the reconstruction and analysis cuts were blind both to the beam in which the decay occurred, and to the position of the regenerator (in the top or bottom beam). This ensured that regenerator and vacuum beam events were treated identically and avoided a major class of biases. Only after all analysis was complete were the events divided into the regenerator beam and vacuum beam subsets for background subtractions, for comparisons to the simulations, and for fitting. No cuts were applied on decays from one beam that were not applied to decays from the other.

A. Charge Mode Reconstruction

1. Tracking-Related Cuts

The basic requirement for a $\pi^+\pi^-$ candidate was the reconstruction of two in-time tracks (see Section III B 3). To minimize misreconstruction, we applied several track quality cuts. The most basic one was on the track segment χ^2 calculated for a linear fit to the locations of the individual hits measured in the drift chambers. A track "segment" is a trajectory measured in either upstream or downstream pair of drift chambers. The distribution of the reduced track segment χ^2 (i.e. χ^2/n_d, where n_d is the number of degrees of freedom) is shown in Fig. 27 after all other cuts for decays from both vacuum and regenerator beams.

The long tail visible in the χ^2 distribution is populated almost entirely by tracks where one hit has a drift time too small to be consistent with the other hits. This is the behavior expected from early-arriving δ-rays because of TDC dead-time. This observed distribution agrees in absolute level (to 20%) and in shape with expectations from a simple δ-ray production model.

The δ-ray production probability is nearly independent of momentum for our pion momenta, and is also independent of the position in the chambers. As a result, the production probability is identical in the vacuum and regenerator beams so the event loss from the χ^2 cut cancels in the charge mode single ratio, as shown in Fig. 27.

We also cut on the distance d_o (Fig. 28) between upstream and downstream track segment projections at the bend plane of the magnet. The resolution on d_o is

$$\sigma_{d_o}[\text{microns}] = 140 \oplus \frac{3020}{\mathrm{p}_\pi[\text{GeV/c}]}. \tag{46}$$

The first term is due to chamber resolution and the second to multiple scattering. We make a very loose cut – a momentum dependent cut, which corresponding to 6.8 standard deviations on average, though there are non-gaussian tails present.

We require that the two tracks are consistent with originating from a common vertex by calculating their distance of closest approach d_c. The observed distribution for d_c is shown in Fig. 29a for both the regenerator and vacuum beams. The small mismatch between the two beams arises because the resolution on d_c varies (almost linearly) with the distance Δz from the decay location to the first chamber. To eliminate the difference in this distribution introduced by the difference in the z distributions, we cut on the scaled quantity $d_c/\Delta z$
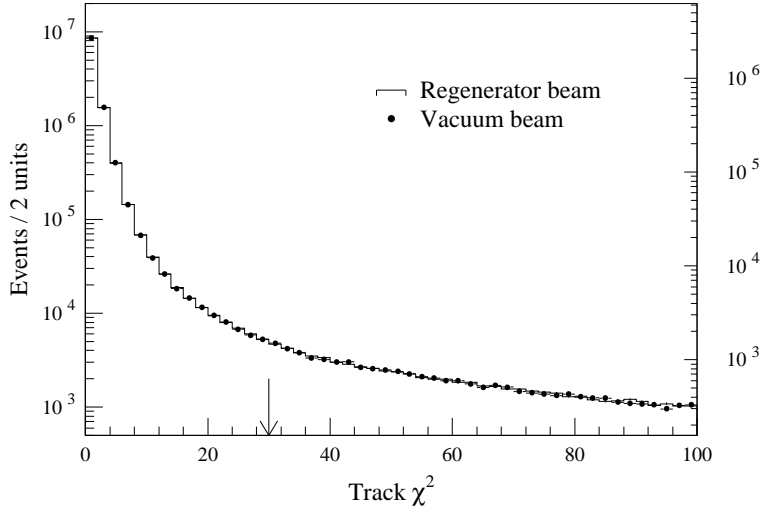
FIG. 27. Track segment χ^2 (per degree of freedom) for the pion tracks from $\pi^+\pi^-$ decays. The histogram depicts the regenerator beam distribution (left scale), and the dots depict the vacuum beam distribution (right scale). The arrow indicates the position of the cut. All but the track quality cuts have been applied.
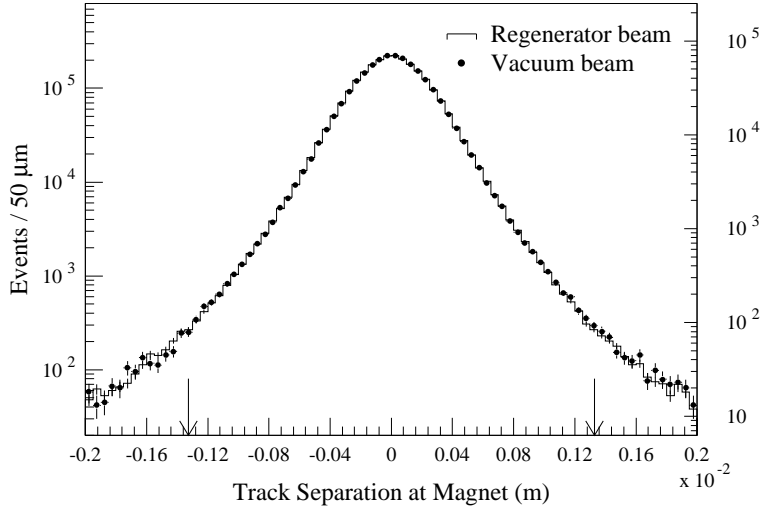
FIG. 28. Separation d_o of upstream and downstream track-segment projections at the magnet bend-plane for the $\pi^+\pi^-$ samples after all other cuts. The histogram depicts the regenerator beam distribution (left scale), and the dots depict the vacuum beam distribution (right scale). The arrows show the cut for an average track momentum of about 20 GeV/c.

48
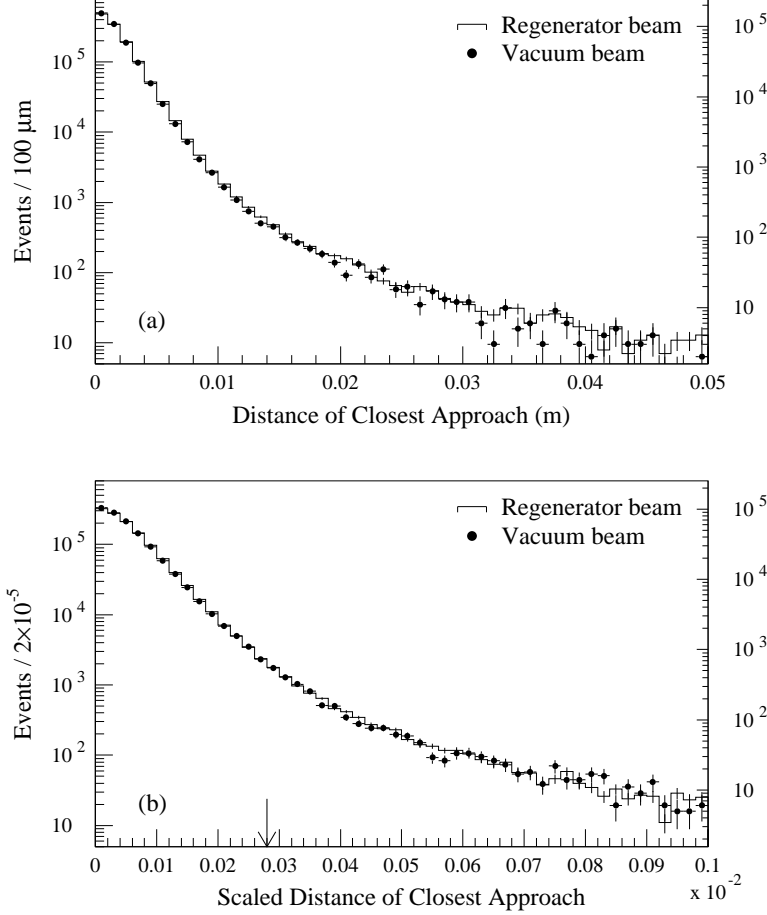
FIG. 29. Distance of closest approach d_c for the two tracks measured in $\pi^+\pi^-$ decays after all other cuts. The histogram depicts the regenerator beam distribution (left scale), and the dots depict the vacuum beam distribution (right scale). (a) Raw d_c. (b) d_c scaled by the distance from the decay location to Chamber-1. The arrow marks the location of the average cut.

shown in Fig. 29b. The tail is due mostly to multiple scattering. The applied cut was $d_c/\Delta z < 4\sigma_{d_c}$, where

$$\sigma_{d_c} = 2.45 \times 10^{-5} + 8.5 \times 10^{-3} \left(\frac{1}{p_1^2} + \frac{1}{p_2^2} \right), \tag{47}$$

with the two track momenta, p_1 and p_2, measured in GeV/c.

The decay vertex was initially defined as the midpoint of the shortest line segment joining the two tracks. We then improved the measurement of the vertex on average by using the fact that the higher momentum pion in a decay suffers less from multiple scattering than the lower momentum pion. Using our initial vertex and two upstream track trajectories as starting values, the vertex and trajectories were refit with the two pion trajectories weighted according to their multiple scattering probabilities and measurement smearing. This led to a 10% improvement in the transverse position resolution on the vertex, for an average resolution (in the x or y view) of 1.0 mm. The z resolution varied from 10 cm at the downstream end of the decay volume to 25 cm at the upstream end (z=110 m).

49

The matching of the x track segments to y track segments was done by projecting to the appropriate cluster in the calorimeter. An ambiguity occurred when the separation of the two tracks in x was small. Because of the left-right symmetry requirement of the trigger, this happened only when the pions were near the center of the array. The matching ambiguity was eliminated by requiring the x separation of the projection of the two tracks to the lead glass to be larger than 2 cm when either pion projected within the two central columns of blocks.

This ambiguity was particularly important in the x view because the x segment carries the momentum information. A similar ambiguity did exist in the matching of the y segments to clusters when a pion landed within the central two rows of lead glass blocks. A mismatch in this view, however, has little effect on the reconstruction because neither the E/p calculation nor the kinematics are strongly affected (see "Kinematics and Background Reduction"); no cut was applied.

<center>*2. Kinematics and Background Reduction*</center>

We now turn to the identification of $K \to \pi^+\pi^-$ decays and rejection of backgrounds. Since $K_{\mu 3}$ decays were largely removed by the trigger, the most copious source of two-track triggers was K_{e3} decays, outnumbering $\pi^+\pi^-$ by two orders of magnitude! These were most important in the vacuum beam. There were also significant contributions from $K \to \pi^+\pi^-\pi^0$ and $\Lambda \to p\pi^-$ decays. The most serious background in the regenerator beam was from kaon scattering in the regenerator itself.

We made fiducial cuts on the tracks at the calorimeter. The resolution for projecting the x or y track segments to the calorimeter is of order 220μm. Events were cut if the tracks projected beyond the inner half of the outer blocks in the array. Tracks were required to project at least 1 mm outside of the CA as well. Events with a track which projected into the beam hole, missing both the CA and the calorimeter, were also removed. We also required that both tracks project within the Mu2 veto bank and that their momentum be greater than 7 GeV/c to ensure efficient rejection of $K_{\mu 3}$.

The K_{e3} decays could be efficiently rejected with little loss of $\pi^+\pi^-$ decays using E/p. The E/p distribution is shown in Fig. 30a for pions and for electrons. The E/p for pions from $\pi^+\pi^-$ decays after all other cuts are applied is shown in Fig. 30b. The distributions shown are after the first analysis which loosely categorized the different decays and eliminated obvious backgrounds. The $\pi^+\pi^-\pi^0$ decays could be isolated from K_{e3} decays using the kinematics of the observed tracks and photons, so no E/p cut was necessary to isolate this sample from K_{e3} decays. This made the $\pi^+\pi^-\pi^0$ sample useful for studying $\pi^+\pi^-$ loss due to the E/p cut.

The peak at low E/p corresponds to pions which do not shower. The difference between the vacuum and regenerator beams in this "minimum-ionizing" peak is due mainly to the difference in the momentum spectra. Since the minimum-ionizing peak is far from the cut, this difference does not affect the fraction of events lost. Furthermore, we generally compare the vacuum and regenerator beam distributions in small kaon momentum bins, so the difference in the overall momentum spectra is not important.

For the final analysis, we require that both pions have $E/p < 0.80$. The electron E/p resolution was about 3%, so only the most pathological electrons survive this cut of almost

<center>50</center>
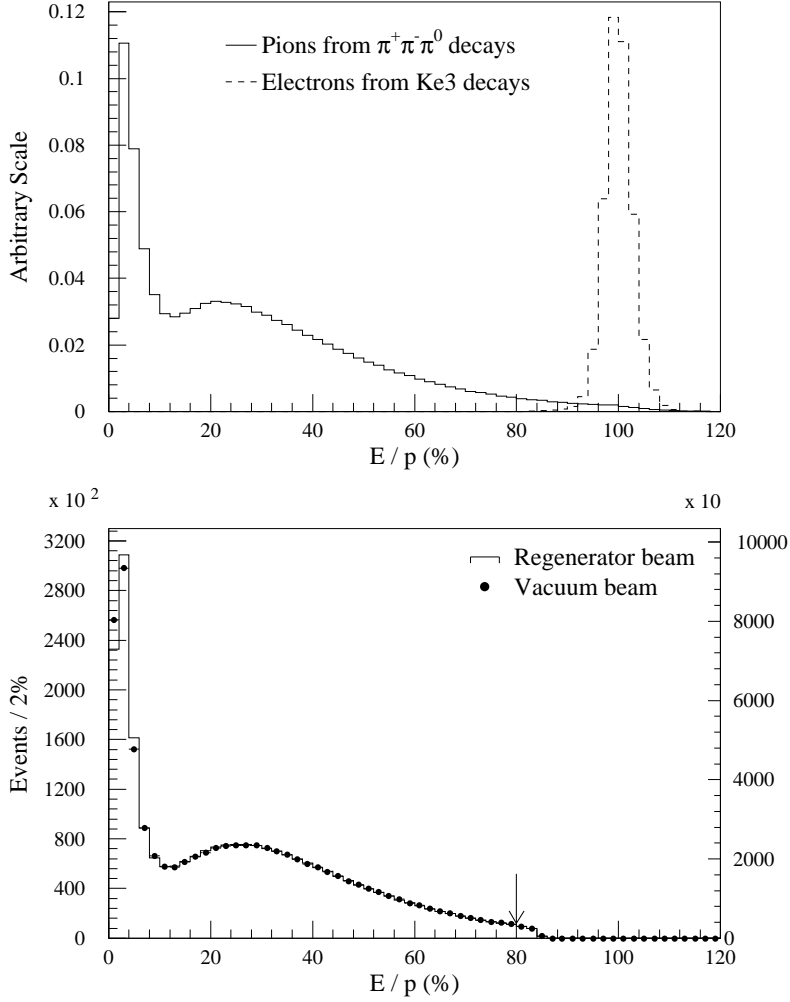
FIG. 30. Shape of the E/p distribution for pions and electrons. (a) The solid histogram shows the spectrum for pions for a subset $\pi^+\pi^-\pi^0$ decays, and the dashed histogram shows the spectrum for electrons for a subset of K_{e3} decays. The normalization of the two samples is arbitrary. (b) The E/p distribution for pions from $\pi^+\pi^-$ decays after all other cuts. The histogram shows the distribution for decays in the regenerator beam (left scale), and the dots show the distribution for decays in the vacuum beam (right scale). The cutoff at 0.85 is a result of the initial loose cut in the initial data reduction analysis pass. The final cut at 0.80 is indicated by the arrow.

51

7 standard deviations. On the other hand, from the E/p distribution in $\pi^+\pi^-\pi^0$ decays, we find that the probability for a pion to have $E/p > 0.8$ is 3.3%. The loss of $K \to \pi^+\pi^-$ decays is then 6.5%, and the K_{e3} rejection is very close to 100%. One possible way for a bias to enter into the vacuum-to-regenerator beam ratio in a momentum bin would be if the regenerator beam pions showered in blocks with a systematically different gain mismeasurement. From the K_{e3} calibrations, the gains of the majority of the blocks are determined at a level of 0.2% of themselves or better. Even in the outer blocks with the least illumination, the gains are known to better than 1% of themselves. Suppose (very unrealistically) that the showering pions from the regenerator beam consistently saw blocks that were 0.3% high in calibration compared to vacuum beam events. From the level of E/p near the cut, this would bias the single ratio by less than 0.01%.

After the semileptonic backgrounds had been reduced, the largest remaining backgrounds, dominated by Λ decays, had hadronic final states. The relevant quantities are the two pion mass,

$$m_{\pi^+\pi^-} = \sqrt{\left(\sqrt{m_\pi^2 + |\vec{p_1}|^2} + \sqrt{m_\pi^2 + |\vec{p_2}|^2}\right)^2 - |\vec{p_1} + \vec{p_2}|^2}, \tag{48}$$

and the $p\pi$ mass,

$$m_{p\pi} = \sqrt{\left(\sqrt{m_p^2 + |\vec{p_p}|^2} + \sqrt{m_\pi^2 + |\vec{p_\pi}|^2}\right)^2 - |\vec{p_p} + \vec{p_\pi}|^2}. \tag{49}$$

To reconstruct the $p\pi$ mass, the track with the greater momentum $(\vec{p_p})$ is associated with the proton (or antiproton).

Only the most energetic Λ's live long enough to reach the decay volume. Since the decay proton carries most of the Λ momentum, these events usually fail the cut which requires that both tracks miss the CA – collar anti. To remove the remaining Λ decays, we use the property that the proton and pion momenta must satisfy $p_p/p_\pi > 3$. After all other cuts, 19% of the remaining $\pi^+\pi^-$ candidates have a track momentum ratio greater than 3. We plot $m_{p\pi}$ for this sub-sample in Fig. 31, showing separate distributions for decays with $E_\Lambda > 100$ GeV and $E_\Lambda < 100$ GeV. There is clearly no Λ signal below 100 GeV, and in fact, the signal does not appear until the Λ energy is above 130 GeV. Conservatively we eliminate any $\pi^+\pi^-$ candidate if it satisfies $E_\Lambda > 100$ GeV and has a mass $m_{p\pi}$ in the range from 1.10 GeV/c^2 to 1.13 GeV/c^2. The resolution of $m_{p\pi}$ measured in the Λ sample was 2.1 MeV/c^2. The Λ mass cut was left quite broad to keep background from nongaussian tails at a negligible level.

Λ decays are not noticeable in the regenerator beam; nevertheless, the samples were treated identically.

Our resolution on the $\pi^+\pi^-$ mass (Fig. 32) is 3.5 MeV/c^2, and we isolate the sample using a cut on the mass from 484 MeV/c^2 to 512 MeV/c^2, completely eliminating $\pi^+\pi^-\pi^0$ decays. No cuts are made in the $\pi^+\pi^-$ analysis on clusters in the calorimeter unassociated with tracks since hadronic showers can produce spurious clusters.

The broadening of the lower half of the $\pi^+\pi^-$ mass distribution due to the radiative decay $K \to \pi\pi\gamma$, common to both the K_S and K_L, is clearly visible. The background in the wings of the vacuum beam distribution is from residual semileptonic decays. This is only visible in the regenerator beam distribution at high mass where it is not hidden by the
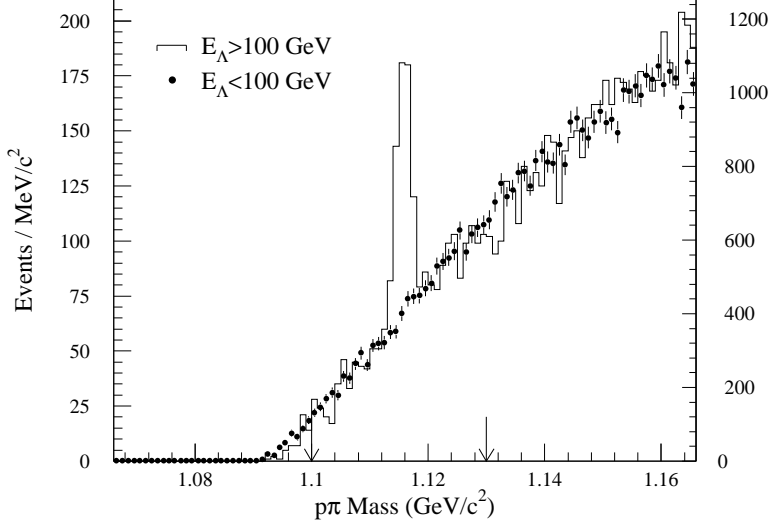
FIG. 31. Reconstructed $p\pi$ mass for all $\pi^+\pi^-$ decay candidates in the vacuum beam which are consistent with $p_p/p_\pi > 3$. All $\pi^+\pi^-$ analysis cuts except the Λ rejection cuts have been applied. The Λ peak is visible for $E_\Lambda > 100$ GeV (solid histogram, left scale), but not for $E_\Lambda < 100$ GeV (dots, right scale). The arrows indicate the mass cut used on events with $E_\Lambda > 100$ GeV.

radiative tail. The K_L radiative decay has a contribution from decays where the photon is emitted directly from the interaction vertex as well as from inner bremsstrahlung [45,46]. The photon from the direct emission process tends to be energetic in the K_L rest frame so the resulting $\pi^+\pi^-$ mass is shifted outside of the signal region. The remaining direct emission contribution to $Re(\varepsilon'/\varepsilon)$ is quite small and is estimated to be about 0.05×10^{-4}.

In Fig. 33, the mass distributions for the entire data set are shown with the distribution from the NC set used for our initial result [18]. The shapes are quite similar even though the NC set was collected at three times the proton intensity of the other subsets.

The final kinematic cut requires that the reconstructed momentum of the kaon from $\pi^+\pi^-$ candidate is nearly parallel to the incident kaon trajectory. For each $\pi^+\pi^-$ candidate, the square of the transverse momentum, p_t^2, was calculated by assuming that the kaon had scattered in the regenerator (see Fig. 34). The scattering angle θ between the initial and final kaon trajectories is then used to calculate the square of the transverse momentum:

$$p_t^2 = p_K^2 \sin^2 \theta. \tag{50}$$

Since the distance from the target to the regenerator is large compared to the length of the regenerator, this p_t^2 calculation is insensitive to the location of the scattering site inside the regenerator. This cut reduces both the residual semileptonic background in the vacuum beam and the diffractive and inelastic $\pi^+\pi^-$ backgrounds in the regenerator beam. We use the same calculation of p_t^2 for the vacuum and regenerator beams to avoid bias in losses of coherent kaons due to the smearing of the measured p_t^2.

The p_t^2 distributions for the two beams are plotted in Fig. 35. In the regenerator beam, the decays with large p_t^2 are from kaons which regenerated inelastically. Near the coherent peak, the contribution from diffractively regenerated kaons, with a steeper p_t^2 spectrum than the inelastically regenerated kaons, results in the upturn in the spectrum, as seen in Fig. 35c. The bulge in the distributions just outside the p_t^2 cut of 250 $(MeV/c)^2$ is due to the radiative
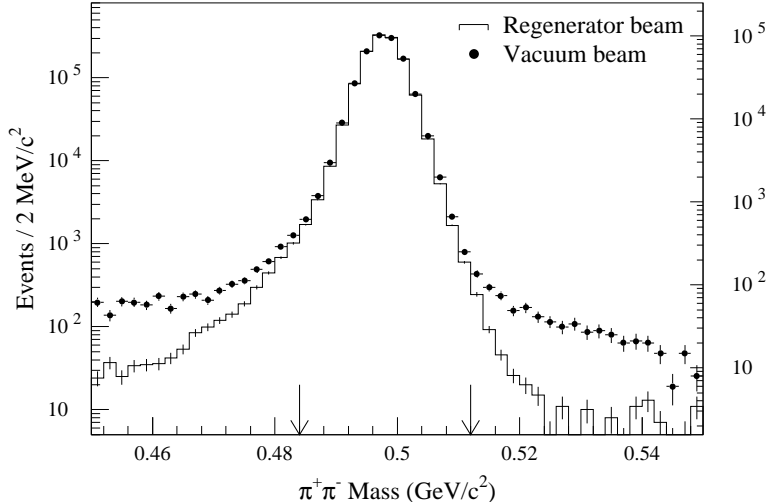
FIG. 32. The reconstructed two-pion mass for $\pi^+\pi^-$ candidates after all other cuts. The regenerator beam distribution is given by the histogram (left scale), and the vacuum beam distribution by the dots (right scale). The arrows indicate the position of the cuts used in the analysis. The radiative tail from $K \to \pi^+\pi^-\gamma$ decays is clearly visible in both beams.

decay $K \to \pi\pi\gamma$. The semileptonic decays give the steeply falling tail in the vacuum beam, as seen in Fig. 35d. The very small, flatter component visible at larger p_t^2 in the vacuum beam distribution is consistent with interactions of the beam with residual gas in the decay tank.

3. Other Cuts and Summary

The final class of cuts was designed to reduce potential biases from the acceptance correction. Accidental activity in the detector could sometimes cause an event to satisfy the trigger even though the decay products themselves would not. Since the accidental activity is common to the vacuum and regenerator beams, we expected the gain of events from this process to be identical in the two beams. However, to make comparisons between the data and the Monte Carlo samples more meaningful, we reverified the triggers using the reconstructed tracks. We required the reconstructed decay vertex to be upstream of the HDRA, the hits on the track in the second drift chamber to satisfy the east–west trigger requirement in that chamber, and the B and C hodoscope counters through which the tracks project to satisfy the trigger logic for those counter banks.

In addition to the trigger reverification, we also rejected decays where the tracks projected to within a few millimeters of the limiting apertures. This reduced the sensitivity of the charged sample to the exact location of these apertures. For decays in the vacuum beam upstream of the mask, both tracks had to pass through the mask aperture for the proper beam.

For coherent Monte Carlo events that are in our final sample, the fractional loss due to each cut is shown in Table VI. The momentum range in the table relevant to the $Re(\varepsilon'/\varepsilon)$ measurement is 40 GeV/c to 160 GeV/c; 20 GeV/c to 160 GeV/c is used for the remaining measurements. The distribution of kaon energy after all other cuts have been made is shown
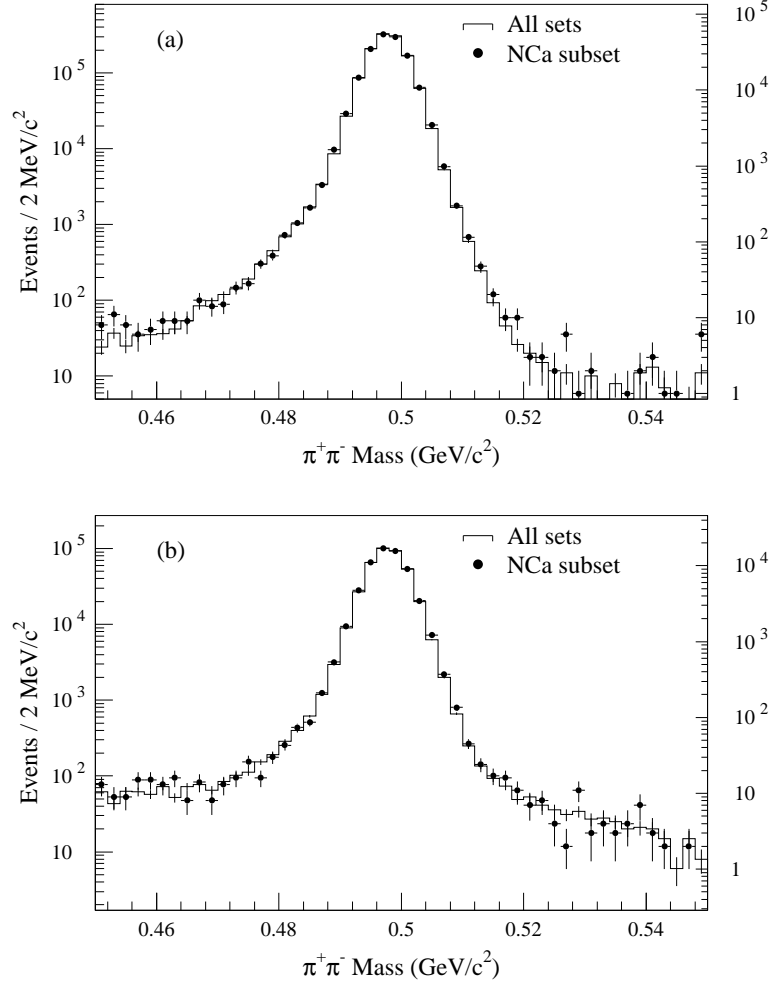
FIG. 33. The reconstructed two-pion mass for $\pi^+\pi^-$ candidates after all other cuts for the entire $\pi^+\pi^-$ data set and for the NC subset only. The histogram shows the distribution for the entire data set (left scale), and the dots show the distribution for the NCa subset (right scale). (a) Regenerator beam. (b) Vacuum beam.
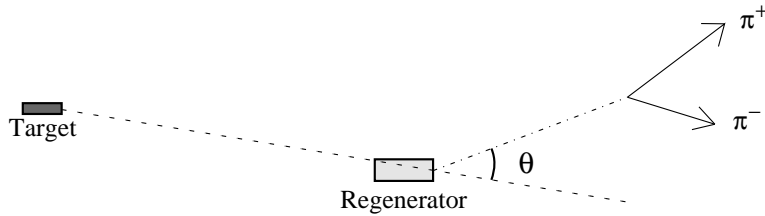
FIG. 34. Schematic representation of the method used to calculate the kaon scattering angle in the regenerator. The momenta of the two pions measured in the drift chambers (solid lines) are combined to determine the kaon trajectory. The kaon is then projected from the decay vertex to the downstream face of the regenerator (dot-dash line). The original kaon trajectory is defined by the line connecting the projected kaon position at the regenerator to the target. The scattering angle θ is the angle between the two trajectories.
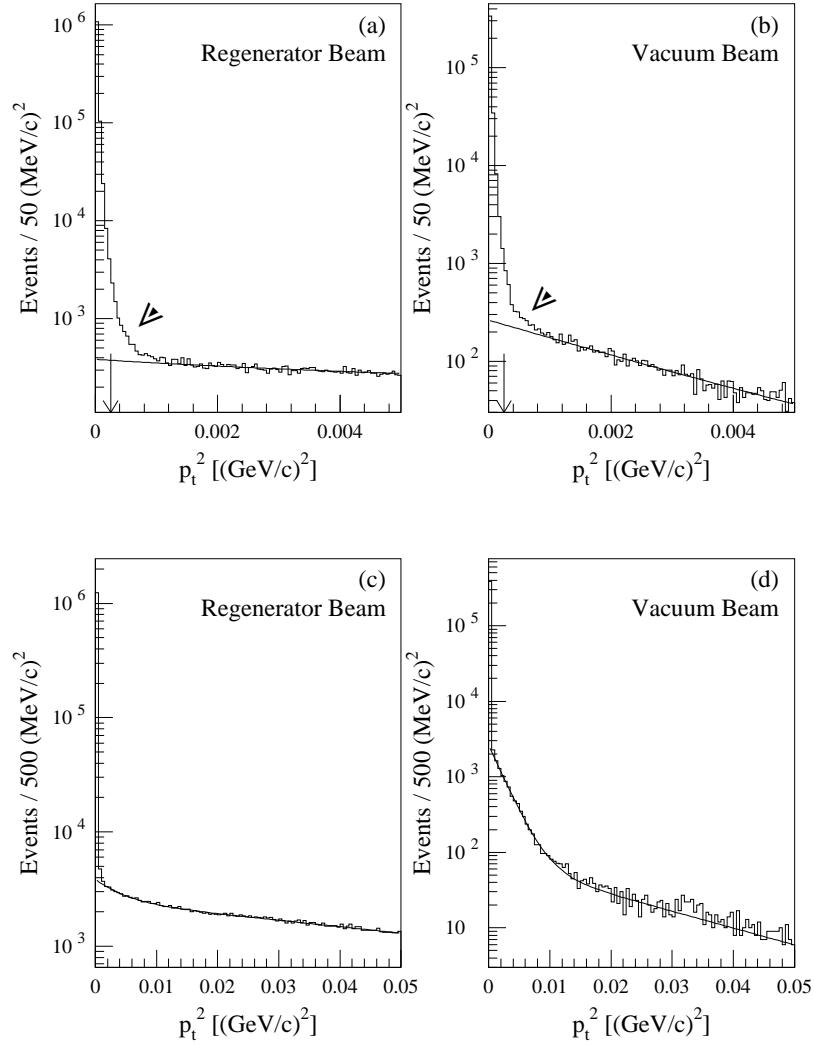
FIG. 35. The p_t^2 distribution for $\pi^+\pi^-$ candidates after all other cuts are applied for two different ranges of p_t^2. Parts (a) and (b) show the distribution for $p_t^2 < 5000\ (\mathrm{MeV}/c)^2$ for the regenerator and vacuum beams, respectively. At this scale, the structure of the coherent peak, the location of the analysis cut (vertical arrow) and the radiative tail (hollow arrow) from $\pi^+\pi^-\gamma$ decays are all visible. Parts (c) and (d) show the distribution for $p_t^2 < 50,000\ (\mathrm{MeV}/c)^2$ for the regenerator and vacuum beams, respectively, where the contributions from different background sources (see text) are more apparent. In all four parts, the solid line is the best fit to the overall background shape.

TABLE VI. The fraction of coherent $\pi^+\pi^-$ decays lost as each analysis cut is applied sequentially, and when a cut is applied as the final cut. For the first sequential cut, the loss is relative to the number of $\pi^+\pi^-$ events which reconstruct within the fiducial energy and z region used in the fits. Each cut thereafter is normalized to the number of kaons left after the preceding cut. Here "K_L" and "K_S" have been used as shorthand for the vacuum and regenerator beams, respectively. The two momentum ranges are given in GeV/c.

Analysis cut	Sequential loss (%)				Loss as Final Cut (%)			
	40–160		20–160		40–160		20–160	
	K_L	K_S	K_L	K_S	K_L	K_S	K_L	K_S
Pions within calorimeter	3.77	4.68	7.12	7.93	1.09	1.35	2.14	2.49
Vacuum Window Aperture	0.04	0.05	0.15	0.22	0.02	0.03	0.11	0.16
Analysis Magnet Aperture	0.55	0.74	1.16	1.62	0.30	0.40	0.73	1.16
HDRA Aperture	0.03	0.01	0.05	0.02	0.02	0.00	0.04	0.01
Tracks Remain in Helium Volume	0.02	0.09	0.30	0.44	0.02	0.07	0.29	0.47
Λ cuts	2.71	1.98	2.38	1.75	0.56	0.34	0.48	0.30
$p_\pi > 7$ GeV/c	3.16	3.38	4.10	3.87	0.79	0.91	1.41	1.13
Track χ^2 [a]	0.04	0.05	0.04	0.05	0.02	0.02	0.02	0.02
Distance of Closest Approach	0.95	0.94	0.90	0.91	0.86	0.89	0.79	0.83
Track Separation at Magnet	0.04	0.05	0.06	0.06	0.03	0.04	0.05	0.04
$\pi \to \mu\nu$ decay veto	1.86	2.09	2.29	2.41	2.23	2.47	2.69	2.80
Mask Aperture	1.00	0.01	0.92	0.01	1.06	0.00	0.95	0.00
No pions in CA or beam hole	21.99	21.05	19.68	18.84	19.38	18.54	17.23	16.50
Chamber 2 Trigger Reverify	0.01	0.00	0.01	0.00	0.01	0.00	0.01	0.00
BC Hodoscope Trigger Reverify	1.89	1.95	1.92	1.92	1.74	1.80	1.77	1.77
$\pi^+\pi^-$ Mass	1.36	1.39	1.47	1.54	0.39	0.40	0.40	0.42
p_t^2	0.55	0.48	0.49	0.43	0.55	0.48	0.49	0.43

---

[a] Without $\delta - rays$. See text for loss estimates from $\pi^+\pi^-\pi^0$ studies.

in Fig. 36 for both the regenerator and vacuum beams. The similarity in the spectra for the two beams is apparent. The vertex distribution for the $K \to \pi^+\pi^-$ decays ("z distribution") from the production target after all other cuts is shown in Fig. 37. The downstream end of the regenerator is associated with the sharp edge at 123.5 m in the regenerator beam. The fall-off in the rate of accepted decays upstream of 120 m in the vacuum beam is governed by the upstream active mask, which cleanly defines the acceptance in the upstream region.

B. $\pi^+\pi^-$ Background Subtraction

After applying the cuts discussed above, the residual backgrounds in the $\pi^+\pi^-$ decay mode were typically 0.1% to 0.3%. They could not, however, be neglected in the measurement of $Re(\varepsilon'/\varepsilon)$. For both samples, the background is estimated by fitting the shape of the p_t^2 spectrum in the range 1500 (MeV/c)^2 to 20,000 (MeV/c)^2, and extrapolating underneath

FIG. 36. Distribution of the kaon energy for the final $\pi^+\pi^-$ sample. The arrows mark the location of the cuts used in the $Re(\varepsilon'/\varepsilon)$ analysis. (a) Vacuum beam. (b) Regenerator beam.

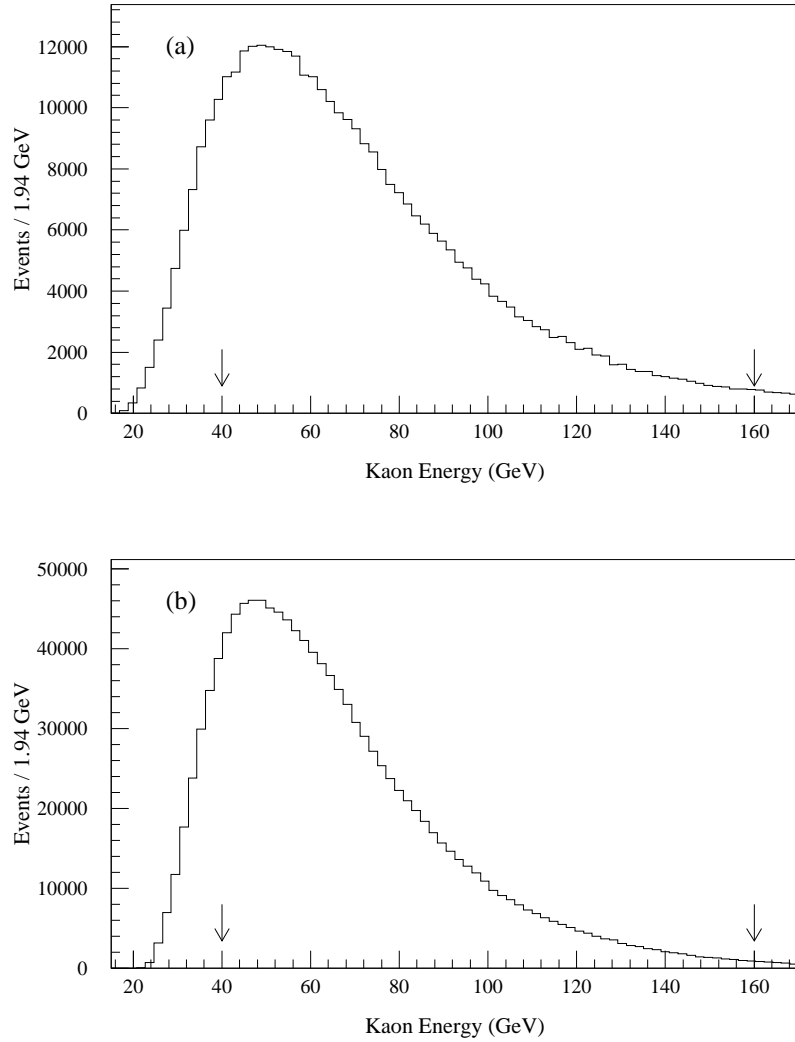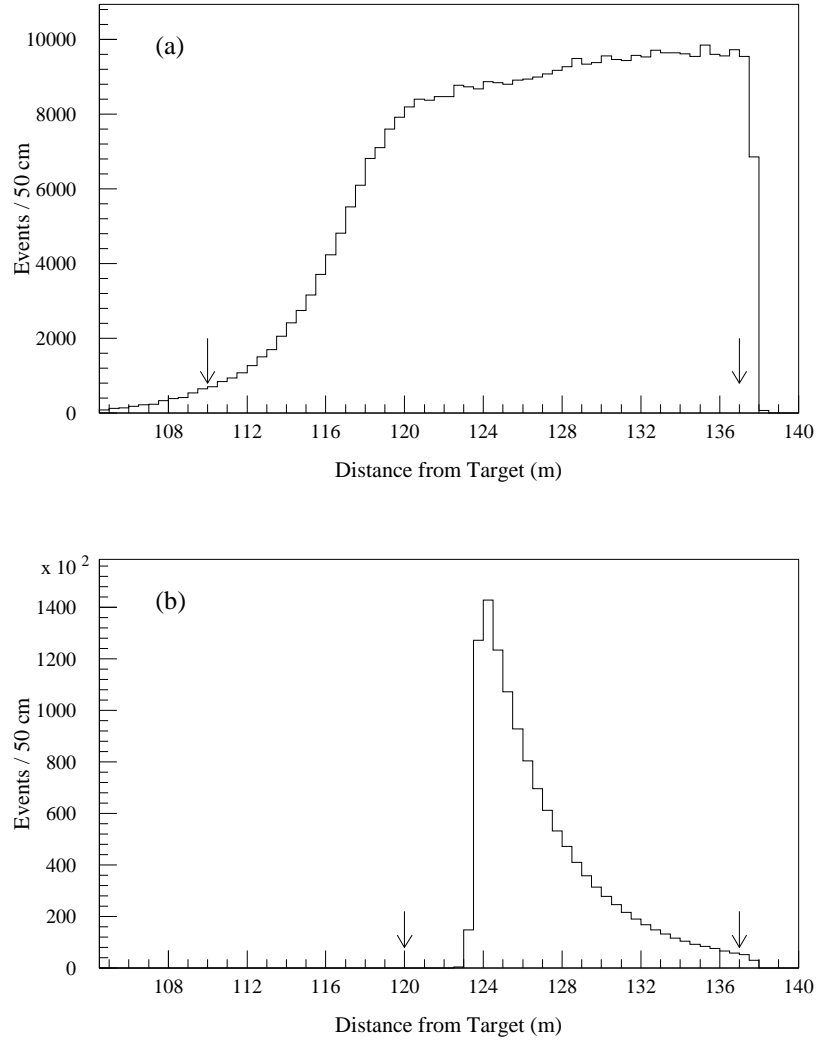FIG. 37. Distribution of the distance of the decays from the production target for the final $\pi^+\pi^-$ sample. The arrows mark the location of the cuts used in the $Re(\varepsilon'/\varepsilon)$ analysis. (a) Vacuum beam. (b) Regenerator beam.

the coherent peak (0 to 250 $(\text{MeV}/c)^2$).

The small background from beam-gas scattering in the vacuum beam is visible at large p_t^2 in Fig. 35d, where all the momentum bins have been combined. However, the low statistics of this background made a two exponential fit in individual momentum bins difficult. In this beam, therefore, the p_t^2 spectrum for decays within each 10 GeV/c momentum bin was fit using the form

$$\frac{dN_v(p_t^2)}{dp_t^2} = \alpha e^{-\beta p_t^2} + c, \tag{51}$$

where α, β and c are parameters of the fit. The exponential slopes (β) obtained in the fits are compatible with the hypothesis that the background is dominated by K_{e3} decays. The constant term c accommodates the average beam interaction background.

The background level under the coherent peak in each p bin and the number of coherent $K \rightarrow \pi^+\pi^-$ decays remaining after subtraction are listed in Table VII. The overall background level was $0.341\% \pm 0.010\%$, where the latter error is statistical only.

Combining all of the momentum bins, we can fit the vacuum beam p_t^2 spectrum to the sum of two independent exponentials for $p_t^2 < 50,000$ $(\text{MeV}/c)^2$. The result of this fit is plotted as the curve in both Figs. 35b and 35d. The individual semileptonic slopes measured within each momentum bin were consistent with the overall slope of 424 ± 15 $(\text{GeV}/c)^{-2}$. The slope obtained for the beam-interaction component of the background for this fit was 51 ± 10 $(\text{GeV}/c)^{-2}$.

The systematic error in the background level is dominated by the uncertainty in the slope of the semileptonic background. This has been evaluated in part by varying the slope within the limits allowed by the fits to the p_t^2 spectra in the 1500 $(\text{MeV}/c)^2$ to 20,000 $(\text{MeV}/c)^2$ range, and also by varying the range over which the fits were performed. In addition, the background fits were modified to use a beam-interaction component with fixed exponential slopes as large as 60 $(\text{GeV}/c)^{-2}$. This modification introduced only small differences into the total number of events subtracted. The total systematic uncertainty in this background is 0.010%, giving a total error in the $\pi^+\pi^-$ vacuum beam background fraction of 0.014%. In Monte Carlo studies of the semileptonic background, we found the p_t^2 spectrum begin to deviate from a perfect exponential for $p_t^2 < 2500$ $(\text{MeV}/c)^2$. While this rolloff would mean we are overpredicting the background level, the mismeasurement is at most 0.003%, well within the systematic uncertainty.

We fit the p_t^2 spectrum in the regenerator beam after the acceptance correction with a pair of exponentials and find

$$\frac{dN}{dp_t^2} \propto e^{-5.156 p_t^2} + 0.546 e^{-222.78 p_t^2}, \tag{52}$$

where p_t^2 is measured in $(\text{GeV}/c)^2$. The latter, steeper, term corresponds to the diffractive regeneration background. The shallower term corresponds to the inelastic contribution, and is consistent with the inelastic slope measured in previous experiments [47]. The functional form we use to fit the momentum bin p_t^2 spectra fixes the inelastic and diffractive slopes to the values given in Eq. (52), but allows the relative size of the two contributions to vary. The acceptance is expected to introduce an additional exponential falloff between the true and measured p_t^2 spectra, so the final functional form used in the fits was

60

TABLE VII. The number of coherent $\pi^+\pi^-$ decays after background subtraction, and the total background fraction subtracted in each 10 GeV/c bin. The background levels are given in percent. Indicated errors include only statistical uncertainties.

Momentum Range	Vacuum Beam		Regenerator Beam	
(GeV/c)	Data	Background (%)	Data	Background (%)
20-30	11712	0.31 ± 0.05	19059	0.158 ± 0.029
30-40	42092	0.34 ± 0.03	144363	0.165 ± 0.011
40-50	59701	0.37 ± 0.02	230593	0.160 ± 0.008
50-60	59983	0.40 ± 0.03	222405	0.157 ± 0.008
60-70	52227	0.37 ± 0.03	185010	0.153 ± 0.009
70-80	42380	0.34 ± 0.03	136064	0.150 ± 0.010
80-90	32525	0.32 ± 0.03	97159	0.145 ± 0.012
90-100	24702	0.28 ± 0.03	66862	0.144 ± 0.015
100-110	17689	0.27 ± 0.04	44144	0.143 ± 0.018
110-120	13241	0.26 ± 0.04	30246	0.143 ± 0.022
120-130	9704	0.26 ± 0.05	20461	0.142 ± 0.026
130-140	7056	0.25 ± 0.06	13414	0.142 ± 0.033
140-150	5486	0.25 ± 0.07	8656	0.141 ± 0.040
150-160	4286	0.24 ± 0.08	5654	0.141 ± 0.050
20-160	382783	0.340 ± 0.009	1224088	0.154 ± 0.004
40-160	328980	0.341 ± 0.010	1060667	0.152 ± 0.004

$$\frac{dN_r(p_t^2)}{dp_t^2} = \alpha e^{-ap_t^2} \left(e^{-5.156p_t^2} + re^{-222.78p_t^2} \right), \tag{53}$$

where α, a and r are all parameters of the fits. Data in the range of 1500 $(\mathrm{MeV}/c)^2 < p_t^2 < 20{,}000$ $(\mathrm{MeV}/c)^2$ were employed by the fit. The values for the diffractive-to-inelastic ratio r obtained in the 10 GeV/c momentum bin fits were statistically consistent with the value of 0.546 in the acceptance-corrected spectrum in Eq. (52).

The background levels are listed in Table VII along with the number of regenerator beam events remaining after subtraction. The total background in the regenerator beam came to $0.152\% \pm 0.004\%$ for the momentum range used in the $Re(\varepsilon'/\varepsilon)$ analysis. The error here is statistical only.

The systematic error in the regenerator beam background level was conservatively estimated at 0.012%. If the various exponential slopes — the acceptance, diffractive and inelastic — are allowed to vary within the limits prescribed by the fits to the p_t^2 spectra in the range $p_t^2 > 1500$ $(\mathrm{MeV}/c)^2$, the change in the background level is much smaller than this systematic estimate. Fits where the diffractive-to-inelastic ratio r was fixed at 0.546 also resulted in a change much smaller than this systematic error. Finally, the spectrum in each 10 GeV/c momentum bin was fit to the sum of two independent exponentials. In some momentum bins, the statistical precision at high p_t^2 was marginal when performing a two-exponential fit. In spite of this, the backgrounds predicted using these fits differed very little in most of the momentum bins from those listed in Table VII. In the end, we increased the systematic uncertainty to a level comparable to that in the vacuum beam. Combining the statistical and systematic uncertainties, yielded a background level of $0.152 \pm 0.013\%$.

In principle, there are contributions to the regenerator beam background from semileptonic decays as well. We can estimate this from the number of events in the high side tail of the K_s mass distribution, where the $\pi^+\pi^-\gamma$ tail does not contribute: the result is approximately $2 - 3 \times 10^{-5}$. This level agrees with our estimate based on the vacuum beam level of the order of 3×10^{-5}. This corresponds to a bias in $Re(\varepsilon'/\varepsilon)$ of 0.05×10^{-4}.

Fig. 38 shows the background-subtracted p_t^2 spectra for the vacuum and regenerator beams. In spite of the differences in the sources which contribute to the backgrounds in the two beams, the subtracted spectra are in excellent agreement — down to the shape of the radiative tail from $\pi^+\pi^-\gamma$ decays. The agreement between the two spectra over four orders of magnitude helps to give confidence in the background systematic uncertainties estimated above.

Implicit in the above discussion of the background subtraction is the assumption that the background fraction is constant as a function of z in each momentum bin. This is a good assumption in the regenerator beam, since both the background and the coherent signal are dominated by K_s decays. In the vacuum beam, there are differences in, for example, the variation of the $\pi^+\pi^-$ and K_{e3} acceptance as a function of p and z, which could lead to small variations in the background as a function of z. Fortunately, for all of the measurements we make, our fitting technique requires only that we know the average number of events in the vacuum beam in each momentum bin. However, we still examine the z shape in this beam.

Because of the low background levels, it is difficult to examine this approximation in individual 10 GeV/c momentum bins. We combine the momentum bins and study in smaller z bins, and the resulting z dependence of the backgrounds is shown in Fig. 39.

For the regenerator beam, all of the momentum bins have been integrated together, and
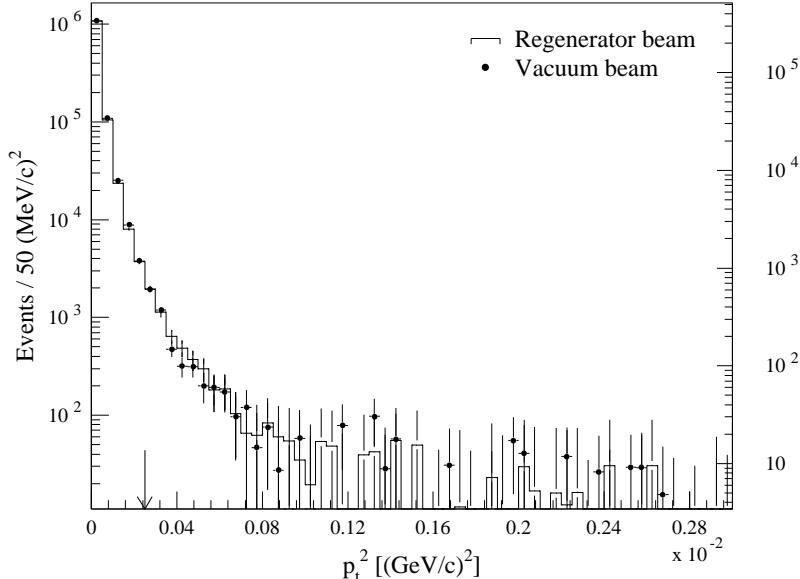
FIG. 38. Overlay of the vacuum and regenerator beam p_t^2 spectra after background subtraction. The arrow indicates the position of the cut used in this analysis.

we see no noticeable change in the background level across the fiducial z region. For the vacuum beam, we cannot combine data of all momenta together to examine the background z dependence. At low momentum, the backgrounds are somewhat higher than at high momentum. However, very few low momentum $\pi^+\pi^-$ decays are accepted upstream of the active mask. Integrating all of the momentum bins together would thus introduce an artificial step at the mask. To avoid this issue, we have examined the background fraction versus z in 40 GeV/c momentum bins, but have doubled the z bin size relative to the regenerator beam study. The background fractions obtained in each 40 GeV/c bin are also plotted in Fig. 39. Above 80 GeV/c, the shape is flat within our level of sensitivity. In the 40 GeV/c to 80 GeV/c range, the background tends to increase as a function of z. If we substitute the background levels obtained as a function of z for this momentum range, the change in the background level is much less than the systematic uncertainty assigned to the background subtraction.

C. Charge Mode Conclusion

For the $Re(\varepsilon'/\varepsilon)$ measurement, we collected a sample of $328,980 \pm 574 \pm 46$ $\pi^+\pi^-$ decays from the vacuum beam (after background subtraction), and $1,060,667 \pm 1030 \pm 138$ decays in the regenerator beam. The first errors are the statistical errors for the signal, and the second errors are the uncertainties from the background subtraction. The backgrounds in both beams were small, and relatively simple to understand at the required level of precision. The overall background levels in the vacuum and regenerator beams were 0.340% and 0.152%, respectively. We estimate that these were known with fractional uncertainties of 4% and 8.5%.

This completes the discussion of the analysis and background subtraction for the $\pi^+\pi^-$ decay samples. Details of the charged mode acceptance calculation is presented after dis-
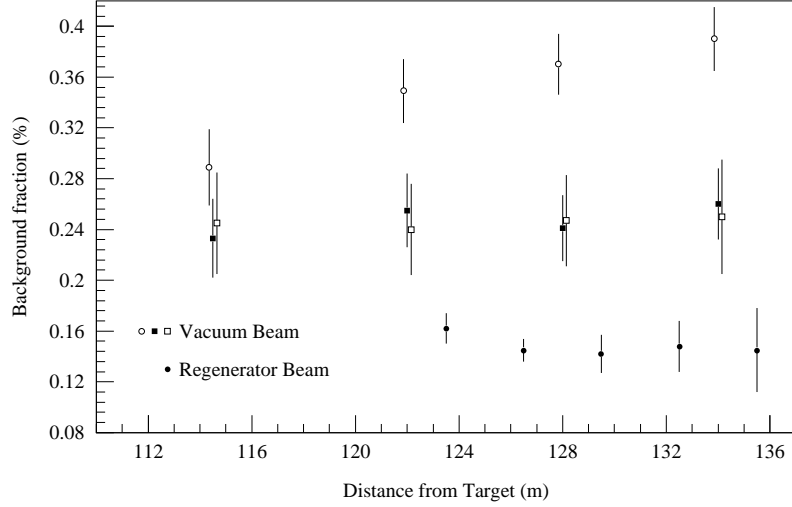
FIG. 39. The measured $\pi^+\pi^-$ background fractions as a function of z. The solid dots are the regenerator beam background levels. The other points are the vacuum beam levels, where the circles have been measured in the momentum range $40 - 80$ GeV/c, the open squares in the range $80 - 120$ GeV/c, and the solid squares in the range $120 - 160$ GeV/c. The coarse binning in the vacuum beam data reflects the reduced statistical precision relative to the regenerator beam data.

cussion of the $2\pi^0$ analysis.

VI. $2\pi^0$ ANALYSIS

Here we review the reconstruction in $2\pi^0$ decays from four photons and describe the background subtraction in detail.

A. Neutral Mass and Z Reconstruction

Reconstruction begins with the energies and positions of the four photons measured in the calorimeter. To reconstruct the position of the kaon decay and the four photon mass, the photons were paired using the π^0 mass as a constraint. Fig. 40 illustrates the procedure. If we have paired photons a and b, then the z position z_{ab} of the π^0 decay is related to the π^0 mass by

$$m_{\pi^0}^2 = 2E_a E_b (1 - \cos\theta_{ab}) \simeq E_a E_b \frac{r_{ab}^2}{(z_{glass} - z_{ab})^2}, \tag{54}$$

where E_a and E_b are the energies of the two photons, θ_{ab} is the angle between the two photon trajectories, and r_{ab} is the separation of the photons in the calorimeter. We formed a second vertex position z_{cd} from the other pair of photons. The χ^2 for the hypothesis that $z_{ab} = z_{cd}$ is,

$$\chi^2 = \frac{(z_{ab} - z_{cd})^2}{\sigma_{z_{ab}}^2 + \sigma_{z_{cd}}^2}, \tag{55}$$

taking into account the resolution for each photon's energy and position. The pairing with the best χ^2 was then chosen. The resulting χ^2 distribution is shown for both the regenerator and vacuum beams in Fig. 41 after all other cuts.

The z of the kaon decay was taken as the weighted average of z_{ab} and z_{cd}. The $2\pi^0$ mass was reconstructed from the four photon energies and positions using

$$m_{\pi^0\pi^0}^2 = 2\sum_{i>j} E_{\gamma_i} E_{\gamma_j}(1 - \cos\theta_{ij}). \tag{56}$$

The cosine of the angle between the two photon trajectories, $\cos\theta_{ij}$, is calculated assuming that the kaon decayed on the z axis. Finite beam size has negligible effect on the mass value.

The $2\pi^0$ mass distribution for regenerator beam data and Monte Carlo is shown in Fig. 42. Residual nonlinearities in the calibration lead to shifts in the reconstructed mass. We have observed such shifts in our data, and they are listed in Table VIII for each of the $2\pi^0$ subsets. Separate shifts are listed for events with and without photon clusters centered in one of the 24 "pipe blocks" surrounding the two beam holes. For comparing line shapes, we shifted the $2\pi^0$ mass of data events by the values in the Table. The Monte Carlo simulates the mass spectra quite well. The shifts were not applied as part of the standard analysis; we use them (in Section X) to estimate systematic effects of residual nonlinearities.

The mass resolution is about 5.5 MeV. Our $2\pi^0$ mass cut (474 to 522 MeV) was loose enough to be insensitive to residual nonlinearities.

Because of fluctuations in the electromagnetic showers, we occasionally chose the wrong pairing. To keep misreconstruction background to a minimum, we eliminated events if the second-best pairing had a χ^2 within 8 of that of the best pairing, and a mass in the range from 470 to 526 MeV. About 1% of otherwise good kaons fail the mispairing cut.
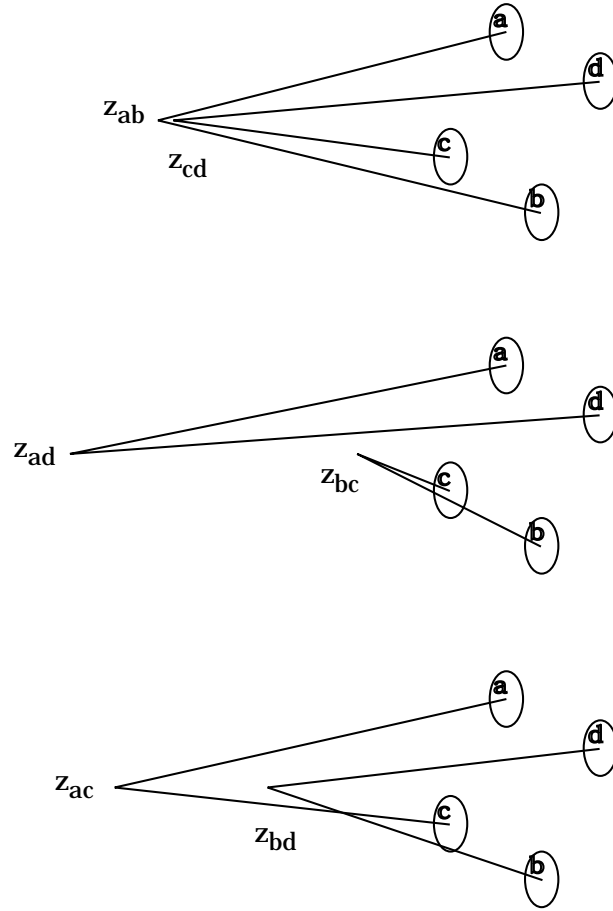
FIG. 40. The z-locations obtained for both π^0 decays in each of the three possible pairings of the four photons from a $K \to \pi^0\pi^0$ decay. The top pairing gives the best χ^2 for $z_{ab} = z_{cd}$.
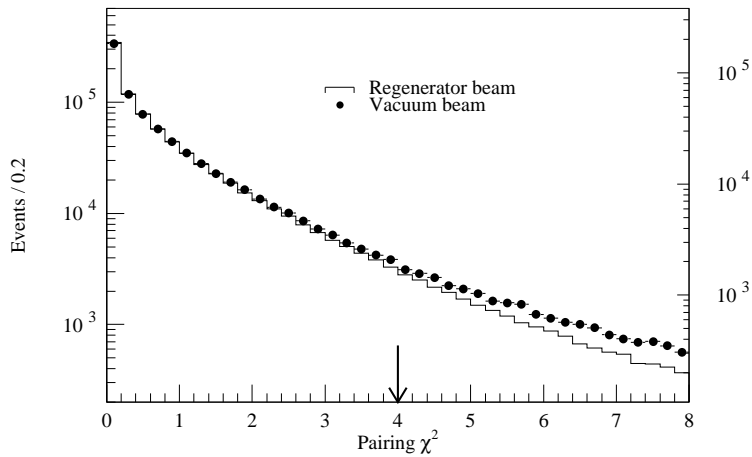
FIG. 41. The $2\pi^0$ pairing χ^2 distribution for the regenerator and vacuum beams after all other cuts. The regenerator beam distribution is shown by the histogram (left axis) and the vacuum beam distribution is shown by the dots (right axis). The shapes of the two distributions differ at higher values of χ^2 because of the larger $3\pi^0$ and beam interaction backgrounds in the vacuum beam. The arrow marks the location of the analysis cut.

TABLE VIII. Reconstructed $2\pi^0$ mass shift δm in MeV of data relative to Monte Carlo simulation in the five neutral subsets. Two of the subsets have been subdivided into time periods for which separate calibrations have been used. A negative shift implies the $2\pi^0$ mass in the data was lower than that in the Monte Carlo.

$2\pi^0$ subset sample	N1a	N1b	N2	N3	N4	NCa	NCb
δm (no pipe block cluster)	-0.76	-0.83	-0.71	-0.74	-0.63	-0.43	-0.44
δm (≥ 1 pipe block clusters)	-1.07	-1.40	-0.90	-0.94	-0.82	-0.65	-0.60
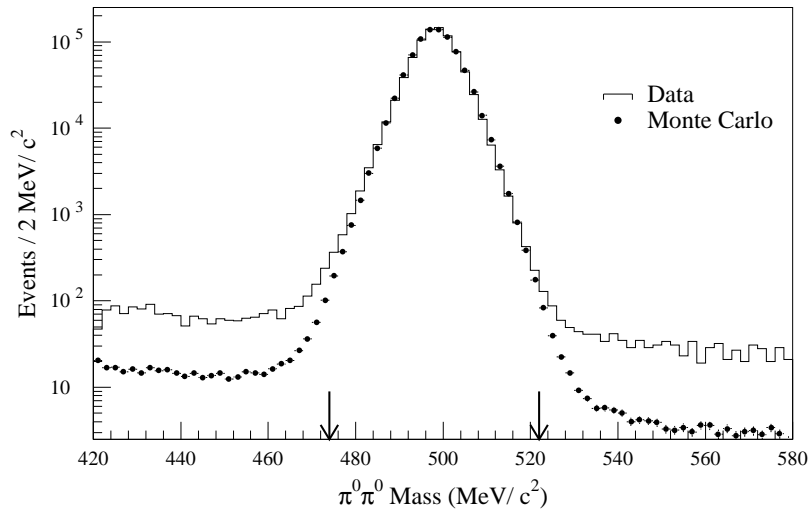
FIG. 42. The reconstructed $2\pi^0$ mass after all other cuts for regenerator beam events. The predicted signal shape from the coherent Monte Carlo simulation is overlaid. The data have been shifted set by set according to the values in Table VIII. Background has not been subtracted.

B. Neutral Ring Number

Unlike the situation in the $\pi^+\pi^-$ mode, the precise transverse location of a kaon decay could not be determined in the $2\pi^0$ mode. This means that we could not measure the p_t^2 of the kaon to reduce the noncoherent kaon background. Instead we considered the center of energy (x_{CE}, y_{CE}) of the photons in the lead glass (the location where the kaon would have passed through the calorimeter had it not decayed) given by

$$x_{CE} = \frac{\sum_{i=1}^{4} E_i x_i}{\sum_{i=1}^{4} E_i} \tag{57}$$

$$y_{CE} = \frac{\sum_{i=1}^{4} E_i y_i}{\sum_{i=1}^{4} E_i}, \tag{58}$$

where x_i and y_i are the x and y positions of the ith photon in the lead glass calorimeter. For non-scattered kaons, the center of energy should reconstruct within the beam. The two beams are clearly defined in the plot of the reconstructed center of energy in Fig. 43. All vacuum (regenerator) beam decays have been mapped to the "upper" ("lower") beam in the plot. While the two beams are clearly well separated, some kaons reconstruct outside of the beams. The distribution of these falls off as one moves away from the regenerator beam. These events are inelasticly and diffractively scattered kaons in the regenerator (or in the HDRA). Some of the kaons scattered hard enough in the regenerator to reconstruct under the vacuum beam, and this constitutes the largest background in this mode.

We divided the center of energy plot into concentric square "rings" of area 1 cm², centered on each beam. Each event was then assigned the number of rings into which the center of energy reconstructed. The "ring number" distribution for each beam is shown in Fig. 44. To keep the signal to background ratio manageable, we accepted only events with ring number less than 112.

C. Other Cuts

Several other cuts were applied to reduce background in the signal region, defined by good $2\pi^0$ mass and small ring number. One set of cuts reduced the $3\pi^0$ and neutron interaction background, while a second set reduced the inelastic background. Finally, several fiducial cuts simplified the acceptance determination.

Several types of cuts helped to reduce the background from $3\pi^0$ decays. The first tightened the restrictions on signals in the lead-lucite photon veto counters, reducing the chance for a photon to escape the detector. The photon veto cuts for both the low and high intensity data samples are listed in Table IX. The cuts were chosen to optimize the signal to background ratio. The first veto bank (VA1) was quite close to the regenerator, and because of accidental activity from interactions in the regenerator, we could not use it in the high intensity sample.

Photons which landed too close together in the calorimeter were not resolvable. These fused clusters sometimes lead to the misidentification of a $3\pi^0$ decay as a four-cluster event when other photons also escaped or fused. Many of these fused photons were eliminated

68
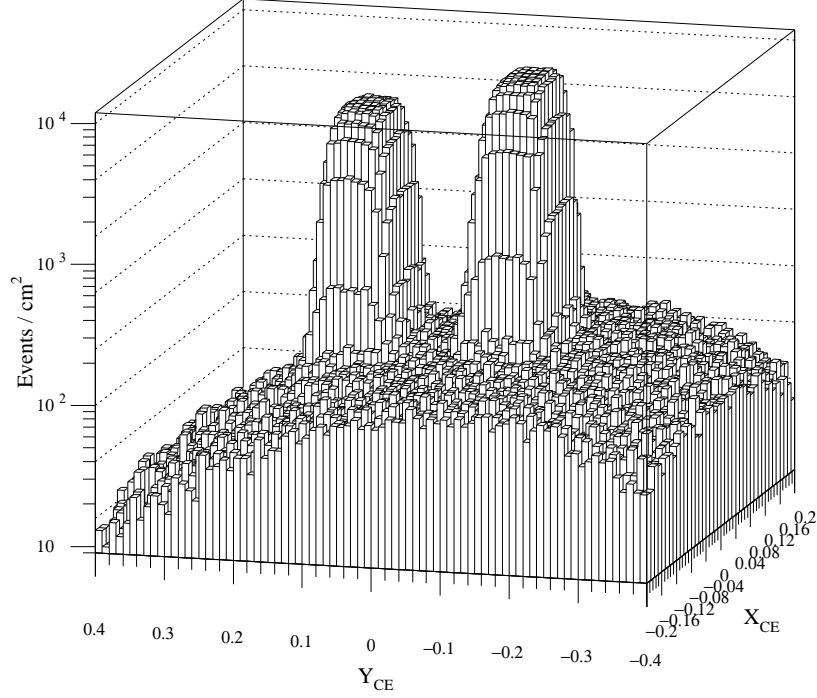
FIG. 43. Distribution of the center of energy of $2\pi^0$ events passing all but the ring-number cut. The y-position has been negated when the regenerator was in the top beam. Regenerator beam decays are hence at right $(-y)$ and vacuum beam decays are at left $(+y)$. The distribution on log scale, clearly shows a small, broad contribution centered on the regenerator beam from kaons which scatter in the regenerator.
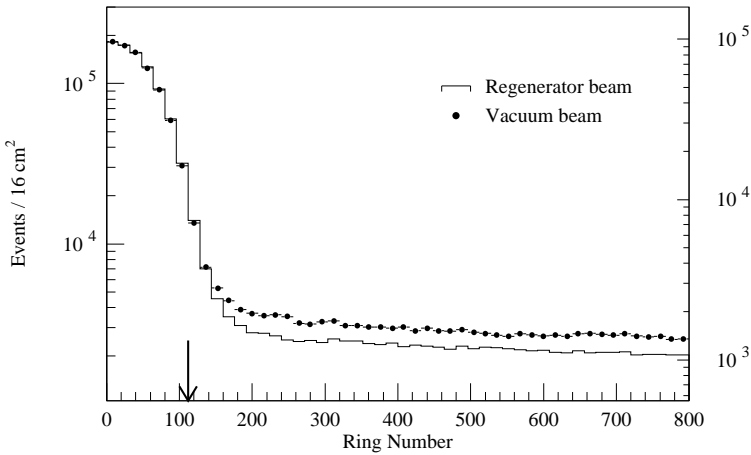
FIG. 44. Ring number distribution for $2\pi^0$ decays in the regenerator (histogram, left scale) and vacuum (dots, right scale) beams after all other cuts. No backgrounds have been subtracted. The arrow marks the position of the cut.

69

TABLE IX. Photon veto cuts in minimum ionizing equivalents (MIPs) applied in the $2\pi^0$ sample.

Veto Detectors	Low Intensity cut	High Intensity Cut
VA1	2.6	none
VA2	1.3	6.0
DRAC	0.5	1.2
DRAN	0.6	1.5
VA3	1.0	1.8
VA4	1.5	3.0
MA	2.0	1.8
LGA	2.5	5.0
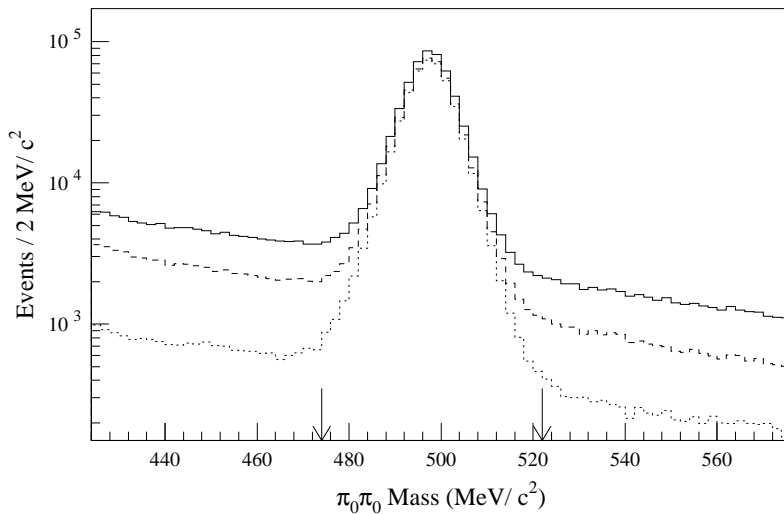
FIG. 45. Effect of the photon veto and fusion cuts on the vacuum beam $2\pi^0$ mass distribution. The solid histogram has all cuts but the photon veto, fusion and soft cluster cuts, the dashed histogram has the photon veto cuts added, and the dotted histogram has all cuts added. The arrows show the location of the mass cuts.

by comparing the observed cluster shape with the shape expected for an electromagnetic cluster. We used, for example, the ratio of energy in a 3×3 cluster to that in a 5×5 cluster, and the ratios of energies in the outer rows (or columns) to the cluster energy.

Very soft photons from $3\pi^0$ decays could be lost if the resulting cluster was below the hardware cluster-finding threshold of about 1 GeV. A direct search for soft clusters in the lead glass was infeasible because of remnant "clusters" from showers in other buckets in the long ADC gate. However, the "adders" had a very short gate, and hence were not affected as severely by accidental clusters. By comparing the energy observed in the adders with that in the clusters, events with extra soft clusters above roughly 600 MeV could be eliminated effectively.

The effects on the mass distribution of these cuts is shown in Fig. 45.

To reduce the inelastic kaon scattering background (and the beam interaction background), we use the fact that extra charged particles are often produced in such events. By

TABLE X. The fraction of coherent $2\pi^0$ decays in the regenerator beam lost after each analysis cut is applied as determined from the Monte Carlo simulation. In the "Sequential Loss" columns, the loss of the first cut is normalized to all $2\pi^0$ events which reconstructed within the fiducial energy and z region used for the $Re(\varepsilon'/\varepsilon)$ fits. Each cut thereafter is normalized to the number of kaons left after the preceding cut. The precision in this table is approximately 0.03% (only a small portion of the MC was used).

Analysis cut	Sequential loss (%)		Loss as Final Cut (%)	
	Pb Sheet	No Pb Sheet	Pb Sheet	No Pb Sheet
Chamber and hodoscope hits	21.37	1.12	15.49	0.06
Ring number	3.28	2.26	2.74	1.81
Photon veto	0.00	0.00	0.00	0.00
Minimum cluster energy	1.35	1.43	0.89	1.00
Maximum cluster energy	8.81	8.67	7.77	7.82
Cluster fusion cuts	0.90	0.80	0.90	0.79
Best pairing χ^2	3.09	2.50	2.76	2.21
Mispairing cuts	1.74	1.61	0.99	0.93
$2\pi^0$ mass	0.26	0.21	0.26	0.21

cutting on the number of hits in the drift chambers and the presence of activity in the B and C hodoscopes, we eliminated many inelastic events not vetoed at the trigger level. In rare cases when a photon from a $2\pi^0$ decay converted at the HDRA so that a single conversion electron cluster carried most of the photon energy, the event could have an acceptable pairing χ^2 and mass. Such cases were suppressed by the cut on the number of drift chamber and hodoscope hits.

As we mentioned in Section III, the collar anticounter (CA) cleanly defined the inner edge of the acceptance for $2\pi^0$ decays. This counter was in veto at the trigger level, but the veto itself was quite loose. In the offline analysis, we tightened the cut to 5 MIPs.

For the final sample, to give less sensitivity to the threshhold behavior of the hardware cluster finder, we required the minimum photon energy to be above 1.5 GeV. We also required the photon energy to be below 60 GeV as discussed in some detail in Sections VII and X.

The effects of the selection criteria on coherent $K \to \pi^0\pi^0$ decays within our final fiducial volume are listed in Table X. The loss of coherent events due to the cut on the drift chamber and B and C hodoscope activity is large in the lead sheet subset because of photon conversions in the lead sheet.

The final energy distributions for the vacuum and regenerator beams are shown in Fig. 46. The two distributions are similar, though the vacuum spectrum is enhanced at the low energy end because of the high acceptance for low energy decays downstream of the HDRA.

D. Neutral Energy Scale

The final step in neutral reconstruction was the adjustment of the energy scale of the photons relative to that of electrons in the calorimeter.
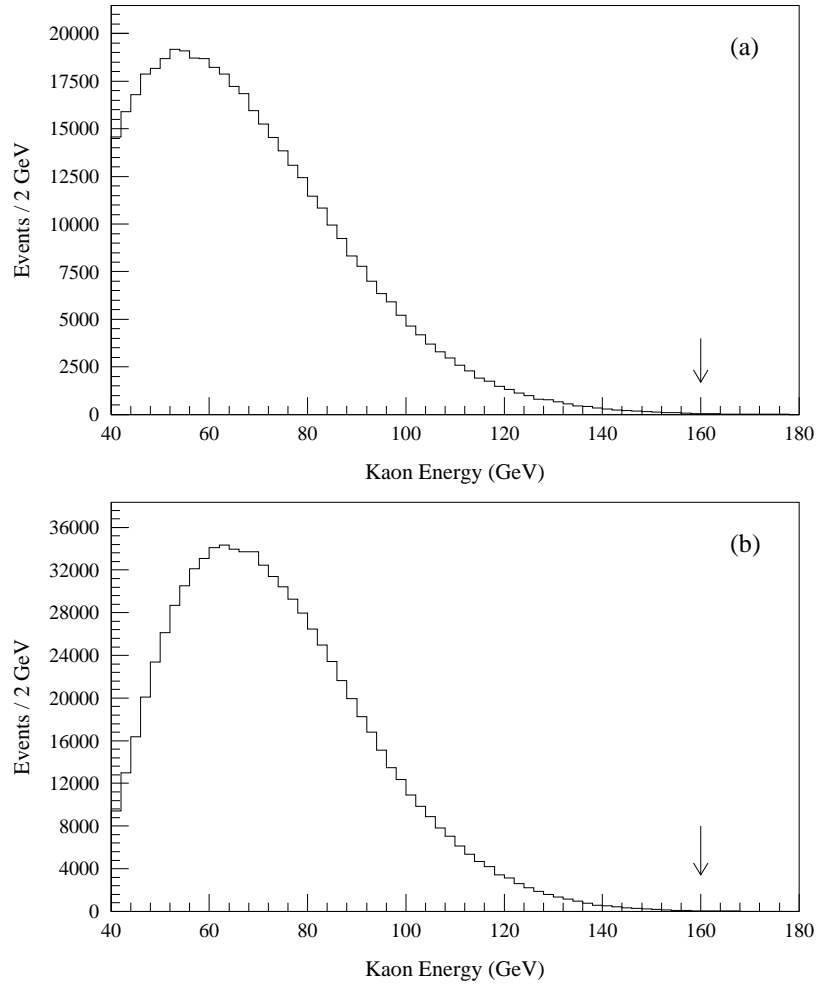
FIG. 46. The kaon energy distribution for the entire $2\pi^0$ data set after all other cuts. (a) Vacuum beam. (b) Regenerator beam. The arrow marks the maximum energy used in the analysis.

TABLE XI. The parameters for the photon energy scale corrections, and the average correction applied, in the each $2\pi^0$ subset.

Subset	Slope ($E_K < 80$ GeV) [% per GeV]	Slope ($E_K > 80$ GeV) [% per GeV]	80 GeV correction [%]	Average Correction [%]
N1a	-1.7×10^{-3}	$+0.4 \times 10^{-3}$	-0.094	-0.06
N1b	-4.2×10^{-3}	-2.9×10^{-3}	-0.041	0.02
N2	-4.2×10^{-3}	-6.5×10^{-3}	+0.065	0.11
N3	-4.3×10^{-3}	-2.8×10^{-3}	+0.080	0.14
N4	-4.5×10^{-3}	-7.0×10^{-3}	+0.176	0.22
NCa	-5.0×10^{-3}	-3.3×10^{-3}	+0.324	0.39
NCb	-3.2×10^{-3}	$+0.9 \times 10^{-3}$	+0.313	0.37

To quantify remaining nonlinearities, we took advantage of the coupling of the decay z and energy scales and examined the reconstructed position of the regenerator edge as a function of the kaon energy. We transformed the shift into a photon energy correction, which we parametrized as a bilinear function of kaon energy with a knee at 80 GeV. Table XI lists the slopes (% per GeV) above and below 80 GeV, the correction at 80 GeV, and the mean correction for each $2\pi^0$ subset.

A comparison of the z edge in the upstream region of the regenerator beam in the data and Monte Carlo is shown in Fig. 47a after the correction. On average the edges match quite well. As shown in Fig. 47b, introducing a shift in the energy scale of only 0.05% degrades the agreement noticeably: the χ^2 increases by a factor of 3, and the shift is clearly visible. We estimate that the residual uncertainty in the *average* energy scale is under 0.03%. The residual uncertainty in the nonlinearity dominates the systematic error from photon reconstruction.

The coupling of the energy scale and z position has some subtle effects when the lead sheet is in place. Approximately 25% of events upstream of the HDRA in the lead sheet data are lost to conversions and of course this factor must be very well known and corrected for. But residual uncertainties and nonlinearity in the energy scale can cause decays on one side of the HDRA to reconstruct on the other side and these would be falsely corrected. To minimize the sensitivity to this effect for the lead sheet data, we eliminated decays in the z region from 137 to 139 m from the final sample.

E. Neutral Mode Background Subtraction

There were four classes of backgrounds that had to be subtracted from the coherent $2\pi^0$ data. The largest source was $2\pi^0$ decays of scattered kaons. There were two sites producing this noncoherent background: the regenerator and the HDRA. Backgrounds from these two were treated independently. Background from $3\pi^0$ decays which reconstructed with only four clusters in the calorimeter was particularly important downstream of the HDRA. Finally, inelastic interactions of neutrons with material in the detector, particularly in the HDRA,
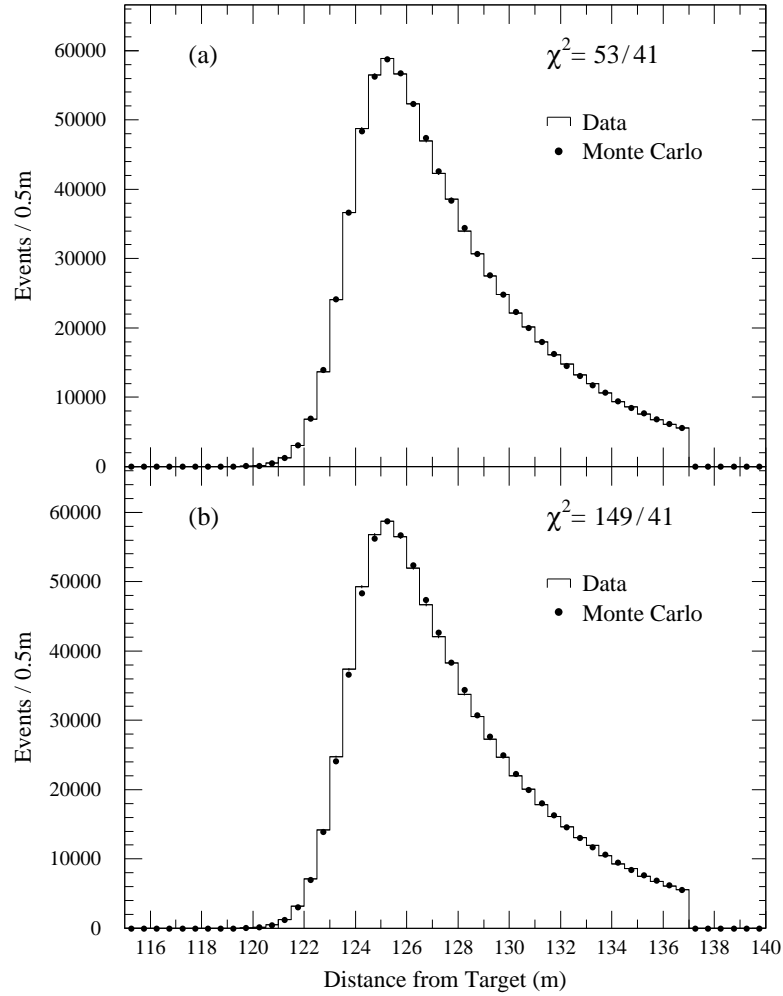
FIG. 47. Data and Monte Carlo comparison of the reconstructed regenerator edge after energy scale adjustments. (a) The data has the standard adjustments. (b) The data has an additional 0.05% energy scale adjustment.
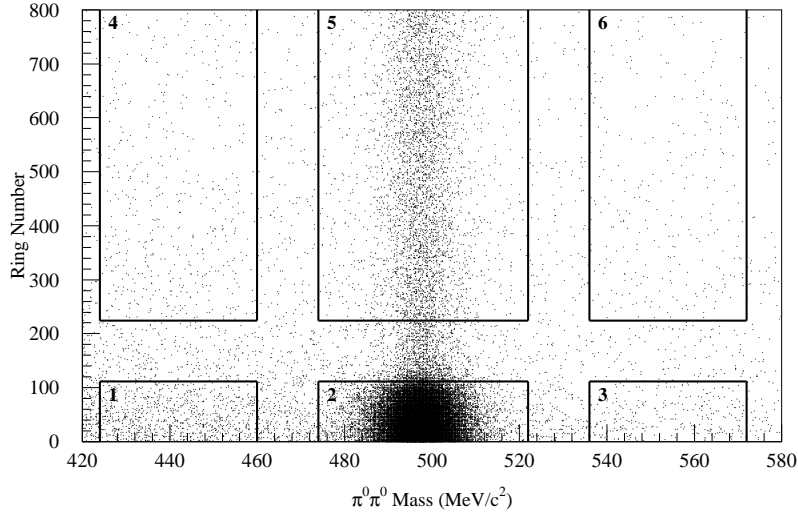
74

FIG. 48. The six regions in the vacuum $2\pi^0$ mass versus ring-number distribution used for background subtraction.

TABLE XII. The $2\pi^0$ background sources and fractions.

Source	Vacuum Beam Fraction (%)	Regenerator Beam Fraction (%)
$3\pi^0$ background	1.78 ± 0.03	0.049 ± 0.003
Beam Interaction	0.21 ± 0.02	0.027 ± 0.004
Regenerator Noncoherent Scattering	2.26 ± 0.04	2.53 ± 0.04
HDRA Diffractive Scattering	0.78 ± 0.02	0.027 ± 0.002
HDRA Inelastic Scattering	0.13 ± 0.02	0.027 ± 0.011

would sometimes produce two π^0s that reconstructed under the kaon mass peak.

The background subtraction technique used the reconstructed $2\pi^0$ mass and ring number variables as seen in Fig. 48. The plot has been divided up into six regions; one contains the signal (region 2), while the others (region 1,3,4,5,6) – used for normalizing Monte Carlo simulations of the different backgrounds – were populated only by background. In essence, the $3\pi^0$ and beam interaction backgrounds were subtracted from the coherent *and* noncoherent kaons by extrapolating the sidebands under the mass peak. The noncoherent backgrounds were then extrapolated from large ring number to the coherent peak region. The subtractions were made in individual 1 m by 10 GeV bins after the normalizations of the Monte Carlo background samples were determined globally for the entire p and z fiducial region.

A breakdown of the z distributions (for the no lead sheet data set) of the different backgrounds is shown in Fig. 49. The contribution from each background source is summarized in Table XII.
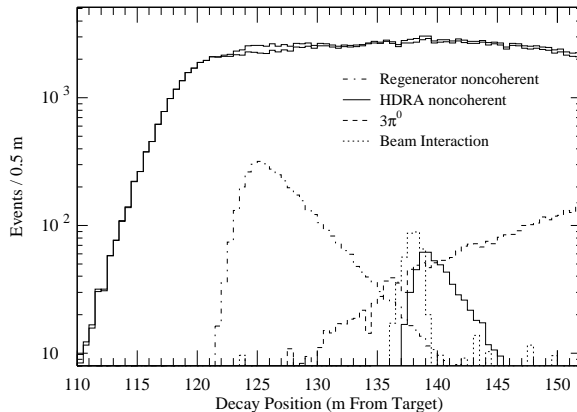
FIG. 49. The z-distribution of the different backgrounds to the vacuum beam $2\pi^0$ sample for the data subset with no lead-sheet. Also shown are the $2\pi^0$ z-distributions before and after background subtraction. All cuts have been applied.

1. $3\pi^0$ and Beam Interaction Backgrounds

The $3\pi^0$ subtraction used a Monte Carlo to interpolate from the mass sidebands under the $2\pi^0$ mass peak. The simulation of the $3\pi^0$ background shape used photon veto resolutions and gains determined from $K_L \rightarrow \pi^+\pi^-\pi^0$ decays (see [39]). To obtain a background sample about 5 times that of the data required simulating 6×10^9 $K_L \rightarrow 3\pi^0$ decays. This was accomplished with 3 months of dedicated use of a Fermilab ACP farm of 25 computers each of 25-MIPS.

The $3\pi^0$ background Monte Carlo sample was normalized to the data using regions 1 and 3 outlined in Fig. 48. Several pitfalls had to be avoided in this normalization. First of all, beam interactions with material in the beam produced a flat background in mass. Fortunately the material in the beam is localized at the two locations, the HDRA and the regenerator. The peak from the HDRA in the vacuum beam is clearly visible in Fig. 49. To avoid miscalculating the $3\pi^0$ normalization factor, only events reconstructing in the z regions 110m-122m, 125m-134m, and 142m-152m were used.

A similar normalization problem arose from the misreconstructed signal $2\pi^0$ events that appear in the sidebands, for example, from residual mispairings. These misreconstructions occur both in data and signal Monte Carlo, and because of the way we define our acceptance, we do not want to subtract these events. The level of these misreconstructions can be seen clearly in the Monte Carlo mass distribution for the regenerator beam shown in Fig. 42, where the misreconstructions constitute a significant fraction of the events in the sidebands (this is not the case in the vacuum beam). To avoid biasing the $3\pi^0$ normalization, the signal Monte Carlo was used to predict the ratio r of coherent events in the mass sidebands to coherent events in the mass peak. If d_s and d_p are the number of data in the signal region and in the mass sidebands, respectively, and b_s and b_p are the similar quantities for the $3\pi^0$ background, it is simple to show that the desired $3\pi^0$ normalization factor $a_{3\pi}$ is

$$a_{3\pi} = \frac{d_s - r d_p}{b_s - r b_p}.$$ (59)

If we had neglected this effect, the $3\pi^0$ background in the vacuum beam would have been overestimated by about 3% of itself. In the regenerator beam, however, the $3\pi^0$ background
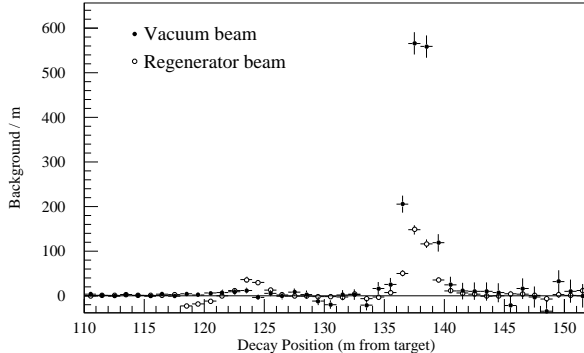
76

FIG. 50. The z-distribution of the calculated beam interaction background.

is much smaller, and had we neglected the $2\pi^0$ misreconstructions, we would have overestimated the background by almost 70% of itself. Neglecting this effect would have shifted $Re(\varepsilon'/\varepsilon)$ by 0.38×10^{-4}.

After subtracting the $3\pi^0$ background, the beam interaction backgrounds were estimated by linearly interpolating the residual background in the mass sidebands into the signal region in each pz bin. In regions of the detector with no material, this prediction should be consistent with zero as can be seen in Fig. 50. The width and position of the large peak are consistent with the z resolution and HDRA location. The relative areas for the two beams are proportional to their expected hadronic content. A small background from beam interactions with the regenerator can also be seen. The only evidence of a problem in the subtraction is in the regenerator beam upstream of the regenerator; this is simply due to a small resolution mismatch between the data and the Monte Carlo, and is negligible at the 10^{-5} level in $Re(\varepsilon'/\varepsilon)$.

The mass distributions for candidate $2\pi^0$ events and the predicted background shapes are shown in Fig. 51. For the vacuum beam, the distributions for the entire z region and for the normalization z region are plotted. The agreement is excellent in both cases, the former checking the combination of $3\pi^0$ and beam interaction shapes and the latter isolating the $3\pi^0$ shape. The agreement is also very good for the regenerator beam. In all three data distributions, the expected level of coherent misreconstruction in the mass sidebands has been subtracted.

The $3\pi^0$ and beam interaction backgrounds have been studied in individual 1 m z bins in the vacuum and regenerator beams for both the lead sheet and no lead sheet data samples. The mass distributions for 9 of these bins for the vacuum beam sample are shown in Fig. 52 where the lead sheet and no lead sheet data have been combined. Excellent agreement between the predicted and observed background shape was found in every z bin. The backgrounds were studied in 10 GeV momentum bins, and we found good agreement there as well.

The statistical error on the $3\pi^0$ background subtraction amounted to 0.023% (0.003%) in the vacuum (regenerator) beam. It includes the errors from the number of events subtracted and the finite statistics of the $3\pi^0$ background Monte Carlo sample and the normalization. The statistical errors on the beam interaction subtraction were 0.02% and 0.004% in the vacuum and regenerator beams, respectively.

Several checks were done to estimate the systematic contribution from the mass background subtraction. We have varied the $3\pi^0$ normalization method, using, for example,
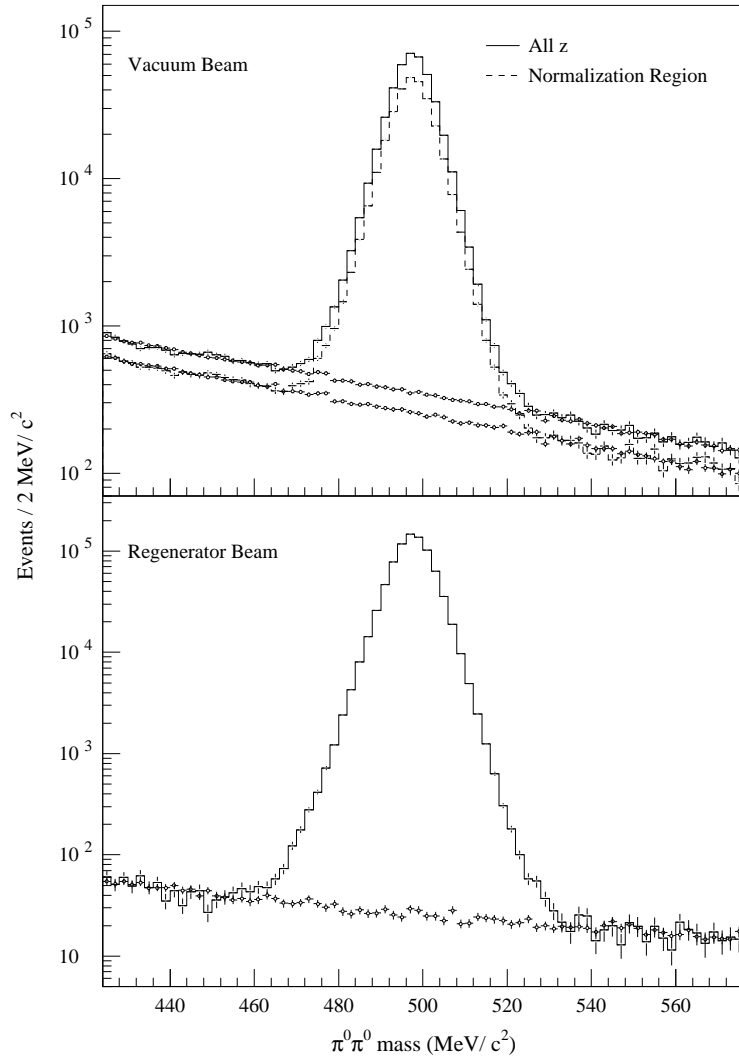
FIG. 51. The $2\pi^0$ mass distribution and the background prediction. *Top*: The vacuum beam distributions for the fiducial z region (solid histogram) and the $3\pi^0$ background normalization z region (dashed histogram). *Bottom*: The regenerator beam distribution for the fiducial z region.
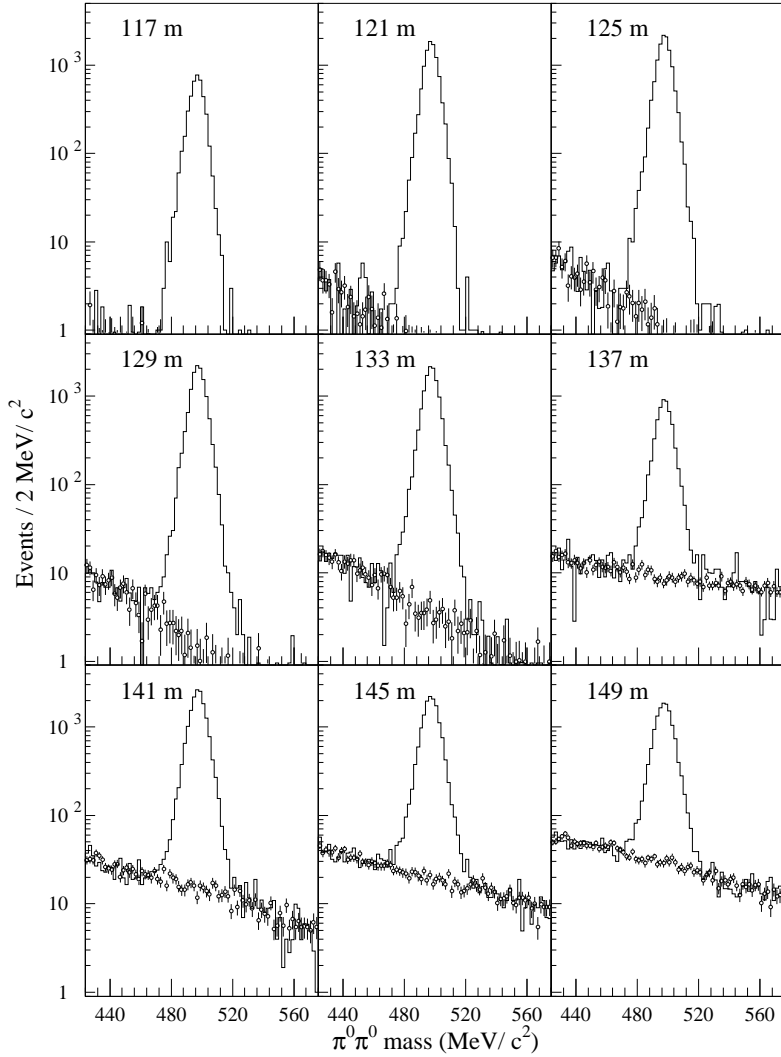
FIG. 52. Observed $2\pi^0$ mass distribution and the $3\pi^0$ and beam interaction backgrounds in 9 individual 1 meter z bins. The $3\pi^0$ Monte Carlo normalization is common to all bins. Each plot is labelled with the upstream edge of the z bin. In the 137 m bin, we only used the data from the $2\pi^0$ subset with no lead-sheet.

different normalizations for events with photons which hit the downstream photon vetoes rather than a single overall normalization constant. We have also studied the fluctuations in the result for different $2\pi^0$ mass cuts. All studies were consistent with a limit on the systematic error for the $3\pi^0$ plus beam interaction background of 0.015%.

2. Noncoherent Backgrounds

Since we accept $2\pi^0$ decays from downstream of the HDRA, there are two sources of scattered kaons: the regenerator and the HDRA. As Fig. 49 shows, the backgrounds from these two sources are generally well separated in z. The shape of the backgrounds in ring number for each source of noncoherent kaons was simulated with our Monte Carlo. The generation and normalization procedures for the two different scattering locations are described below.

*a. Regenerator Noncoherent Background*   The fundamental ingredient for simulating the noncoherent backgrounds was the p_t^2 spectrum for the scattered kaons. For the regenerator, the p_t^2 spectrum could be measured with the $\pi^+\pi^-$ sample. As discussed in [37], the spectrum was corrected for acceptance as a function of p_t^2 and parametrized as the sum of two exponentials, a steep exponential for the diffractive contribution and a shallower exponential for the inelastic contribution. The resulting spectrum for our regenerator was

$$\frac{dN}{dp_t^2} \sim 3431 e^{-5.2p_t^2} + 1875 e^{-222.8p_t^2}, \tag{60}$$

where p_t^2 is measured in $(\text{GeV}/c)^2$. This parametrization was fed into the Monte Carlo simulation to generate a sample of $2\pi^0$ decays from scattered kaons.

The charged sample used to determine the p_t^2 spectrum was the NC set, where charged and neutral data sets were collected simultaneously. This was also the highest intensity charged subset.

The Monte Carlo background simulation was normalized to the noncoherent tail in the ring number plot (region 5 in Fig. 48). This was done using only events upstream of 134 m to avoid any contamination from the HDRA noncoherent background. The same z region around the regenerator excluded in the $3\pi^0$ normalization was also excluded here, to avoid double subtracting the beam interaction background.

b. HDRA Noncoherent Background   Since the HDRA formed part of the charged trigger, there was not a sample of $\pi^+\pi^-$ events to give us the kaon p_t^2 spectrum for the HDRA. Fortunately, the forward amplitudes have been measured at the precision we need [32,48,49]. The exceptions were oxygen and nitrogen, whose forward amplitudes could be reliably obtained from that of carbon using the measured atomic number dependence $A^{-0.758}$ [50] of the kaon regeneration amplitude. Optical model calculations reproduce the measured p_t^2 spectra reliably [47]. All these amplitudes were fed into the Monte Carlo and scattered kaons were generated in both the vacuum and regenerator beams with the correct amplitude and phase relative to the coherent kaons.

To normalize the diffractive sample, we subtracted from the data the regenerator noncoherent background, the $3\pi^0$ background and the beam interaction background in the range from 110m to 134m. The HDRA backgrounds do not affect this region, so we were left with the number of coherent data events in this z range. By comparing this number to the

number of coherent Monte Carlo events in this region, we automatically obtained the correct normalization factor for the HDRA diffractive background Monte Carlo.

After the diffractive backgrounds were subtracted, there was a residual background from inelastic interactions of kaons in the HDRA which were not eliminated by the cuts on activity in the drift chambers and the B and C hodoscopes. To simulate the shape of this background, we use a previous measurement [47] of the p_t^2 spectrum of inelasticly scattered kaons. The spectrum was found to have approximately a $e^{-6p_t^2}$ dependence, independent of kaon momentum. We generated a Monte Carlo sample with kaons scattered according to this spectrum at the location of the HDRA. The final result was insensitive to the exact value of the slope used. The generated sample was then normalized to the residual background in region 5 of Fig. 48 after all of the previously discussed backgrounds were subtracted. This was done in the z range from 142 m to 150 m, though the final result was insensitive to the z range used.

To double check the inelastic shape, a sample of inelastic events was isolated by making a tighter cut on activity in the T hodoscope. The predicted inelastic background as a function of ring number and z agreed very well with the observed distribution in this sample.

c. Noncoherent Background Summary and Errors   The overall agreement between data and Monte Carlo in the ring number distribution is illustrated in Fig. 53. The predicted ring number distribution agrees very well with the data, both in the upstream region ($z < 134$m) where only the regenerator noncoherent background contributes, and overall, where both the HDRA and regenerator backgrounds contribute. The same is true for the regenerator beam distributions, though here the contribution from kaons scattering in the HDRA is very small. The data shown here have had the $3\pi^0$ and beam interaction backgrounds subtracted in each ring number bin. The overall agreement is excellent.

The predicted ring number shapes have also been studied in 1 m bins for both the vacuum and regenerator beams in the lead sheet and no lead sheet samples. Fig. 54 shows the data and Monte Carlo distributions for the same nine bins in Fig. 52. The predicted and observed ring number shapes and levels agreed well in all of the z bins. The data in the 1 m z bin plots shown has again had the $3\pi^0$ and beam interaction backgrounds subtracted to allow a direct comparison of the noncoherent backgrounds. Note in particular the z bin for 121 to 122 m. The only significant background here is the regenerator noncoherent background. The regenerator itself is located 2 m downstream of the end of this bin, so this background is entirely from noncoherent decays which have "smeared" upstream in the reconstruction. There is excellent agreement between the predicted and observed background levels in the ring number normalization region. We have also studied these backgrounds in 10 GeV momentum bins, with similar results.

The statistical error on the number of noncoherent background events from scattering in the regenerator is 0.023% (0.018%) in the vacuum (regenerator) beam. As mentioned before, the statistical errors include contributions from the number of background events subtracted from the data, the statistical error on the Monte Carlo sample, and the normalization error. The systematic uncertainty was limited by studying the shape of the ring number distribution for the two beams and extrapolating the uncertainty to ring 0. The studies were statistically limited, and from the individual z bins and the overall shape, we have limited the uncertainty on the noncoherent background level from scattering in the regenerator to 1.2% of itself. The background in the vacuum and regenerator beam from the regenerator
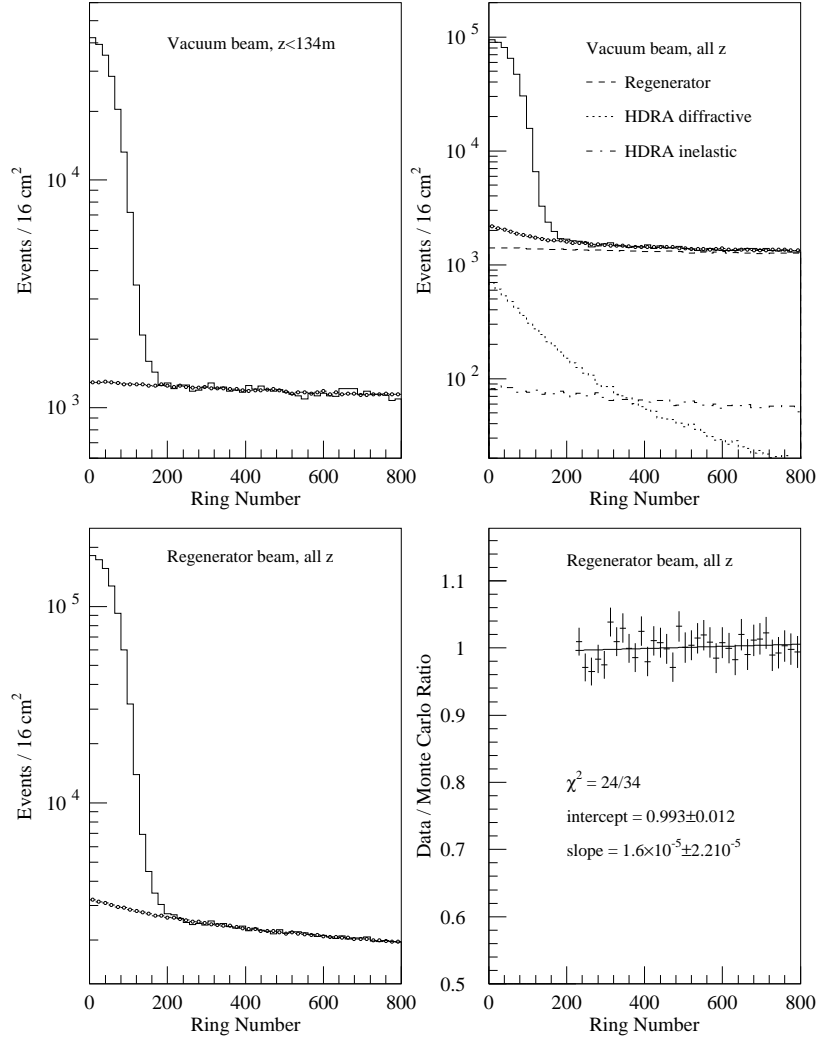
FIG. 53. Observed ring-number distributions in the $2\pi^0$ samples and the predicted backgrounds. In the first 3 plots, the solid histogram is data with the $3\pi^0$ and beam interaction backgrounds subtracted, and the dots are the total predicted noncoherent background. The last plot is the ratio of regenerator beam data to Monte Carlo in the normalization range of the ring-number variable. The slope of the vacuum beam ratio is also consistent with zero.
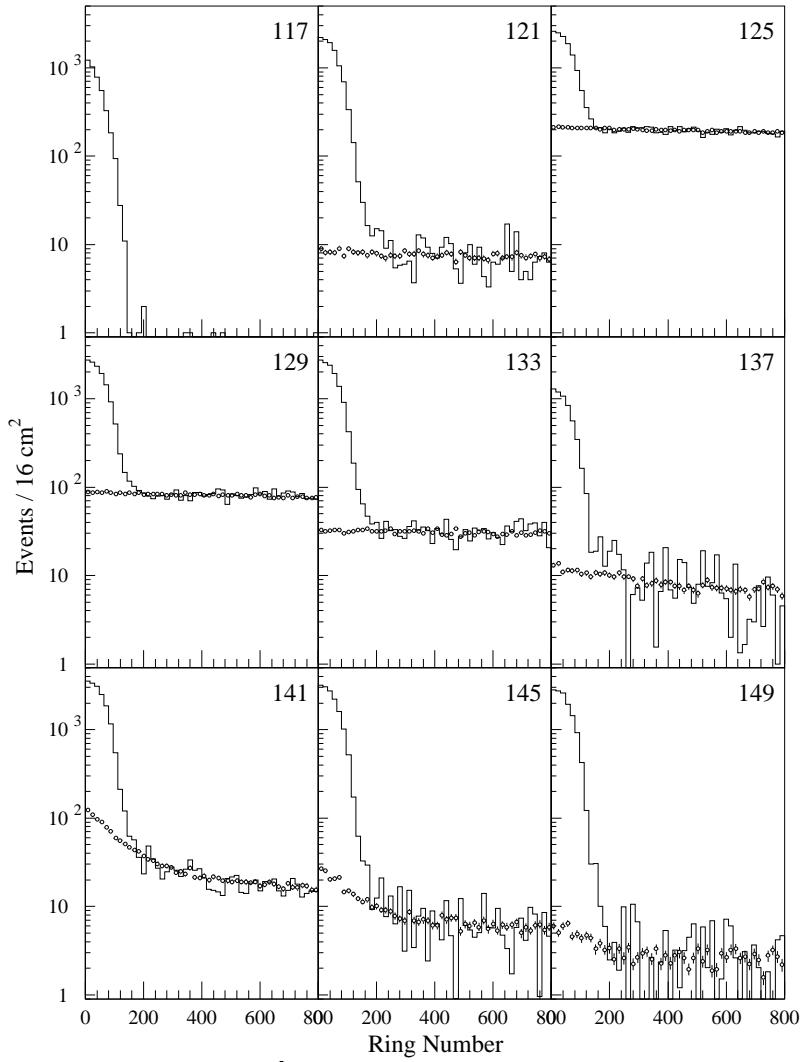
FIG. 54. Observed vacuum beam $2\pi^0$ ring-number distribution and predicted background shape in 9 individual 1 meter z bins. Each plot is labelled with the upstream edge of the z bin. In the 137 meter bin, we only used the data from the $2\pi^0$ subset with no lead-sheet.

are correlated — if the regenerator beam background fraction were smaller, the vacuum beam fraction would also be smaller. Furthermore, this background largely cancels in the vacuum to regenerator beam ratio. However, we have chosen to ignore this correlation when assigning a systematic error, and have taken the full 1.2% error for each of the beams.

The technique used to subtract the diffractive background from the HDRA relies upon knowledge of the regeneration amplitude and p_t^2 distribution for the materials in the HDRA. The uncertainty in the contributions from lead and carbon dominate, and they contribute at the level of 1.3%. Where necessary, we have corrected older amplitude measurements using the world average value for η_{+-}, and its uncertainty has been included in the background uncertainty given above. The statistical uncertainties were 0.014% (0.002%) in the vacuum (regenerator) beam.

The inelastic HDRA contribution was the most difficult to limit systematically because of its low level. The vacuum beam ring number shape agreed well, both within the total sample and the isolated inelastic sample mentioned previously. The inelastic contribution was compared to the Monte Carlo inelastic sample by subtracting all of the other background components from the data. From studies of the shape of the tail of the ring number distribution for the inelastic samples, both overall and in 1 m bins, we have limited the uncertainty to 18% of itself.

In the regenerator beam studies of the isolated inelastic samples, we did observe a discrepancy in the overall ring number distribution at the level of 2 standard deviations. Since this background is so small, it was difficult to make meaningful studies in smaller z bins. The exact shapes of the inelastic contributions from the HDRA are tricky to mimic, as there are comparable contributions expected from kaons which have scattered in the vacuum beam and crossed into the regenerator beam, and from kaons which have scattered within the regenerator beam itself. We have thus assigned a fairly conservative systematic uncertainty of 40% (of itself) to this background source. The statistical uncertainties on the background from inelastic scatters in the HDRA in the vacuum and regenerator beams were 0.006% and 0.002%, respectively.

F. Neutral Mode Conclusion

This completes the discussion of the $2\pi^0$ reconstruction and background subtraction. Table XII shows the level of backgrounds with all errors combined. The total number of events in each of the 10 GeV momentum bins, along with the total background fraction in each bin, is summarized in Table XIII.

The final ingredient needed before we can extract the desired physics from the data samples is the acceptance for both the $\pi^+\pi^-$ and $2\pi^0$ decay modes. We now turn to a more detailed discussion of the Monte Carlo simulation and the acceptance determination.

TABLE XIII. The number of coherent $2\pi^0$ decays after background subtraction and the total background fraction in each 10 GeV bin for the lead sheet and no lead sheet data samples. The background levels are given in percent.

| Momentum Range (GeV/c) | Lead | | | | No Lead | | | |
| | Vacuum | | Regenerator | | Vacuum | | Regenerator | |
	Data	Bkg(%)	Data	Bkg(%)	Data	Bkg(%)	Data	Bkg(%)
40-50	45812	4.8	45667	1.6	30096	3.5	34700	1.4
50-60	51102	5.0	83563	1.7	34659	3.8	62948	1.6
60-70	46171	5.5	93830	2.2	31852	4.3	70311	2.0
70-80	36369	6.2	83444	2.7	25862	5.0	61841	2.6
80-90	26301	6.3	63474	3.2	18617	5.5	47401	3.1
90-100	16965	6.6	41124	3.9	12106	5.9	30694	3.7
100-110	9869	6.8	24102	4.5	7043	6.1	17605	4.4
110-120	5267	6.6	12821	5.2	3855	6.0	9360	5.2
120-130	2682	5.9	6188	5.8	1898	6.1	4383	6.0
130-140	1348	4.7	2626	6.4	941	4.8	1766	7.1
140-150	618	3.2	955	7.2	424	2.9	675	7.4
150-160	277	1.6	308	7.8	195	0.6	215	7.8
Total	242779	5.6	458101	2.7	167547	4.5	341897	2.6

VII. MONTE CARLO SIMULATION

A. Introduction

The difference in the z-distributions in the vacuum and regenerator beams drives the need for an understanding of the acceptance of the detector as a function of z. We can define two categories of acceptances: an "outer" acceptance which is defined by the limiting apertures of the experiment, and an "inner" acceptance, which is determined by thresholds and the granularity of calorimeter and drift chambers. We devote this section to the description of the modelling of both the outer and inner acceptances.

To determine potential systematic biases in the acceptance, we use the K_{e3} and $3\pi^0$ modes. These modes offer much better sensitivity to biases, both because of higher statistics and because a higher fraction of these decays probe the outer and inner acceptances.

In the simulation package the treatment of the kaon beam, propagation of the decay product, and detector response were common to all of the simulations. The only differences were the kaon decay modes and their intrinsic dynamics. Furthermore, to prevent biases in the $\pi\pi$ acceptance determinations, the tuning of the simulation hardly used the $\pi\pi$ data samples. Only the kaon production spectrum was tuned using the observed $\pi\pi$ distributions, but since we bin the data in small momentum bins which introduces negligible bias.

Important inputs to the simulation package were based on survey measurements, EGS [44] electromagnetic shower simulations, and previous experimental measurements. The high statistics decay modes and data from muon runs were used for final tuning, including counter and drift chamber wire efficiencies ("inner" acceptance issues). For the "outer" acceptances, the locations of the limiting apertures were tracked with the electrons from K_{e3} decays after the final chamber alignment (see Section IV A 2).

This section describes the three major components of the Monte Carlo: kaon beam simulation, kaon decays and propagation of daughter particles, and detector response. A representative comparison of the simulation to the $\pi\pi$ data is shown at each stage. Finally, after all the various elements of the simulation have been discussed, the z-distributions of the different decay modes can be examined. First presented are the high statistics modes, from which the limit on the systematic bias is obtained. Then for completeness, the $\pi^+\pi^-$ and $2\pi^0$ z-distributions are presented.

For many of the figures, reconstructed distributions in the $\pi^+\pi^-$ and $2\pi^0$ data are presented with the Monte Carlo simulation overlaid. In these cases, the full Monte Carlo statistics (scaled to the size of the data samples) is shown. The $\pi^+\pi^-$ simulation sample size was 25 times the $\pi^+\pi^-$ data sample size and the $2\pi^0$ simulation size with (without) the lead sheet was 22 (26) times the data size.

B. Kaon Beam

We are not strongly sensitive to the details of the kaon beam for the measurement of $Re(\varepsilon'/\varepsilon)$ and the other parameters, but having the correct beam shape and kaon momentum spectrum helps in several ways in studies of the detector acceptance. With the correct momentum spectrum, we can compare data to the simulation integrated over a broad momentum region, increasing the sensitivity to subtle biases. Furthermore, the acceptance

86

variation near the edges of some of the limiting apertures depends on the beam shape; having it correct simplifies the study of these edges.

Finally, though our detector was located far from the target, effects of $K^0 - \bar{K}^0$ interference were clearly visible in the data sample, particularly at high momentum in the vacuum beam. While not a serious bias, it was very useful to directly compare the simulated and measured decay distributions, which required the incorporation of the interference effects.

The full quantum mechanical description of the $K^0 - \bar{K}^0$ system was used for production and propagation of the kaon beam; this was easily generalized from $\pi\pi$ to other kaon decays. Required inputs were: the production spectra of K^0 and $\bar{K}^0$; the transport function for the propagation of the kaons through the vacuum and various absorbers in the beam; and the relative positions and orientations of the collimators which determine the final shapes of the two beams.

1. Production Spectrum

The basis for the energy and angular distributions of the produced kaons was the Malensek [51] parametrization of the K^+ and K^- production spectrum for protons incident on a beryllium target.

For production of a particle with momentum p into a solid angle $d\Omega$ centered at a polar angle θ and an azimuthal angle ϕ, Malensek presents a general form for the spectrum of

$$\frac{d^2N}{dp\,d\Omega} = \frac{B}{400} x \frac{(1-x)^A(1+5e^{-Dx})}{(1+p_t^2/M^2)^4}.$$

(61)

In this expression, x is the ratio of the produced particle's momentum p to the beam energy E_B, $x = p/E_B$, and p_t is the transverse momentum of the produced particle relative to the incident beam direction, $p_t = p\sin\theta$. Parameters B, A, D and M^2 were then determined using experimental data at 400 GeV/c. For charged kaons, the best parametrizations had these values:

	B	A	D	M^2
K^+	14.15	2.924	19.89	1.164
K^-	12.33	6.107	17.78	1.098

We need to know how the dilution factor d_K, defined by

$$d_K \equiv \frac{K^0 - \bar{K}^0}{K^0 + \bar{K}^0},$$

(62)

is related to the relative numbers of K^+ and K^- produced. The dilution factor extracted by the CERN NA31 experiment as part of their dedicated $\Delta\phi$ measurement [24] indicated that a good representation is given by

$$d_K = \frac{K^+ - K^-}{K^+ + 3K^-}.$$

(63)

A simple argument [52] shows that this form follows from the valence quark content of the beam particles.
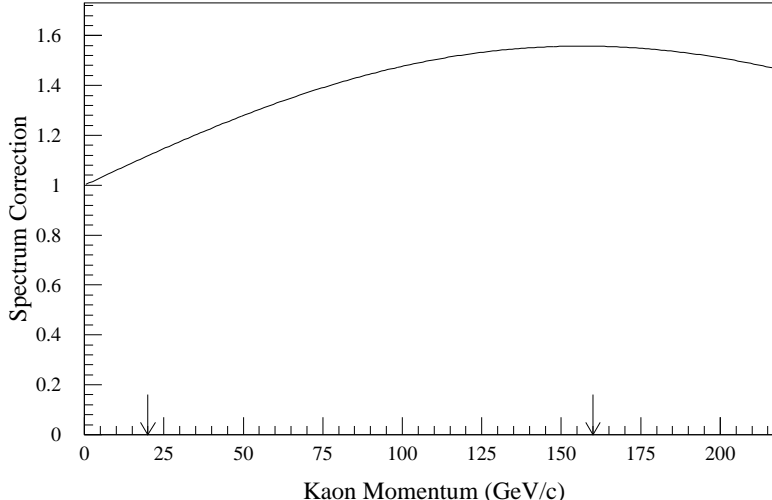
FIG. 55. Momentum-dependent correction factor needed to bring the Malensek energy spectrum into agreement with the vacuum beam spectrum observed in our $\pi^+\pi^-$ NC subset. The arrows denote the limits of the kaon momentum range used in our analyses.

Because there were uncertainties of order 10% in the data at only one beam energy used to derive this spectrum, we did not expect the Malensek spectrum to be perfect. We therefore tuned the spectrum using 80% of the vacuum beam $\pi^+\pi^-$ decays in the NC subset (about 20% of the total sample of $\pi^+\pi^-$ decays) over 20 to 500 GeV/c reconstructed kaon momentum range. The correction factor (which is applied to the overall rate in the beam but not to the dilution factor or to the p_t spectrum) is plotted in Fig. 55. This changes by 20% from 40 to 150 GeV/c, while the spectrum itself drops by a factor of 4.5 over the same range.

The final energy spectrum in each data sets was obtained by adjusting the primary beam targetting angles. The nominal angles were 4.8 mrad in x and 0 mrad in y. If the y-targetting angle were non-zero, there would be a small shift in the average kaon energy of the top beam relative to the bottom beam with a dependence of roughly

$$E_t - E_b \approx 0.5\theta_y[\text{mrad}], \tag{64}$$

where E_t (E_b) is the mean kaon energy in the top (bottom) beam in GeV, and θ_y is the y targetting angle. (When $\theta_y > 0$, the proton beam falls relative to the kaon beam.) A deviation of the x targetting angle from the nominal angle shifts the average kaon energy of both beams together. The targetting angles that we input to the simulation for each data subset, based on the observed kaon energies in the beams, are plotted in Fig. 56. The x targetting angle is stable and independent of intensity.

The y targetting angle was found to be correlated with the intensity of the proton beam which was adjusted by a vertical beam tune far upstream of the target. The beam tune for the high intensity sets appears to have been quite similar. At lower intensity, a much different beam tune appears to have been used in the early data sets (C1 and C2). The last data set (NC), with an intensity between the low and high intensity, has an intermediate y targetting angle.

The final energy spectra produced in the Monte Carlo are compared to the observed $\pi^+\pi^-$ and $2\pi^0$ spectra in Figs. 57 and 58. The spectra agree quite well in both sets, though
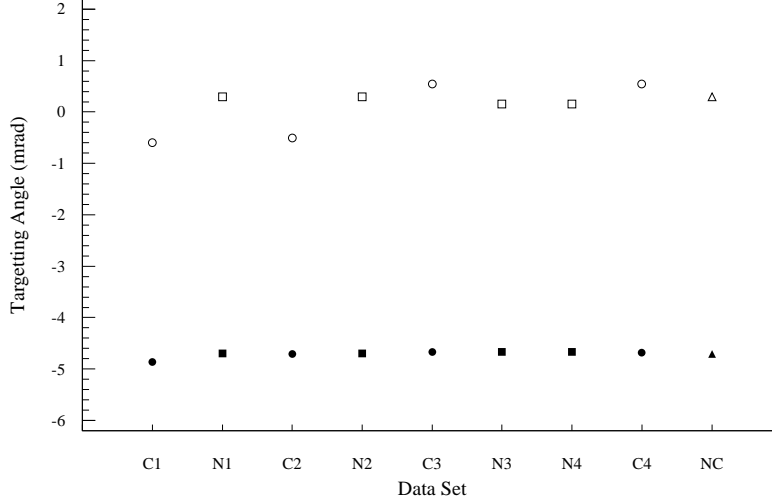
FIG. 56. Inferred x and y targetting angles for the nine data collection periods. The x (y) targetting angles are plotted as solid (hollow) points. For both the x and the y angles, the highest intensity points are the squares, the medium intensity are the triangles, and the lowest intensity are the circles.

there is perhaps a residual bowing of a few percent in the charged mode.

2. Kaon Transport

The K^0 and $\bar{K}^0$ components are written as an incoherent sum of initial K_S and K_L amplitudes. Given these, propagation through the vacuum is trivial:

$$\begin{pmatrix} a_S \\ a_L \end{pmatrix} \rightarrow e^{-\imath m_L} \begin{pmatrix} a_S e^{\tau(\imath \Delta m - \Gamma_S/2)} \\ a_L e^{-\tau \Gamma_L/2} \end{pmatrix}, \tag{65}$$

where a_S and a_L are the initial K_S and K_L amplitudes, and the proper time τ is related to the propagation distance Δz and the momentum p by

$$\Delta z = \frac{p[\text{GeV}/c]}{m_K[\text{GeV}/c^2]} c\tau. \tag{66}$$

The kaon passes through the remainder of the target and the common absorber. If the kaon is in the regenerator beam, it also passes through the shadow absorber and then through the regenerator. In addition to attenuation, scattering and regeneration affect the relative K_S and K_L content, the final energy spectrum, and the angular spread of the beam.

Coherent regeneration of the kaons is handled exactly. The forward regeneration and overall attenuation can be incorporated into a simple matrix form:

$$\begin{pmatrix} a_S \\ a_L \end{pmatrix} \rightarrow e^{-x/2} \begin{pmatrix} T_{SS} & T_{SL} \\ T_{LS} & T_{LL} \end{pmatrix} \begin{pmatrix} a_S \\ a_L \end{pmatrix}, \tag{67}$$

where x is the total number of interaction lengths through which the kaon passes. The elements of the transformation matrix T depend on the forward scattering amplitudes $f(0)$

89

FIG. 57. The kaon energy spectrum for the $\pi^+\pi^-$ decay sample in data and Monte Carlo simulation. *Top:* The data spectrum is plotted as a histogram and the simulation as dots. *Bottom:* The ratio of data events to Monte Carlo simulation.
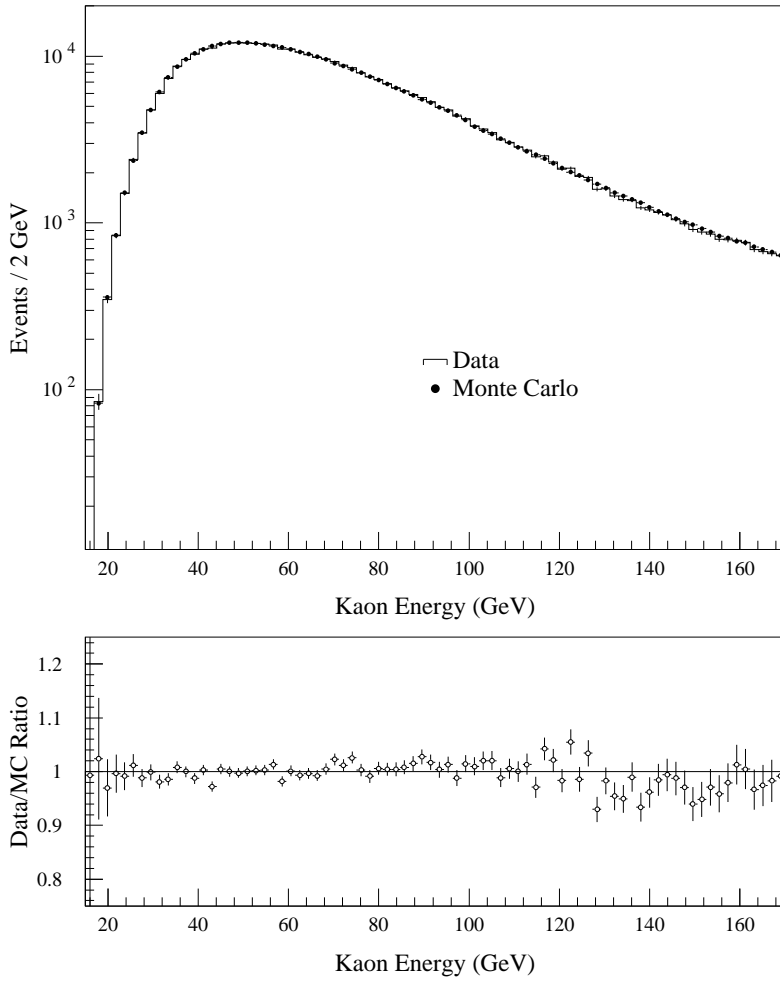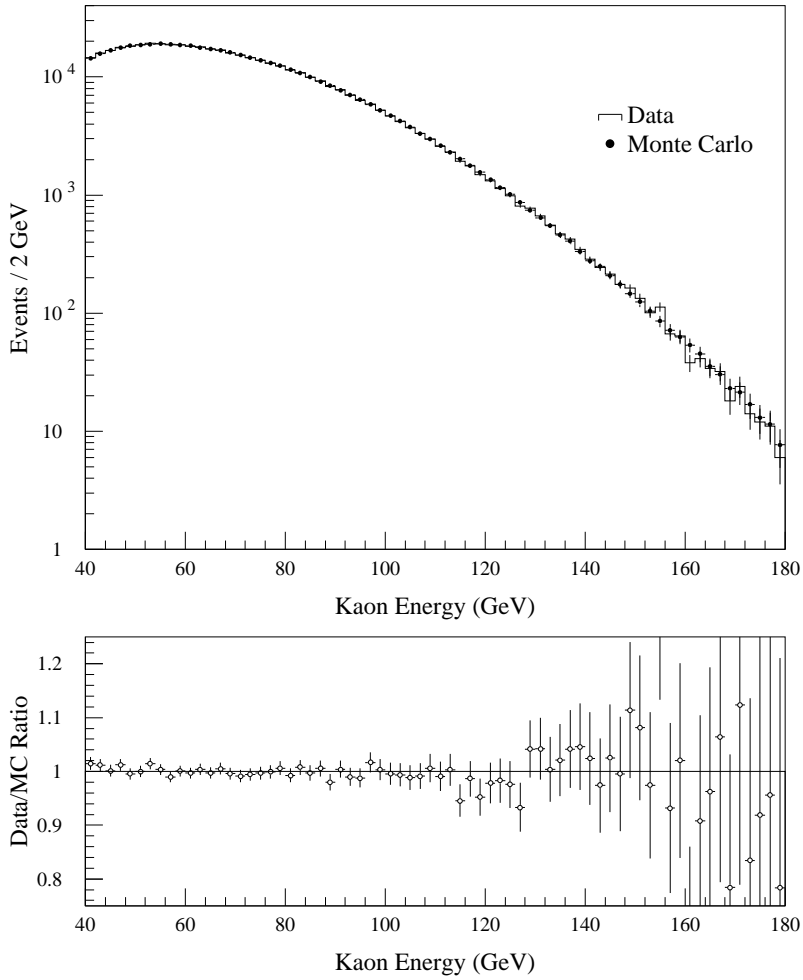
FIG. 58. The kaon energy spectrum for the $2\pi^0$ decay sample in data and Monte Carlo simulation. *Top:* The data spectrum is plotted as a histogram and the simulation as dots. The predicted background contributions have been added to the coherent $2\pi^0$ Monte Carlo simulation. *Bottom:* The ratio of data events to the Monte Carlo simulation.

TABLE XIV. Probability and exponential slope for single elastic scattering of kaons in each of the absorber elements in the kaon beam.

Absorber Component	Single Scattering Probability (%)	Exponential Slope ($[\text{GeV}/c^2]^2$)
Beryllium, Common Absorber	8.6	65
Lead, Common Absorber	17.8	420
Beryllium, Movable Absorber	7.8	65

and $\bar{f}(0)$ of the K^0 and $\bar{K}^0$ for the material in the kaon beam. The form for the elements of T can be found in reference [1].

Scattered kaons essentially modify the spectrum $dN/dp\,dp_t^2$ entering the decay volume; scattering also tends to blur out the edges of the beam.

As kaons passed through the absorber materials — the lead and beryllium portions in the common absorber and the beryllium in the shadow absorber — we allowed them to have a single elastic scatter in the Monte Carlo simulation. The scatters were distributed with a p_t^2 spectrum of $\exp(-\alpha p_t^2)$. The slope α and scattering probability were taken from the K^+ and K^- elastic scattering cross sections measured by Schiz $et\ al$ [53]. The values used are listed in Table XIV.

The scattering and coherent regeneration were included before the final spectrum tuning mentioned above was made.

3. Beam Collimation and Targetting

The last ingredient for the simulation of the beam was the fine tuning of the collimator positions and the inclusion of the finite size of the proton beam at the target. In general, the effect of a particular collimator face could be identified in a unique region of the beam profile, allowing both the average collimator position and the angle of the collimator slab relative to the z axis to be extracted.

The position of the beam spot was measured several times during each 20 second beam spill. The intensity profile of the beam itself was roughly a Gaussian with a width of 0.8 mm in x and y. This beam jitter would blur the edges of the beam profile, just as the elastic scattering did. The beam spot movement was incorporated into the Monte Carlo simulation through these measurements.

In the charged mode, the beam shapes were studied using the projected kaon position at the regenerator. For the neutral mode, the beams shapes for a given $2\pi^0$ subset were initially based on the collimator positions measured in the bracketing $\pi^+\pi^-$ subsets. The final tuning was then done based on the center of energy distributions measured in the lead glass calorimeter for the $2\pi^0$ and $3\pi^0$ decays. The final shapes are shown for the charged mode in Fig. 59 and for the neutral beam in Fig. 60.
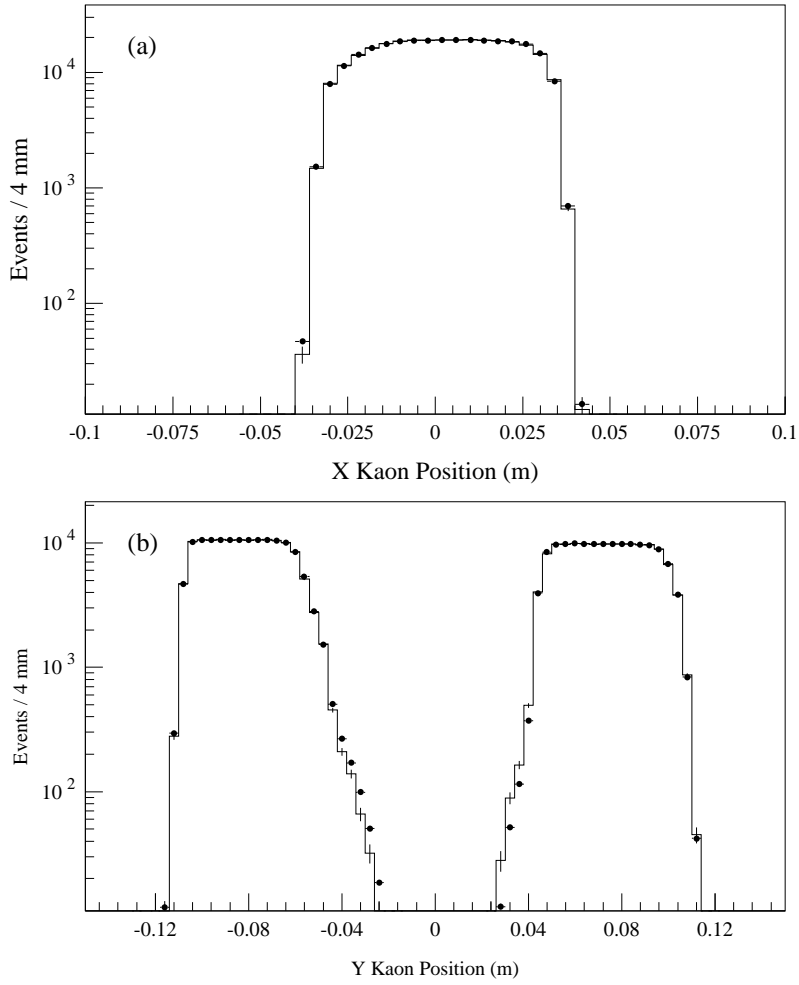
FIG. 59. The projection of the kaon trajectory to the regenerator position for all $\pi^+\pi^-$ decays collected from the vacuum beam. The x projection is shown in (a), and the y position in (b). The Monte Carlo simulation (dots) has been overlaid on top of the data distribution (histogram).
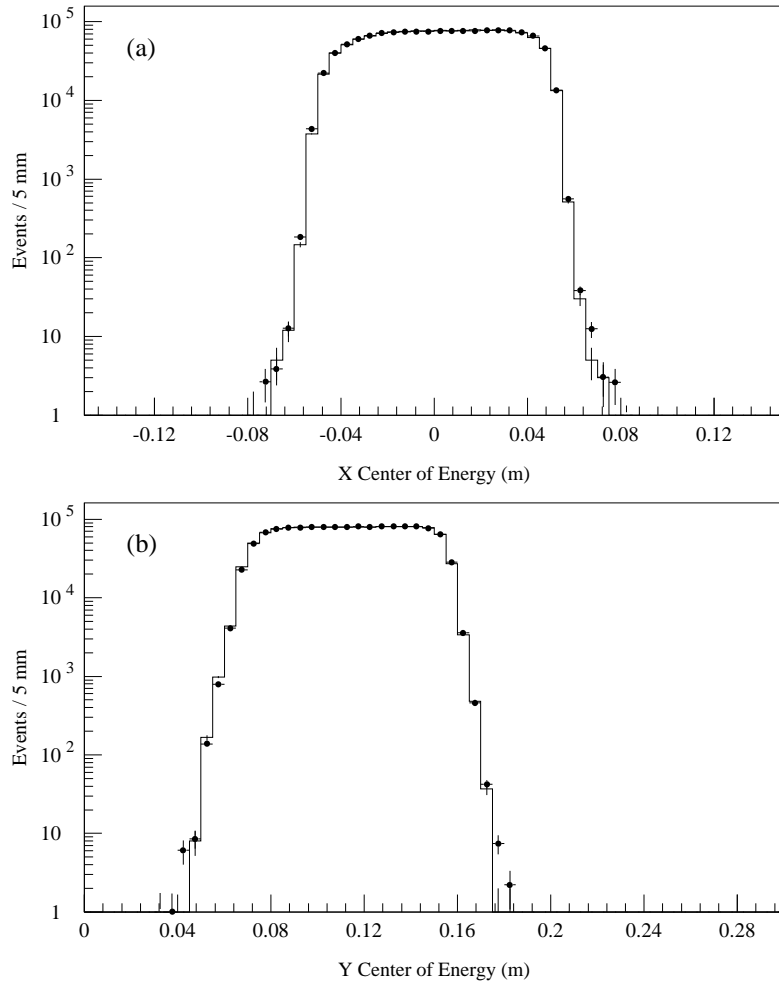
FIG. 60. The center of energy distribution measured in the lead-glass calorimeter for all $3\pi^0$ decays collected from the vacuum beam. The x projection is shown in (a), and the y position in (b). The Monte Carlo simulation (dots) has been overlaid on top of the data distribution (histogram).

C. Decays and Interactions

1. Particle Decays

The dynamics for all decay modes were fully simulated. In the K_{e3} decays, the time dependent charge asymmetry is used to decide whether the final state is $\pi^+ e^- \bar{\nu}_e$ or $\pi^- e^+ \nu_e$:

$$\delta\tau = \frac{R(\pi^- e^+ \nu) - R(\pi^+ e^- \bar{\nu})}{R(\pi^- e^+ \nu) + R(\pi^+ e^- \bar{\nu})}, \tag{68}$$

with the decay probabilities R given in terms of the K_S and K_L amplitudes $a_S(\tau)$ and $a_L(\tau)$ by

$$R(\pi^- e^+ \nu) = \frac{|1+\varepsilon|^2}{2(1+|\varepsilon|^2)} |a_S(\tau) + a_L(\tau)|^2$$

$$R(\pi^+ e^- \bar{\nu}) = \frac{|1-\varepsilon|^2}{2(1+|\varepsilon|^2)} |a_S(\tau) - a_L(\tau)|^2. \tag{69}$$

The form factor governing this decay is included. Similarly, the decay probabilities for the $\pi\pi$ and $\pi\pi\pi$ decays also included the CP–violating amplitudes,

$$R(\pi\pi) = |a_S(\tau) + \eta a_L(\tau)|^2$$

$$R(\pi\pi\pi) = |\eta a_S(\tau) - a_L(\tau)|^2. \tag{70}$$

For $\pi^+\pi^-$ and K_{e3} decays, the $\pi^+\pi^-\gamma$ and $K_{e3\gamma}$ radiative decay modes were included at the proper level, with 5 MeV and 1 MeV center-of-mass photon energy cutoffs, respectively.

The decays of daughter particles are also implemented. Of particular importance were decays-in-flight of the charged pions from $\pi^+\pi^-$ decays. Most muons produced in pion decay hit the muon veto bank or introduced a substantial kink in the flight path, causing the parent $\pi^+\pi^-$ decay to be rejected. About 5% of the pions decay before the leadglass calorimeter with momentum above the 7 GeV/c cut (Section V A 2). But because of the difference in the z-distributions, there is only about 0.2% greater loss in regenerator beam than in vacuum beam. Including the decay in flight in the simulation correctly compensates this asymmetry.

2. Interactions with the Detector Material

Interactions of daughter particles with material in the detector was also simulated, including multiple scattering, and bremsstrahlung and conversions, the latter producing "grandaughter" particles. Characteristics of the material in the detector are given in Table XV. It was sufficient to group helium and helium bag windows with the closest drift chamber, and to collapse each chamber to a single plane.

Photon conversions at the HDRA were particularly important, since the HDRA is near the center of the $2\pi^0$ decay volume, and there are different fractions of $K \to \pi^0\pi^0$ decays in the vacuum and regenerator beams which occur upstream of the lead sheet. A straightforward calculation shows that if c is the (average) probability for at least one of the four photons to convert at the HDRA, f_v (f_r) is the fraction of $2\pi^0$ decays upstream of the HDRA

TABLE XV. Scattering and photon conversion locations and the thickness of material in radiation lengths.

Detector Element	Location from Target (m)	Thickness (Radiation Lengths)
V hodoscope	137.792	3.23×10^{-3}
Pb sheet[a]	137.804	9.36×10^{-2}
T hodoscope	137.815	3.43×10^{-3}
Vacuum Window	158.965	2.50×10^{-3}
Drift Chamber 1	159.292	3.42×10^{-3}
Drift Chamber 2	165.867	3.86×10^{-3}
Drift Chamber 3	171.857	3.63×10^{-3}
Drift Chamber 4	178.004	2.10×10^{-3}
Chamber Field Wires[b]	—	5.70×10^{-3}
Chamber Sense Wires[c]	—	6.43×10^{-3}
C Hodoscope	179.502	4.0×10^{-2}
B Hodoscope	179.520	4.0×10^{-2}

———

[a]Used only in $2\pi^0$ lead sheet subsets. Average radiation length is listed.

[b]This contribution is identical in all four chambers. Only the 9.9% of the tracks which hit these wires (per chamber) see this contribution.

[c]This contribution is identical in all four chambers. Only the 0.7% of the tracks which hit these wires (per chamber) see this contribution.

in the vacuum (regenerator) beam, and there is a bias of Δ in the conversion probability in the Monte Carlo ($c_{MC} = c[1 + \Delta]$), then the bias introduced into the vacuum to regenerator beam ratio R_{00} is

$$R_{00} \rightarrow R_{00} \left\{ 1 + (f_r - f_v)\frac{c}{1 - c}\Delta \right\}. \tag{71}$$

Here f_r and f_v are 92% and 66%, respectively. About 23.7% of $K \rightarrow \pi^0\pi^0$ decays upstream of the Pb sheet have at least one conversion. Only 2% of the decays have conversion from the rest of the material. Since the lead sheet was present for 65% of the data taking, making the average probability for one or more conversion to be 17.1%. A mismeasurement Δ in the conversion probability would therefore bias R_{00} by 0.054Δ. To keep the bias in $Re(\varepsilon'/\varepsilon)$ under 10^{-4}, we have to keep $\Delta < 1.1\%$. As we discuss in Section X E, we have achieved this by using a combination of direct measurement of the sheet over its entire surface, and measuring the step in the $3\pi^0$ z-distribution at the HDRA. The simulation included the measured variation in the sheet thickness and the energy dependence of the photon cross section in lead calculated by Hubbell, Gimm, and Øverbø [54].

3. Limiting Apertures

The fractional loss of events near the edge of an aperture is generally compensated twice in the measurement of $Re(\varepsilon'/\varepsilon)$, once in the vacuum to regenerator beam ratio and again when comparing the $\pi^+\pi^-$ mode to the $2\pi^0$ mode. To ensure that the biases would be minimal, we measured the effective aperture edges as precisely as possible, using the large sample of electrons from K_{e3} decays.

The components of the detector serving to limit the acceptance were the active mask, the HDRA, the vacuum window aperture, and the collar anti. The limiting apertures were adjusted in size and transverse location by comparing illuminations of electrons from K_{e3} decays in a portion of the NC subset to those from simulated decays for that subset. Then, the sizes of the apertures were fixed and their locations were tracked by comparing the K_{e3} data from different subsets to the reference subset. The z positions of the apertures were measured directly in a survey at the completion of the run.

For the aperture farthest upstream at the Mask Anti, the space resolution for the x or y projection was of order 1.2 mm for a typical track, where about 0.6 mm (1 mm) comes from chamber resolution (multiple scattering). For the Collar Anti, the resolution was closer to 0.2 mm, with roughly equal contributions from chamber resolution and scattering in the trigger hodoscopes. These two apertures were the most critical. The K_{e3} electron illumination at one edge of each of these locations is shown in Fig. 61 before the final adjustment.

To determine the relative position of a given aperture edge between data and Monte Carlo, the Monte Carlo illumination is shifted in $100\mu m$ steps relative to the data, and a χ^2 by comparing both to come from the same parent distribution is calculated.

When the illumination is plotted with a binning small relative to the (single event) resolution, and the shift is small, χ^2 depends quadratically on the shift. For the Mask edge illumination pictured in Fig. 61, this quadratic behavior is clear in the plot of χ^2 versus shift in Fig. 62. When the shift is much larger than the resolution, χ^2 behaves linearly.
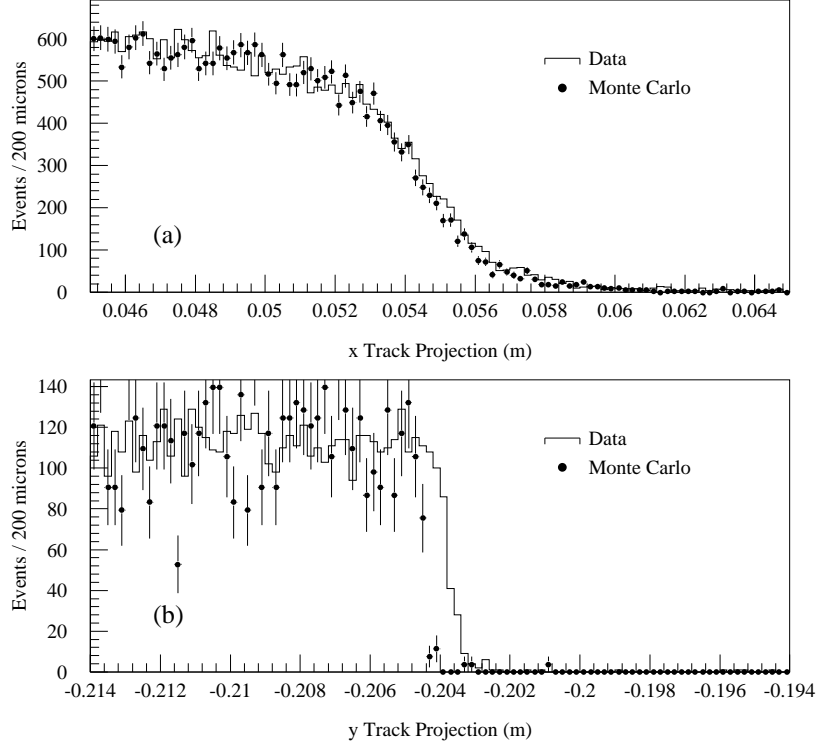
97

FIG. 61. Illumination of two of the aperture edges by electrons from K_{e3} decays in the NC subset. The histogram shows the data illumination, while the dots show the MC prediction before the final tuning of the aperture positions. (a) Horizontal edge of the active mask. (b) East half of the bottom edge of the Collar Anti surrounding the lower beam. These edges showed the largest misalignment of their respective apertures before the final position adjustment. The mask edge is shifted about 230μm, and the Collar Anti edge by about 700μm.

The shifts were determined, with a quadratic fit at the minimum, statistically to better than 10μm for the Mask and the Collar Anti. This procedure relies on the shape of the illumination in Monte Carlo and data agreeing. To evaluate the systematic uncertainty, the procedure was repeated with windows of different sizes around each edge, with different ranges of fits, and by fitting to the expected linear behavior farther from the edge rather than to the quadratic behavior near the edge. From these studies, we have limited the systematic uncertainty on each measured edge to under 50μm.

This systematic error does not include the position uncertainty from the chamber alignment. This uncertainty cancels in determining the *size* of the aperture, since the bias is identical for all edges of the aperture and cancels when looking at the difference between the left and right or top and bottom edges of an aperture. It enters only when tracking the edges as a function of time. As we discuss in Section X D 1, there is an additional uncertainty of 60μm from chamber alignment for each measurement of the Mask Anti shift, but only 15μm for the Collar Anti.

The shifts measured for the Mask and the Collar Anti are plotted in Fig. 63. The Collar Anti position was stable since it was rigidly attached to the lead glass which defined one end of the coordinate system. The Mask Anti appears to have drifted on the order of 800μm in y and 600μm in x over the course of the run. This is an artifact of tying the global coordinate
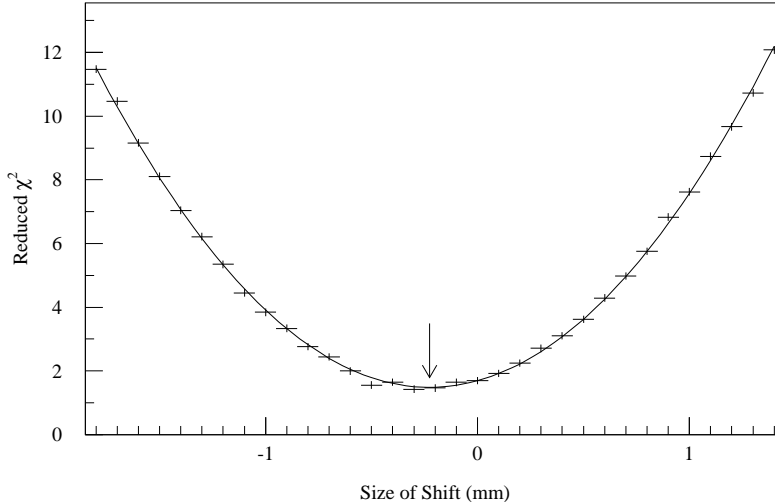
98

FIG. 62. Distribution of the reduced χ^2 for the data and Monte Carlo $+x$ Mask edge illuminations to come from the same parent distribution versus the Monte Carlo shift. The curve is the best fit quadratic, and the arrow indicates the minimum at $-226 \pm 7\mu$m.

system to the target. The entire target pile was sinking over the course of the run, dropping several millimeters. The apparent shift of the Mask and other apertures and collimators were consistent with the target pile motion.

After all the fine tunings based on the K_{e3}, it is interesting to compare the illuminations of some of the apertures in $\pi^+\pi^-$ and $2\pi^0$ decays. The Mask illuminations for the two decay modes are shown in Fig. 64 (the x view) and Fig. 65 (the y view). Only the vacuum beam illuminates the mask. Overall, the agreement is excellent in both modes except for the small excess in the Monte Carlo simulation over the data at the $-x$ edge in the neutral mode. This mismatch is consistent with a small mismatch in the $2\pi^0$ beam shape at that edge. If attributed to an incorrect mask aperature, the mismatch of 650μm at one edge shifts the vacuum to regenerator beam ratio (after acceptance corrections) by -0.030%, and hence biases $Re(\varepsilon'/\varepsilon)$ by -0.50×10^{-4}.

The vacuum and regenerator beam illuminations at the HDRA are shown in Figs. 66 and 67 for the x and y views, respectively. Finally, the illuminations at the lead glass are pictured in Figs. 68 and 69 for the x and y views.

With the apertures under control, the "outer" acceptance has been defined. We now examine our modelling of the response of the detector elements, which determines the "inner" acceptance of the detector.

D. Detector Response

We describe in this section the simulation of the detector elements; in particular the lead glass calorimeter response, the drift chamber response, and the response of scintillator and veto hodoscopes.

99
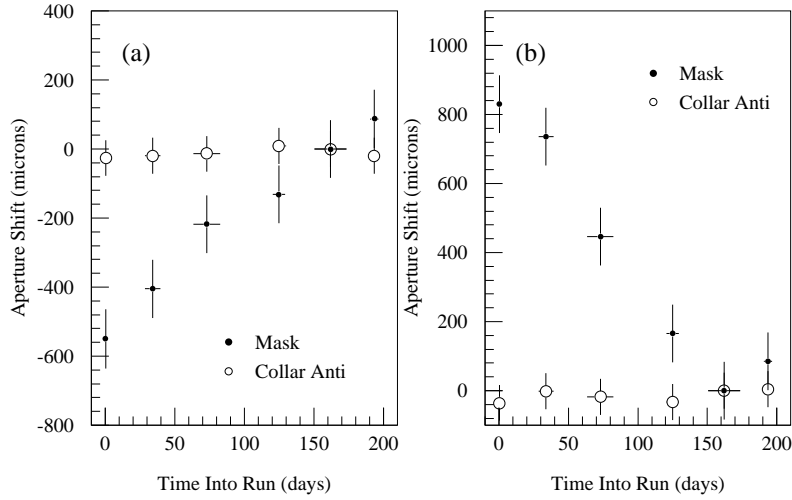
FIG. 63. Apparent motion of the Collar Anti and Mask apertures with time. (a) Horizontal motion. (b) Vertical motion. The shifts are measured relative to th NCa subset (fifth data point).

FIG. 64. Vacuum beam $\pi^+\pi^-$ track illumination and $2\pi^0$ photon illumination in the x-view at the plane of the active mask for data and Monte Carlo simulation. (a) $\pi^+\pi^-$ track projection. (b) $2\pi^0$ photon projection. The arrows indicate the locations of the mask edges.

FIG. 65. Vacuum beam $\pi^+\pi^-$ track illumination and $2\pi^0$ photon illumination in the y-view at the plane of the active mask for data and Monte Carlo simulation. (a) $\pi^+\pi^-$ track projection. (b) $2\pi^0$ photon projection. The arrows indicate the locations of the mask edges. Only the vacuum beam illuminations are shown.

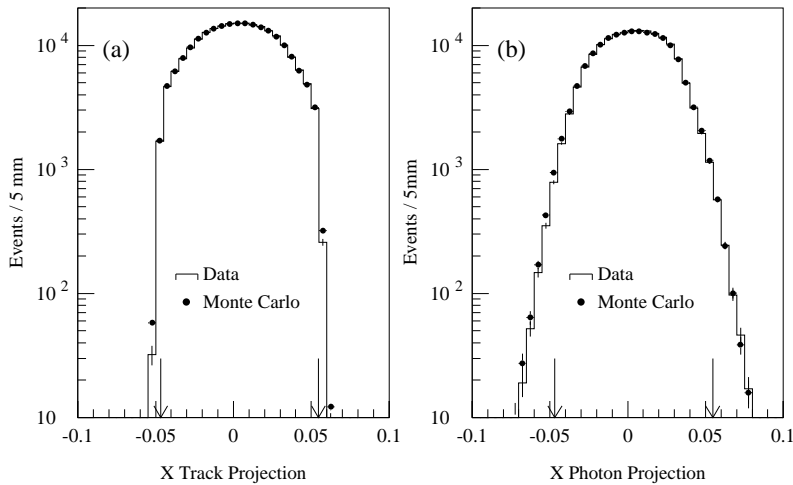FIG. 66. $\pi^+\pi^-$ track illumination and $2\pi^0$ photon illumination in the x-view at the plane of the HDRA for data and Monte Carlo simulation. (a) Vacuum beam $\pi^+\pi^-$ track projection. (b) Regenerator beam $\pi^+\pi^-$ track projection. (c) Vacuum beam $2\pi^0$ photon projection. (d) Regenerator beam $2\pi^0$ photon projection. The arrows indicate the locations of the HDRA edges.

FIG. 67. $\pi^+\pi^-$ track illumination and $2\pi^0$ photon illumination in the y-view at the plane of the HDRA for data and Monte Carlo simulation. (a) Vacuum beam $\pi^+\pi^-$ track projection. (b) Regenerator beam $\pi^+\pi^-$ track projection. (c) Vacuum beam $2\pi^0$ photon projection. (d) Regenerator beam $2\pi^0$ photon projection. The arrows indicate the locations of the HDRA edges.
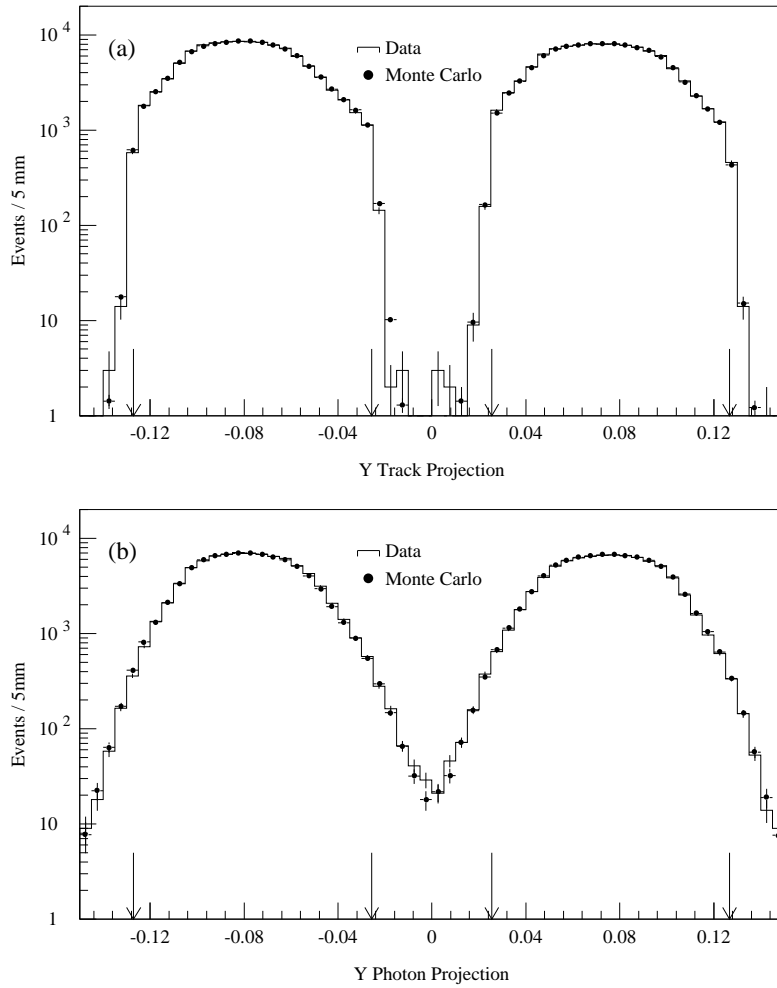
103

FIG. 68. $\pi^+\pi^-$ track illumination and $2\pi^0$ photon illumination in the x-view at the plane of the lead-glass for data and Monte Carlo simulation. (a) Vacuum beam $\pi^+\pi^-$ track projection. (b) Regenerator beam $\pi^+\pi^-$ track projection. (c) Vacuum beam $2\pi^0$ photon position. (d) Regenerator beam $2\pi^0$ photon position.
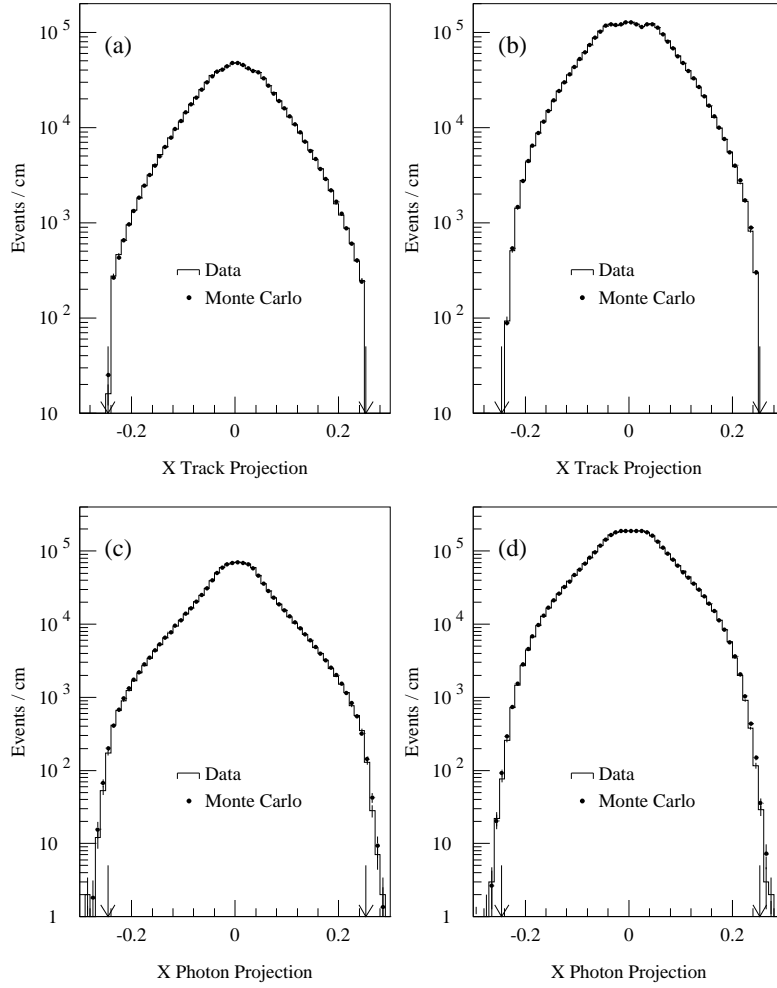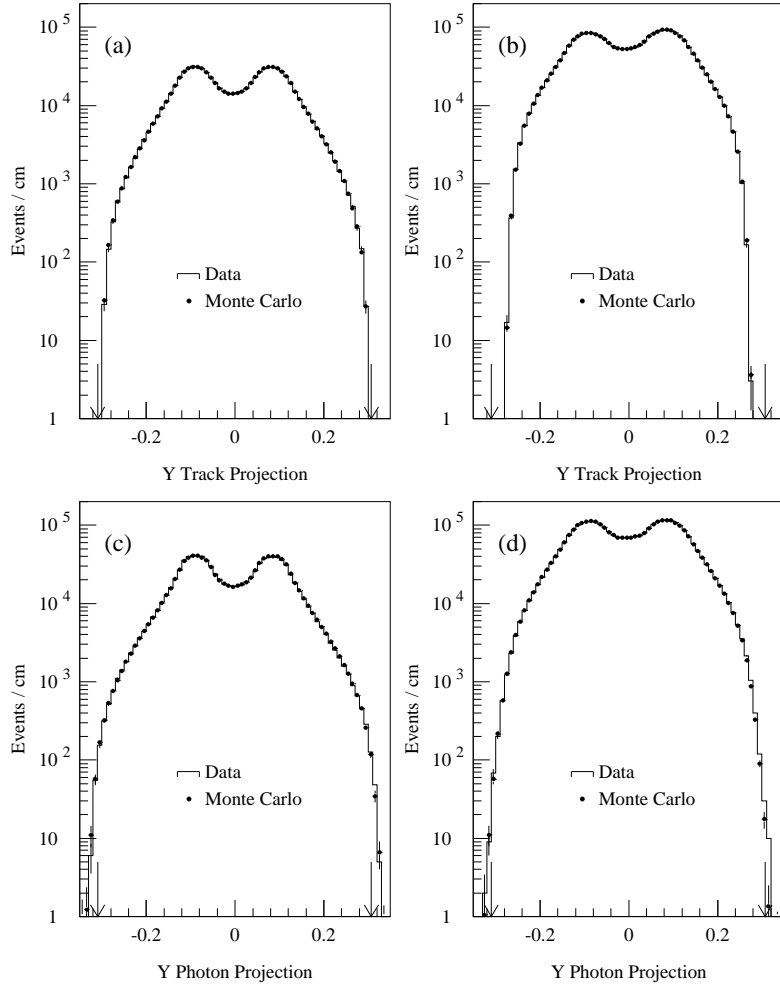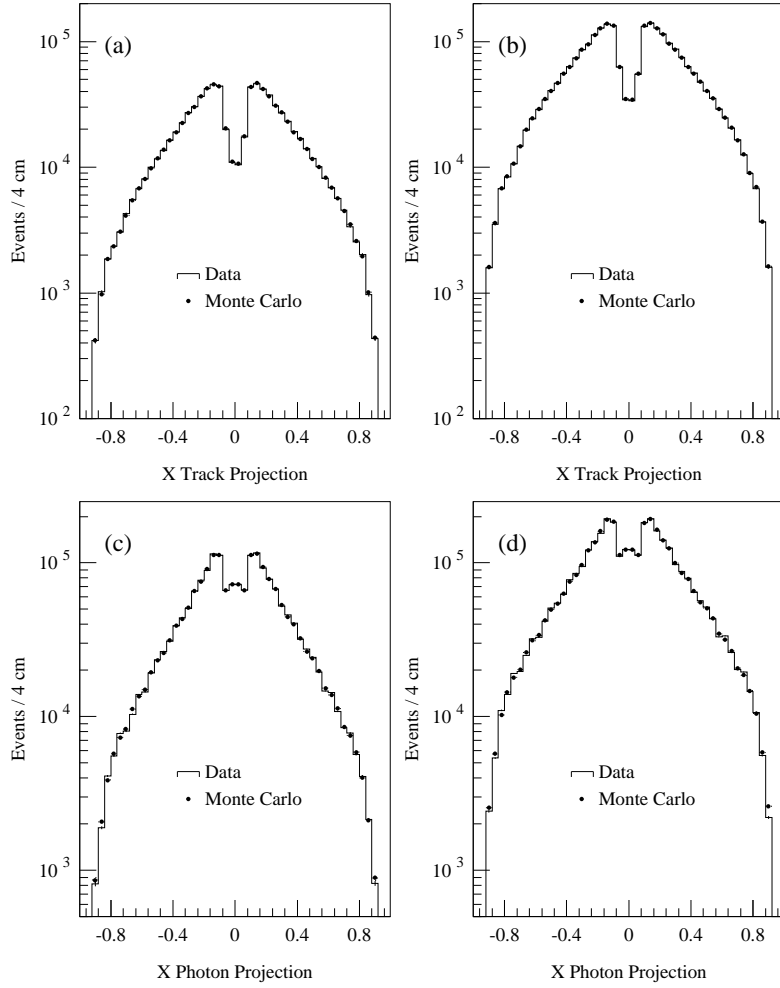
FIG. 69. $\pi^+\pi^-$ track illumination and $2\pi^0$ photon illumination in the y-view at the plane of the lead-glass for data and Monte Carlo simulation. (a) Vacuum beam $\pi^+\pi^-$ track projection. (b) Regenerator beam $\pi^+\pi^-$ track projection. (c) Vacuum beam $2\pi^0$ photon position. (d) Regenerator beam $2\pi^0$ photon position.
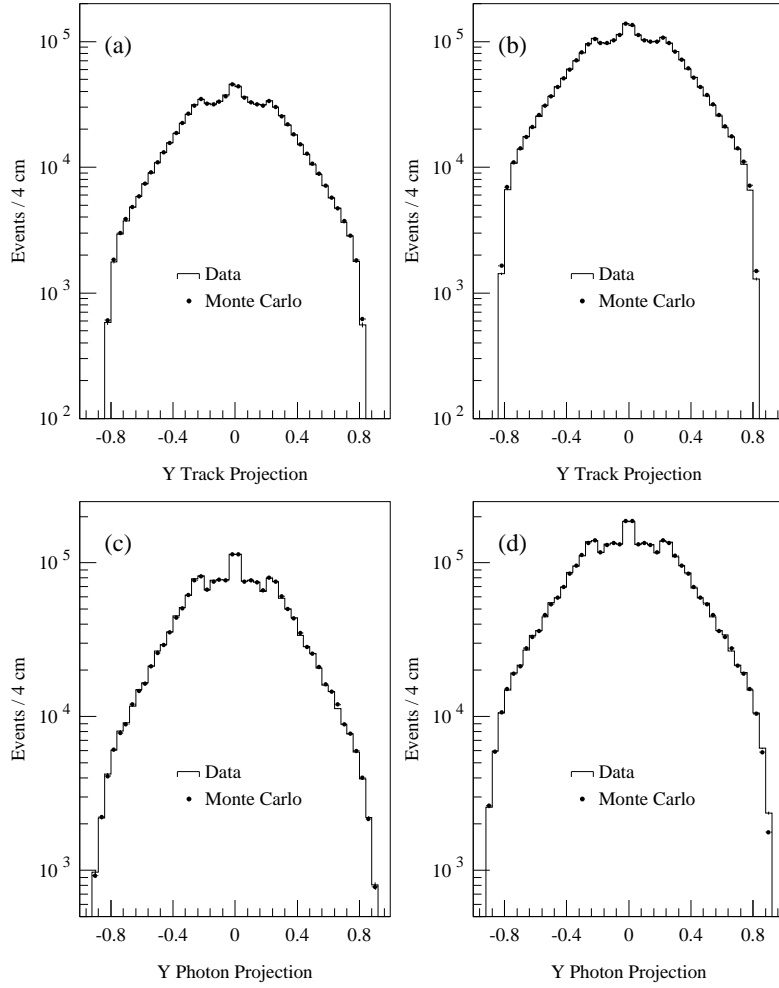
1. Simulation of the Lead Glass Calorimeter Response

For each electron or photon striking the lead glass calorimeter, we did not simulate a complete electromagnetic shower. Instead the response of the lead glass was parametrized as a function of electron energy, Čerenkov light absorption coefficient α (see Section IV B), and depth of photon conversion based on a stand-alone study of lead glass using the EGS4 [44] shower simulation package. The model for the attenuation length was described in Section IV B 1, and, along with the EGS cluster generation, in reference [37].

a. Parametrization of the lead glass response to electrons The response of the lead glass to electron showers was modelled by assuming that the absorption of Čerenkov light is uniform through the length of the block. We have calibrated the leadglass with this assumption, and from each electron calibration we have extracted an average absorption coefficient α (typically 3% to 4% per radiation length) for each block. We expect the variations in response of the lead glass to be dominated by the depth t_{max} of the maximal energy deposition. Since t_{max} depends logarithmically on E_i [43,55], we used the EGS4 package to generate showers with energies spaced uniformly in lnE_i, from 0.25 GeV to 90.51 GeV. For each shower, the track length of each charged particle was weighted by the number of Čerenkov photons that the particle would radiate, $N_c = 1 - 1/n^2\beta^2$, where n is the index of refraction. The sum of the total weighted track length was then recorded in cells measuring $0.36 \times 0.36 \times 0.5$ radiation lengths, covering a volume of 30 radiation lengths deep and 7×7 block-widths wide transversely.

For each generated electron shower, the Čerenkov light in each cell was attenuated using a given absorption coefficient to the back of a block of a given length. (For the modelling of photons, it was useful to calculate the response for blocks of different lengths.) The response of the block to that shower was defined by the ratio of the total Čerenkov light reaching the back of the block to the total Čerenkov light produced. For each shower we calculated the response using a set of attenuation coefficients which spanned the range of coefficients measured in the various electron calibrations. As discussed in Section IV B 1, we treat a photon by having it first convert at a depth t_0 in the block, and then treat the photon shower as 2 independent electron showers in a block of length $18.7 - t_0$ radiation lengths.

The block response was accumulated for each pair of absorption coefficient and block-length parameters. It was then parametrized with a simple functional form depending upon the absorption coefficient, the electron energy, and the conversion depth. This parameterization was used as the parent distribution in the Monte-Carlo.

For our earlier result [18,37] based on the NC subset, the responses were parametrized by a simple Gaussian using the means and RMS widths of the shower distributions. Unfortunately, there are sizable tails in many of the response distributions: tails on the high side from showers fluctuating deeper into the block and hence having less attenuation of the Čerenkov radiation, and tails on the low side from showers which lose many of the charged particles out the back of the block. From studies of electrons from K_{e3} decays, we found that this parametrization resulted in slightly poorer resolution in the Monte Carlo than we observed in the data since the tails had inflated the RMS width.

For this simulation, we have incorporated the tails explicitly into the parametrization. For each distribution of shower responses, we first fit a Gaussian form. If over 1.25% of the distribution fell higher (lower) than 2.5 times the width of this Gaussian, then a high (low)
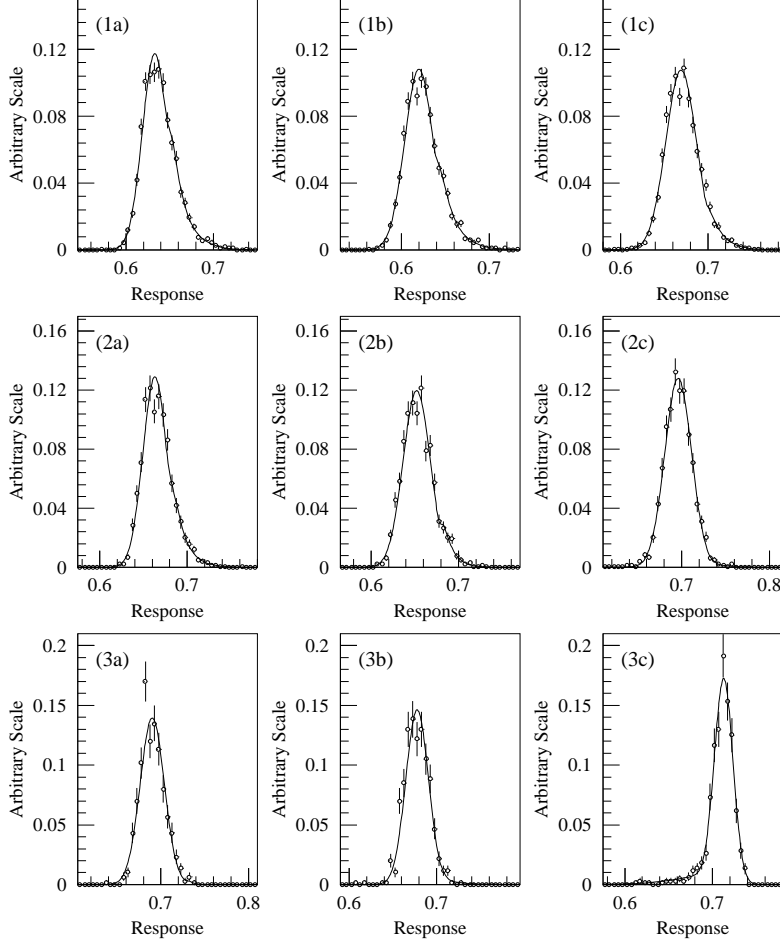
FIG. 70. The distribution of the fractional response for EGS electron showers. Rows 1 to 3 correspond to energies of 2 GeV, 8 GeV, and 32 GeV, respectively. The absorption coefficient α and block length L in radiation lengths for each column are (a) $\alpha = 0.034, L = 18.7$, (b) $\alpha = 0.040, L = 17.2$, and (c) $\alpha = 0.038, L = 15.7$. In each plot, the curve is the best fit parametrization.

side tail was added to the parametrization. If one or both tails were needed, the distribution was refit simultaneously to the sum of the Gaussian+tail(s). The parametrization for the high side tail we used was

$$\frac{dN}{df} = \begin{cases} \gamma(f - f_0)e^{-\beta(f-f_0)}, & f > f_0 \\ 0, & f < f_0 \end{cases}. \tag{72}$$

Here, f is the response, and f_0, β, and γ were parameters for each of the distributions. An analogous parametrization was used for the low side tail. This parametrization was successful over the range of absorption coefficients, block lengths and energies of interest as shown in Fig. 70.

The fits generally resulted in a smooth variation of the parameters as a function of the absorption coefficient and block length. For electron energies E between the EGS shower energies, the parameters were interpolated linearly in $\ln E$.

The above recipe parametrizes the smearing of the calorimeter response due to electromagnetic shower fluctuations. Additional smearing occurs due to random fluctuations in

FIG. 71. The average number of photoelectrons obtained from the shower of a 1 GeV electron for each of the 804 blocks.

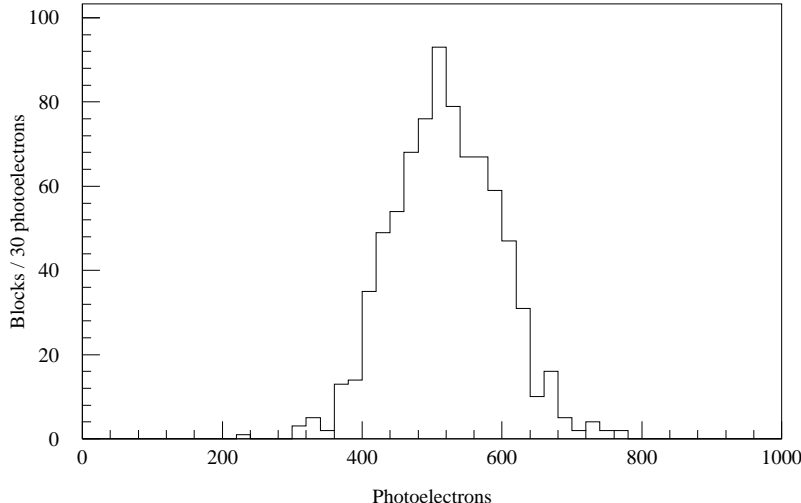the number of photoelectrons liberated from the photocathode. This term was determined using a flasher system; the average number of photoelectrons obtained in each of the 804 blocks for a 1 GeV electron is plotted in Fig. 71.

b. Generating a cluster from shower response   To properly simulate the energy sharing, we accumulated a large cluster library using a clean sample of electrons from the e^+e^- calibration samples where no minimum readout threshold was used. For each cluster in the library, we have stored the pattern of the energy distribution within a 5×5 array of blocks centered on the block struck by an electron. The clusters are grouped according to the incident electron energy and the position in the block where the electron landed, both of which were measured with the charged spectrometer. Details on this library are given in reference [38].

For photons, the signal in each block from the shower simulated for each conversion electron is summed. Similarly, the signals in any overlapping blocks for two nearby showers are summed. To complete the simulation, the signal in each block of the array is converted to ADC counts using the block gain measured in electron calibration, and the readout threshold is applied.

The final stage of the simulation of the lead glass array involved simulating the hardware cluster finder (HCF). The correct threshold for each block above which the HCF would register a "hit" could be found in [38]. Once the pattern of hit blocks was obtained, the software simulation of the cluster finding algorithm was straightforward.

To compensate for remaining effects in the modeling of the electron response, we needed to make small adjustment to the parametrization for absorption coefficients $\alpha > 0.032$. The width and the exponential slope of the high side tail were changed linearly as a function of $\alpha - 0.032$, such that for a block with $\alpha = 0.04$, which was fairly common near the center of the array, the Gaussian width was reduced by 4% of itself and the area under the high side tail was halved. The two parameters that accomplished this were the only tunable parameters introduced into the electron response simulation. The agreement between the data and Monte Carlo electron resolution as a function of energy and absorption was reasonable as
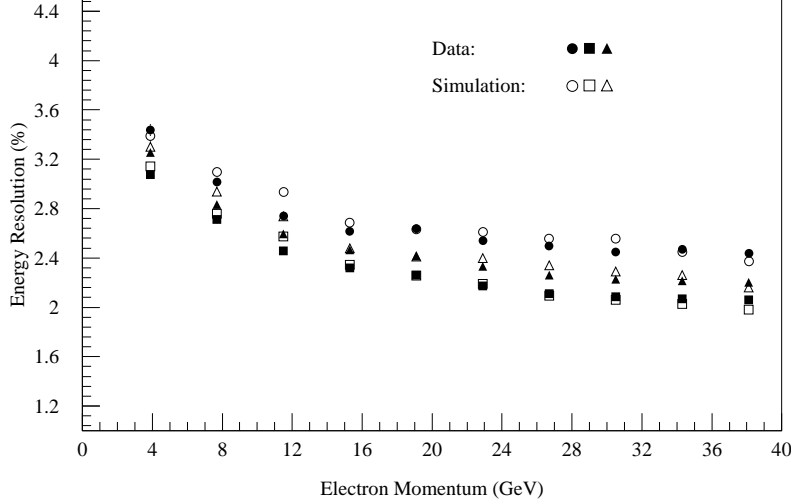
108

FIG. 72. K_{e3} electron energy resolution versus incident electron energy for 3 different ranges of the lead glass absorption coefficient, α. The resolution is measured using the events in all blocks within a quoted range of α to obtain adequate statistics. The data electrons are the solid points, the Monte Carlo electrons are the hollow points. The three absorption coefficient ranges (in percent per radiation length) are *squares: 3.4–3.6*, *triangles: 3.8–4.0*, and *circles: 4.2–4.4*.

seen in Fig. 72. For the data, the resolution contribution on the track momentum p was subtracted using Eq. (29). The worsening of the resolution at low energies results from finite photostatistics. The effect of the damaged blocks was to increase the resolution at high momentum from about 2% to 2.6%.

  c. *Photons, $\pi^+\pi^-\pi^0$ Data and Monte Carlo simulation* To check the photon response, we studied the reconstructed π^0 mass in $\pi^+\pi^-\pi^0$ decays. We found that the simulated photon resolution was slightly wider than the resolution in the data. The difference can be understood with a model where the absorption increases toward the back of the block. The deeper a photon converts in a block, the less the Čerenkov light from its shower is attenuated. If the absorption is increasing from front to back however, the spread of absorptions is smaller than for a block with uniform absorption. Hence for photons (as well as electrons), we expect the radiation damage to compensate the fluctuations into the block. Since we can not directly measure the absorption profile, we allowed one tunable parameter in the photon simulation. Assuming that the absorption is increasing into the block, the average absorption α_t seen by the e^+e^- pair from the photon conversion varies with the conversion depth, t_0. We parametrize this change as

$$\alpha_t = \alpha(1 + 0.03t_0), \tag{73}$$

where α is the absorption coefficient of the block measured in calibration. The 3% per radiation length constant was determined from the study of the reconstructed $\gamma\gamma$ mass width in $\pi^+\pi^-\pi^0$ decays.

  The $\gamma\gamma$ mass in $\pi^+\pi^-\pi^0$ decays was quite useful for studying photons in the lead glass. Since the z location of the kaon can be measured directly from the charged pions in the drift chamber system, the $\gamma\gamma$ mass obtained from Eq. (54) is directly related to the two measured photon energies. We compared the $\gamma\gamma$ mass distributions for $\pi^+\pi^-\pi^0$ decays in data and
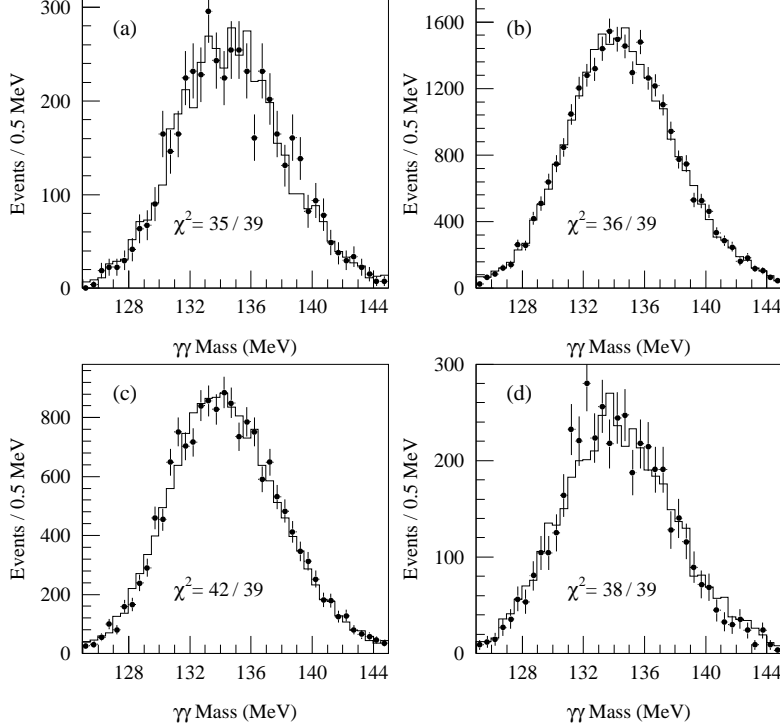
FIG. 73. $\gamma\gamma$ mass for $\pi^+\pi^-\pi^0$ decays from the NC subset. The Monte Carlo simulation (dots) has been overlaid on top of the data distribution (histogram) with reduced χ^2 for comparison. The events have been divided into different ranges of the average absorption coefficient $\bar{\alpha} = (\alpha_1 + \alpha_2)/2$ of the two photon clusters. (a) $0.032 \leq \bar{\alpha} < 0.033$. (b) $0.035 \leq \bar{\alpha} < 0.036$. (c) $0.038 \leq \bar{\alpha} < 0.039$. (d) $0.040 \leq \bar{\alpha} < 0.041$.

Monte Carlo as a function of the average of absorption coefficients of the two photon clusters. The $\gamma\gamma$ mass distribution for four different ranges of the average absorption coefficient is plotted in Fig. 73. Tuning was done using only the NC set, yet the Monte Carlo described the data quite well in earlier subsets as well. For example, the $\gamma\gamma$ mass resolution as a function of the average absorption is plotted for the NC subset and the C2 subset in Fig. 74. The data and Monte Carlo agree well in both subsets in the region $\alpha > 0.032$, where we tuned. In the earlier subsets, the Monte Carlo resolution seems somewhat better at very low values of α than we observe in the data. These low absorptions occur at the outside of the array where photon illumination is low, and have little effect on the average resolution. The overall effect of an average resolution mismatch is discussed in Section X.

d. What about $2\pi^0$ decays? The energy and overall photon illumination are well simulated, as we have seen earlier in this section. We have also seen in Section VI A that the line shapes of the $2\pi^0$ mass distributions match well, aside from an overall shift due to the residual nonlinearity in the data. In Section X later, we see that a small difference in the $2\pi^0$ mass shape for decays from the vacuum beam and the regenerator beam, due to the differences in the energy spectra of the two beams, is also faithfully reproduced by the simulation.

The pairing χ^2 for combining the four photons into two π^0s is plotted for $2\pi^0$ data and simulation in Fig. 75. The overall shape agrees well over the bulk of the distribution, with the data showing some excess for badly reconstructed events; some of this is expected from
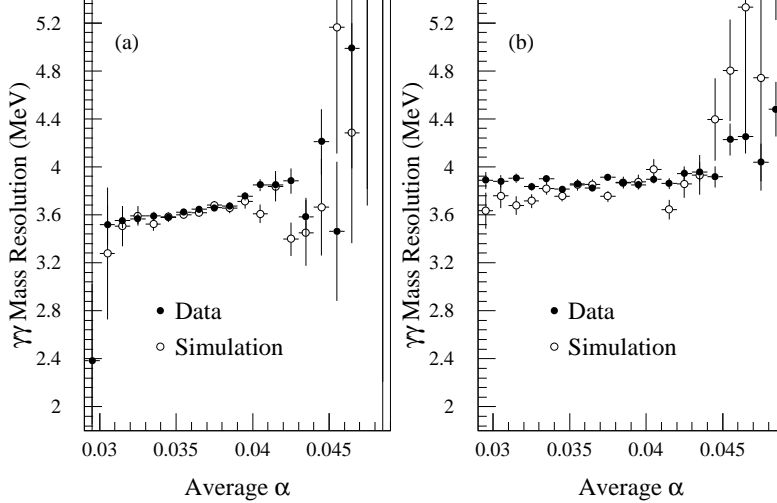
110

FIG. 74. Resolution on the $\gamma\gamma$ mass in $\pi^+\pi^-\pi^0$ data and Monte Carlo simulation. The resolution is plotted as a function of the average absorption coefficient $\bar{\alpha} = (\alpha_1 + \alpha_2)/2$ of the two photon clusters. (a) NC subset. (b) C2 subset.

accidental activity in the detector.

Directly related to the cluster simulation is the distribution of cluster separation (Fig. 76) in the $2\pi^0$ data and Monte Carlo simulation. The shape of this distribution is affected by the cluster shape cuts used to reduce the $3\pi^0$ background, and by the remaining $3\pi^0$ background in the $2\pi^0$ sample. The agreement between the two distributions extends over four orders of magnitude in both beams, including the region where clusters overlap.

The individual cluster energies are also interesting to examine. The one distribution where the simulation failed to precisely describe the data was in the maximum cluster energy distribution. This distribution is shown in Fig. 77 for the entire $2\pi^0$ sample in both vacuum and regenerator beams. Also shown are the regenerator beam distributions for the subsets with and without the lead sheet. The change in the vacuum beam distributions for these two sets is identical to the change in the regenerator beam. While the Monte Carlo describes the data quite well below energies of about 60 GeV, the data shows a higher acceptance on average than the Monte Carlo at high photon energy. This discrepancy is time dependent, appearing at a much reduced level in later subsets.

The bulk of the discrepancy comes from the blocks surrounding the beam pipe, with the remainder from the ring of blocks just outside of these pipe blocks. The discrepancy seems to be related to the actual acceptance of high energy photons and not an effect due to smearing, since the smearing required to mimic this problem would make the $2\pi^0$ mass distribution extremely broad. Excess smearing would also distort the low end of the maximum cluster energy distribution, which agrees with the data without such a smearing.

We decided to restrict ourselves to the subsample of $2\pi^0$ decays where the maximum cluster energy was under 60 GeV/c. This has the further advantage of limiting the $2\pi^0$ cluster energy to the kinematic regime which is occupied by $3\pi^0$ sample. Since we used the $3\pi^0$ decays to limit the systematic error for the neutral acceptance, this seemed like the most conservative course. We later return to this issue as part of our systematic discussion in Section X B. This problem was "solved" in a subsequent experiment and we comment

111
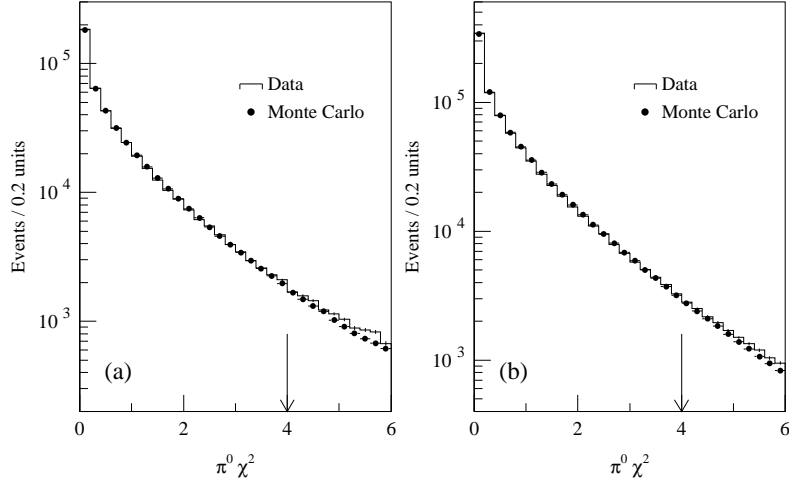
FIG. 75. Pairing χ^2 for $2\pi^0$ decays in the data and Monte Carlo simulation. (a) Vacuum beam. (b) Regenerator beam. The expected background contribution has been added to the Monte Carlo prediction. The arrow in each plot marks the position of the analysis cut.
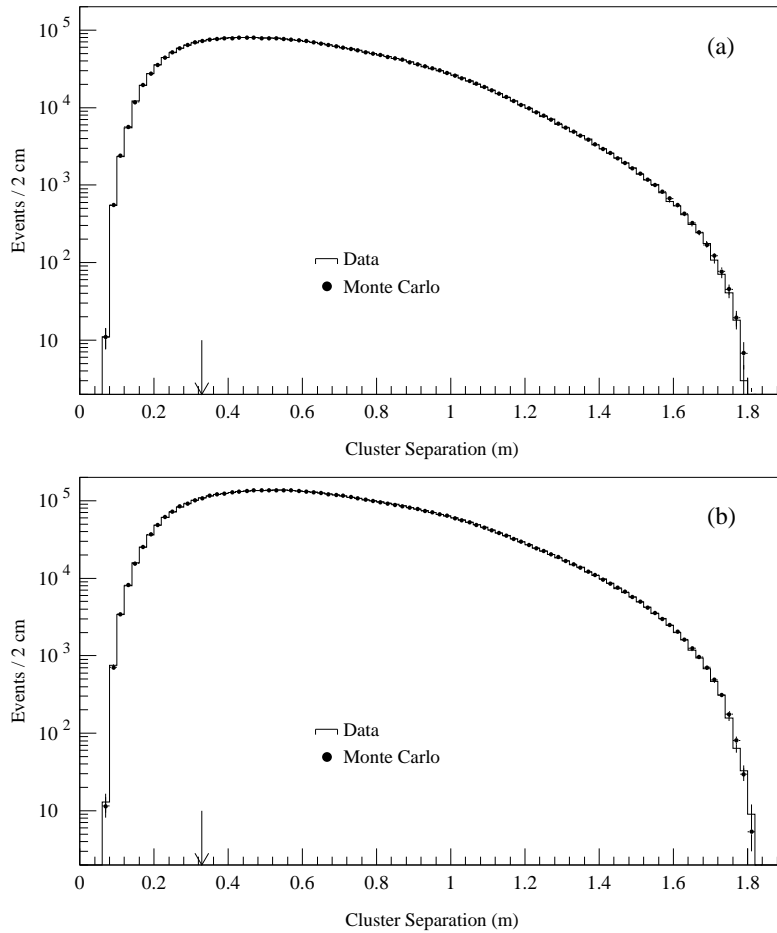
FIG. 76. Cluster separation for $2\pi^0$ decays in the data and Monte Carlo simulation. The arrow indicates the minimal separation for each of the standard 3×3 block clusters to be distinct (complete separated). No cut is made on this variable. (a) Vacuum beam. (b) Regenerator beam. The predicted background level has been add to the $2\pi^0$ Monte Carlo simulation.

112
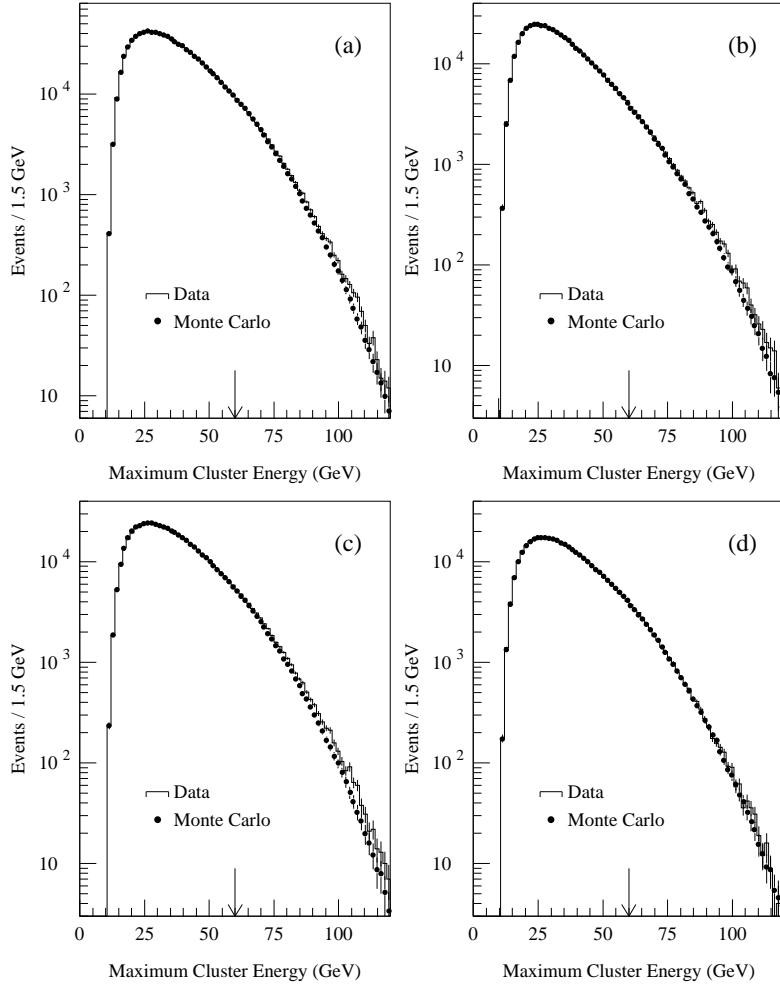
FIG. 77. Distribution of the maximum cluster-energy for $2\pi^0$ decays in the data and Monte Carlo simulation. The arrow indicates the position of the analysis cut. (a) Vacuum beam distributions for the entire data set. (b) Regenerator beam distributions for the entire data set. The regenerator beam distributions are plotted separately for (c) the $2\pi^0$ subset with the lead-sheet, and (d) the subset without the lead-sheet. Background contributions have been included in all of the Monte Carlo overlays.
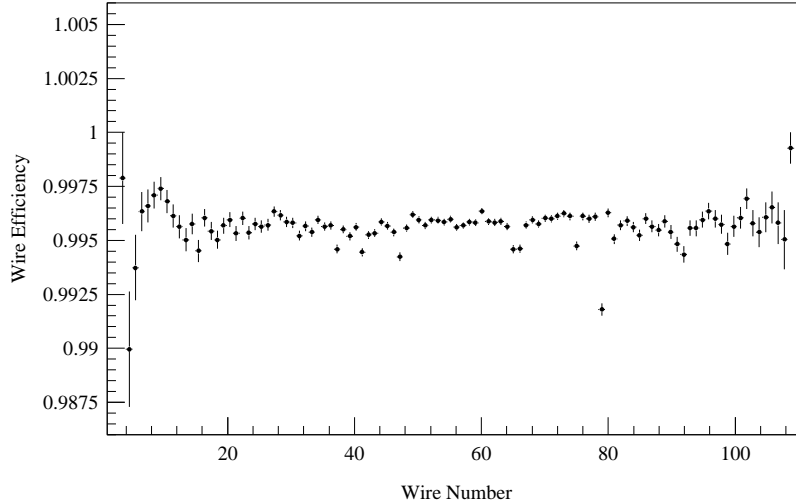
FIG. 78. Individual wire efficiency for the downstream y-plane in Chamber-2 measured with the K_{e3} data in the NC subset.

later on the implications for the analysis in question.

2. Drift Chamber Simulation

Relative to the lead glass, the drift chamber simulation was simple. The TDC distribution was simulated by inverting the measured time to distance function (see Section IV A 1) for the time period used in the data. The chamber resolution was included by first smearing the true position of the particle in the drift chamber sense plane using a Gaussian distribution whose width was determined from data. This smeared distance was then converted to a TDC time using the inverted time to distance function.

The measured drift chamber efficiencies were also included. The individual wire efficiencies were quite uniform across a plane (Fig. 78). This was true even in the most inefficient plane, allowing us to characterize the efficiency for each plane with a single number. Roughly 25 wires that were missing, disconnected, or had efficiencies significantly lower than the average were handled individually. If such wires were at the edge of the chamber, where the illumination was low, they were required to be more than 5% away from the mean; however, in the central regions this figure was 0.5%. The efficiency measured individually for each of these wires was used in the simulation, and this wire was excluded from measurement of the average efficiency of the sense plane to which it belonged.

Only three of the inefficient wires were in a high rate region of the chamber system. The tracking algorithm was forgiving of missing hits, particularly in the y view, and very few tracks were seriously misreconstructed or missed entirely because of these inefficient wires. Hence these few wires had little affect on the acceptance. The illumination before and after a x-view sense-wire broke in a fairly high rate region is shown in Fig. 79. There is not a great change in the illumination near this wire, but the deficit in the NC set is visible.

The track separation is shown for one plane in Fig. 80. The simulation accounts for the acceptance change as the pion track separation decreases to the size of a drift cell.

One shortcoming of the simulation was the lack of δ-rays. Broad tails in track quality

114
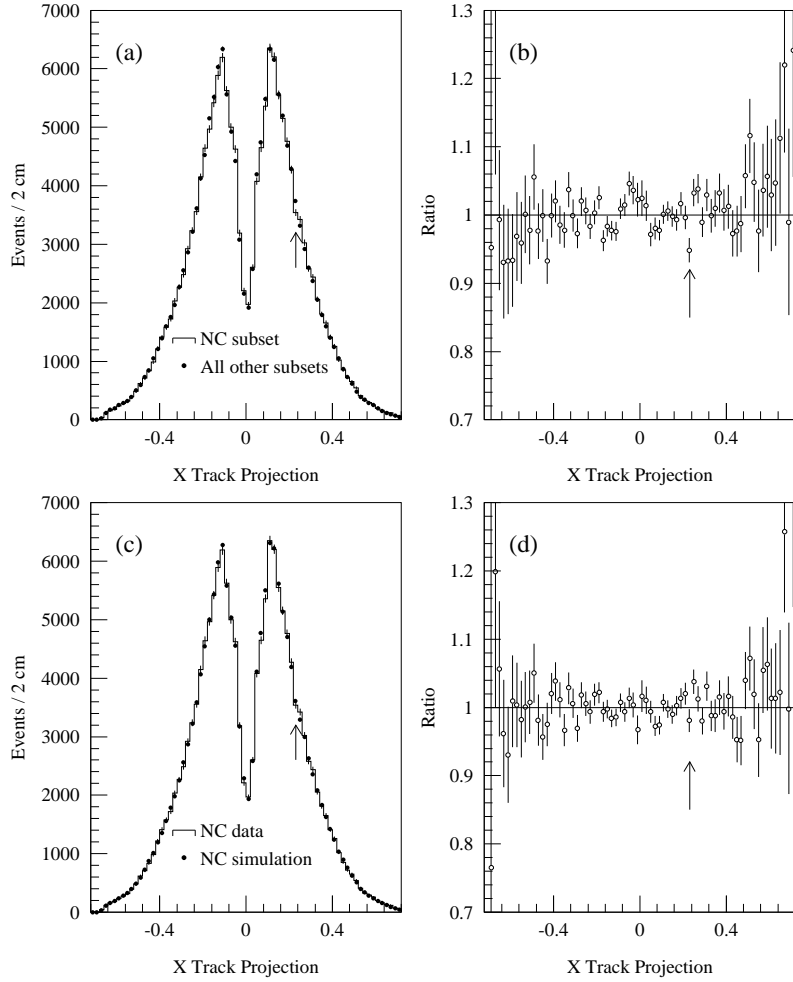
FIG. 79. Chamber-2 x illumination by pions from $\pi^+\pi^-$ decays in data before and after one x-view sense-wire broke. (a) The data collected before the wire broke (dots) overlaid on the NC subset data collected after the wire broke (histogram), and (b) the ratio of these distributions. (c) Monte Carlo simulation for the NC $\pi^+\pi^-$ data subset (dots) overlaid on the data for that set (histogram), and (d) the ratio of these distributions. The arrows indicate the position of the wire in question.
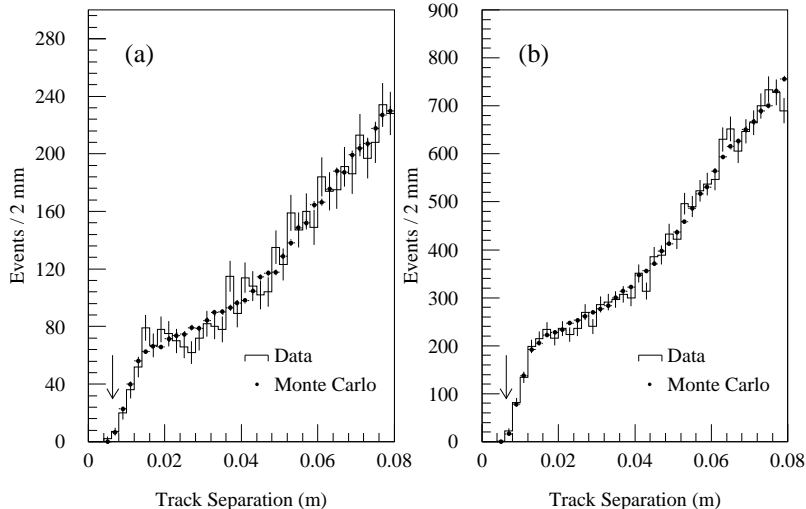
FIG. 80. Separation of the two pion-tracks in the x-view at Chamber-4 for the $\pi^+\pi^-$ data and Monte Carlo simulation. (a) Vacuum beam. (b) Regenerator beam. The arrows indicate a separation the size of one drift cell. No cut is made on this variable.

variables were thus not simulated, but, as we have seen in Section V, δ-rays affect the decays in vacuum beam and regenerator beam identically; we further investigate our sensitivity in Section X.

3. Hodoscope and Photon Veto Response

The simulations of the hodoscope banks and photon veto counters were elementary. The average trigger and latch efficiencies, the former over 99.9% and the latter over 99% efficient, were determined with muon tracks. In addition, the cracks between counters were mapped using the chamber alignment muon samples and the gaps were included in the Monte Carlo. In Section X, we examine the insensitivity of $Re(\varepsilon'/\varepsilon)$ to the efficiency of the individual counters.

The photon veto responses were important for the simulation of the four cluster $3\pi^0$ background. A technique [39] that utilized $\pi^+\pi^-\pi^0$ decays with one photon detected in the calorimeter was employed to map the response of these counters. The direction and energy of the missing photon could be inferred from the kinematics of the charged pions and reconstructed photon. By comparing the observed signals in the veto counters to the predicted energy of the "undetected" photon, the gains and resolution of the counters were extracted. A mismeasurement of the photon veto response would be seen in the distribution of the $3\pi^0$ background. The predicted and observed z shapes of the $3\pi^0$ background agree well (Section VI).

E. Z Comparisons

We now examine the distribution most crucial to the $Re(\varepsilon'/\varepsilon)$ analysis, the z-distribution of kaon decays. When we fit for $Re(\varepsilon'/\varepsilon)$, we integrate the contents of each 10 GeV/c momentum bin over the entire z range. A bias in the acceptance versus z, coupled with the

116

difference in the vacuum and regenerator beam z-distributions, would lead to a bias in the ratio of events in the vacuum and regenerator beams.

From the plots already shown, it is clear that our simulation of the apparatus mocks up the data quite well. We therefore expect that any bias in the acceptance is small, and expect the z-distributions to match well. For most problems that would affect the acceptance, such as a misplaced aperture edge, a bias in resolving closely spaced tracks or closely spaced clusters, we expect the acceptance to either increase or decrease fairly uniformly in z, comparing data to Monte-Carlo. For example, if an aperture is too wide, $2\pi^0$ decays near the z location of the aperture are not affected, while $2\pi^0$ decays farther upstream, whose photons have had a chance to spread and approach the aperture's edges, are accepted more often in the simulation than they should. We therefore look for a linear bias as a function of z. In all of the studies we have done, the χ^2 for a linear fit to the ratio of data to Monte Carlo have been excellent, indicating that higher order terms are not necessary.

We display, in Figs. 81 and 82 and in Figs. 83 and 84, the distributions in the vacuum beam for the 60 GeV/c to 70 GeV/c bin (near the mean kaon energy for both modes), and the 110 GeV/c to 120 GeV/c bin (picked randomly). The χ^2 comparing the data and simulation are all very good.

When fitting for a linear bias in the ratio of data to Monte Carlo, the observed slopes were consistent with what one might expect from statistical fluctuations. For example, for the 48 momentum bins in the two neutral subsets, the slopes in 24 bins had significances under 1 standard deviation (σ), 15 between 1 and 2 σ and 9 over 2 σ. Many of the slopes over 2 σ occurred in bins with low statistics. The relative numbers of positive and negative slopes observed were also consistent with expected statistical fluctuations.

To probe any residual biases at a much more sensitive level, it is convenient to combine all of the momentum bins and also to use the K_{e3} and $3\pi^0$ data. Because the energy spectrum and beam shapes are well simulated, the z-distribution in the Monte Carlo simulation integrated over all momenta, should match the observed z-distribution in the data well. This is particularly true in the modes with charged final states. In the neutral mode, we must be more careful because of the coupling between the measured z position of the kaon decay and the measured photon energies. A bias in the photon energy measurement can mimic an acceptance problem.

In the case of the $3\pi^0$ decays, the photons in the lead glass have a higher probability to overlap than photons from $2\pi^0$ decays. Hence the $3\pi^0$ decays are also more sensitive to problems with the cluster simulation than the $2\pi^0$ decays. With the increased sensitivity of the high statistics modes to potential biases, limits on the acceptance for $\pi\pi$ decays obtained using the high statistics modes are fairly conservative estimates.

The K_{e3} z-distribution for one of the data subsets is shown in Fig. 85. The z-distributions in the data and in the simulation agree very well over the entire decay volume, even upstream of the 110 m $\pi^+\pi^-$ analysis cut, where the simulation tracks an order of magnitude drop in acceptance over 5 m reliably. We have conservatively estimated the acceptance bias in the charged mode at the level of 0.03% per meter, while the K_{e3} samples had slopes which were consistent with being flat at the 0.02% per meter level.

In order to bound the acceptance bias for the $2\pi^0$ mode, the $3\pi^0$ sample we used was limited to a region away from the active mask, where the rapid change in the $3\pi^0$ acceptance
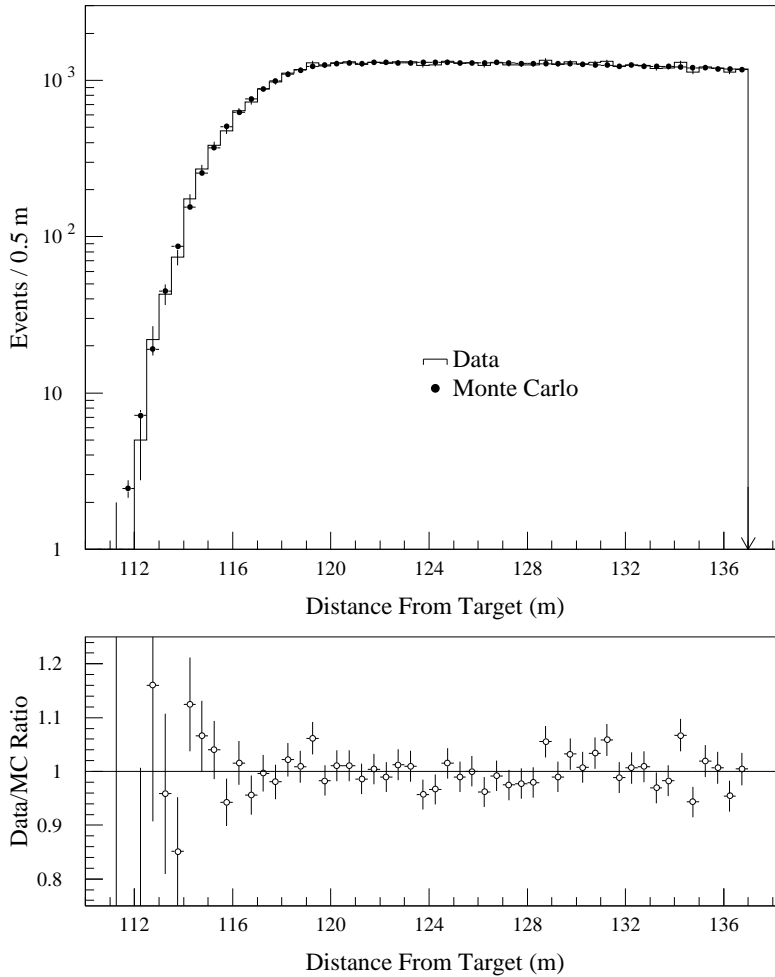
FIG. 81. Vacuum beam z-distribution for the $\pi^+\pi^-$ data and Monte Carlo simulation in the 60 GeV/c to 70 GeV/c bin momentum bin. All final cuts have been made. *Top:* The z-distribution for the two event samples, with the simulation statistics normalized to the data statistics. *Bottom:* The ratio of data events to simulated events in each 0.5 m bin.
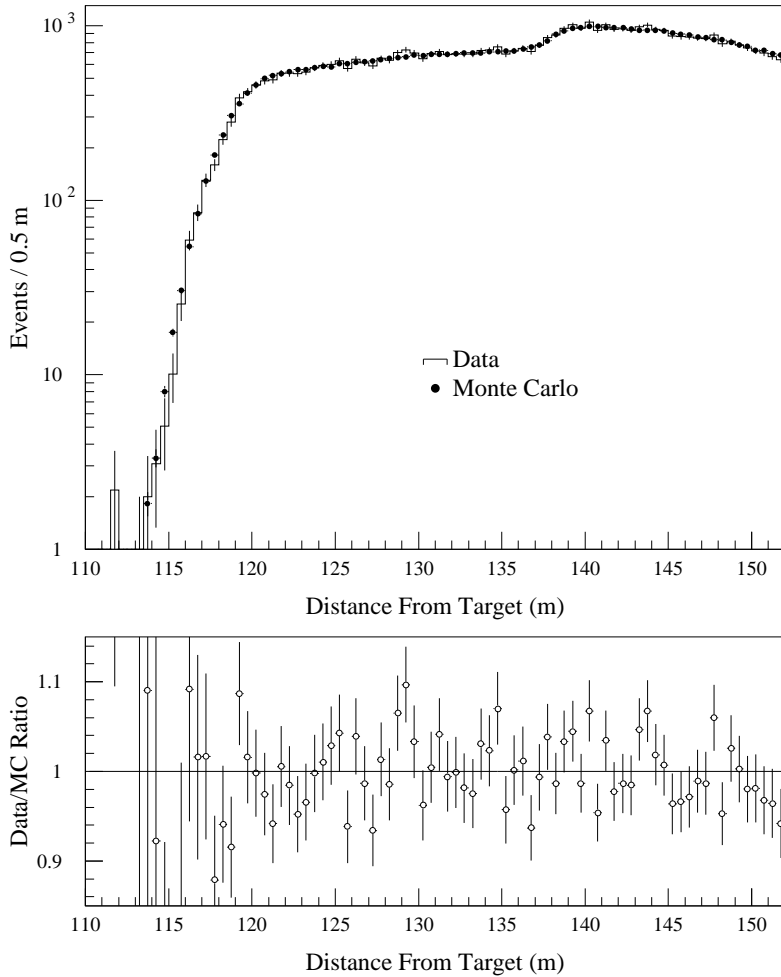
FIG. 82. Vacuum beam z-distribution for the lead-sheet subset of the $2\pi^0$ data and Monte Carlo simulation in the 60 GeV/c to 70 GeV/c bin momentum bin. All final cuts have been made. *Top:* The z-distribution for the two event samples, with the simulation statistics normalized to the data statistics. *Bottom:* The ratio of data events to simulated events in each 0.5 m bin.

119
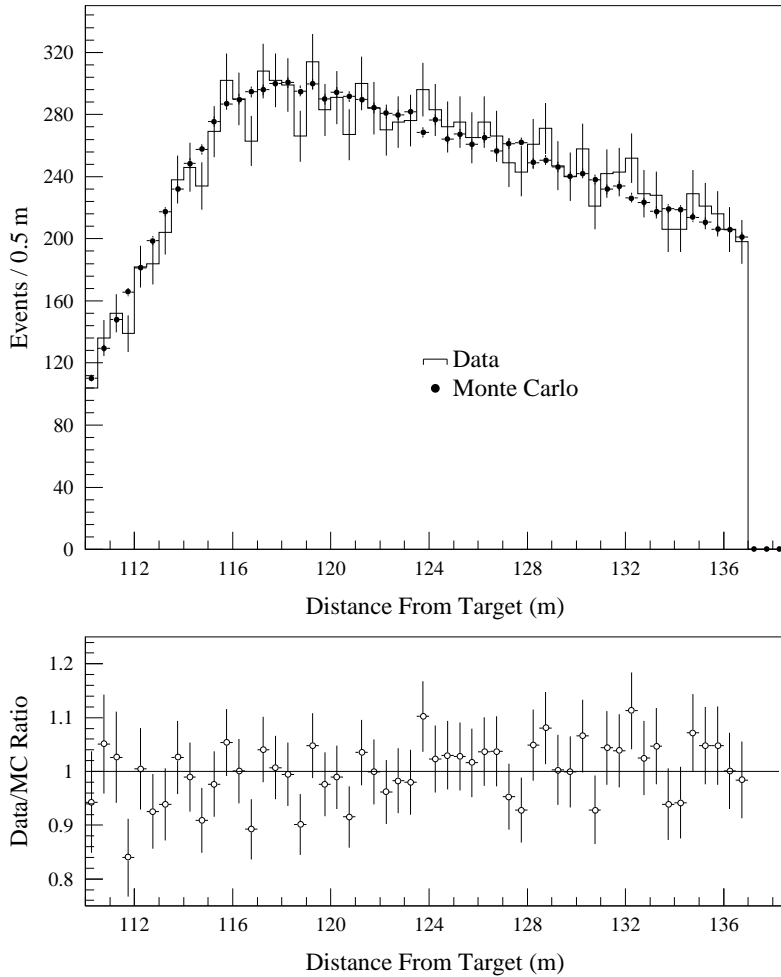
FIG. 83. Vacuum beam z-distribution for the $\pi^+\pi^-$ data and Monte Carlo simulation in the 110 GeV/c to 120 GeV/c bin momentum bin. All final cuts have been made. *Top:* The z-distribution for the two event samples, with the simulation statistics normalized to the data statistics. *Bottom:* The ratio of data events to simulated events in each 0.5 m bin.
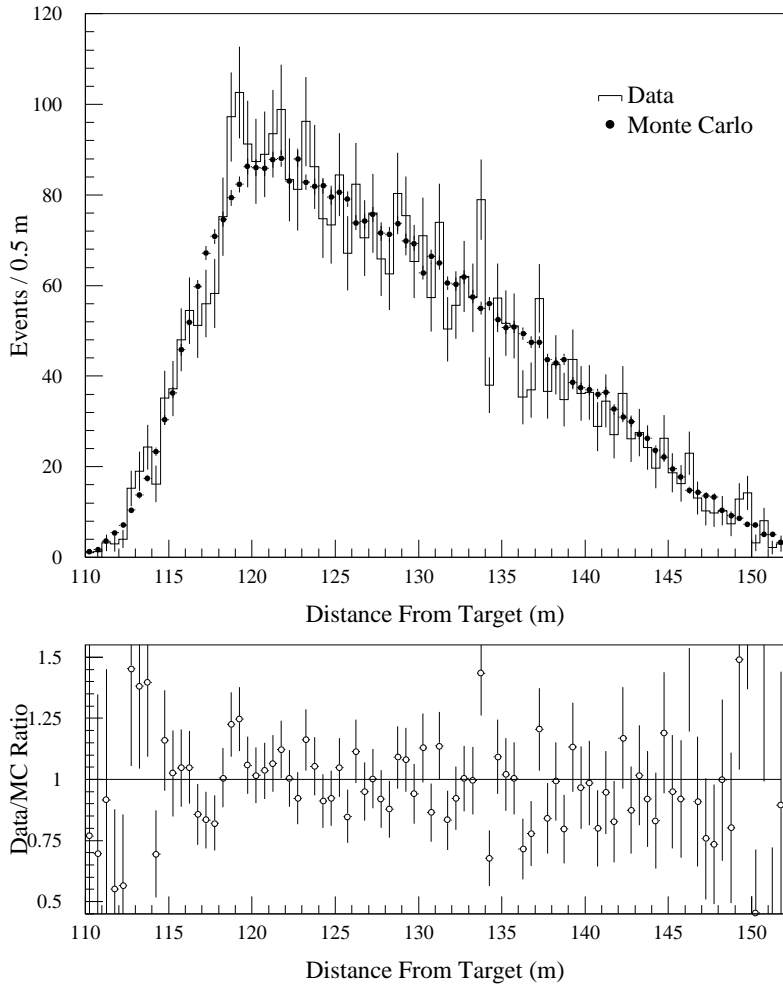
FIG. 84. Vacuum beam z-distribution for the subset of the $2\pi^0$ data and Monte Carlo simulation without the lead-sheet in the 110 GeV/c to 120 GeV/c bin momentum bin. All final cuts have been made. *Top:* The z-distribution for the two event samples, with the simulation statistics normalized to the data statistics. *Bottom:* The ratio of data events to simulated events in each 0.5 m bin.

FIG. 85. Vacuum beam z-distribution for K_{e3} decays in the data and Monte Carlo simulation after all other cuts. The sample shown is a portion of the NC subset. *Top:* The z-distribution for the two event samples, with the simulation statistics normalized to the data statistics. *Bottom:* The ratio of data events to simulated events in each 0.5 m bin. The solid line is the best fit slope of $-0.021\% \pm 0.018\%$ per meter. The dashed line is the slope used for the systematic estimate, 0.03% per meter. The dotted line is the slope required to shift the final result for $Re(\varepsilon'/\varepsilon)$ by 10^{-3}. The arrows in the ratio plot indicate the z fiducial region used in the $\pi^+\pi^-$ analysis.

FIG. 86. The z-distribution for $3\pi^0$ decays in the data and Monte Carlo simulation after all other cuts. The sample shown had no lead-sheet installed. *Top:* The z-distribution for the two event samples, with the simulation statistics normalized to the data statistics. *Bottom:* The ratio of data events to simulated events in each 1 m bin. The solid line is the best fit slope of $-0.0036\%\pm0.0074\%$ per meter. The dashed line is the slope used for the systematic estimate, 0.074% per meter. The dotted line is the slope required to shift the final result for $Re(\varepsilon'/\varepsilon)$ by 10^{-3}.

shape coupled with residual uncertainties in the photon energy reconstruction might yield misleading discrepancies that do not affect $Re(\varepsilon'/\varepsilon)$. For the subset with no lead sheet, the z distribution in data and Monte Carlo is shown in Fig. 86; the agreement is excellent and places a 0.074% percent per meter limit on the acceptance bias for $2\pi^0$. Upstream, the acceptance changes shape rapidly, and there is a dip in the ratio of data to Monte Carlo, about 1% at 120 m. A few more meters upstream, the data to Monte Carlo ratio is again consistent with one when the accepted decay distribution is relatively flat. An overall energy scale shift of about 0.02% would cause this effect.

It is interesting to note that at our mean kaon energy, we would have introduced a slope of order 0.04% per meter into the overlay had we ignored the K_L lifetime in the simulation.

Finally, we have the $\pi^+\pi^-$ and $2\pi^0$ distributions themselves. The distribution of vacuum $\pi^+\pi^-$ decays (Fig. 87) is simulated well over the entire decay volume. The vacuum distri-
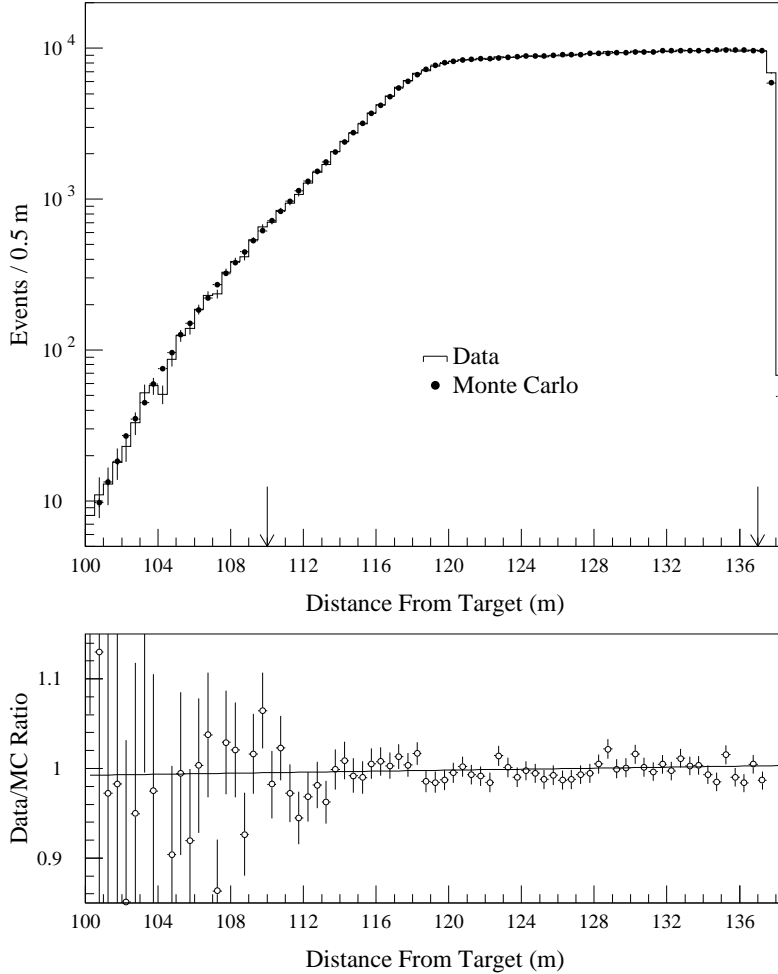
FIG. 87. The z-distribution for vacuum beam $\pi^+\pi^-$ decays in the data and Monte Carlo simulation after all other cuts. The sample shown is a portion of the NC subset. *Top:* The z-distribution for the two event samples, with the simulation statistics normalized to the data statistics. The arrows indicate the fiducial z region used in the analysis. *Bottom:* The ratio of data events to simulated events in each 0.5 m bin. The solid line is the best fit slope of $0.025\% \pm 0.022\%$ per meter.

butions for $2\pi^0$ decays without the lead sheet is shown in Fig. 88 and with the lead sheet is shown in Fig. 89. The simulation is again good; the z region from 137 m to 139 m was excluded because of the sensitivity of that area to biases in the photon energy scale. There does appear to be an excess of data over Monte Carlo in part of that region, consistent with an energy scale shift of under 0.03%.

The shape of the regenerator beam distribution depends on physics parameters, such as ρ and Δm that are used in the Monte Carlo simulation. The $\pi^+\pi^-$ z-distribution for this beam is shown in Fig. 90, and the $2\pi^0$ distribution in Fig. 91. The simulated regenerator beam distributions agree fairly well with the data. In particular, the agreement in the z shape at the sharp turn on of decays at the regenerator is very good; this is determined by the resolution function, yet even in the $2\pi^0$ mode the Monte Carlo predicts the number of data events at the 10% level three orders of magnitude down from the peak.

124
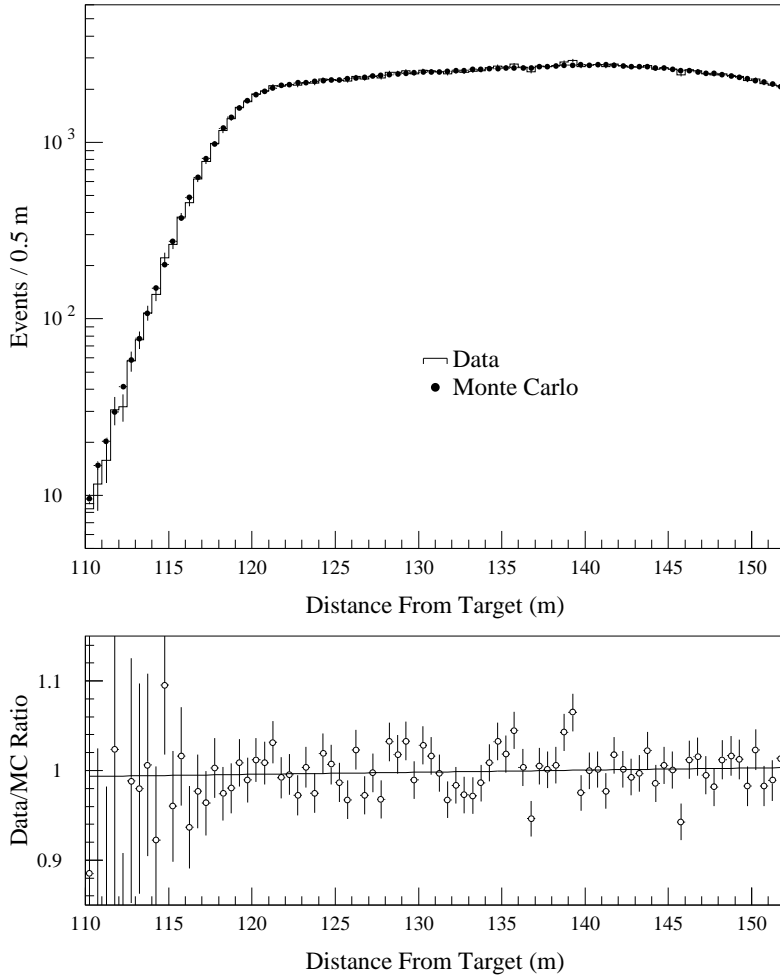
FIG. 88. The z-distribution for vacuum beam $2\pi^0$ decays after all other cuts from the data and simulation subsets with no lead-sheet. *Top:* The z-distribution for the two event samples, with the simulation statistics normalized to the data statistics. *Bottom:* The ratio 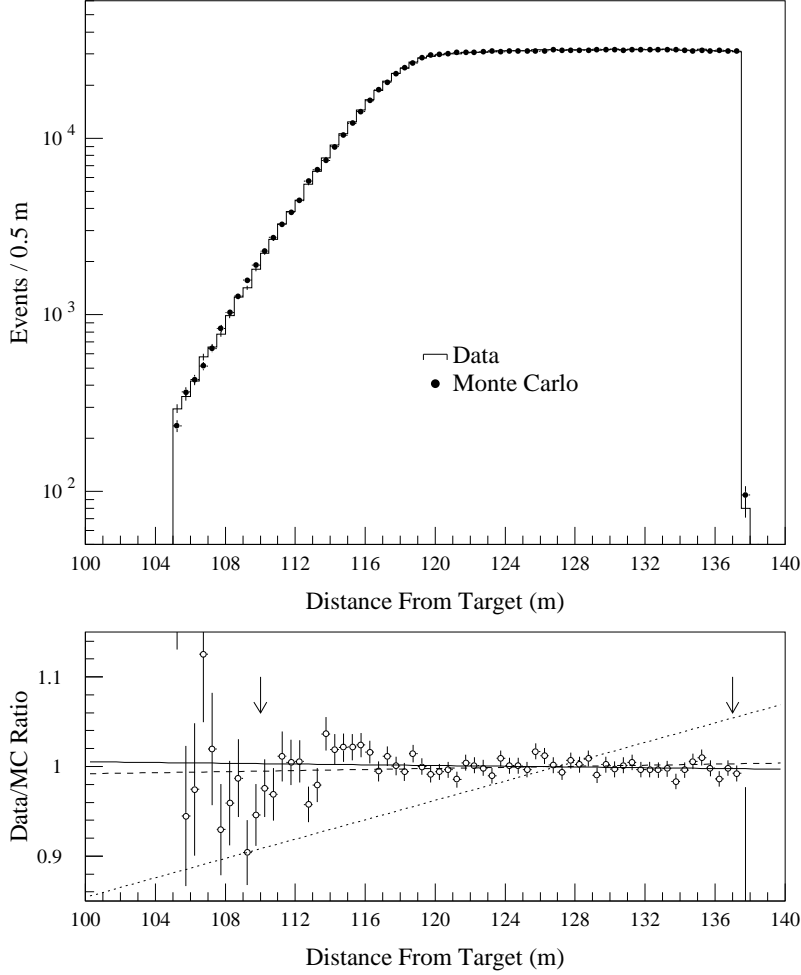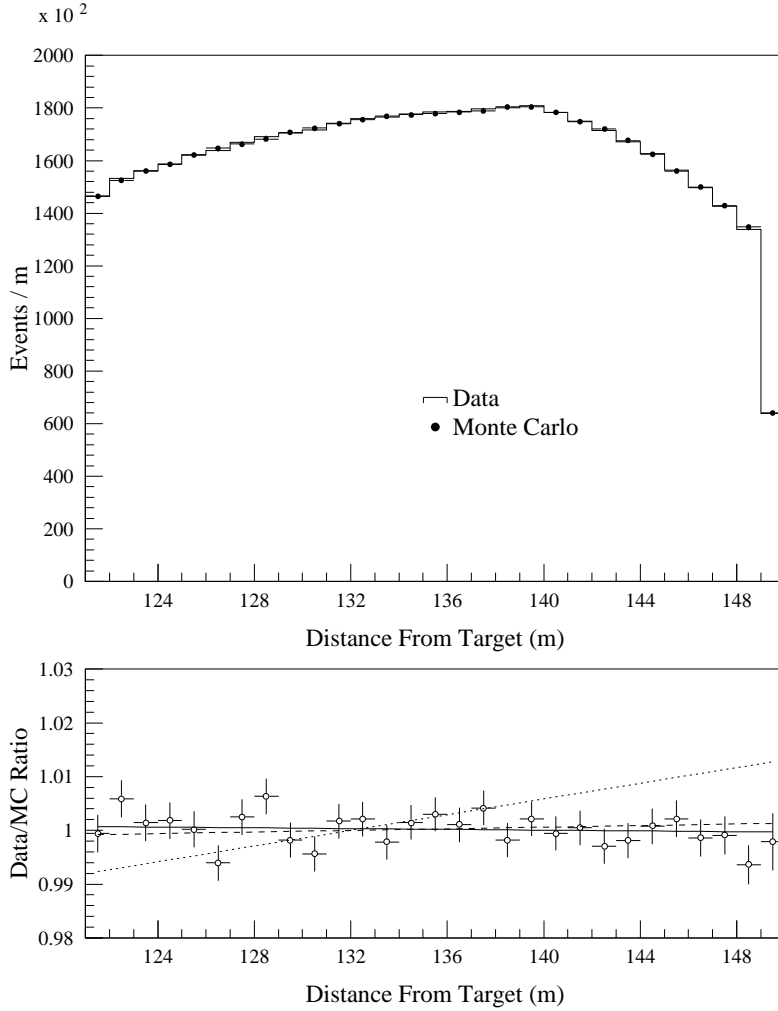of data events to simulated events in each 0.5 m bin. The solid line is the best fit slope of $0.024\% \pm 0.028\%$ per meter.
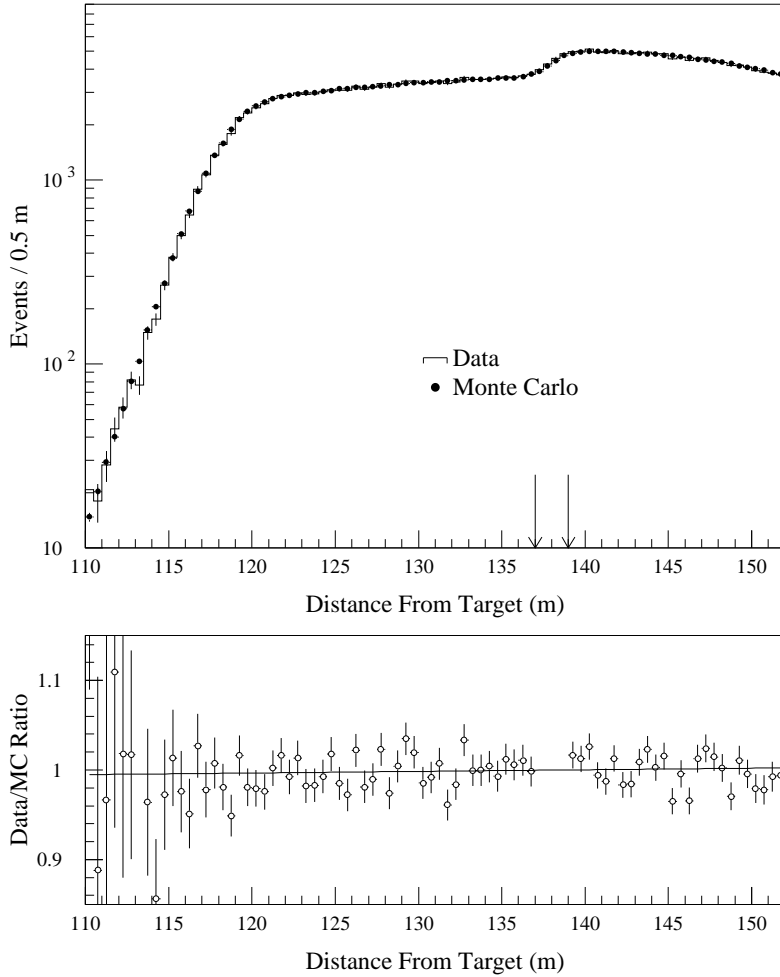
FIG. 89. The z-distribution for vacuum beam $2\pi^0$ decays after all other cuts from the data and simulation subsets with the lead-sheet. *Top:* The z-distribution for the two event samples, with the simulation statistics normalized to the data statistics. The arrows mark the region around the HDRA excluded from the fits. *Bottom:* The ratio of data events to simulated events in each 0.5 m bin. The solid line is the best fit slope of $0.018\% \pm 0.021\%$ per meter.

126
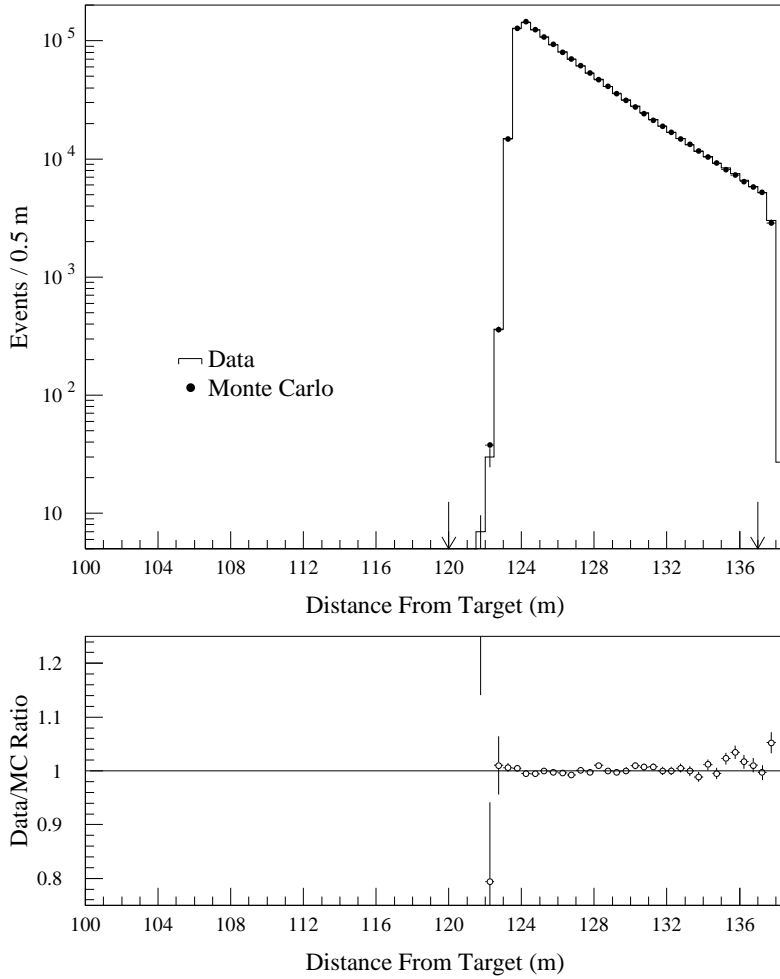
FIG. 90. The z-distribution for regenerator beam $\pi^+\pi^-$ decays after all other cuts for the data and Monte Carlo simulation. *Top:* The z-distribution for the two event samples, with the simulation statistics normalized to the data statistics. *Bottom:* The ratio of data events to simulated events in each 0.5 m bin. The solid line at one is for reference only.

127
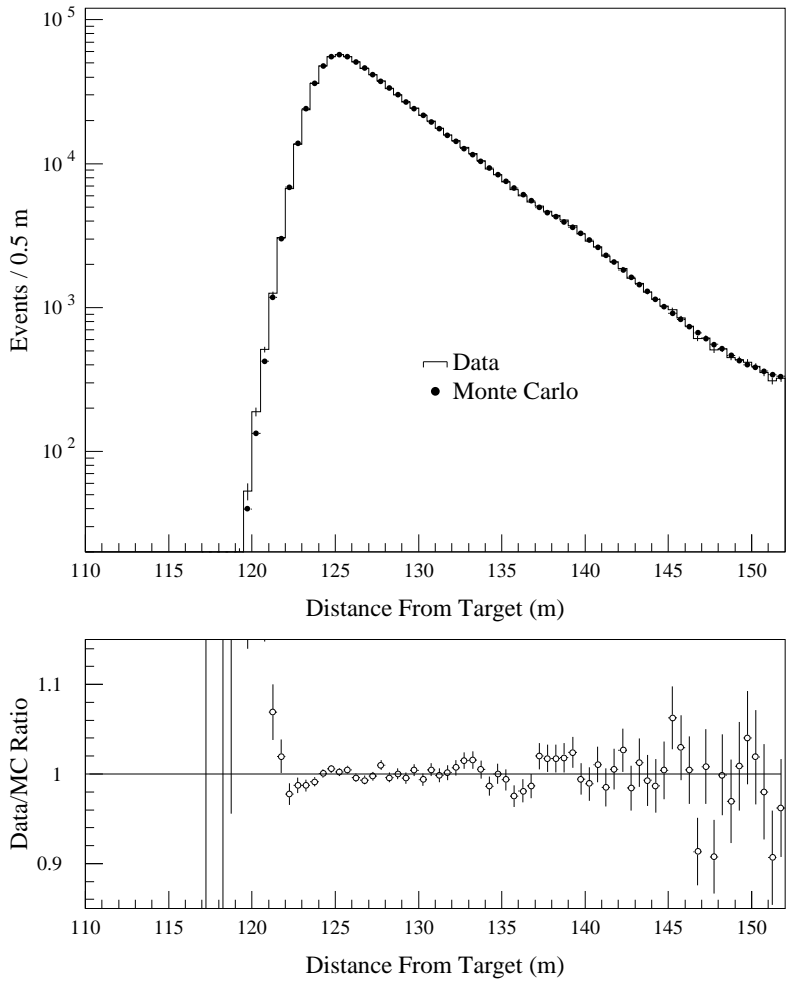
FIG. 91. The z-distribution for regenerator beam $2\pi^0$ decays after all other cuts for the data and simulation with the lead-sheet and no lead-sheet subsets combined. *Top:* The z-distribution for the two event samples, with the simulation statistics normalized to the data statistics. *Bottom:* The ratio of data events to simulated events in each 0.5 m bin. The solid line at one is for reference only.

F. Summary of the Monte Carlo Simulation

The most apt summary of the Monte Carlo simulation is the plot of the vacuum beam z overlays for the five different data sets considered in this experiment (Fig. 92). The $3\pi^0$ plot shows agreement even upstream of the mask.

In all but the $3\pi^0$ case, the χ^2 values are within about one standard deviation fluctuation. In the neutral mode plots, both $2\pi^0$ and $3\pi^0$, the excess in the χ^2 tends to come from the upstream region right at the rolloff in acceptance, where the z-distribution is the most sensitive to residual problems with the photon energy scale. This is particularly true for the $3\pi^0$ case, where 52 units of χ^2 come from the 4 bins in the range 116 m to 120 m.

The $\pi\pi$ data samples shown range in size from 150,000 to 350,000 events, and the Monte Carlo samples from about 4 million to 8 million events. The K_{e3} sample shown has about a million events in both the data and Monte Carlo samples. The $3\pi^0$ sample has about 5 million data events and 6 million Monte Carlo events.

In spite of the different characteristics of the decay modes, the Monte Carlo reproduces the data, not only for the z-distributions, but also for many of the other distributions. We can now take the accepted and generated $\pi\pi$ distributions from the Monte Carlo and use these to extract values for $Re(\varepsilon'/\varepsilon)$ and other parameters of the neutral kaon system. We turn to the description of the techniques used to determine these parameters.
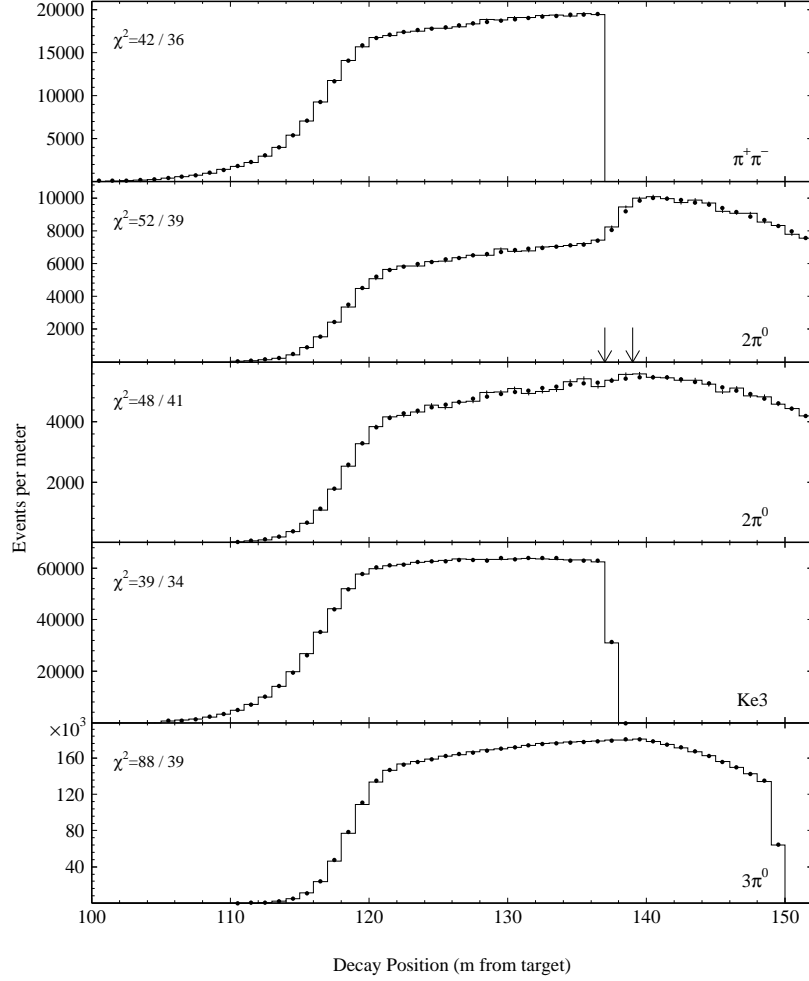
FIG. 92. The vacuum beam z-distributions in the data and Monte Carlo simulation for the $\pi^+\pi^-$, $2\pi^0$, K_{e3} and $3\pi^0$ kaon decay modes. The two $2\pi^0$ subsets with and without the lead sheet are shown separately. The χ^2 for the z overlay is listed for each distribution. All other cuts have been applied. For the $3\pi^0$ overlay, 52 units of χ^2 come from the 4 z bins at 116 to 120 m, where the data is most sensitive to an energy scale mismatch. The arrows shown for the $2\pi^0$ lead sheet subset indicate the z region excluded from the analysis.

VIII. FITTING PROCEDURES

We used two distinct fitting techniques in the analysis of $\pi\pi$ data sets. The first, refered to as the "constrained" fit, was used to determine the values of parameters which characterize the shape of the regenerator beam z distribution: Δm, τ_S, ϕ_{+-}, and $\Delta\phi$. The vacuum beam data in each 10 GeV/c bin, corrected for acceptance in a single, large z bin, was used to determine the incident flux. The second, "unconstrained" fit, was used for fitting $Re(\varepsilon'/\varepsilon)$. For the measurement of $Re(\varepsilon'/\varepsilon)$, it is the total number of decays in each beam, rather than their shape, that matters. Effectively, the incident kaon flux cancels when the ratio of the two beams is taken in each 10 GeV/c momentum bin.

We now describe in detail how the prediction for either the number of events in a pz bin in the regenerator beam, or for the vacuum to regenerator beam ratio in a p bin is determined.

A. Functional and General Fit Procedure

A fit compares the observed number of events in bins of reconstructed kaon momentum p and decay position z in the vacuum and regenerator beams to the number expected, given a set of decay parameters. Suppose that for a pz bin with the momentum range p_i to $p_i + \Delta p$ and z range z_j to $z_j + \Delta z$, we observe d_{ij} events in one of the beams. The number of events d_{ij} is given by

$$d_{ij} = \int_{p_i}^{p_i+\Delta p} dp \int_{z_i}^{z_i+\Delta z} dz \int dp' \, F(p') \int dz' \, s(p, z; p', z') \, a(p', z') \, r(p', z'). \qquad (74)$$

In this expression, the primed quantities p' and z' represent the true momentum and the true decay position. Function $F(p')$ is the flux of K_L entering the decay volume with momentum p'. The detector acceptance and response functions are given by $a(p', z')$ and $s(p, z; p', z')$ respectively. Function $a(p', z')$ is the probability that a kaon of momentum p' decaying at z' reconstructs in the final sample — independent of what p and z are reconstructed. Function $s(p, z; p', z')$ incorporates all of the resolution and misreconstruction effects, giving the probability that a kaon with momentum in the range p' to $p' + \delta p'$ and decaying in the range from z' to $z' + \delta z'$ reconstructs in the ranges from p to $p + \delta p$ and z to $z + \delta z$.

All of the physics of the decay process is incorporated in Eq. (74) via the decay rate function $r(p', z')$. Each of these functions are discussed in detail after we treat the general fitting procedure.

1. General Fitting Procedures

a. Binning In all fits, the momentum bins were 10 GeV/c wide. For fits depending upon the shape of the decay distribution in a beam, we subdivided it into several z regions; otherwise a single z bin was used.

In the fits, we used the rate in one beam either to constrain the incident kaon flux in the other beam, or to predict the ratio of the rates in the two beams in each pz bin. Were the

incident kaon flux in the two beams identical, the decay rates in the vacuum and regenerator beams would be independent of the regenerator up or down position.

We now analyze the effect of slightly differing intensities for the two beams. Let the flux in the top beam be greater than that in the bottom beam, $I_t > I_b$. The trigger rate is dominated by (non $\pi\pi$) kaon decays in the vacuum beam, so it would be higher with the regenerator in the lower beam position leading to a difference in the livetimes L_u and L_d for the up and down regenerator positions. The different intensities will lead to configuration-dependent accidental rates in the detector and hence a difference in the efficiency of reconstructing $\pi\pi$ decays for the two configurations. Let the fractional loss of events due to accidental activity be $(1 - \varepsilon_u)$ when the regenerator is up, and $(1 - \varepsilon_d)$ when the regenerator is down.

Finally, the relative number of decays collected in the two configurations depends on the fraction of time f_d that the regenerator spends in the lower beam. The incident kaon flux in the top beam was about 8% higher than that in the bottom beam, and f_d differed from 50% by of order 1%, varying over the data sets.

Let n_v (n_r) be the probability for a kaon entering the decay region to decay and be reconstructed in a given pz bin in the vacuum (regenerator) beam. Then the number of events we would collect for the regenerator sample in the top (bottom) beam would be $N_r^t = f_u L_u \varepsilon_u I_t n_r$ ($N_r^b = f_d L_d \varepsilon_d I_b n_r$), while for the vacuum beam we would have $N_v^t = f_d L_d \varepsilon_d I_t n_v$ ($N_v^b = f_u L_u \varepsilon_u I_b n_v$). The arithmetic mean of the data samples from the top and bottom beams gives

$$\frac{N_v^t + N_v^b}{N_r^t + N_r^b} = \frac{(f_d L_d \varepsilon_d I_t + f_u L_u \varepsilon_u I_b) n_v}{(f_u L_u \varepsilon_u I_t + f_d L_d \varepsilon_d I_b) n_r}. \tag{75}$$

In general, this differ from the "true" ratio n_v/n_r that we need to obtain.

The factors depending on the different intensities of the two beams cancel in the geometric mean:

$$\frac{(N_v^t N_v^b)^{\frac{1}{2}}}{(N_r^t N_r^b)^{\frac{1}{2}}} = \frac{(f_d L_d \varepsilon_d I_t)^{\frac{1}{2}} (f_u L_u \varepsilon_u I_b)^{\frac{1}{2}} n_v}{(f_u L_u \varepsilon_u I_t)^{\frac{1}{2}} (f_d L_d \varepsilon_d I_b)^{\frac{1}{2}} n_r} = \frac{n_v}{n_r}. \tag{76}$$

We therefore combined the information from the two beams using the geometric mean.

We used the program MINUIT to perform χ^2 minimizations.

b. Unconstrained Fitting The unconstrained fit was used to extract $Re(\varepsilon'/\varepsilon)$. The data were binned in momentum only and the functional was used to predict the ratio $q = N_v/(N_r + N_v)$, in each momentum bin. The χ^2 in this fit is then given by

$$\chi^2 = \sum_{i=1}^{n_p} \frac{(q_i - q_i')^2}{\sigma_i^2}, \tag{77}$$

where n_p is the number of momentum bins, q_i is the observed ratio, and q_i' is the predicted ratio, containing the acceptance corrections to the decay rates in the two beams.

The error σ_i appearing in Eq. (77) is

$$\sigma_i^2 = \frac{q_i'(1 - q_i')}{N_{r_i} + N_{v_i}} + \sigma_{q_i'}^2, \tag{78}$$

where the first term is the binomial error on the predicted ratio and the second term is the error from the acceptance correction.

132

c. Constrained Fitting   Here, the entire vacuum beam sample was used to predict the flux of kaons incident on the regenerator in each momentum bin by constraining the shape of the vacuum beam momentum spectrum. In unconstrained fit, the regenerator beam was normalized to the vacuum beam in each individual momentum bin, which essentially allowed the kaon flux to float independently from momentum bin to momentum bin. The constrained technique has the advantage of enhancing the sensitivity to the kaon parameters τ_S, Δm, ϕ_{+-} and $\Delta\phi$. On the other hand, it depends on knowing the kaon energy spectrum well.

If the spectrum in the Monte Carlo describes the data perfectly, then the normalization would be simple – we would simply fit for a scale factor α to make the number of vacuum beam decays in the data and Monte Carlo match. However there are small discrepancies between the kaon spectra in the data and Monte Carlo (Fig. 57) vacuum samples. We therefore include two additional parameters β_1, β_2 for a correction $c(p; \beta_1, \beta_2)$ to the Monte Carlo spectrum. If $F_{MC}(p)$ is the kaon spectrum in the Monte Carlo, then the normalization factor n_i for the ith momentum bin is given by

$$n_i = \alpha \frac{\int_{p_i}^{p_i+\Delta p} dp\, F_{MC}(p) \int_{z_u}^{z_d} dz\, r_v(p, z)\, c(p; \beta_1, \beta_2)}{\int_{p_i}^{p_i+\Delta p} dp\, F_{MC}(p) \int_{z_u}^{z_d} dz\, r_v(p, z)}, \tag{79}$$

where $r_v(p, z)$ is the vacuum beam decay rate and z_u and z_d are the upstream and downstream limits of the decay volume used for the normalization. We use both quadratic and piecewise linear correction functions.

There are two separate contributions to the total χ^2 in this type of fit. The first one is the implementation of the vacuum beam constraint as a "soft" constraint through the term

$$\chi^2_{constraint} = \sum_{i=1}^{n_p} \frac{(N_{v_i} - n_i D_{v_i}^{MC} \bar{\varepsilon}_{v_i})^2}{(1 + n_i) N_{v_i}}. \tag{80}$$

N_{v_i} is the total number of vacuum beam events in the ith momentum bin in the data sample, while $D_{v_i}^{MC}$ is the total number of kaon decays, whether accepted or not, in the Monte Carlo sample. Here $\bar{\varepsilon}_{v_i}$ is the average vacuum beam acceptance for that momentum bin. The n_i term in the denominator arises from the combination of statistical errors from $D_{v_i}^{MC}$ and $\bar{\varepsilon}_{v_i}$.

The functional for this type of fits was the expected number of accepted kaon decays, $N'_{r_{ij}}$ in a pz bin of the regenerator beam. For the ith momentum bin and jth z bin, we have

$$N'_{r_{ij}} = \frac{n_i D_{v_i}^{MC}}{d_{v_i}} p_{r_{ij}}. \tag{81}$$

Here $p_{r_{ij}}$ is the probability for this pz bin of accepting a kaon decay in the regenerator beam, and d_{v_i} is the probability of a kaon decaying in the vacuum beam in this momentum bin. The fraction on the right hand side is simply the number of kaons incident on the regenerator beam. The total χ^2 for a constrained fit is then

$$\chi^2 = \chi^2_{constraint} + \sum_{i=1}^{n_p} \sum_{j=1}^{n_z} \frac{(N_{r_{ij}} - N'_{r_{ij}})^2}{N'_{r_{ij}} + (N'_{r_{ij}} \sigma_{\bar{\varepsilon}_{r_{ij}}} / \bar{\varepsilon}_{r_{ij}})^2} \tag{82}$$

133
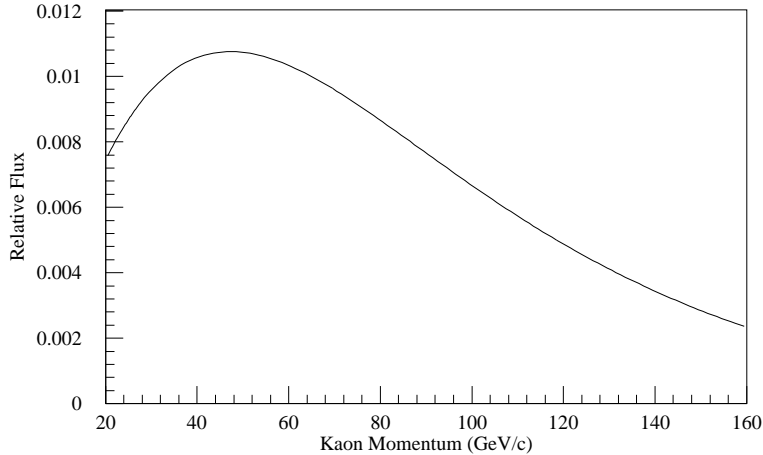
FIG. 93. The Monte Carlo prediction for the momentum spectrum of kaons incident at $z = z_{reg}$ in the vacuum beam.

2. Kaon Flux $F(p)$

In both types of fits, the final results were quite insensitive to the exact shape of the kaon flux used in the functional approximating Eq. (74). What was more important was the difference in the K_L flux between the vacuum and regenerator beams. There are small deviations of the regenerator beam flux shape from the vacuum shape because of kaon interactions with the additional material in the regenerator beam. The flux shape modifications due to kaon interactions in the common absorber were implicitly accommodated by the direct measurement of the vacuum beam $\pi^+\pi^-$ spectrum. The modifications to the regenerator beam spectrum arose from three distinct effects, primary $K_S \to K_L$ regeneration in the shadow absorber, elastic scattering in the shadow absorber, and the energy dependence of the kaon absorption in the shadow absorber and regenerator.

The spectrum of kaons predicted by our final Monte Carlo simulation to enter the decay volume in the vacuum beam is shown in Fig. 93. The corrections to the spectrum were small perturbations on this shape.

a. Primary $K_S \to K_L$ Regeneration Regeneration works both ways, and the primary $K_S \to K_L$ regeneration slightly modified the shape of the final K_L spectrum incident on the regenerator. This effect was easily calculated; the relative shape change included was at most a few tenths of a percent.

b. Kaon Scattering in the Absorbers Some kaons which elastically scattered in the shadow absorber remained in the beam and this effect is momentum dependent. The fraction was as large as 3% at the highest momentum and was readily included in the functional. While not affecting the extraction of $Re(\varepsilon'/\varepsilon)$, it was important to include this effect so as to obtain the proper regeneration power law.

Because of a small misalignment of the collimators, it was possible for a kaon to scatter, survive collimation, and miss the regenerator. The fraction of such incident kaons was at most 0.3% and was also included in the functional.

c. Kaon Absorption in the Absorber and Regenerator The final modification to the shape of the regenerator spectrum is due to the small energy dependence of the kaon-nucleus total cross section, and hence of the kaon absorption in the shadow absorber and regenerator. The average transmission has been accurately measured by comparing the

134

vacuum and regenerator beam samples in the $3\pi^0$ and $\pi^+\pi^-\pi^0$ modes. The measurements were made using kaons in the momentum range from 40 GeV/c to 150 GeV/c, and yielded $(6.33 \pm 0.03)\%$ for the $3\pi^0$ mode and $(6.43 \pm 0.06)\%$ for the $\pi^+\pi^-\pi^0$ mode. Combining these, we get average kaon transmission of $(6.35 \pm 0.03)\%$, but we need to incorporate the energy dependence.

The kaon-nucleon total cross sections are fairly well understood [56] and predictions are in good agreement with the measured energy dependence of the cross sections. The largest uncertainty in the calculation of the cross section is in the size of the correction due to inelastic screening. The uncertainty in the correction is estimated at 30% of itself.

Because of the small piece of lead at the end of the regenerator, we also need to know the total cross section for kaon-lead scattering. This cross section is well measured and predictions are again in good agreement with the measurements [56].

To implement the energy dependence of the absorption, the shape of the total cross section for Carbon (given by a Glauber-Franco model) was scaled to Boron-Carbite and Beryllium using the measured average cross sections. Because of the uncertainty in the inelastic screening correction, we introduce a correction parameter μ for each of the fits i.e. allowed it to float in the fit. The rise in the cross sections at high energy is roughly quadratic, and the correction is parametrized as a quadratic with the same minimum, having the form $\mu(p - 56)^2$ [1]. The lead cross-section (and its shape again from a Glauber-Franco model) is used without modification. The fits yield a small correction (up to 1.5%) to the kaon-Carbon cross section of -2.8 ± 1.1 mbarn at 156 GeV/c, to maintain the measured average cross-section.

In summary, the kaon flux in the regenerator beam relative to the vacuum beam is given by

$$F_r(p) = \bar{t} F_v(p) c(p), \tag{83}$$

with the bulk of the difference incorporated in the average kaon transmission $\bar{t} = 6.35\%$ and $c(p)$ a small correction factor for momentum-dependent effects, of order 0.4% at our average kaon energy.

B. Decay Rates

All of the kaon physics in which we are interested is embodied in the 2π decay rates $r_v(p, z)$ and $r_r(p, z)$ for the vacuum beam and regenerator beam, respectively. For a pure K_L beam, the 2π decay rate is given by

$$r_v(p, z) = \frac{dN_v}{dp \, dz} = |\eta_{+-(00)}|^2 e^{-(z - z_{reg})/\gamma\beta c\tau_L}, \tag{84}$$

where $\gamma\beta = p/m_K c^2$. The K_L amplitude has been normalized to one at $z = z_{reg}$, the downstream end of the regenerator.

The 2π decay rate in the regenerator beam depends on the regeneration amplitude $\rho(p)$. For a pure incoming K_L, the regenerator beam decay rate is

135

$$r_r(p, z) = \frac{dN_r}{dp\, dz}$$
$$= |\rho(p)|^2 e^{-(z-z_{reg})/\gamma\beta c\tau_S} + |\eta_{+-(00)}|^2 e^{-(z-z_{reg})/\gamma\beta c\tau_L}$$
$$+ 2|\rho(p)||\eta_{+-(00)}|\cos(\Delta m(z-z_{reg})/\gamma\beta c + \phi_\rho - \phi_{+-(00)})e^{-(z-z_{reg})/\gamma\beta c\tau_{av}}. \tag{85}$$

The quantity τ_{av} is defined by

$$\frac{1}{\tau_{av}} = \frac{1}{2}\left(\frac{1}{\tau_S} + \frac{1}{\tau_L}\right), \tag{86}$$

and $\phi_\rho = \arg(\rho)$. Recall that $|\rho/\eta|$ is of order 15, so the K_S decay term dominates the total decay rate.

We use the thick regeneration approximation, ignoring higher order regeneration effects, such as the secondary regeneration of K_S back to K_L, and the only normalization term in the regenerator beam relative to the vacuum beam is the kaon attenuation. This approximation gives the K_S regeneration amplitude at the end of the regenerator as

$$\rho(p) = \imath\pi\gamma\beta cn\frac{f(0) - \bar{f}(0)}{k}\left(\frac{p}{70}\right)^\alpha g(L), \tag{87}$$

with

$$n = \frac{N_A d}{A}. \tag{88}$$

The parameters in the above expressions are defined as follows:
n density of scattering sites,
N_A Avogadro's Number,
d Density of the regenerator material,
A Atomic Number of the regenerator material
$f(0), \bar{f}(0)$ K^0, $\bar{K}^0$ forward scattering amplitude at 70 GeV/c,
k kaon wave number,
α slope of momentum power-law dependence,
$g(L)$ geometric factor dependent on the length L of the regenerator.

The function $g(L)$ is a complex geometric factor originating in the kaon propagation through the regenerator. It is given by

$$g(L) = \frac{1 - \exp[-L(\frac{1}{2\tau_S} - \imath\Delta m)/\gamma\beta c]}{(\frac{1}{2\tau_S} - \imath\Delta m)}. \tag{89}$$

In both fitting program and Monte Carlo, we actually use the full propagation treatment of the kaon amplitude through the regenerator [57]. (We have also used the thick regenerator approximation in fitting, and for $Re(\varepsilon'/\varepsilon)$, it gives identical results within 2×10^{-5}). However, the important issues are more transparent in discussion using the thick regenerator formulation.

In Eq. (87), we have explicitly incorporated the expected power-law momentum dependence of the difference of the K^0 and $\bar{K}^0$ forward scattering amplitudes:

$$\left| \frac{f(0) - \bar{f}(0)}{k}(p) \right| = \left| \frac{f(0) - \bar{f}(0)}{k}(70) \right| \left(\frac{p[\text{GeV}/c]}{70} \right)^{\alpha}. \tag{90}$$

This dependence results from the difference in scattering being dominated by the exchange of the ω trajectory (see, for example, [34]).

To measure Δm and ϕ_{+-}, it is clear from Eq. (85) that we need to know the regeneration phase ϕ_ρ. There are two contributions to this phase, $\phi_\rho = \frac{\pi}{2} + \phi_g + \phi_{f-\bar{f}}$. The geometric phase $\phi_g \equiv \arg[g(L)]$ can be trivially calculated, which leaves the phase contribution from the forward scattering amplitude, $\phi_{f-\bar{f}} \equiv \arg[(f(0) - \bar{f}(0))/k]$. Fortunately, the dispersion relations which result from requiring analytic behavior of the forward scattering amplitudes determine this phase. For a power-law dependence as in Eq. (90), the phase is related to the power-law slope α via

$$\phi_{f-\bar{f}} = -\frac{\pi}{2}(2 + \alpha). \tag{91}$$

To calculate the regeneration amplitude, we need to take into account the compound structure of the regenerator. The regenerator consists of 4 separate blocks of boron-carbide of length $L_{B_4C} = 19.00$ cm separated by vacuum gaps of length $L_v = 3.75$ cm each. At the end of the regenerator is a piece of lead which is $L_{Pb} = 1.25$ cm thick. If ρ_{B_4C} is the regeneration amplitude for one of the boron-carbide blocks, and ρ_{Pb} is that for the lead piece, then the total regeneration at the end of the regenerator is

$$\rho_{total} = \rho_{B_4C}\left(e^{-3(L_{B_4C}+L_v)\Lambda_S} + e^{-2(L_{B_4C}+L_v)\Lambda_S} + e^{-(L_{B_4C}+L_v)\Lambda_S} + 1\right)e^{-L_{Pb}\Lambda_S} + \rho_{Pb}, \tag{92}$$

with

$$\Lambda_S \equiv \frac{1}{\gamma\beta c}\left(\frac{1}{2\tau_S} - i\Delta m\right). \tag{93}$$

In each of our standard fits, the power-law dependence α_{B_4C} and scattering amplitude difference at 70 GeV/c, $|(f(0) - \bar{f}(0)/k)|_{70}$, for boron-carbide are parameters of the fit. The scattering phase for the boron-carbide is obtained from the analyticity relation (Eq. (91)). For the lead parameters we use the values obtained in a previous experiment [47]. The values of the regeneration parameters used in the fits are summarized in Table XVI. For typical values of the boron-carbide parameters, the lead piece accounts for 3.3% of the regeneration amplitude at 70 GeV/c.

These are the basic concepts that we implement in calculating the decay rates. There are two issues that complicate the fitting procedure beyond what we have discussed. The first complication involves the assumption made above that the beams arriving at the decay volume are pure K_L beams. The second involves the modification of the decay rate to accommodate the material in the HDRA. The former affects all fits, while the latter affects only neutral mode data downstream of the HDRA.

1. Primary K_S Corrections

The absolute primary K_S correction was small and easy to account for, as the largest fractional correction was only 10^{-4} at which we had the fewest data: the far upstream z

137

TABLE XVI. Regeneration parameters for the boron-carbide and lead in the regenerator used in the fits. For the boron-carbide, values of regeneration parameters which float in the fitting are presented.

Material	Atomic Weight	Density (gm/cm^3)	$(f - \bar{f})/k$ (mbarn)	Power-Law Slope	Phase (degrees)
B_4C	55.26	2.52	5.791 [a]	-0.604[a]	-125.6 [b]
Pb	207.19	11.35	9.71 ± 0.14 [c]	-0.654 ± 0.018 [d]	-122.2 ± 1.8[d]

[a]Always extracted as a parameter in the fits. This is a typical value.

[b]Always obtained via analyticity from the current value of α_{B_4C} in the fits. This is a typical value.

[c]Value obtained using the data in [47], with a correction for the change in η_{+-}. The error includes the error quoted in [47] added in quadrature with the contribution from the uncertainty of η_{+-}.

[d]From [47]. Although the analyticity of Lead is only good to a few degrees, the Lead is only a small contribution here.

region and high kaon momentum. The fraction of the total number events in the momentum range from 40 GeV/c to 160 GeV/c and z range from 110 m to 137 m was corrected as a function of momentum and z. The total correction in the charged sample in this range is -0.62% $(+0.0013\%)$ for the vacuum (regenerator) beam sample. Almost half of the vacuum correction comes from the 160 GeV/c momentum bin alone. For the same z and p range in the neutral sample, the correction is -0.14% $(+0.0035\%)$. The size of the correction is under 0.002% for both beams in the neutral sample downstream of 137 m.

Good checks are done when fitting for Δm and τ_S– we have found that fits using this correction technique in the Monte Carlo test samples yield the proper values of Δm and τ_S to within 10% of the statistical precisions that we can obtain in this experiment. Fits to $Re(\varepsilon'/\varepsilon)$ is even less sensitive to this correction, with the level of discrepancy well below 10^{-5}, when the values for Δm, τ_S and the K^0-$\bar{K}^0$ dilution factor are varied over ranges commensurate with their uncertainties.

2. Regeneration in the HDRA

In all of our fits involving the neutral mode, the data came from a z region extending beyond the HDRA. For any portion of a z bin upstream of the HDRA, the decay rate given in the previous discussion is still correct. For the z region downstream of the HDRA, however, the K_S and K_L amplitudes have to be modified to include regeneration and attenuation in the HDRA.

The components of the HDRA (see Table III) are very thin. To give an idea of the effect of the HDRA material on the measured parameters, if one neglected the regeneration,

$Re(\varepsilon'/\varepsilon)$ would shift by -4×10^{-4}. Since the physical properties of the material in the HDRA are known at the percent level, the uncertainty in $Re(\varepsilon'/\varepsilon)$ from the HDRA material is negligible.

The other measurements affected most in principle are the mass difference and phase measurements, which depend on the shape of the downstream decay distribution. For the typical kaon momentum of 70 GeV/c, the K_S amplitude contributed from regeneration in the HDRA is under 2% of the K_S amplitude from the regenerator propagated to the HDRA. In any of the fits, the regeneration parameters and thicknesses of the materials in the HDRA are known well enough that the uncertainty from the HDRA regeneration is negligible.

C. Acceptance Corrections

The last ingredient needed for our prediction functional is the acceptance. The physical parameters (Δm, τ_S, $(f - \bar{f})/k$ for B_4C, etc.), used in the Monte Carlo were very close to the parameters derived in the final fit. The average acceptance over a certain range in momentum and z is defined as the ratio of events *reconstructed* in this range to the number of actual decays in this range. In the terms of Eq. (74), the acceptance $\bar{\varepsilon}_{v(r)_{ij}}$ in the vacuum (regenerator) beam for the pz bin starting at momentum p_i and decay position z_j is

$$\bar{\varepsilon}_{v(r)_{ij}} = \frac{\int_{p_i}^{p_i+\Delta p} dp \int_{z_i}^{z_i+\Delta z} dz \int dp' \, F_{v(r)}(p') \int dz' \, s(p, z; p', z') \, a(p', z') \, r_{v(r)}(p', z')}{\int_{p_i}^{p_i+\Delta p} dp' \, F_{v(r)}(p') \int_{z_i}^{z_i+\Delta z} dz' \, r_{v(r)}(p', z')}. \tag{94}$$

As before, if the integration variables are unprimed, they refer to reconstructed quantities, and if primed, to true quantities.

The acceptances are shown for the two charged mode beams in Fig. 94 and the two neutral mode beams (no lead sheet) in Fig. 95. The bin sizes are 1 GeV/c in momentum and 1 m (3 m) in z in the charged (neutral) figure. On a p and z scale of 1 GeV/c by 0.5 m, the vacuum and regenerator beam acceptances are nearly identical. Even at 20 GeV/c, where both the acceptance and decay distributions change most rapidly as a function of p and z, the decay distribution is locally flat enough that the effect of smearing in and out of the bin is very similar in both beams.

The similarity of the vacuum and regenerator beam acceptances is demonstrated in Fig. 96, where the average acceptances as a function of z in four different 10 GeV/c momentum bins are shown. The regenerator and vacuum beam acceptances are noticeably different in the 20 GeV/c momentum bin, slightly different at 40 GeV/c, and virtually identical above 60 GeV/c. These differences arise, because the change in the decay rate across a 10 GeV/c momentum bin is much larger in the regenerator beam than in the vacuum beam at the lowest momenta. Since the acceptance also varies quite rapidly across the lowest two momentum bins, the acceptance *weighted* by the decay rate is different in the two beams. In the 20 GeV/c and 40 GeV/c bins, the regenerator beam acceptances from the Monte Carlo have been overlaid with the acceptances predicted by weighting the vacuum acceptance calculated in 1 GeV/c bins with the shape of the regenerator beam decay rate across the momentum bin; the agreement is excellent.
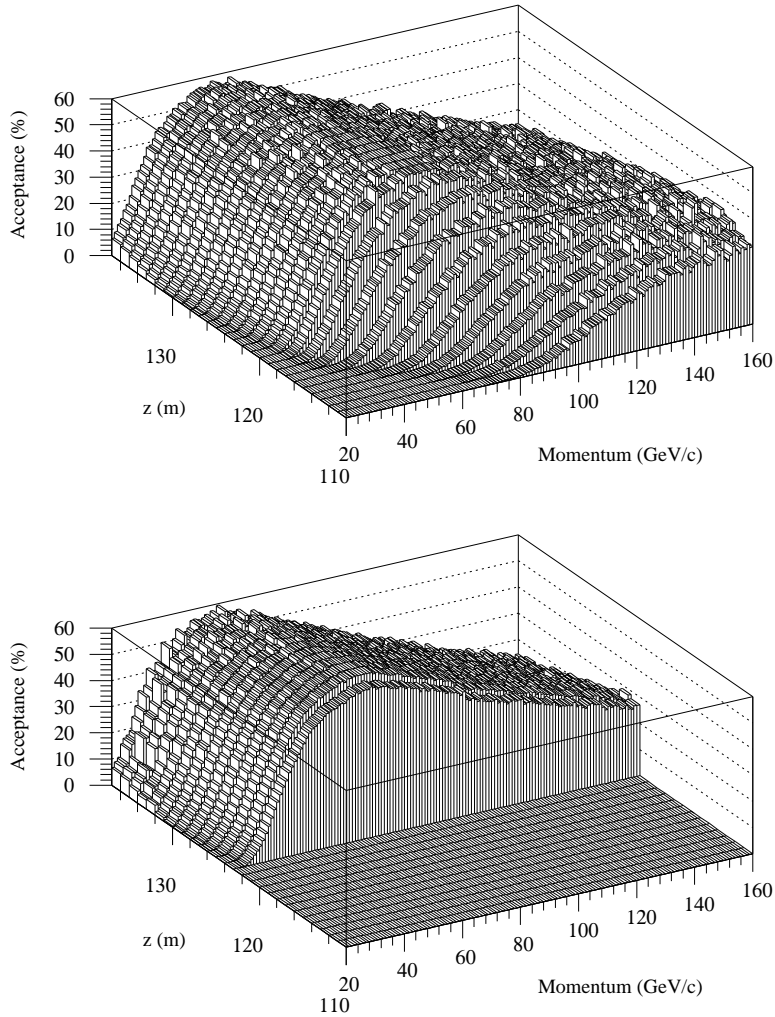
FIG. 94. Acceptance as a function of momentum and z for $K \to \pi^+\pi^-$ decays. The acceptance for the vacuum (regenerator) beam is the top (bottom) plot. The upstream acceptance in the vacuum beam is limited by the mask anti. The regenerator is located at 123.5 m.
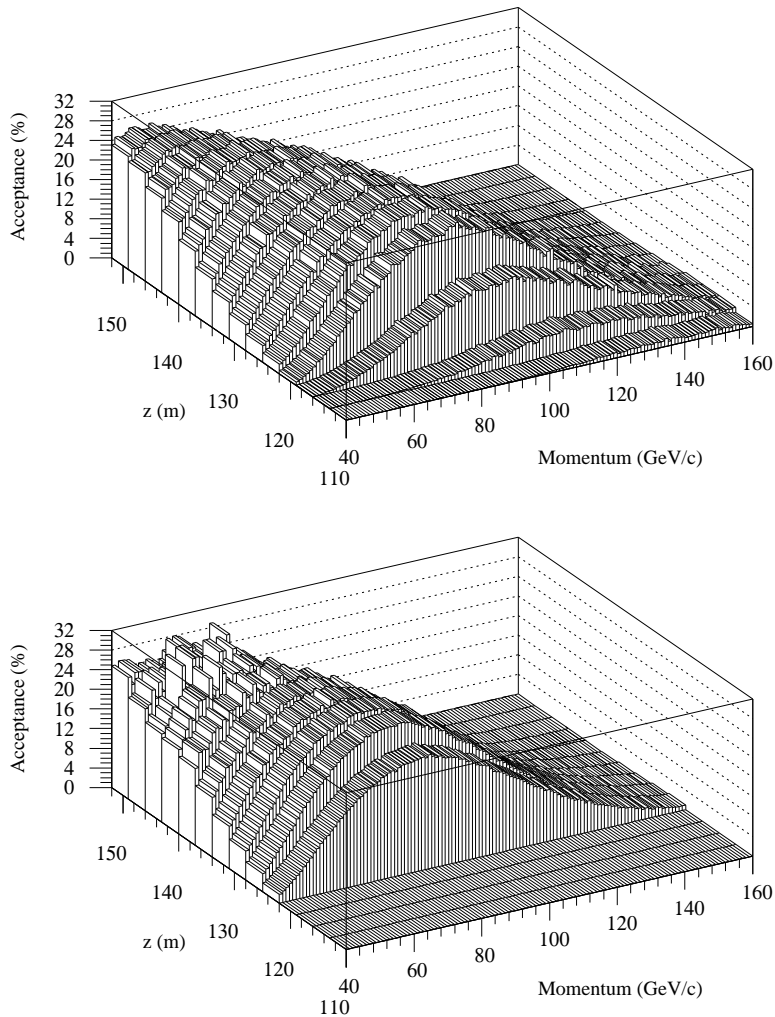
FIG. 95. Acceptance as a function of momentum and z for $K \to \pi^0 \pi^0$ decays with the lead sheet removed. The acceptance for the vacuum (regenerator) beam is the top (bottom) plot. The upstream acceptance in the vacuum beam is limited by the mask anti. The regenerator is located at 123.5 m.
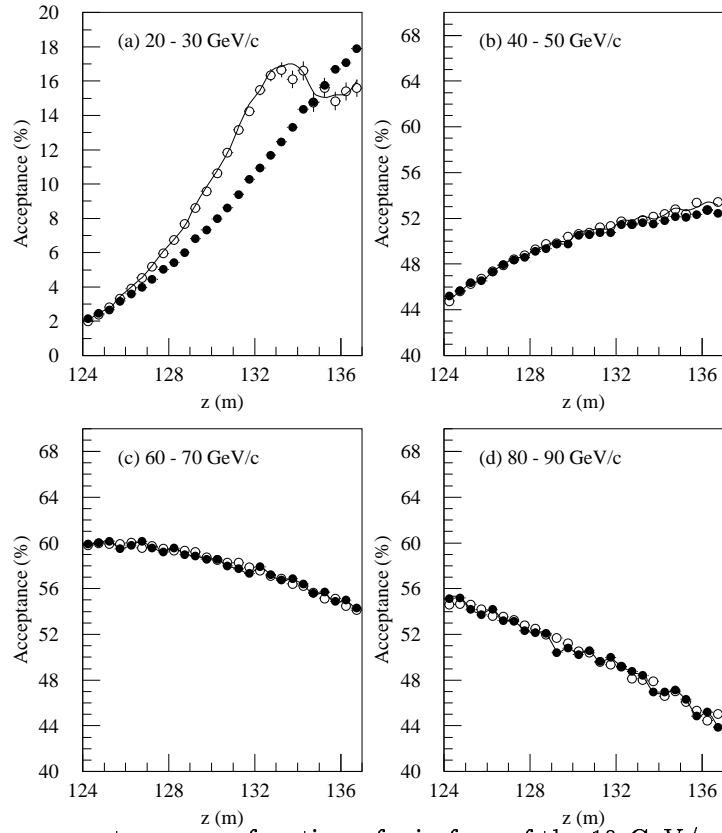
FIG. 96. The $\pi^+\pi^-$ acceptance as a function of z in four of the 10 GeV/c momentum bins. The vacuum (regenerator) acceptance is shown as solid (hollow) circles. The lines are the regenerator beam acceptances predicted by weighting the vacuum beam acceptances in 1 GeV/c momentum bins with the regenerator beam decay rates.

D. Prediction Functional

We have discussed all of the ingredients entering the prediction functional we used in our fits. We finish this section by mentioning a few additional small factors.

For z bins which begin upstream of z_{reg}, the z integral for the regenerator beam in the charged mode begins at $z = z_{reg}$. In the neutral mode, there is a small probability for all four of the photons to pass through the lead piece at the end of the regenerator without converting. The Monte Carlo begins all decays at the downstream edge of the regenerator and we correct for this in the fit. The convolution of this survival probability with K_S regeneration is easily calculated. The resulting rate corresponds to an effective increase in the decay volume of 1.8 mm, that is, the integral for a z bin containing the regenerator begins at $z = z_{reg} - 0.0018$ for the neutral mode. The only fit using a z region upstream of the regenerator is the fit for $Re(\varepsilon'/\varepsilon)$, and the correction in this case shifts the final result by $\Delta Re(\varepsilon'/\varepsilon) = -0.8 \times 10^{-4}$.

In z, the average acceptance is calculated in the bin size used in the fit. Acceptances are calculated in 1 GeV/c bins in momentum largely because the decay rate and acceptance vary fairly rapidly across the momentum range from 20 to 30 GeV/c in the regenerator beam, and are sensitive to the values of Δm and τ_S. To avoid biases, we acceptance-correct the predicted decay rates on a scale insensitive to the fit parameters. No difference was found between fits using 1 GeV/c and 0.5 GeV/c bins for the acceptance correction.

Finally, because of the step introduced by photon conversions in the lead sheet in the middle of the decay volume, the two subsets were treated independently: for each pz bin we obtained a prediction in each of the two subsets independently, and each subset added an independent contribution to the total χ^2.

This ends the discussion of all of the details used in our fits to the 2π data samples. We now move on to discuss the results of the fits themselves.

IX. RESULTS OF THE FITS

This section gives the final results for $Re(\varepsilon'/\varepsilon)$, the measurement for which this experiment was designed, and for Δm, τ_S, $\Delta\phi$, and for ϕ_{+-}.

A. Fitting for $Re(\varepsilon'/\varepsilon)$

In the fits for $Re(\varepsilon'/\varepsilon)$, the momentum range 40 GeV/c to 160 GeV/c was used for both charged and neutral samples.

We initially determined the power-law behavior in the individual subsets, performing unconstrained fits with $Re(\varepsilon'/\varepsilon)$ fixed at zero. The three parameters for which we fit in all cases are $(f(0) - \bar{f}(0))/k$ at 70 GeV/c (which we call $\Delta f|_{70}$), the regeneration slope α and the cross section correction μ. One fit was to the entire charged sample, one to the entire neutral sample, and to the two individual neutral subsets. For the charged mode fits, the z range used was 110 m to 137 m, and for the neutral fits, the range was 110 m to 152 m.

Since $Re(\varepsilon'/\varepsilon)$ is fixed at zero in these fits, a nonzero value for $Re(\varepsilon'/\varepsilon)$ would force ρ away from its true value, and shift $\Delta f|_{70}$. Since ε' shifts η_{+-} and η_{00} in opposite directions, we would see a shift in $\Delta f|_{70}$ in the charged and neutral fits. On the other hand, the measured power α should not be biased. Only one regenerator was used so the same power α should be measured in all subsets.

The results of these fits are summarized in Table XVII and in Fig. 97. The χ^2 for each fit is excellent, as is the agreement in the powers. From the figure, it is clear that $Re(\varepsilon'/\varepsilon)$ is small. The fractional deviations from a common power (a simultaneous fit to the $\pi^+\pi^-$ and $2\pi^0$ data) show no obvious bias vs. momentum.

We fit the charged and neutral data simultaneously to extract $Re(\varepsilon'/\varepsilon)$ with common regeneration and absorption parameters. The result is

$$Re(\varepsilon'/\varepsilon) = (7.4 \pm 5.2(stat.)) \times 10^{-4}, \qquad (95)$$

with a χ^2 of 26 for 32 degrees of freedom. The remaining parameters are listed in Table XVII. The χ^2 contours for $Re(\varepsilon'/\varepsilon)$ versus each of the 3 other parameters are well behaved as shown in Fig. 98.

The values of the fixed parameters, their precision, and influence on $Re(\varepsilon'/\varepsilon)$ in the fit are listed in Table XVIII. It is clear that $Re(\varepsilon'/\varepsilon)$ is quite insensitive to these parameters. We used values of Δm and τ_S obtained from our data (see Section IX B), comparable in precision to current world averages. For $|\varepsilon|$, we used the Particle Data Group average of $|\eta_{+-}|$ [27]. Also CPT symmetry is implicit in our use of the natural phase [9,3] for the phase of ε, $\phi_\varepsilon = \tan^{-1}[2\Delta m/(\Gamma_S - \Gamma_L)]$. The phase of ε' is derived from the $\pi\pi$ phase shift analysis of Ochs [16].

As a final check, we relax the power-law assumption for the momentum dependence of $(f(0) - \bar{f}(0))/k$, and fit for $Re(\varepsilon'/\varepsilon)$ and the regeneration amplitude in each momentum bin. $Re(\varepsilon'/\varepsilon)$ as a function of momentum is shown in Fig. 99. The average from these fits is only 0.15×10^{-4} larger than the "standard" fit.

Measuring $Re(\varepsilon'/\varepsilon)$ by taking the momentum bin average has the advantage of being insensitive to the energy dependence of the absorption cross section. In tests of the fitting

TABLE XVII. Results of the unconstrained fits used to determine $Re(\varepsilon'/\varepsilon)$ which is fixed at 0 in the first four fits to the charged and neutral subsets so that the regeneration parameters from these sets may be compared. The cross section correction is quoted in terms of the correction to the carbon cross-section at 156 GeV/c.

Fit	$Re(\varepsilon'/\varepsilon)$ $(\times 10^{-4})$	$\Delta f\|_{70}$ (mbarns)	α	$\Delta\sigma_T$ (mbarns)	$\chi^2/d.o.f$
$\pi^+\pi^-$	0^a	5.786 ± 0.008	-0.605 ± 0.007	-3.1 ± 1.4	$8.9/9$
$2\pi^0$(Pb Sheet)	0^a	5.799 ± 0.009	-0.598 ± 0.010	-2.4 ± 2.8	$8.2/9$
$2\pi^0$(No Pb Sheet)	0^a	5.801 ± 0.011	-0.609 ± 0.011	-1.8 ± 3.2	$6.2/9$
$2\pi^0$(Combined)	0^a	5.800 ± 0.007	-0.603 ± 0.007	-2.1 ± 2.1	$16.8/21$
Simultaneous $\pi^+\pi^-$ and $2\pi^0$	7.4 ± 5.2	5.791 ± 0.005	-0.604 ± 0.005	-2.8 ± 1.1	$25.8/32$

^{a}Fixed at this value for this fit.

TABLE XVIII. Variation of the extracted value for $Re(\varepsilon'/\varepsilon)$ with the values of physical constants in the fit. The units assumed for each of the constants is given in square brackets in the first column. Here $\Delta Re(\varepsilon'/\varepsilon)$ is the change in $Re(\varepsilon'/\varepsilon)$ for an increase in the constant by one standard deviation. The correction to $Re(\varepsilon'/\varepsilon)$ as a function of the physical constants is presented in the last column.

Parameter	Value	Error	$10^4 \times \Delta Re(\varepsilon'/\varepsilon)$ ($+1\sigma$ variation)	$10^4 \times Re(\varepsilon'/\varepsilon)$ dependence
Δm $[10^{10}\hbar s^{-1}]$	0.5286	0.0028	$+0.41$	$77.2(\frac{\Delta m - 0.5286}{0.5286})$
τ_S $[10^{-10}s]$	0.8929	0.0016	-0.26	$-147(\frac{\tau_S - 0.8929}{0.8929})$
τ_L $[10^{-8}s]$	5.17	0.004	$+0.05$	$5.8(\frac{\tau_L - 5.17}{5.17})$
$|\varepsilon|$ $[10^{-3}]$	2.279	0.022	-0.11	$-11.4(\frac{|\varepsilon| - 2.279}{2.279})$
ϕ_ε	$43.4°$	$0.2°$	-0.15	$-0.75(\phi_\varepsilon - 43.4°)$
$\phi_{\varepsilon'}$	$47°$	$6°$	-0.11	$-0.018(\phi_{\varepsilon'} - 47°)$
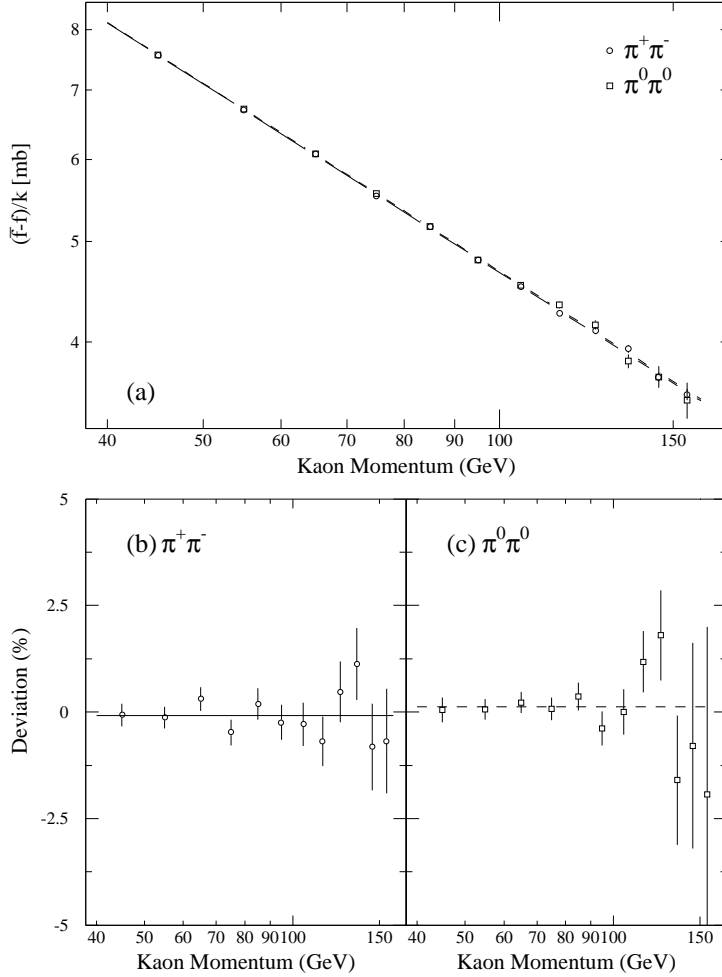
FIG. 97. Regeneration amplitude versus kaon momentum. (a) The average amplitude in each momentum bin for the $\pi^+\pi^-$ (open circles) and $2\pi^0$ (open squares) data. The solid line is the best fit power to the $\pi^+\pi^-$ data. The best fit power for the $2\pi^0$ data is just visible as a dashed line above the $\pi^+\pi^-$ power. (b),(c) The fractional deviation of the average amplitude in each momentum bin from the simultaneous fit to the $\pi^+\pi^-$ and $2\pi^0$ data. The line is the average deviation.
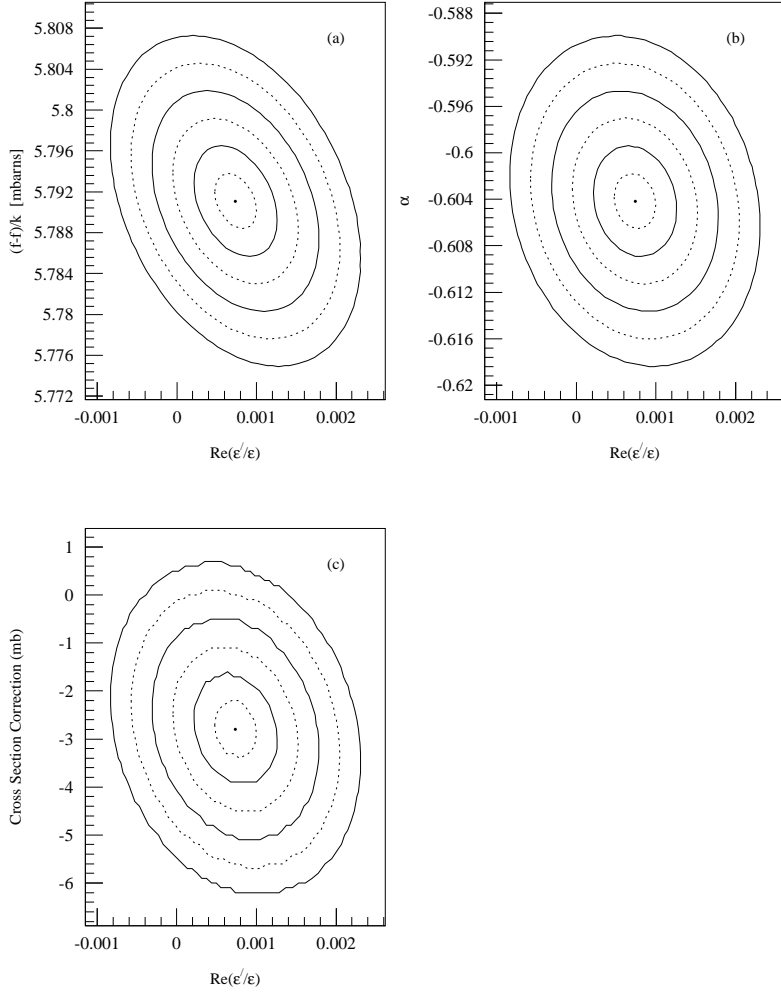
FIG. 98. Contours of equal χ^2 in the fit for $Re(\varepsilon'/\varepsilon)$. The contours are plotted in steps of 1/2 standard deviations. (a) $[f(0) - \bar{f}(0)]/k|_{70GeV/c}$ versus $Re(\varepsilon'/\varepsilon)$. (b) α versus $Re(\varepsilon'/\varepsilon)$. (c) Kaon-Carbon total cross section correction parameter (at 156 GeV/c) versus $Re(\varepsilon'/\varepsilon)$.
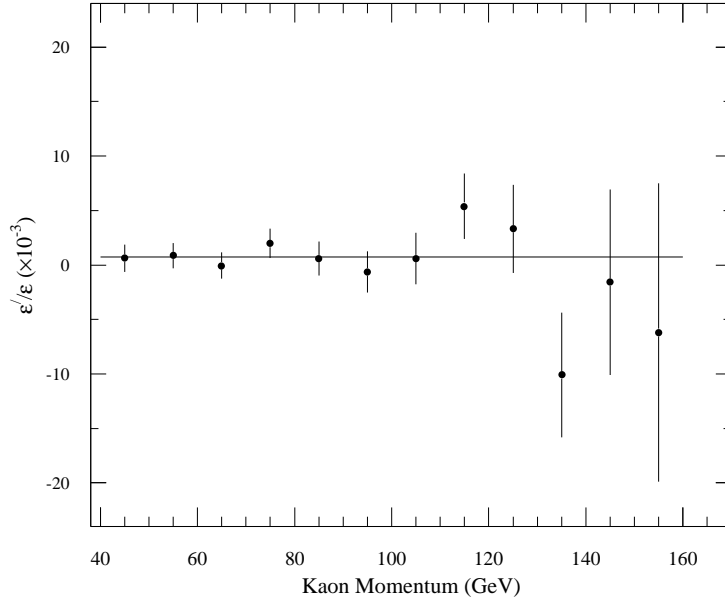
FIG. 99. Momentum dependence of $Re(\varepsilon'/\varepsilon)$. The values of $Re(\varepsilon'/\varepsilon)$ in each momentum bin (dots) have been determined independently, with no regeneration power-law constraint. The line is the weighted average of the individual momentum bin fits.

procedure, the observed sensitivity to the energy dependence of the absorption cross section was an order of magnitude smaller for the bin average than for the power-law fit. For this result, the power-law constraint does not increase the statistical sensitivity; we report the value using the power-law for consistency with the remaining fits that rely more heavily on the power-law to obtain the regeneration phase.

1. $Re(\varepsilon'/\varepsilon)$ and Accidental Biases

While the double beam technique leads to a cancellation of accidental effects to first order, there are second order effects that could potentially bias the result. The determination of such effects, using random triggers overlaid on Monte Carlo $\pi\pi$ decays, is detailed in the next section. Here we present the results.

In the charged mode sample, the highest intensity subset was NC subset. Here the change in the vacuum to regenerator ratio was $-0.04\% \pm 0.07\%$, consistent with zero. We therefore made no correction in the charged sample.

In the highest intensity neutral samples, accidentals do introduce a shift in the relative vacuum and regenerator beam acceptances. The correction is $-0.17\%(-0.15\%) \pm 0.06\%$ for the high intensity subsets with (without) the lead sheet. We can compare this result to the accidental study in the lower intensity NC subset presented in reference [37] by scaling the high intensity result by the ratio of intensities. This scaling implies we should have a correction in the NC subset of -0.06%, consistent with [37], where a correction of $-0.04\% \pm 0.07\%$ was found. When the high and low intensity accidental corrections are applied, the final result for $Re(\varepsilon'/\varepsilon)$ shifts by $\Delta Re(\varepsilon'/\varepsilon) = +2.5 \times 10^{-4}$. This correction has already been made in the fits presented in the previous section.

148

2. Summary of $Re(\varepsilon'/\varepsilon)$ Fit Results

The value extracted for $Re(\varepsilon'/\varepsilon)$ from our entire data sample is $Re(\varepsilon'/\varepsilon) = (7.4 \pm 5.2) \times 10^{-4}$. This is the result from the power-law fit, and it includes the very small corrections for both accidental biases and for photons which do not convert within the regenerator.

We have also refit the data subset used to obtain our previously published value [18] of $Re(\varepsilon'/\varepsilon) = (-4 \pm 14 \pm 6) \times 10^{-4}$. There were many improvements in analysis, Monte Carlo simulation, and fitting technique since that publication. The systematic error for that result was dominated by uncertainty in the energy scale, and as Figs. 21 and 26 demonstrate, our understanding has improved substantially. The new central value for this subset is -2.4×10^{-4}; the shift is well within the systematic uncertainty, and indicates the robustness of the technique.

This ends the discussion of the fit for $Re(\varepsilon'/\varepsilon)$. The systematic evaluation is treated after we give the results of the constrained fits for the other kaon parameters.

B. Δm and τ_S Fits

In fitting for Δm and τ_S, we extract values for the charged and neutral mode data separately.

The fits assumed no direct CP violation: $Re(\varepsilon'/\varepsilon) = 0$. We also assumed CPT symmetry by using the natural phase $\tan^{-1}[2\Delta m/(\Gamma_S - \Gamma_L)]$ for the phase of ε. For $|\varepsilon|$, we use the same value as in the $Re(\varepsilon'/\varepsilon)$ fits (see Table XVIII). Then Δm, τ_S, $\Delta f|_{70}$, and α are the parameters to be fit. In addition, there are three vacuum beam constraint parameters and the cross-section correction parameter (Section VIII A 1). The charged sample and two neutral samples have separate constraint parameters to allow for flux variations from set to set.

From Monte Carlo studies, we have found that systematic biases in the measurement of Δm and τ_S are exacerbated when trying to use the z region including the regenerator edge. Thus we use only the z region in the regenerator beam downstream of 124.5 m (125 m) in the charged (neutral) mode fits.

The z bin sizes used for these fits were chosen to be commensurate with the z resolution of the individual mode. For $\pi^+\pi^-$ decays, the z resolution varied from 10 cm (downstream) to 25 cm (upstream), so the z bin sizes used in the fits were at least 1 m. For the neutral mode, the resolution was closer to 1 m, so the z bins used in the fit were at least 2 m.

For increased sensitivity, the charged mode fits began at 20 GeV/c. This has systematic ramifications because the momentum dependence of $(f - \bar{f})/k$ may begin to deviate from a pure power-law — increasing the uncertainty in the associated regeneration phase — and the decay rate, acceptance and incident kaon flux all vary rapidly in the 20 GeV/c to 30 GeV/c range. This latter problem is most severe at the downstream end of the $\pi^+\pi^-$ decay volume, and for this reason, the z range was restricted to 135 m in the charged mode fits. In spite of these limitations, the overall sensitivity was enhanced by using lower momentum events.

The lower limit of the momentum range used in the neutral mode is limited by the E_T trigger threshold, so the fits again used 40 GeV/c to 160 GeV/c. Even so, the extended z range available in the $2\pi^0$ mode resulted in the $2\pi^0$ sample yielding the best statistical precision.

TABLE XIX. Summary of fits for Δm and τ_S for both the $\pi^+\pi^-$ and $2\pi^0$ modes. Numbers in parentheses are the statistical errors to the least significant figure.

Sample	z bin size	Δm $(10^{10}\hbar s^{-1})$	τ_S $(10^{-10}s)$	$\Delta f\vert_{70}$ (mbarn)	α	$\chi^2/d.o.f.$
$\pi^+\pi^-$	1 m	0.5302(44)	0.8952(15)	5.774(9)	$-0.590(3)$	157/160
$\pi^+\pi^-$	2 m	0.5319(45)	0.8953(15)	5.773(9)	$-0.590(3)$	92/90
$2\pi^0{}_{all}$	2 m	0.5277(30)	0.8911(16)	5.804(11)	$-0.602(7)$	335/302
$2\pi^0{}_{all}$	3 m	0.5274(30)	0.8912(17)	5.802(11)	$-0.603(7)$	221/203
$2\pi^0{}_{Pb}$	3 m	0.5289(39)	0.8904(22)	5.803(15)	$-0.604(10)$	118/99
$2\pi^0{}_{NoPb}$	3 m	0.5251(47)	0.8920(25)	5.803(17)	$-0.601(11)$	100/99

A summary of the results for the two modes with different binnings is shown in Table XIX. For Δm in charged mode, we average the values for the two binnings, giving $\Delta m = (0.5311\pm 0.0044) \times 10^{10}\hbar s^{-1}$. For τ_S in charged mode, we find $\tau_S = (0.8952 \pm 0.0015) \times 10^{-10}s$. The results from neutral fits with 2 m and 3 m binnings were close, and we take the 3 m results, this binning being better matched to the 1 m resolution. The two neutral subsets give consistent results. The combined average values for Δm and τ_S are then $\Delta m = (0.5286 \pm 0.0025) \times 10^{10}\hbar s^{-1}$ and $\tau_S = (0.8929 \pm 0.0011) \times 10^{-10}s$ with statistical error only. Before the charged and neutral mode results can be compared directly, however, the systematic contributions must be determined.

The absorption correction parameters obtained in these fits were consistent with those in the $Re(\varepsilon'/\varepsilon)$ fits. As for the shape corrections to the Monte Carlo vacuum flux, neutral mode needed no correction while charged data preferred the flux at the extremes of the momentum range to be several percent lower than in the center, consistent with overlays given in the previous section.

Elliptical χ^2 contours showing correlations between the most important parameters of the fit are given in Fig. 100 for charged and Fig. 101 for neutral modes.

The values of τ_S and Δm are insensitive to most of the fixed parameters in the fit. The one exception is the phase of ϕ_{+-}; for τ_S this variation is $-0.09\%/$degree, and for Δm it is $+0.59\%/$degree.

Fixing τ_S and the regeneration, absorption, and flux parameters at the values from one of the above fits, one can extract the *average* value of the cosine term in Eq. (85) in each pz bin. Similarly, by fixing Δm one can extract the average value of the K_s decay term. We have done this in both the neutral and charge data using 1 m by 10 GeV/c bins. The results (choosing kaon momenta under 90 GeV/c) are plotted against the average proper time for that bin in Figs. 102 (charged mode) and 103 (neutral mode). The proper time $\tau = 0$ corresponds to the downstream face of the regenerator.

C. Extracting the Phases

The fitting methods used to extract $\Delta\phi$ and ϕ_{+-} are in essence identical to those used to extract Δm and τ_S. We need to measure the intercept of the interference curve at proper
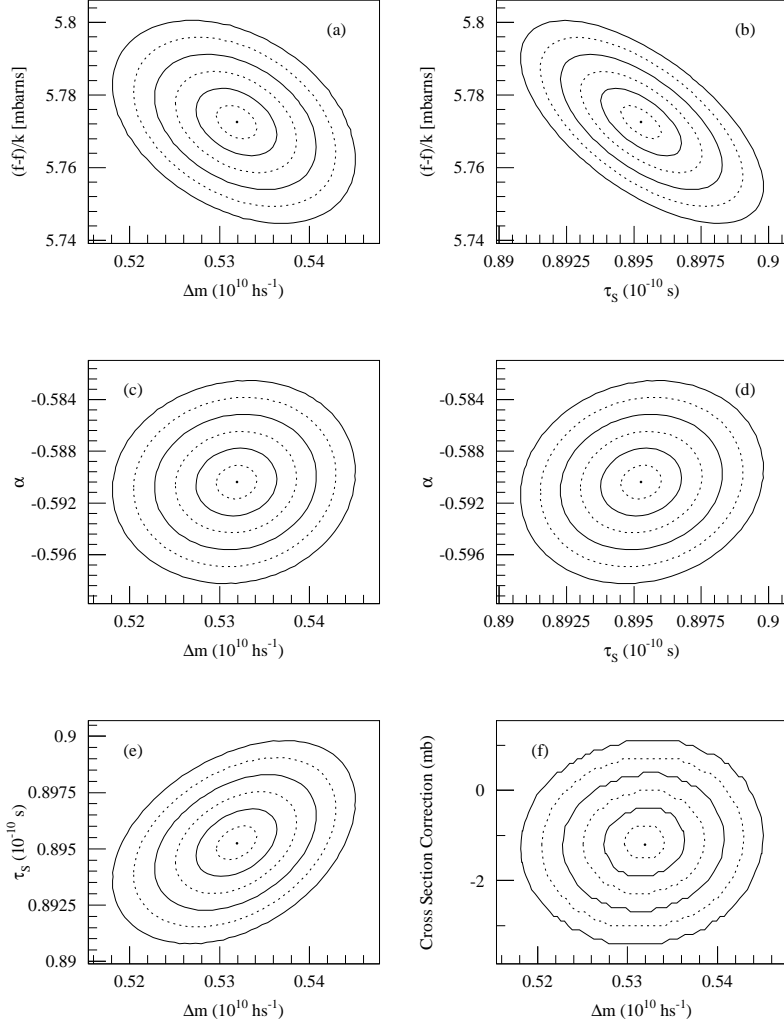
FIG. 100. Contours of equal χ^2 in 1/2 standard deviation intervals in the fit (with 2 m bins) for Δm and τ_S to the $\pi^+\pi^-$ data. (a) $\Delta f|_{70}$ versus Δm. (b) $\Delta f|_{70}$ versus τ_S. (c) Power-law slope α versus Δm. (d) Power-law slope α versus τ_S. (e) τ_S versus Δm. (f) Kaon-carbon cross-section correction (at 156 GeV/c) versus Δm.
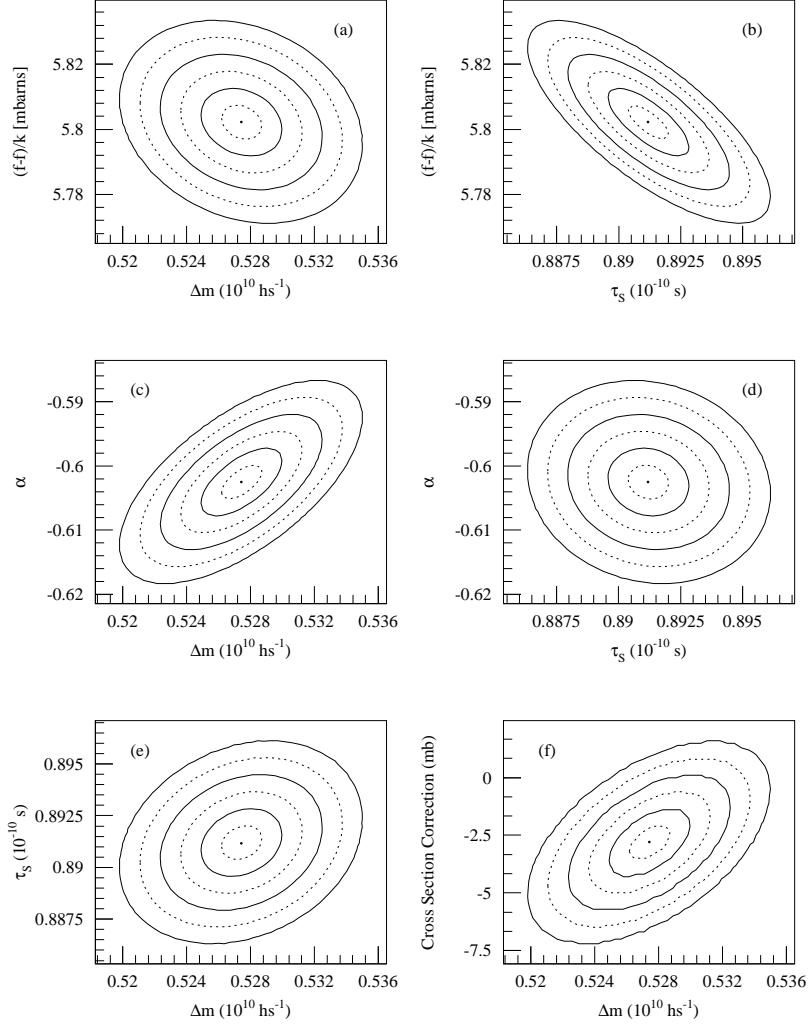
FIG. 101. Contours of equal χ^2 in 1/2 standard deviation intervals in the fit for Δm and τ_S to the $2\pi^0$ data. (a) $\Delta f|_{70}$ versus Δm. (b) $\Delta f|_{70}$ versus τ_S. (c) Power-law slope α versus Δm. (d) Power-law slope α versus τ_S. (e) τ_S versus Δm. (f) Kaon-carbon cross-section correction (at 156 GeV/c) versus Δm.
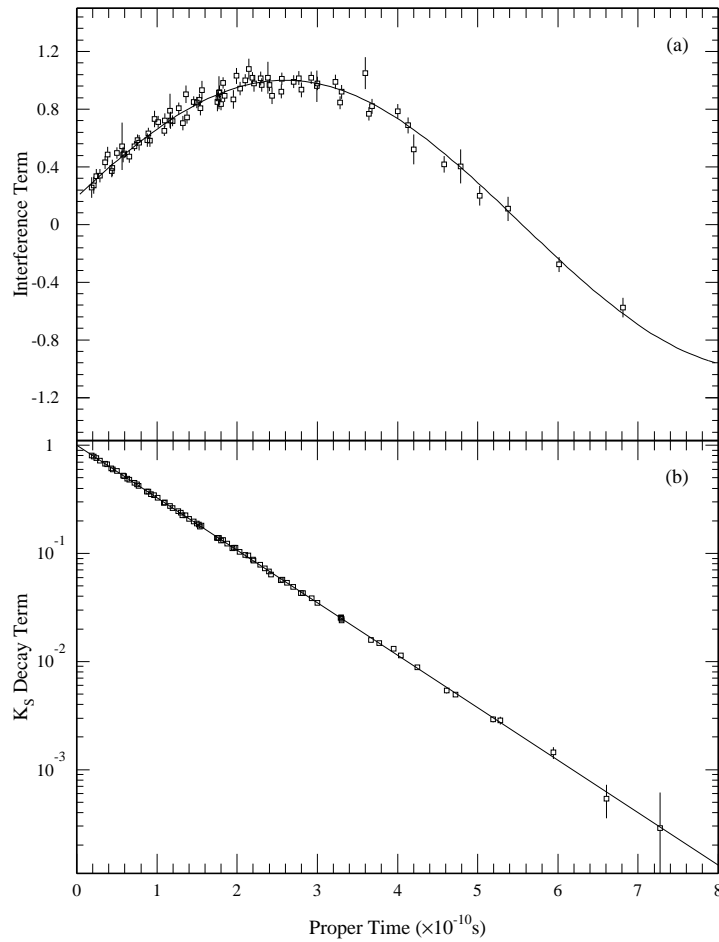
FIG. 102. The interference and K_S decay curves measured for $\pi^+\pi^-$ decays with momentum under 90 GeV/c. (a) The average interference versus the average proper time in 1 m by 10 GeV/c bins. (b) The K_S decay term versus proper time, both measured at the center of the 1 m by 10 GeV/c bin. The Δm and τ_S results from the grand fit to the $\pi^+\pi^-$ data are shown as the curves.
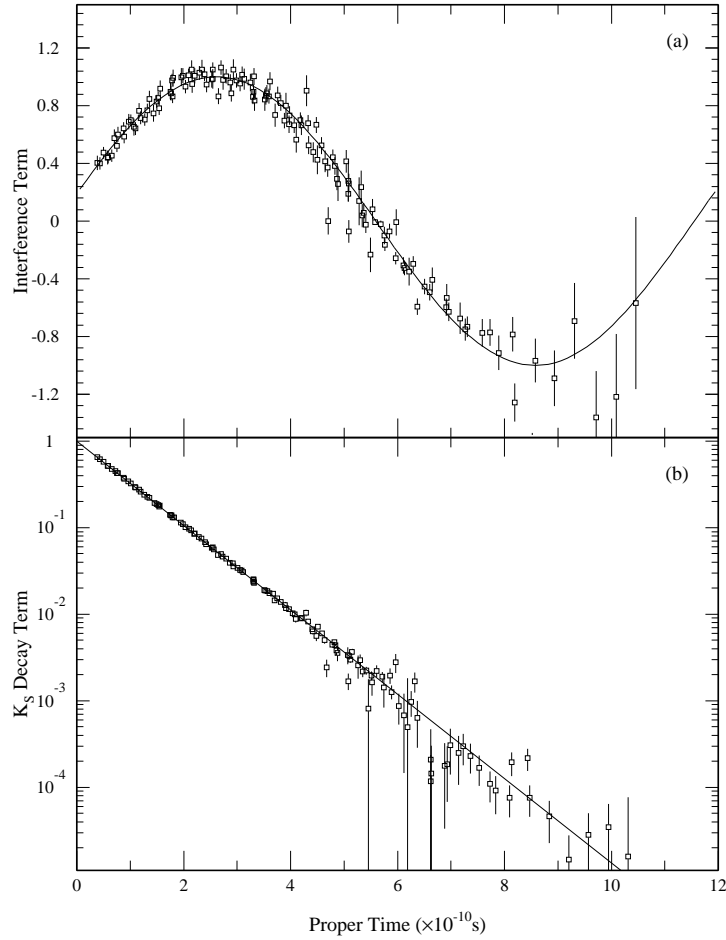
FIG. 103. The interference and K_S decay curves measured for $2\pi^0$ decays with momentum under 90 GeV/c. (a) The average interference versus the average proper time in 1 m by 10 GeV/c bins. (b) The K_S decay term versus proper time, both measured at the center of the 1 m by 10 GeV/c bin. The Δm and τ_s results from the grand fit to the $\pi^+\pi^-$ data are shown as the curves.

TABLE XX. Results of the fits for $\Delta\phi$ and ϕ_{+-}. Numbers in parentheses are the statistical errors to the least significant figure.

fit	$\Delta\phi$	ϕ_{+-}	$Re(\varepsilon'/\varepsilon)$ (10^{-4})	$\Delta f\|_{70}$ (mbarns)	Power α	Δm $(10^{10}\hbar s)$
$\Delta\phi$ (1m bins)	$-1.7° \pm 1.0°$	$44.1° \pm 0.9°$[a]	3.2 ± 6.7	$5.787(7)$	$-0.592(3)$	0.5286[b]
$\Delta\phi$ (2m bins)	$-1.4° \pm 1.0°$	$43.8° \pm 0.9°$[a]	4.7 ± 6.7	$5.785(7)$	$-0.592(3)$	0.5286[b]
ϕ_{+-}	$-1.7° \pm 1.0°$	$42.2° \pm 1.3°$	8.8 ± 6.7	$5.781(9)$	$-0.592(3)$	$0.5257(49)$

---

[a]Correlated with assumed values of Δm and τ_S (see text).

[b]Held constant in this fit.

time $\tau = 0$. The value of the intercept for $\pi^+\pi^-$ ($2\pi^0$) decays is $\cos(\phi_\rho - \phi_{+-(00)})$. The regeneration phase ϕ_ρ cancels when comparing the two modes. To isolate ϕ_{+-}, however, we must use analyticity to obtain the regeneration phase.

In extracting the phases, we make no assumptions regarding either CPT or CP symmetry — $Re(\varepsilon'/\varepsilon)$, $\Delta\phi$ and ϕ_{+-} all float. The z and momentum ranges are the same as those used in the Δm and τ_S fits. In the fit for $\Delta\phi$, Δm and τ_S are fixed to the average values reported in Section IX B. Since we assumed that ϕ_{+-} had its natural value of $\tan^{-1}(2\Delta m/[\Gamma_S - \Gamma_L])$ in obtaining Δm and τ_S, we then should not use those Δm and τ_S values to obtain ϕ_{+-} because of the inherent bias in the assumption of CPT. We set τ_S to the world average of $0.8922 \times 10^{-10}s$ [27] and float Δm in the ϕ_{+-} fits.

We extracted $\Delta\phi$ using different bin sizes. The results are summarized in Table XX. The fits using the 1 m and 2 m bins again show a small shift, and we again average them, obtaining $\Delta\phi = -1.6° \pm 1.0°$. The dependence on Δm and τ_S is given by

$$\Delta\phi = -1.6° \pm \left(190° \frac{\tau_S \times 10^{10}s - 0.8929}{0.8929} \right.$$
$$\left. + 32° \frac{\Delta m \times 10^{-10}\hbar^{-1}s - 0.5286}{0.5286} \right). \tag{96}$$

The results of the fit for ϕ_{+-} with Δm as an additional parameter are also summarized in Table XX. The value of $\Delta m = (0.5257 \pm 0.0049) \times 10^{10}\hbar s^{-1}$ obtained in this fit is consistent with the earlier results.

In both fits, $Re(\varepsilon'/\varepsilon)$ is consistent with the result of the unconstrained fit but since these fits begin downstream of the regenerator, there would be large systematics coming from resolution smearing.

The χ^2 contours of $\Delta\phi$ and ϕ_{+-} versus several of the other parameters are graphed in Figs. 104 and 105, respectively.
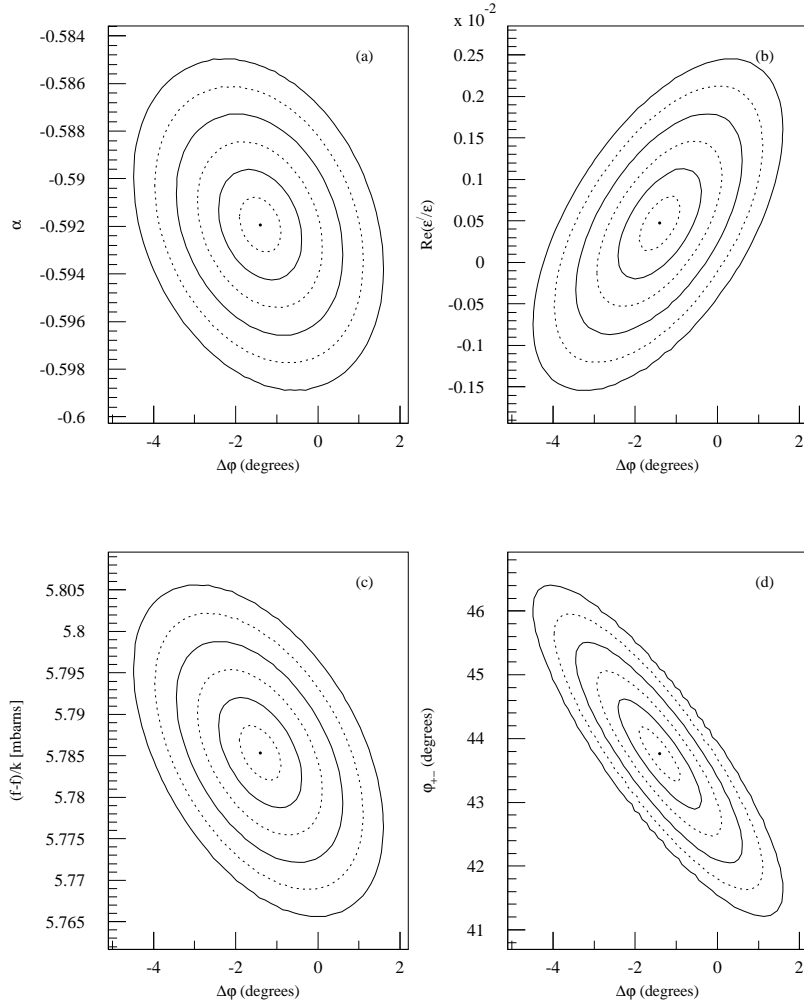
FIG. 104. Contours of equal χ^2 in the fit for $\Delta\phi$ in 1/2 standard deviation intervals. (a) Power-law slope α versus $\Delta\phi$. (b) $Re(\varepsilon'/\varepsilon)$ versus $\Delta\phi$. (c) $\Delta f|_{70}$ versus $\Delta\phi$. (d) ϕ_{+-} versus $\Delta\phi$. The contours are from the fits using a 2 m z binning for the $\pi^+\pi^-$ decays.
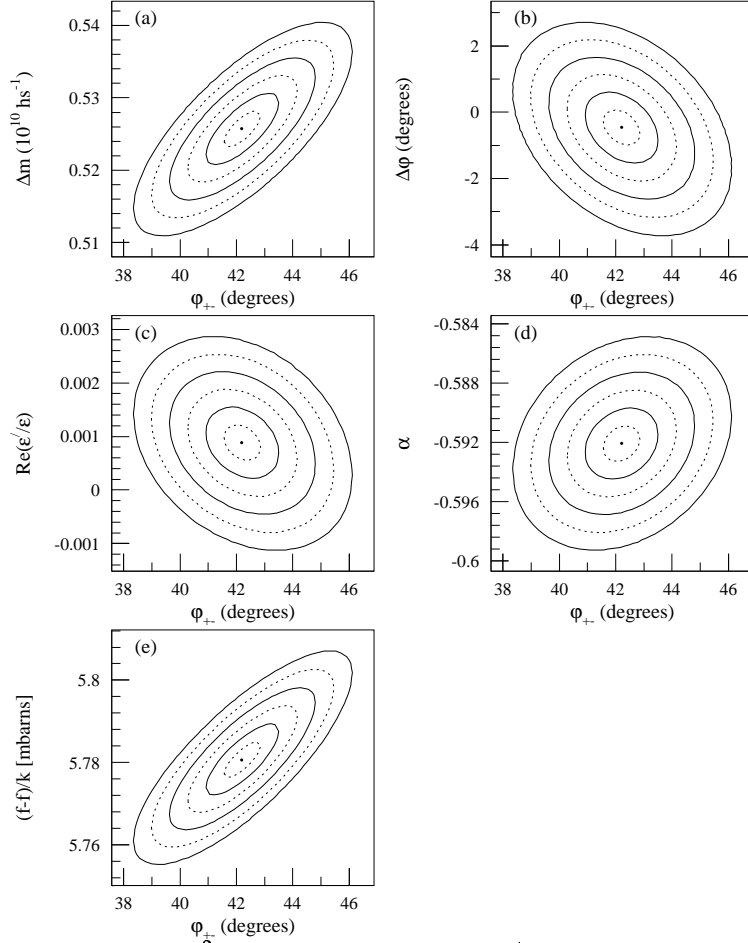
FIG. 105. Contours of equal χ^2 in the fit for ϕ_{+-} in 1/2 standard deviation intervals. (a) Δm versus ϕ_{+-}. (b) $\Delta\phi$ versus ϕ_{+-}. (c) $Re(\varepsilon'/\varepsilon)$ versus ϕ_{+-}. (d) Power-law slope α versus ϕ_{+-}. (e) $\Delta f|_{70}$ versus ϕ_{+-}.

TABLE XXI. The measured regeneration phase and corresponding analyticity predictions in simultaneous fits to the $\pi^+\pi^-$ and $2\pi^0$ data. Numbers in parentheses are the statistical errors to the least significant figure.

Δm $(10^{10}\hbar s^{-1})$	α	ϕ_{pred} (analyticity)	$\phi_{f-\bar{f}}$ (measured)	$\phi_{f-\bar{f}} - \phi_{pred}$
0.5286^a	$-0.5922(25)$	$-126.70° \pm 0.23°$	$-125.92° \pm 0.45°$	$0.78° \pm 0.51°$
0.5351^a	$-0.5912(24)$	$-126.79° \pm 0.23°$	$-127.56° \pm 0.45°$	$-0.77° \pm 0.51°$
$0.5275(47)$	$-0.5925(26)$	$-126.68° \pm 0.23°$	$-125.6° \pm 1.3°$	$1.1° \pm 1.3°$

^{a}Fixed.

1. Analyticity Check

Analyticity, Eq. (91), has been checked before using regenerators of different materials [32,58]. Of course ϕ_{+-} must be taken from elsewhere. The measured regeneration phases agreed with the analyticity prediction Eq. (91) within errors of order 1° to 2° from the measurment of power law slope α.

We extract the regeneration phase $\phi_{f-\bar{f}}$ directly using a technique similar to that used in extracting Δm and τ_s. The regeneration phase becomes an independent parameter of the fit, with Δm and τ_s fixed, and we fit the $\pi^+\pi^-$ and $2\pi^0$ data simultaneously. The fit results using our own value for Δm or the world average Δm are summarized in Table XXI. Using our own Δm, the uncertainty in Δm corresponds to an additional uncertainty in $\phi_{f-\bar{f}}$ of 0.71°. Using the world average, the uncertainty in Δm corresponds to an uncertainty in $\phi_{f-\bar{f}}$ of 0.61°. Adding these in quadrature with the statistical uncertainties on α and $\phi_{f-\bar{f}}$, the predicted and measured phases agree to within an uncertainty of 0.9°. With Δm floating, the phases agree within 1.3°.

The regenerator used in reference [58] was carbon, and we expect it and boron carbide to have similar power-laws. The regeneration phase in that experiment was $-124.7° \pm 1.7°$, in good agreement with the values shown in Table XXI.

D. Summary of the Fit Results

The results of the physics measurements of interest, with statistical errors only, are given below:

$$Re(\varepsilon'/\varepsilon) = (7.4 \pm 5.2) \times 10^{-4}$$
$$\Delta m_{+-} = (0.5311 \pm 0.0044) \times 10^{10}\hbar s^{-1}$$
$$\tau_{s_{+-}} = (0.8952 \pm 0.0015) \times 10^{-10}s$$
$$\Delta m_{00} = (0.5274 \pm 0.0030) \times 10^{10}\hbar s^{-1}$$
$$\tau_{s_{00}} = (0.8912 \pm 0.0017) \times 10^{-10}s$$
$$\Delta\phi = -1.6° \pm 1.0°$$
$$\phi_{+-} = 42.2° \pm 1.3°$$

The next section presents the systematic uncertainties, with a focus on $Re(\varepsilon'/\varepsilon)$.

X. SYSTEMATICS

There are five major issues which affect this measurement of $Re(\varepsilon'/\varepsilon)$: the neutral mode energy reconstruction, detector acceptance, the treatment of the HDRA material, accidental biases and assumptions in the fitting procedure. The uncertainty in the energy reconstruction dominates. After presenting some general consistency checks we then treat each of the five issues.

A. Consistency Checks

The variation of $Re(\varepsilon'/\varepsilon)$ when kinematic cuts are changed or when different data sets are fit should be consistent with the expected statistical fluctuation; significant departures could point to unresolved problems in the background subtraction, photon energy reconstruction, etc.

Over a thousand different fits have been performed, checking for any inconsistency in the fitting routine, between data subsets, between different fiducial regions, between different analysis cuts, and with various defects embedded into the Monte Carlo. The most important checks are presented here.

The results of the more important studies are summarized in Table XXII, grouped into two categories. The first comprises studies changing characteristics of the fit for $Re(\varepsilon'/\varepsilon)$. The second consists of studies changing kinematic or event quality cuts. The latter were computationally intensive, as they require a reanalysis of the final data, signal Monte Carlo and background Monte Carlo event samples, totalling over 3.6×10^7 events in the neutral sample alone.

1. Varying the Fitting Technique and Fiducial Cuts

We have changed the binning for the $2\pi^0$ data, using 3 m in z rather than 42 m. The events upstream of the regenerator position can no longer be used; this statistical loss, combined with different weighting of the events, can lead to a sizable shift in the result. This was estimated with 10 different Monte Carlo samples the same size as the data statistics; it was found to be $(2.21 \pm 0.49) \times 10^{-4}$. The observed shift of -2.48×10^{-4} is then consistent with expectations.

If we limit the momentum range to 150 GeV/c, we reduce the size of the primary K_S correction (Section VIII B) from -0.62% (-0.07%) in the charged (neutral) vacuum beam to -0.33% (-0.04%). The corresponding shift in the result is consistent with arising from the small loss of statistics.

We have also restricted the neutral z range to match that of the charged mode; this has several small systematic advantages. For example, the dependence of $Re(\varepsilon'/\varepsilon)$ on the K_L lifetime (see Table XVIII) virtually disappears, and there is more cancellation of the primary K_S corrections between the two decay modes. In the neutral mode, the momentum distributions in the two beams match even more closely than with our standard $2\pi^0$ z cut so that the mass distributions match almost exactly. In turn, $Re(\varepsilon'/\varepsilon)$ becomes less sensitive to the mass cut when there are residual nonlinearities in the photon energy. Finally, this z

range is upstream of the HDRA and the photon conversion probability now cancels in the neutral ratio.

We use the larger decay volume, however, because these small systematic advantages are heavily outweighed by the doubling of the vacuum beam statistics. Furthermore, the "crossover" background from inelastic kaon scattering in the regenerator beam is reduced by a factor of two relative to the vacuum signal.

When we restrict the size of the neutral decay volume, the shift in $Re(\varepsilon'/\varepsilon)$ is $+0.42 \times 10^{-4}$, within the expected range from the change in statistics. This result is 1.8×10^{-4} higher than our preliminary result for $Re(\varepsilon'/\varepsilon)$ presented in 1991 [59] with the same fiducial regions. That shift is dominated by the increase in Monte Carlo statistics for determining the acceptance. The statistical uncertainty in the older, smaller Monte Carlo sample corresponded to a one standard deviation uncertainty of 1.9×10^{-4} in $Re(\varepsilon'/\varepsilon)$.

The final check involving a change in the fitting procedure, by relaxing the assumption of analyticity to obtain the regeneration phase. Instead, the regeneration phase was set to the previously measured phase for carbon (see Section IX C 1). The shift of -0.22×10^{-4}, was expected, given the dependence of $Re(\varepsilon'/\varepsilon)$ on the phase (Table XVIII).

2. Trial Analysis cuts

The stability of $Re(\varepsilon'/\varepsilon)$ under changes in the background subtraction is probed here. Some of the differences between data and the Monte Carlo simulation are also relevant.

For the first study, we have relaxed the ring number cut from 112 to 128. This increases the noncoherent kaon background (see Fig. 44) by 12.6% (13.3%) in the vacuum (regenerator) beam; while the signal increases by only 1.2% (1.3%).

There are other important issues related to this cut. As the plots of the background subtracted ring number distributions in Fig. 106 show, the regenerator beam is overall marginally wider than the vacuum beam because of kaons scattering in the shadow absorber. In the bottom beam, the broadening of the vacuum beyond the regenerator beam at high ring number is due to kaons which scatter in the common absorber. This is the tail of kaons that can miss the regenerator when it is in the lower beam — the "sneakby" kaons discussed in the Section VIII. Since the regenerator beam $\pi\pi$ samples are dominated by regenerated K_S decays, this beam tail is suppressed by a factor of $|\rho/\eta|^2$ (ie, by 100 to 200). There is no such suppression of this tail in the vacuum beam; the Monte Carlo mimics this small effect well.

With the looser ring number cut, we probe the region where the regenerator and vacuum beam shapes deviate. Since the Monte Carlo reproduces this deviation, we do not expect to observe any significant bias. We observe a change in $Re(\varepsilon'/\varepsilon)$ of 0.46×10^{-4}, consistent with statistics.

If we turn now to studies with different $2\pi^0$ mass cuts, we do not expect as clean a situation because of the residual nonlinearities which shift $2\pi^0$ mass distributions of data relative to Monte Carlo. Since we collect the K_S and K_L decays simultaneously, the resolutions for the two samples are very close, as shown in Fig. 107. However, the vacuum beam $2\pi^0$ mass is somewhat wider than the regenerator beam, this is from the contribution of the lower energy kaons in the vacuum beam downstream of the HDRA.

160
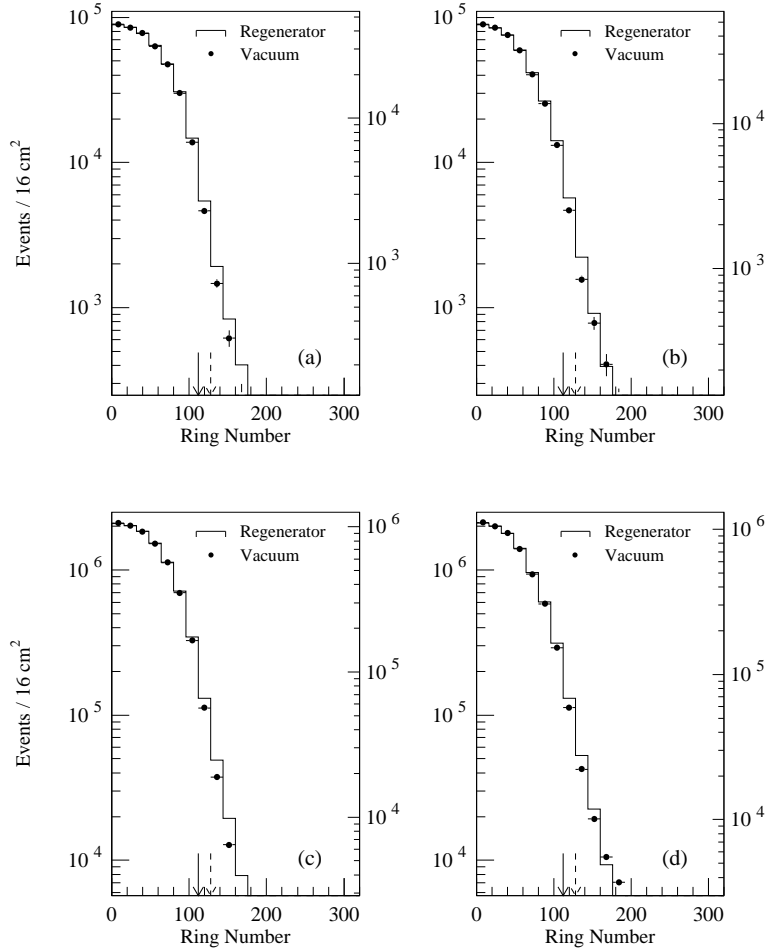
FIG. 106. Regenerator beam and vacuum beam ring-number distributions in the top and bottom beams for the background-subtracted $2\pi^0$ data sample and the coherent Monte Carlo sample. In all plots, the histogram shows the distribution for the regenerator beam (left scale) and the dots show the distribution for the vacuum beam. The solid arrow indicates the cut for the standard analysis, while the dashed arrow indicates the looser cut used in the systematic study. (a) Data, top beam. (b) Data, bottom beam. (c) Monte Carlo, top beam. (d) Monte Carlo, bottom beam.

TABLE XXII. Shifts in $Re(\varepsilon'/\varepsilon)$ for changes in the fitting technique and for changes in the fiducial cuts. For the studies involving the change of a cut, the "allowed" shifts are the one standard deviation shifts expected from the change in statistics alone. For a change in methodology, the shift was predicted using Monte Carlo studies. The shift observed with the mass cut is discussed in the text.

Analysis Change or Fit Modification	$\Delta Re(\varepsilon'/\varepsilon)$ $(\times 10^{-4})$	"Allowed" Shift
Bin $2\pi^0$ data in 3 m $\times$ 10 GeV/c pz bins	-2.48	2.21
Reduce Momentum range to $40-150$ GeV/c	$+0.21$	0.27
Reduce Neutral z range to $110-137$ m	$+0.42$	2.65
Relax analyticity assumption	-0.22	—
Loosen Ring Cut from 112 to 128	$+0.46$	0.47
Tighten Mass cut from ±24 MeV/c^2 to ±18 MeV/c^2	$+1.28$	0.32
Loosen Mass cut from ±24 MeV/c^2 to ±28 MeV/c^2	-0.30	0.19
Loosen charged mode cuts	-0.25	1.01
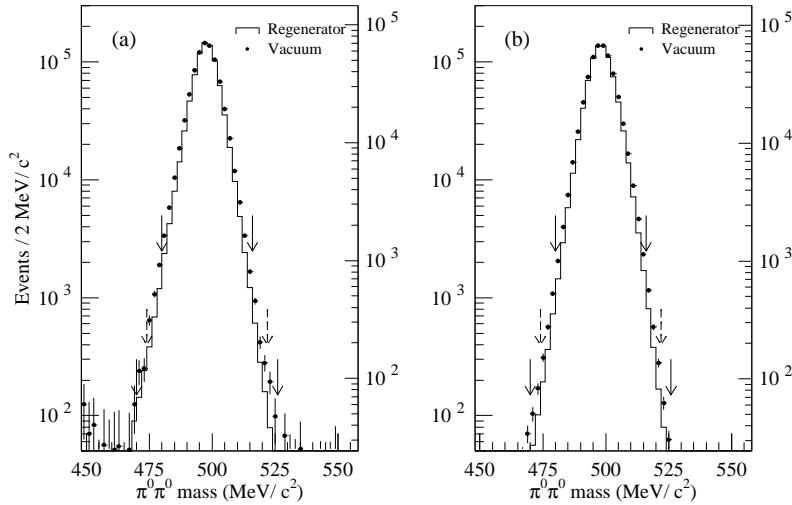
FIG. 107. Overlay of the vacuum and regenerator beam mass distributions for the total $2\pi^0$ data sample. (a) Background subtracted data. (b) Coherent Monte Carlo. The full Monte Carlo sample is plotted, but it has been scaled to the same total area is the data. For both data and Monte Carlo, the histogram is the regenerator beam distribution (left-hand scale), and the dots show the vacuum beam distribution (right-hand). The innermost and outermost pair of arrows indicate the mass cuts used in two of the systematic studies. The dashed pair of arrows show the standard mass cut.

With our standard mass cut of (498 ± 24) MeV/c^2, the number of signal events is small at the cut position. If we tighten the cut to (498 ± 18) MeV/c^2, the signal size increases by an order of magnitude at the cut boundary. The expected bias due to $2\pi^0$ mass shift and tighter mass cut is of the order of $+0.8 \times 10^{-4}$. When we reanalyze with this tighter mass cut, we observe a shift of $+1.28 \times 10^{-4}$. The change in statistics allows a fluctuation of 0.32×10^{-4} so that the observed shift is consistent with expectations.

When we broaden the mass cut, we increase the background, particularly in the vacuum beam (see Figs. 51 and 52). For example, with a mass cut of (498 ± 28) MeV/c^2 in Fig. 107, the $2\pi^0$ vacuum event total increases by 200 while the $3\pi^0$ and beam interaction backgrounds increase by 1800. The allowed statistical fluctuations are dominated by the new background events, though there is a small contribution from the signal statistics. A statistical fluctuation of 0.19×10^{-4} is expected where we observed a -0.30×10^{-4} shift. The errors assigned for either the background subtraction or the residual nonlinearity are more than adequate to account for this shift.

As a final check of the sensitivity of $Re(\varepsilon'/\varepsilon)$ to the analysis cuts, we made the track quality cuts and E/p cut significantly looser. The cut on the track χ^2 was increased from 30 to 100. This quantity (Fig. 27) has a δ-ray tail in the data but we expect this to cancel in the single charged ratio.

Cuts on the segment matching at the magnet (Fig. 28) and the distance of closest approach (Fig. 29) were loosened by a factor of two. The E/p cut was relaxed from 0.80 to 0.84, increasing the semileptonic background in the K_L beam by 25%. The new backgrounds levels were determined using the procedure described in Section V B.

The change in statistics with these relaxed cuts was 8% in each beam, dominated by the relaxation of the χ^2 cut. A one standard deviation statistical fluctuation would be 1.01×10^{-4} and we observe 0.25×10^{-4}.

B. Some Benefits of the Double Beam Technique

Collecting K_S and K_L decays simultaneously from nearly identical beams results in cancellation of many of the effects of the detector. This section examines two studies where the benefits of simultaneously collecting K_S and K_L decays to a particular final state are very apparent. The results of the fits used in these studies are summarized in Table XXIII.

1. Inefficiencies and Cluster Energy Study

In the first of these studies, we introduced a 10% inefficiency into the Monte Carlo response of two of the B-hodoscope counters which form a vertical stripe near the center of the beam; and four drift chamber wires were assigned zero efficiency. Because of the different z distributions, the illuminations of the doctored counters and wires by decays from the vacuum and regenerator beams are not identical. However, when we use the doctored Monte Carlo for the acceptance corrections, $Re(\varepsilon'/\varepsilon)$ is shifted by only -1.5×10^{-4}.

This situation is certainly artificial. The counter efficiencies were determined with muons and the wire efficiencies with the K_{e3} sample at the sub-percent level. Such efficiency mismatches are also obvious, as shown in Fig. 108.

TABLE XXIII. Shifts in $Re(\varepsilon'/\varepsilon)$ for studies demonstrating the stability of $Re(\varepsilon'/\varepsilon)$ due to the simultaneous collection of K_S and K_L decays.

Study	$\Delta Re(\varepsilon'/\varepsilon)$ $(\times 10^{-4})$	"Allowed" Shift
Introduce 90% efficiency into 2 B bank trigger counters, and 0% efficiency into 4 drift chamber wires, in the $\pi^+\pi^-$ Monte Carlo simulation	-1.50	—
Loosen maximum photon energy cut in $2\pi^0$ analysis from 60 GeV to 90 GeV	$+2.00$	1.16
Loosen maximum photon energy cut in $2\pi^0$ analysis from 90 GeV to 120 GeV	$+0.10$	0.27
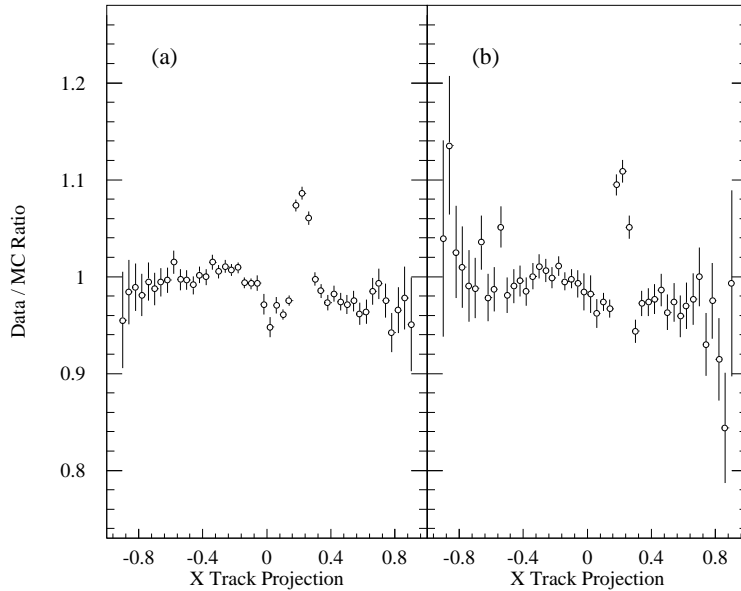
FIG. 108. Ratio of the data and Monte Carlo track-illumination at the lead-glass when a 10% inefficiency is introduced into the response of two of the B hodoscope counters in the Monte Carlo. The two counters form a vertical stripe in the hodoscope bank. The data and Monte Carlo simulation are from the $\pi^+\pi^-$ subset C4. (a) Regenerator beam ratio. (b) Vacuum beam ratio. Additional structure in the plots is due to the left-right $\pi^+\pi^-$ trigger requirement coupled with the inefficiency.
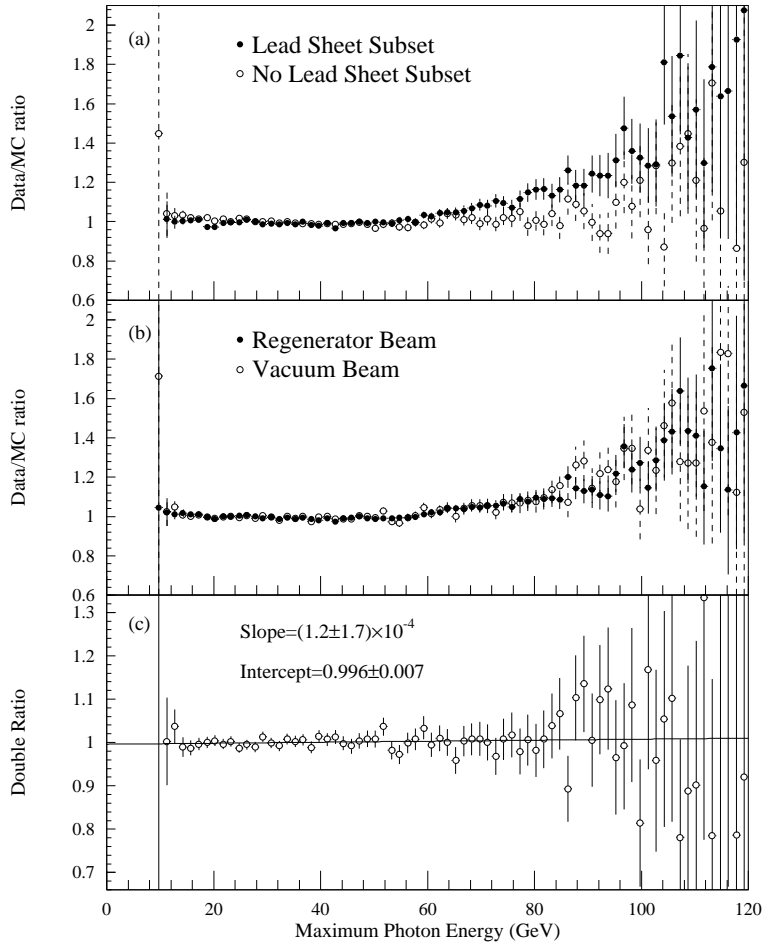
FIG. 109. Ratio of the data and Monte Carlo maximum cluster-energy distribution in $2\pi^0$ decays. The predicted background contribution has been included in the Monte Carlo distribution. (a) The ratio for decays in the regenerator beam for the early $2\pi^0$ subsets with the lead sheet (solid circles) and the later sets without the sheet (open circles). (b) The ratios for the total $2\pi^0$ data set in the regenerator beam (solid circles) and vacuum beam (open circles). (c) The ratio of the two ratios in (b). The best fit line to the double ratio has been superimposed.

The next study probes the one issue which is not fully resolved — the loss of high energy clusters in the Monte Carlo simulation that is not observed in the data. This problem is discussed previously in Section VII D 1. The disagreement is limited mainly to the 24 blocks surrounding the beam pipes, though there is a hint of the problem in the next ring of blocks. The pipe blocks are the blocks most seriously affected by radiation damage in the high intensity runs.

The time dependence is apparent in the maximum cluster-energy distributions for the $2\pi^0$ subsets with and without the lead sheet, as shown in Fig. 109a. The lead sheet subset was collected in the earlier high intensity runs. Most of the data collection for the subset without the lead sheet occurred in the later lower intensity runs after a long shutdown during which the calorimeter underwent a long cure.

However, each beam is affected identically. The ratios of data to Monte Carlo maximum cluster-energy distributions for the entire data set are similar for the two beams (Fig. 109b),

165

and the bias as a function of energy disappears in the ratio of ratios (Fig. 109c). The latter ratio is what affects our experiment, and would not have been flat had we not collected the K_S and K_L decays simultaneously.

Since we accept only events where data and Monte Carlo agree, we are not significantly affected by the problem. To gauge the effect, however, we have relaxed the cut on the maximum cluster-energy from 60 GeV to 90 GeV and 120 GeV, where the mismatch is much more severe. There is again a sizable change in the sample sizes, which allow fluctuations in $Re(\varepsilon'/\varepsilon)$ at the level of 1.2×10^{-4}. The observed shift is $+1.7$ standard deviations, in the direction expected from such a bias.

Since the time this data was published, the source of the cluster-energy mismatch problem was discovered, in the course of the analysis of Fermilab experiment E773 [60]. It was due to the application of cluster fusion cut in Monte-Carlo acceptance simulation without accidental overlay in E731. Since only high energy cluster with large enough leakage outside a 3×3 cluster could fail this cut in Monte-Carlo and for data events accidental activity would fail this cut for lower energy cluster, a mismatch in the cluster energy spectrum was introduced. The higher the intensity of the data subset, the larger the mismatch as shown in Fig. 109a. No bias in the results of E731 would be expected because of this mismatch, as seen in Fig. 109c.

2. Time Dependence – Individual Subsets

For the final topic of this section on systematic studies, we turn to a useful property of our technique which allows us to check both time and intensity dependences. Since the same regenerator is used throughout the experiment, we should measure a consistent regeneration amplitude in each data subset of each decay mode.

The subsets span a range of configurations. Intensities vary by a factor of three between subsets (see Table IV), the lead sheet is only present in some $2\pi^0$ subsets, and radiation damage in the array varies substantially. Note that the average nonlinearities measured in the pipe blocks in different subsets vary up to 40%. In spite of these very different conditions, the regeneration amplitudes measured in each subset agree well, as shown in Fig. 110, within each decay mode.

The systematic studies on time dependence give confidence in the stability of the result. In most tests, the observed shifts in $Re(\varepsilon'/\varepsilon)$ are consistent with expected statistical fluctuations. In the cases where there may be shifts beyond statistics, a regime affected by known problems was purposely entered, and the shifts are compatible with the expected behavior. The following sections describes the methods used to limit the systematic uncertainty on $Re(\varepsilon'/\varepsilon)$ and the other measurements.

C. Neutral Energy Reconstruction

The photon energy reconstruction in the $2\pi^0$ decay has several potential biases. For example, the lead-glass energy resolution yields a z resolution of about 1 m, and a resolution mismatch betwen data and Monte Carlo could bias the acceptance. We investigate the systematic effects from both linear and nonlinear biases in the energy reconstruction.
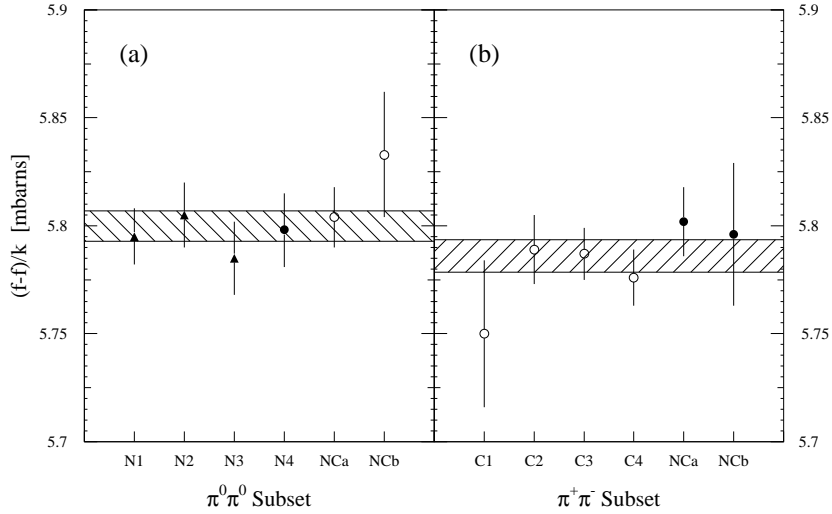
166

FIG. 110. The regeneration amplitude measured in individual data subsets. The $2\pi^0$ measurements are plotted in part (a) and the $\pi^+\pi^-$ measurements in part (b). The one standard deviation bands from the fits to the entire $2\pi^0$ or $\pi^+\pi^-$ sample described in Section IX A have been plotted as well. The highest (lowest) intensity data for each mode is plotted with solid (hollow) points. In part (a), the subsets with (without) the lead sheet are indicated by triangles (circles). Small accidental corrections (see Sections IX A 1 and X H) have been made.

1. Resolution

We would be most sensitive to the resolution if we began our z fiducial region just upstream of the regenerator where events smearing upstream are not compensated by ones smearing downstream. For both our previous result [18] and this result, the upstream z cut completely contained the (smeared) regenerator edge. At the downstream end of the fiducial z region, the event distribution does not change rapidly in either beam so that the smearing of events upstream and downstream of the cut tends to cancel.

We have introduced additional smearing in the reconstructed photon energy to study possible resolution systematics. The $2\pi^0$ z distribution in Fig. 111 with 2% additional smearing shows a glaring mismatch between the data and the standard Monte Carlo. However, refitting for $Re(\varepsilon'/\varepsilon)$ using the smeared data and standard acceptance corrections yields a shift of only 1.5×10^{-4}. By studying this distribution, we limit the resolution mismatch to 0.5% which yields a shift of 0.36×10^{-4}.

For the constrained fits, the choice to begin the fiducial range in z downstream of the regenerator (Section IX B) gives relative insensitivity to resolution effects. A 0.5% smearing gives 0.0004×10^{10} $\hbar s^{-1}$ uncertainty in Δm and 0.0003×10^{-10} s to τ_S in the $2\pi^0$ data, and less than $0.01°$ in $\Delta\phi$.

2. Energy Scale and Nonlinearity

Large effort has gone into the refinement of calibration and simulation of the lead glass calorimeter. This is because a bias in the photon energy scale moves events past both the energy and z fiducial boundaries. The electron response in K_{e3} decays and the photon response
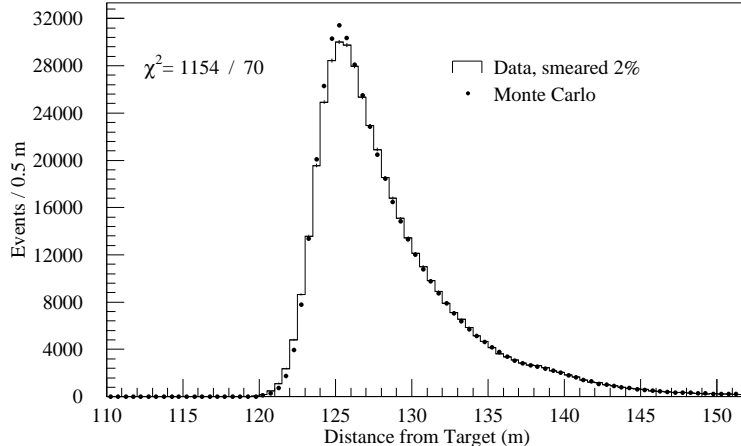
167

FIG. 111. The z-location of $2\pi^0$ decays in the regenerator beam for the data and the Monte Carlo simulation after the photon energies in the data were smeared by an additional 2%. Only the subset with the lead sheet is shown here.

TABLE XXIV. Shift in $Re(\varepsilon'/\varepsilon)$ induced by some of the systematic biases introduced into the photon energy reconstruction procedure. The resolution bias was discussed in the previous section.

Reconstruction bias	$|\Delta Re(\varepsilon'/\varepsilon)|$ $(\times 10^{-4})$
0.5% energy smearing	0.36
0.03% average energy scale change	0.93
$\quad$ $(\Delta E = 3 \times 10^{-4}E)$	
Quadratic energy scale change	1.57
$\quad$ $(\Delta E = qE^2)$	
"Pedestal" shift (20 MeV per cluster)	0.46

in $\pi^+\pi^-\pi^0$ decays are mimicked well by the Monte Carlo (see Section VII D 1); nevertheless shifts in the reconstructed $2\pi^0$ mass (see Table VIII) imply residual nonlinearities in the reconstructed photon energy. This section evaluates the sensitivity to the energy scale.

Results from some of the studies related to the photon energy scale are summarized in Table XXIV. Most followed the same procedure. A bias was introduced into the reconstruction of photons in the data, while that in the Monte Carlo was unmodified. The regenerator edge in the biased data was rematched to the regenerator edge in the Monte Carlo (see Section VI D) as a function of kaon energy, giving a new energy scale correction. The data was then analyzed a second time with both the bias and the new compensating scale correction. We finally fit the reanalyzed data to determine the effect on $Re(\varepsilon'/\varepsilon)$.

When an average energy scale bias of 0.03% was introduced, we did not rematch the edge since this would fully compensate for this bias. The 0.03% scale change resulted in a shift of 0.93×10^{-4}. However, the most troublesome effects come from nonlinear biases in the reconstruction.

When we introduced nonlinear biases into the photon reconstruction, we indeed found that the z edge matching did not completely compensate. To study pedestal shifts, we

168

uniformly shifted the energy of every cluster by 20 MeV, which resulted in a shift in $Re(\varepsilon'/\varepsilon)$ of 0.46×10^{-4}. We have measured pedestal shifts using data with no minimum readout threshold, and determined them in $3\pi^0$ data with a threshold by a study of the invariant mass vs. cluster energy. The pedestals measured with these two techniques agreed well, giving confidence in the pedestals measured using the $3\pi^0$ decays in data sets with a readout threshold. Typical pedestal shifts were of the order of 40 to 50 MeV per cluster, and these could be determined to 10 MeV or better. Corrections for the shifts are applied in the standard analysis.

To estimate the effect of remaining nonlinearities, we introduced a quadratic correction to the cluster energy, $E \to (1 + qE)E$. The value of q was chosen to shift the mean $2\pi^0$ mass in the data to match the Monte Carlo. Typical values of q were 0.00035 (slightly higher for events with pipe block clusters).

After reanalyzing the data with the quadratic biases applied, $Re(\varepsilon'/\varepsilon)$ shifted by -1.57×10^{-4}. While the mean mass is correct, the shape is distorted with large asymmetries appearing. We believe that a distortion as severe as the quadratic bias applied is not favored by the data. However, we take the full shift as an estimate of the residual bias in the energy reconstruction.

Combining the nonlinear bias with the bias from smearing, we have a total systematic contribution from photon energy reconstruction of 1.61×10^{-4}. This is the largest systematic contribution to $Re(\varepsilon'/\varepsilon)$.

The cluster energy reconstruction uncertainties also dominate the systematic uncertainty in the other measurements which use the $2\pi^0$ sample. We have contributions of 0.0012×10^{-10} s in τ_S; 0.0014×10^{10} $\hbar s^{-1}$ in Δm; and $0.52°$ in $\Delta\phi$.

D. Acceptance

1. Acceptance Biases and $Re(\varepsilon'/\varepsilon)$

As discussed in Section VII, the acceptance is largely governed by a few limiting apertures. The active mask and the collar anticounter were the most important since there was a significant rate at their boundaries. The lead glass, trigger counters (T and V) and other outer edges had low enough illuminations to make $Re(\varepsilon'/\varepsilon)$ insensitive to their precise sizes and locations. For example, if one decreases the radius of the vacuum window by 1 mm, the single ratios change by less than 0.001%. The same is true if the lead glass edge were smaller by 1 mm.

Most important is the average effective size of an aperture rather than its exact placement. To keep the systematic uncertainty in $Re(\varepsilon'/\varepsilon)$ from the acceptance correction within the 10^{-4} level requires knowing the average effective size of the apertures at the level of 200μm or better. The effective size of the apertures was determined directly with electrons from K_{e3} decays (Section VII C 3) to compensate for counter thickness, small dead regions, etc. Our systematic estimate on the position of each edge was 50μm, so the average aperture size is measured at the 70μm level, well under the limit we wished to achieve. Size changes due to thermal expansion are well within this systematic estimate.

The value of $Re(\varepsilon'/\varepsilon)$ is less sensitive to an aperture offset since the loss on one side is largely compensated by the gain on the other. However, if the aperture is too large (small)

TABLE XXV. Change in the single ratios and in $Re(\varepsilon'/\varepsilon)$ when the size of a limiting aperture is changed in the Monte Carlo. ΔR_{00} and ΔR_{+-} are the changes in the vacuum to regenerator beam ratios in the charged and neutral mode samples. In each case, the size of the apertures in the x and y were simultaneously changed by 70μm in order to maximize the effect.

Aperture adjustment	ΔR_{00} (percent)	ΔR_{+-} (percent)	$|\Delta Re(\varepsilon'/\varepsilon)|$ ($\times 10^{-4}$)
Change Mask Size by 70 μm	-0.013	-0.014	0.02
Change HDRA size by 70 μm	-0.002	negligible	0.03
Change CA size by 70 μm	-0.021	negligible	0.35

in the Monte Carlo, we over estimate (under estimate) the acceptance.

There is an uncertainty in projecting tracks back to the aperture due to chamber misalignment. In addition, there is uncertainty in the chamber positions relative to the production target and calorimeter. The latter is at the 10 to 20μm level (see Section IV). Since we track the relative locations of two chambers to 10μm, the systematic uncertainty in the track projection is 60μm at the mask, 35μm at the HDRA, and 15μm at the collar anti. These uncertainties, as well as those from thermal expansion of the vacuum pipe stands, are within an uncertainty of approximately 70μm.

We have estimated the effects of the aperture sizes and positions by noting the event gain/loss when the aperture edges in the Monte Carlo are adjusted. Table XXV outlines the effect on $Re(\varepsilon'/\varepsilon)$ for the most important of these studies. We note that $Re(\varepsilon'/\varepsilon)$ is insensitive, for example, to the size of the mask, which affects only the vacuum beam, but has similar effects on $\pi^+\pi^-$ and $2\pi^0$ acceptances. In the end, the result was most sensitive to the size of the collar anti, where a simultaneous decrease (or increase) of both the x and y sizes by 70μm induced a shift of order 0.3×10^{-4} in $Re(\varepsilon'/\varepsilon)$.

Regarding aperture positions, the biggest change occurred when the mask was shifted in neutral mode. For a 1 mm shift, however, the bias was only 0.1×10^{-4}. A shift of this size would have been clearly observable (see Fig. 62).

Apertures do not solely determine the acceptance. Energy thresholds, the minimal separation of two tracks or two clusters, detector resolutions, etc., all have relevance to the acceptance.

To estimate the systematic error from the acceptance, we turn to the high statistics vacuum samples of $K_L \to 3\pi^0$ and $K_L \to \pi e\nu$ which we use to limit an acceptance bias as a function of z, to which the $Re(\varepsilon'/\varepsilon)$ measurement is most sensitive. As with the $\pi\pi$ decay modes (Section VII), we have checked the track and cluster aperture illuminations, track and cluster separations, etc., in the Monte Carlo relative to the data, with no surprises.

For the charged mode, we have spot checked the z acceptance with K_{e3} subsets, with results similar to that shown in Fig. 85. As we discussed in Section VII, we have limited the bias in acceptance for the $\pi^+\pi^-$ mode by determining the slope in the ratio of the z distributions for data and Monte Carlo. We refer to this slope as the "acceptance bias" for the remainder of this discussion. In the charged mode, we used a fraction of the K_{e3} statistics to limit the acceptance bias to 0.03% per meter; this induces a shift of 0.65×10^{-4}

in $Re(\varepsilon'/\varepsilon)$.

The longer neutral decay region and mean separation between K_S and K_L decays makes the neutral mode much more sensitive to a z bias. To limit the acceptance bias we have used the full sample of $3\pi^0$ decays. The lower average photon energy for $3\pi^0$ decays means a greater illumination at the detector edges than for $2\pi^0$. Also six photons probes the photon identification in the lead glass better than four. Thus the use of the $3\pi^0$ sample should be conservative.

We find an acceptance bias of less than 0.007% per meter (Fig. 86). (The uncertainty introduced by the lead sheet is evaluated later (Section X E)). This shifts $Re(\varepsilon'/\varepsilon)$ by 1.00×10^{-4}.

Combining the charged and neutral mode values, we have a total acceptance uncertainty on $Re(\varepsilon'/\varepsilon)$ of 1.19×10^{-4}.

2. Acceptance Biases and the Constrained Fit Results

Because the acceptance bias is strictly limited by the $3\pi^0$ sample, the uncertainty in the constrained fit results which use the $2\pi^0$ sample is small. For the neutral Δm measurement, there is a 0.0001×10^{10} $\hbar s^{-1}$ contribution, and for the neutral τ_S measurement, 0.0002×10^{-10} s. These include uncertainties from accidental affects (see Section X H). The effect on $\Delta\phi$ is negligible.

Because the acceptance was not as crucial for $Re(\varepsilon'/\varepsilon)$ in the charged mode as it was in the neutral mode, we did not push as hard on limiting the acceptance bias as was possible with the K_{e3} sample. One unfortunate side effect of this is a large contribution to the systematic uncertainty in the results from the constrained fits using the $\pi^+\pi^-$ sample. For the Δm and τ_S measurements in the $\pi^+\pi^-$ sample, we have systematic contributions of 0.0009×10^{10} $\hbar s^{-1}$ and 0.0020×10^{-10} s. These include contributions from the shifting of the results as the z bin size was varied. Similar studies for $\Delta\phi$ and ϕ_{+-} give $0.35°$ for the systematic error on each.

3. Regenerator Anticounters

One acceptance detail which affects only the measurement of $Re(\varepsilon'/\varepsilon)$ is the location of the last regenerator anticounter relative to the regenerator. The anticounter introduces a small asymmetry between the $\pi^+\pi^-$ and $2\pi^0$ decay modes since $\pi^+\pi^-$ decays upstream of (and inside of) the anticounter are vetoed. The uncertainty in the number of decays vetoed by this anticounter depends on its position relative to the regenerator. From direct measurements, we know this distance to about 1.2 mm. This geometrical uncertainty corresponds to a systematic error of 0.59×10^{-4} in $Re(\varepsilon'/\varepsilon)$.

E. HDRA and Regenerator Lead Piece

The thickness of the materials in the HDRA and the regeneration amplitudes are not perfectly known. To account for systematic uncertainty, the background level, acceptance,

etc. are modified simultaneously for a given change in material thickness or regeneration amplitude.

1. Contribution of the HDRA to the Systematic Uncertainty on $Re(\varepsilon'/\varepsilon)$

The regeneration amplitudes from lead and carbon have been measured at the 1.4% level [47,48,50]. The regeneration amplitudes for oxygen and nitrogen were scaled from that of carbon (also scaled to the modern value for η_{+-}) using the measured A-dependence [50] of the regeneration amplitude. When the regeneration amplitude for lead (carbon) was varied within the uncertainty given above, the shift in $Re(\varepsilon'/\varepsilon)$ observed was 0.31×10^{-4} (0.15×10^{-4}); these are dominated by the change in the diffractive background.

Chemical analysis shows the sheet to have been 99.9793% pure, with bismuth as the dominant impurity [61]. When we varied the lead regeneration parameters, the contribution to the regenerator beam rate from the lead in the regenerator was treated simultaneously; however, its effect was less than 0.1×10^{-4}.

Uncertainty in the thickness of the material in the HDRA was most important. The lead sheet had an average thickness of 518μm, and was initially measured on a 5 cm grid to an accuracy of 10μm. The sheet was flat horizontally within 10μm but vertically had a taper of order 50μm over 62 cm. This structure was put into the Monte Carlo; we then compared the size of the acceptance step in z (see, for example, the lead sheet $2\pi^0$ plot in Fig. 89) in both top and bottom vacuum beams in $3\pi^0$ decays. This gives a direct measurement of the 6 photon transmission probability, and we found it to be underestimated in the bottom beam by $1.1\% \pm 0.2\%$ (corresponding to roughly 13μm). The Monte Carlo was adjusted accordingly.

The accuracy of the 6 photon conversion probability corresponds to an accuracy on the 4 photon conversion probability of 0.16% for each beam. We take this value for the *average* uncertainty for the $2\pi^0$ sample to allow for residual nonuniformities in the thickest of the sheet. The value of $Re(\varepsilon'/\varepsilon)$ varies accordingly by 0.96×10^{-4}. The variations in backgrounds and coherent regeneration are included, but the photon transmission dominates.

The bulk of the remaining material was the 1 mm scintillator used in the T and V counters; their thicknesses were known to 25 microns. We used the equivalent of 50 microns of scintillator uncertainty to cover the remaining membranes (see Table III); $Re(\varepsilon'/\varepsilon)$ changes by 0.46×10^{-4}, again dominated by uncertainty in photon transmission.

Regarding background, the errors quoted in Section VI E 2 correspond to an uncertainty in $Re(\varepsilon'/\varepsilon)$ of 0.23×10^{-4} from the diffractive statistical uncertainty and 0.42×10^{-4} from the inelastic background.

Combining all of the errors associated with the HDRA, we have a total uncertainty in $Re(\varepsilon'/\varepsilon)$ of 1.22×10^{-4}, one of the larger sources in this measurement.

2. Effect of the HDRA on the Constrained Fit Results

In the constrained fits, the vacuum beam was used to predict the number of kaons incident on the regenerator; this depends mostly on the acceptance and background level

TABLE XXVI. Contribution to the systematic uncertainty in $Re(\varepsilon'/\varepsilon)$ from backgrounds.

Background Source	Uncertainty	
	$\pi^+\pi^-$	$2\pi^0$
Incoherent Regeneration (in regenerator)	0.18×10^{-4}	0.84×10^{-4}
Semileptonic Decays	0.23×10^{-4}	—
$3\pi^0$ Decays and Beam Interactions	—	0.60×10^{-4}
Total	0.29×10^{-4}	1.03×10^{-4}

for the vacuum beam, and on absorption in the shadow absorber and regenerator; the uncertainties in the vacuum beam from the HDRA have negligible effect.

In the regenerator beam, the dominant uncertainty comes from HDRA inelastic background. This is a small fraction of the regenerator beam $2\pi^0$ sample, and even with the 40% uncertainty (see Section VI E 2), it plays a minor role in the $Re(\varepsilon'/\varepsilon)$ measurement. The constrained fits, however, depend on the shape of the decay distribution and hence on the relative numbers of events upstream and downstream of the HDRA. The HDRA inelastic background is about 0.2% (0.9%) of the downstream events in the $2\pi^0$ sample without (with) the lead sheet. The uncertainty in this background contributes 0.0001×10^{-10} s and 0.0008×10^{10} $\hbar s^{-1}$ to the neutral τ_s and Δm measurements, and 0.2° to the uncertainty in $\Delta\phi$. The photon conversion probability and regeneration amplitudes are known well enough to give negligible uncertainty.

F. Backgrounds

Sections V B and VI E have already discussed the systematic and statistical uncertainties on the background levels for the $\pi^+\pi^-$ and $2\pi^0$ data samples. The contributions are summarized in Table XXVI. The uncertainty from the HDRA backgrounds have been included in the overall HDRA systematic contribution. The total background uncertainty in the $2\pi^0$ ($\pi^+\pi^-$) sample gives a systematic error of 1.03×10^{-4} (0.29×10^{-4}) to $Re(\varepsilon'/\varepsilon)$.

We have treated the regenerator background in the vacuum and regenerator beams as independent; in fact they are largely correlated and tend to cancel. Hence, our treatment is conservative.

For the constrained fits, the largest uncertainty comes from the level of noncoherent background from the regenerator in the regenerator beam, however this contributes only 0.00007×10^{10} $\hbar s^{-1}$ and 0.00005×10^{-10} s to the neutral Δm and τ_s measurements, and under 0.02° to the $\Delta\phi$ measurement.

G. Uncertainties from the Fitting Procedure

Some systematic issues in the fitting technique have already been discussed. For example, the bias in $Re(\varepsilon'/\varepsilon)$ from the acceptance correction is less than 10^{-5} when the regeneration or kaon decay parameters are varied within several percent of their nominal values. The only

other inputs, apart from the decay rate distribution, are the vacuum momentum spectrum $(F_v(p))$, and the average transmission t, and its energy dependence $c(p)$ for the regenerator beam in Eq. (83). We now discuss the sensitivity to these input spectra, and to the assumption of analyticity for the regeneration phase.

1. Incident Kaon Flux $F_v(p)$

The measurement of $Re(\varepsilon'/\varepsilon)$ is insensitive to the shape of the momentum spectrum in the fitting routine. In Table XXVII, the variation of $Re(\varepsilon'/\varepsilon)$ with modifications to the flux is given. Even a *flat* kaon spectrum (compare with Fig. 93) introduces a bias in $Re(\varepsilon'/\varepsilon)$ of only 1.21×10^{-4}. Note that this change affects only the calculation of the rate in a p and z bin in the fitting routine for a given set of test parameters. It does not change the *acceptance* calculation. Introducing a 10% bowing resulted in a 0.12×10^{-4} shift when applied to both the $\pi^+\pi^-$ and $2\pi^0$ data sets, and a 0.04×10^{-4} shift when applied to the $\pi^+\pi^-$ set only. Figs. 57 and 58 demonstrate that the spectrum has at most a few percent bowing.

The constrained fit quantities are also insensitive to the spectrum shape; a flat spectrum induces of order 1 sigma shifts in the measured quantities (Table XXVIII). These arise mostly from kaons under 40 GeV/c in the $\pi^+\pi^-$ sample: the acceptance in this region changes more rapidly across the bin than at higher momentum. Since much of the Δm information in the $\pi^+\pi^-$ fits comes from these low bins, the result is more sensitive to a change in the momentum distribution across the bin. The Δm and τ_S measurements using $2\pi^0$ decays (kaons in the 40 GeV/c to 160 GeV/c range) shift at most 10% of the (average) shift shown in the table.

When a 10% bowing was introduced, the shifts in Δm and τ_S were completely negligible, and the shifts in $\Delta\phi$ and ϕ_{+-} were small; by this technique, an uncertainty of 0.2° is assigned to the ϕ_{+-} and $\Delta\phi$ measurements.

2. Regenerator Beam Flux Corrections

The corrections to the regenerator beam flux — the average transmission, the shadow absorber corrections, and the correction for kaons "sneakbys" which miss the regenerator — also introduce systematic uncertainties into the fits. Some of the studies involving variations of these corrections are listed in Tables XXVII and XXVIII.

As mentioned previously, we measured the average kaon transmission through the shadow absorber to 0.5% for the regenerator beam. At this level, all of the parameters we measured are reasonably insensitive. In the two measurements ($Re(\varepsilon'/\varepsilon)$ and $\Delta\phi$) where charged and neutral modes are compared, the absorption uncertainty cancels. As $Re(\varepsilon'/\varepsilon)$ is affected at the 0.13×10^{-4} level, and $\Delta\phi$ negligibly. The quantity most affected is ϕ_{+-}, which shifts 0.3°. The values of Δm and τ_S receive contributions of 0.0004×10^{10} $\hbar s^{-1}$ and 0.0002×10^{-10} s, with a strong correlation between the two modes.

For the remaining corrections – shadow absorber scattering and sneakbys, $Re(\varepsilon'/\varepsilon)$ is most sensitive to the *difference* between the charged and neutral data set corrections rather than to the overall flux shape. The difference in the correction for the various data sets is small relative to the overall correction, but it is that difference, not the total correction, to

174

TABLE XXVII. Change in $Re(\varepsilon'/\varepsilon)$ for different modifications to the kaon flux shapes assumed in the fitting program. Note that these changes *are not* made in determining the acceptance, they only affect the relative contribution of the *predicted rate* of a 1 GeV/c momentum bite to the total predicted rate in a 10 GeV/c bin.

Modification to beam spectrum	$\delta Re(\varepsilon'/\varepsilon)$ (10^{-4})
Flat Incident spectrum ($F_v(p) = $ constant)	-1.21
Quadratic distortion — both $2\pi^0$ and $\pi^+\pi^-$ samples $(F'_v(p) = F_v(p)\{1 + 0.1[(p-60)/100]^2\})$	$+0.12$
Quadratic distortion, $\pi^+\pi^-$ sample only	$+0.04$
Increase average regenerator beam transmission by 1 σ $(t \to 1.005t)$	-0.13
No shadow absorber scattering correction to regenerator beam flux	-0.36
Use shadow absorber scattering correction determined for the $\pi^+\pi^-$ sample for all data sets[a]	-0.27
Use shadow absorber scattering correction determined for the $2\pi^0$ lead sheet sample for all data sets	-0.27
Change dilution factor used to calculate change in the relative flux shape between the regenerator and vacuum beam from regeneration in the shadow absorber	$+0.04$
Ignore "sneakby" rate[b]	-0.76
Correct for "sneakby" kaons, but ignore the rate of K_L decay from these kaons	-0.26
Use the "sneakby" rate determined for the $\pi^+\pi^-$ set for all of the subsets	-0.47
Use the "sneakby" rate determined for the lead sheet $2\pi^0$ set for all of the subsets	-0.46

----

[a]See Section VIII A 2.

[b]That is, assume the entire flux of kaons observed in the vacuum beam passes through the regenerator.

175

TABLE XXVIII. Change in Δm, τ_S, $\Delta\phi$ and ϕ_{+-} for different distortions of the vacuum and regenerator beam kaon momentum spectra.

Modification to vacuum or regenerator beam spectrum	$\|\delta\Delta m\|$ $(10^{10}\hbar s^{-1})$	$\|\delta\tau_S\|$ $(10^{-10}s)$	$\|\delta\Delta\phi\|$	$\|\delta\phi_{+-}\|$
Flat Incident spectrum ($F_v(p) = $ constant)	0.0038	0.0007	$1.3°$	$1.2°$
Quadratic distortion: $(F'_v(p) = F_v(p)\{1 + 0.1[(p-60)/100]^2\})$	0.0001	0.0001	$0.3°$	$0.5°$
Change average regenerator beam transmission by 1 standard deviation: $(t \to 1.005t)$	0.0004	0.0002	$< 0.1°$	$0.3°$
No shadow absorber scattering correction to regenerator beam flux	0.0007	0.0002	$0.1°$	$0.3°$
Use the shadow absorber scattering correction determined for the $\pi^+\pi^-$ sample for all data sets	< 0.0001	< 0.0001	$< 0.1°$	$< 0.1°$
Ignore "sneakby" rate	0.0003	0.0002	$0.5°$	$0.3°$
Use the "sneakby" rate determined for the $\pi^+\pi^-$ set for all of the subsets	< 0.0001	< 0.0001	$< 0.1°$	$< 0.1°$

which the result is most sensitive. As we can see in Table XXVII, no matter which data set we chose from for the correction, the bias we observed in $Re(\varepsilon'/\varepsilon)$ was the same. The changes for globally applying the $\pi^+\pi^-$ corrections and the $2\pi^0$ lead sheet corrections are listed in the table. The uncertainty in the shadow absorber scattering and sneakby corrections were dominated by uncertainties in kaon-nucleon elastic cross sections. Cross sections reported in [53] yield an uncertainty of 20%, depending mostly on how the values reported in [53] are interpreted.

The change in the correction from data set to data set is dominated by changes in beam collimation, primarily from sinking of the target pile. These changes were tracked well, but as a conservative estimate we have assigned the uncertainty on the corrections to be 50% of the difference between the most disparate pair of data sets. This corresponds to an uncertainty in $Re(\varepsilon'/\varepsilon)$ of 0.14×10^{-4} (0.23×10^{-4}) for the scattering (sneakby) correction.

Because these corrections vary slowly across the 10 GeV/c bins, they do not contribute significantly to the uncertainty in the other measurements, as seen in Table XXVIII. Ignoring the corrections introduces small biases; but since they are known to about 20%, their affect on the constrained fit measurements is negligible.

3. Analyticity Assumption

We now investigate the systematics associated with the analyticity assumption used to obtain the regeneration phase. If the regeneration amplitude deviated from a pure power behavior, then a bias in the phase extracted from the analyticity relationship could be introduced. Such could result from kaon rescattering, where there can be a Pomeron along with

ω or ρ exchange. The Pomeron affects the regeneration amplitude, contributing logarithmic terms that disrupt the pure power-law behavior; it also has a small real part. Since there would be no longer a pure power-law behavior, the use of analyticity to determine the regeneration phase from the "best fit" power could lead to a small bias in this phase. We originally argued that this could be limited to $< 0.5°$ in fits which use the full momentum range down to 20 GeV/c. Subsequent to the publication of these results, a far more complete analysis by two of us [35] showed that this rescattering together with several other effects was limited to $< 0.35°$. This paper also addresses the criticism of our technique in [36]. The key feature is that the scattering amplitudes are well enough behaved that the local power-law gives an excellent approximation to the local phase even in the presence of multiple trajectory exchange, multiple elements in the target (regenerator), and electromagnetic regeneration. Nonetheless, here we describe the original analysis.

In the fits to charged data below 40 GeV/c, the accuracy of the measured power-law slope α corresponds to an uncertainty of 0.3° in the regeneration phase and the measured parameters already reflect this uncertainty. In addition to this, we included an uncertainty of 0.5° for a non-pure power-law, commensurate with both the limit on the Pomeron contribution and the change in the slope α when the fits are limited to momenta above 40 GeV/c. The contribution to the uncertainty on the charged τ_S fit is 0.0003×10^{-10} s. The Δm measurement is more sensitive to the regeneration phase; its uncertainty contributes 0.0019×10^{10} $\hbar s^{-1}$, since α is floating in these fits.

The ϕ_{+-} measurement is directly correlated with the regeneration phase ϕ_ρ, since what is measured is the difference of phases $\phi_\rho - \phi_{+-}$ (see Eq. (85)). Thus ϕ_{+-} has the 0.5° uncertainty, the dominant systematic. The regeneration phase cancels in the measurement of $\Delta\phi$.

For the neutral Δm and τ_S measurements, the uncertainty in the regeneration phase due to the statistical uncertainty on α already corresponds to 0.7°. The additional uncertainty from nonpure power-law behavior is negligible. This is also true in the $Re(\varepsilon'/\varepsilon)$ measurement, where both the $\pi^+\pi^-$ and $2\pi^0$ samples are restricted to the momentum range above 40 GeV/c.

4. Summary of Uncertainties in the Fits

The measurements we make are not greatly dependent on the shape of the kaon flux in the vacuum and regenerator beams. For $Re(\varepsilon'/\varepsilon)$, the combination of errors due to absorption, scattering in the movable absorber, and sneakbys amounts to 0.30×10^{-4}. For $\Delta\phi$ there is an uncertainty of 0.2° from the kaon spectrum; for ϕ_{+-} there is an uncertainty of 0.4° from the spectrum and transmission in the regenerator beam. These effects on Δm and τ_S are negligible.

The uncertainty from the assumption of analyticity contributes only to fits using the charged mode data below 40 GeV/c. This gives a 0.5° uncertainty on ϕ_{+-}. The corresponding uncertainty for the charged Δm measurement is 0.0019×10^{10} $\hbar s^{-1}$, and for the charged τ_S measurement, it is 0.0003×10^{-10} s.

H. Accidental Activity

The final systematic results from uncertainties in how accidental activity alters the vacuum to regenerator ratios for the two modes. The corrections were given in Section IX A 1; here we describe the method and the uncertainty.

Accidental effects are largest for the highest intensity data samples. For $\pi^+\pi^-$ this is the NC subset; the study of the accidental effects in this data set has been detailed in [18]: for an average proton intensity of 0.8×10^{12}, the vacuum to regenerator ratio changes by $-0.04\% \pm 0.07\%$, requiring no correction. This statistical error, scaled to the remainder of the data (a factor of 2.7 lower in intensity) yields a total uncertainty on $Re(\varepsilon'/\varepsilon)$ of 0.67×10^{-4}.

For the higher intensity $2\pi^0$ data subsets, we have determined the effect on the single ratio. We used the random triggers collected simultaneously with $\pi\pi$; these sampled the same ambient environment of kaon decays and had the same intensity distribution. A trigger was formed when a charged particle produced in the interaction of a proton in the target or dump hit a telescope located at a large angle about 50 m upstream of the regenerator. Detector activity in accidental events was overlaid on Monte Carlo coherent $\pi\pi$ events where it was important that the regenerator position for the event was determined by the overlayed accidental. Dead time effect (as in single-hit drift chamber TDCs) was fully simulated. Each event was analyzed both with and without the overlay to measure the effect on the accepted event samples.

The analysis of the overlaid Monte Carlo sample completely paralleled that of the data. For example, the $2\pi^0$ energy scale corrections based on matching the regenerator edge were applied.

What is important is the change in the vacuum to regenerator ratio from accidental activity. The changes after every cut which resulted in any loss (after the accidental is overlaid) are listed in Table XXIX. A positive change means a smaller fraction of events is lost in the vacuum than in the regenerator beam.

The accidental activity in the calorimeter tends to center around the more intense vacuum beam, resulting in an asymmetry for an accidental cluster to merge with a photon from $2\pi^0$. The asymmetry is apparent: for cuts that eliminate events where extra photons are apparent — the 4 cluster and cluster fusion cuts — there is a greater loss of regenerator events. For cuts that discard events where a hidden accidental cluster affects the kinematics — χ^2, mass, etc. — there is a greater loss of vacuum events. These losses almost compensate and the total asymmetry is quite small.

The losses are not the whole story. Accidental activity can cause events just outside of analysis cuts to satisfy those cuts after the overlay. The most important effect is a small z shift introduced by the accidental overlays (Fig. 112); it is strongly peaked at zero, but with asymmetry between upstream and downstream z shifts. This is expected since extra energy tends to push the reconstructed z away from the calorimeter. Since the fraction of decays near the downstream z cut is larger in the vacuum beam, this asymmetry can change the vacuum to regenerator ratio. When both gains and losses were considered, the total change in the vacuum to regenerator beam ratio was $0.169\% \pm 0.060\%$. This particular study was with the lead sheet data; results without it were similar.

The absolute fraction of $2\pi^0$ events lost in the vacuum and regenerator beam samples

TABLE XXIX. Sequential change in observed $2\pi^0$ vacuum beam to regenerator beam ratio due to accidental event loss as each analysis cut is applied. Events which would not have passed cuts except for the presence of the accidental activity are *not* included in these numbers.

Analysis Cut	Change in Ratio (%)
4 clusters	$+0.065\pm0.021$
Best pairing $\chi^2 < 4$	-0.137 ± 0.013
Cluster fusion	$+0.234\pm0.048$
2nd best χ^2 cuts	-0.017 ± 0.005
Chamber, BC hodoscope hits	$+0.099\pm0.028$
Collar Anti	-0.055 ± 0.012
Cluster energy cuts	-0.002 ± 0.001
Ring number	-0.001 ± 0.003
$2\pi^0$ mass	-0.032 ± 0.004
Total energy	-0.018 ± 0.002
z fiducial cut	-0.051 ± 0.002
Total	$+0.085\pm0.062$

because of accidental activity depended on cuts. For example, the event selection criteria used in $2\pi^0$ analysis, designed to minimize $3\pi^0$ background, tended to remove events where activity in the lead glass was nearby (or on) a photon cluster. Systematically, it was worthwhile to tighten the cuts to reduce the $3\pi^0$ background, which was much larger in the vacuum beam, and live with the increased loss of events. With the final cuts, the change in the sample from accidental activity was about 17% for the high intensity running. The dominant losses came from the combination of the 4 cluster requirement and the fusion and pairing χ^2 cuts.

The total change in the observed vacuum to regenerator beam ratio is $0.169\% \pm 0.060\%$ for the high intensity data with the lead sheet present. This means the required *correction* is -0.169%. The correction without the sheet is slightly smaller at -0.154%. Scaling the latter value to the intensity of the NC set yields a low-intensity correction consistent with the previous study. After weighting according to the fraction of data at high intensity (about 80%) and at low intensity, the total correction to $Re(\varepsilon'/\varepsilon)$ was $+2.51 \times 10^{-4}$ with an uncertainty of 0.84×10^{-4}.

The measurements using constrained fits are not sensitive to the level of the accidental correction. The uncertainty in the vacuum to regenerator beam ratio is almost an order of magnitude lower than that in the kaon absorption in the regenerator beam, and hence is negligible. Of more importance are biases in the vacuum to regenerator ratio vs. energy (this can bias the power-law) and in the regenerator beam z distribution. These are plotted in Fig. 113 and Fig. 114.

The power-law shift associated with the energy dependence changes $\Delta\phi$ by about $0.1°$ and Δm by 0.0004×10^{10} $\hbar s^{-1}$. The other quantities, including $Re(\varepsilon'/\varepsilon)$, are affected negligibly.

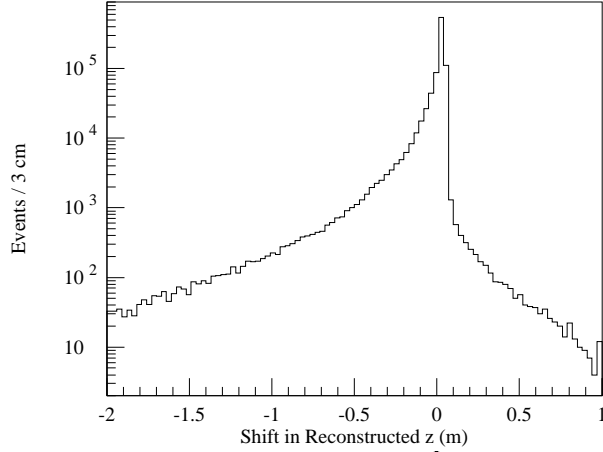The bias in the regenerator z acceptance is consistent with zero. Its uncertainty is

FIG. 112. Shift in the reconstructed z-position in $2\pi^0$ decays as a result of accidental activity in the detector. A negative value corresponds to an upstream shift away from the lead-glass calorimeter.
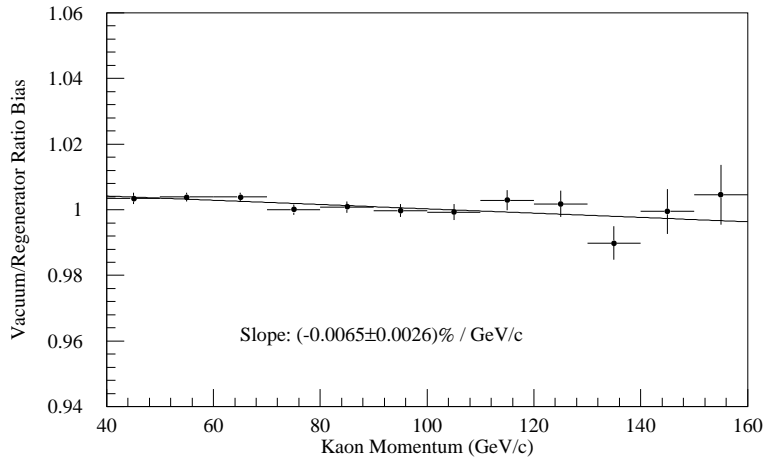

FIG. 113. Bias as a function of energy of the observed vacuum to regenerator beam ratio in the high intensity $2\pi^0$ data due to accidental activity. The line drawn is the best linear fit, which has the slope listed.
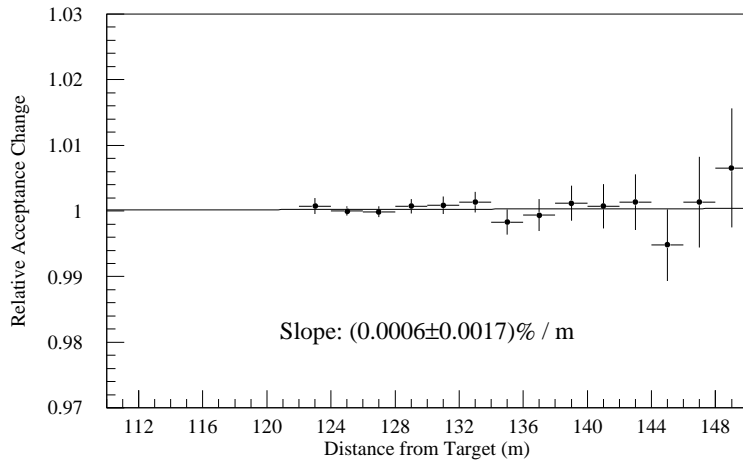

FIG. 114. Bias as a function of z of the regenerator beam acceptance in the high intensity $2\pi^0$ data due to accidental activity. The line drawn is the best linear fit, which has the slope listed.

180

TABLE XXX. Summary of systematic uncertainties on $Re(\varepsilon'/\varepsilon)$, Δm and τ_S measured in the $\pi^+\pi^-$ and $2\pi^0$ decay modes, $\Delta\phi$, and ϕ_{+-}.

Systematic Source	$Re(\varepsilon'/\varepsilon)$ (10^{-4})	τ_S $(10^{-10}\ s)$ $2\pi^0$	$\pi^+\pi^-$	Δm $(10^{10}\ \hbar s^{-1})$ $2\pi^0$	$\pi^+\pi^-$	$\Delta\phi$	ϕ_{+-}
γ energy	1.61	0.0012	—	0.0014	—	0.5°	—
$\pi^+\pi^-$ acceptance	0.65	—	0.0020	—	0.0009	0.4°	0.35°
$2\pi^0$ acceptance	1.00	0.0002	—	0.0001	—	—	—
RA4 position	0.59	—	—	—	—	—	—
HDRA material	1.22	0.0001	—	0.0008	—	0.2°	—
$2\pi^0$ backgrounds	1.03	—	—	—	—	—	—
$\pi^+\pi^-$ backgrounds	0.29	—	—	—	—	—	—
Kaon flux	0.30	0.0002[a]	0.0002[a]	0.0004[a]	0.0004[a]	0.2°	0.4°
Analyticity	—	—	0.0003	—	0.0019	—	0.5°
Accidentals	1.07	—	—	0.0004	—	0.1°	—
Totals	2.87	0.0012	0.0020	0.0017	0.0021	0.7°	0.7°

[a]This error is completely correlated between the $\pi^+\pi^-$ and $2\pi^0$ samples, and is not included in the total error listed here.

included in the acceptance systematic given previously.

I. Conclusion on Systematics

In general, the measurement of the $Re(\varepsilon'/\varepsilon)$ with the double beam technique is robust. The combination of two possible cancellations — between the vacuum and regenerator beam within a decay mode, and between the regenerator samples of the two modes — tends to limit systematics from a variety of effects, such as beam absorption, accidental activity, possible aperture mis-measurements, etc. The contributions to the systematic uncertainty on $Re(\varepsilon'/\varepsilon)$ are summarized in Table XXX; the total is 2.87×10^{-4}.

The systematic uncertainties in Δm and τ_S and in $\Delta\phi$ and ϕ_{+-} are also summarized in Table XXX.

XI. CONCLUSION

A. $Re(\varepsilon'/\varepsilon)$

Combining the results of our fits for $Re(\varepsilon'/\varepsilon)$ from Section IX A with the systematic estimate from the previous section, we have

$$Re(\varepsilon'/\varepsilon) = (7.4 \pm 5.2 \pm 2.9) \times 10^{-4}, \tag{97}$$

where the first error is the statistical uncertainty and the second error is the systematic uncertainty. A brief discussion of this result has been published [19]. Comparing this result to our earlier publication [18] based on approximately 20% of the accumulated data, this is an improvement in the statistical accuracy by a factor of 2.7, and in the systematic uncertainty by a factor of 2.1. We have improved our statistical uncertainty beyond the expected factor of $\sqrt{5}$ by extending the fiducial z regions of $2\pi^0$ mode 15 m downstream. This was not possible in the $\pi^+\pi^-$ mode, which causes the $K_L \to \pi^+\pi^-$ decay to be the statistically limiting decay mode with a total of 328,980 decays after background subtraction. The dominant systematic contribution came from the uncertainty in the energy scale of the lead glass calorimeter.

Combining the statistical and systematic uncertainties in quadrature, we have

$$Re(\varepsilon'/\varepsilon) = (7.4 \pm 5.9) \times 10^{-4}, \tag{98}$$

which is not significantly different from zero. This result is consistent with no direct CP violation in $K_L \to \pi\pi$ decays, and the superweak hypothesis can not yet be excluded based on this measurement. At the 95% confidence level, we can place an upper limit on the value of $Re(\varepsilon'/\varepsilon)$ of

$$Re(\varepsilon'/\varepsilon) < 17 \times 10^{-4}. \tag{99}$$

This result is compared to previously published measurements of $Re(\varepsilon'/\varepsilon)$ in Fig. 115. After the initial publication of this result [19], a final result from CERN NA31 was published [20]. Their result, $Re(\varepsilon'/\varepsilon) = (23 \pm 6.5) \times 10^{-4}$, is more than 3σ from zero and does not agree very well with ours. Though the central value of the NA31 result has decreased, there is still a discrepancy at the 1.8 standard deviation level between their result and our new result.

1. Standard Model Predictions

The great experimental effort by both groups to improve the precision in the measurement of $Re(\varepsilon'/\varepsilon)$ has been paralleled by attempts to improve the precision in the calculation of $Re(\varepsilon'/\varepsilon)$ in the Standard Model. The calculation of $Re(\varepsilon'/\varepsilon)$ is quite difficult, particularly since the matrix elements $\langle(\pi\pi)_I | Q_i(\mu) | K\rangle$ for the decay of the neutral kaon into the $I = 0, 2$ $\pi\pi$ final states receive contributions from long–distance effects in QCD where perturbative approaches are not applicable. The calculation uncertainties are exacerbated by uncertainties in many of the physical parameters needed for the final evaluation, such as the top quark and strange quark masses m_t and m_s, the size of CKM matrix elements $|V_{cb}|$ and $|V_{ub}|$, and the QCD scale $\Lambda_{\overline{MS}}$. While the strong penguin diagram dominates the contribution to CP violation for low top mass, Flynn and Randall [62] noticed that for higher
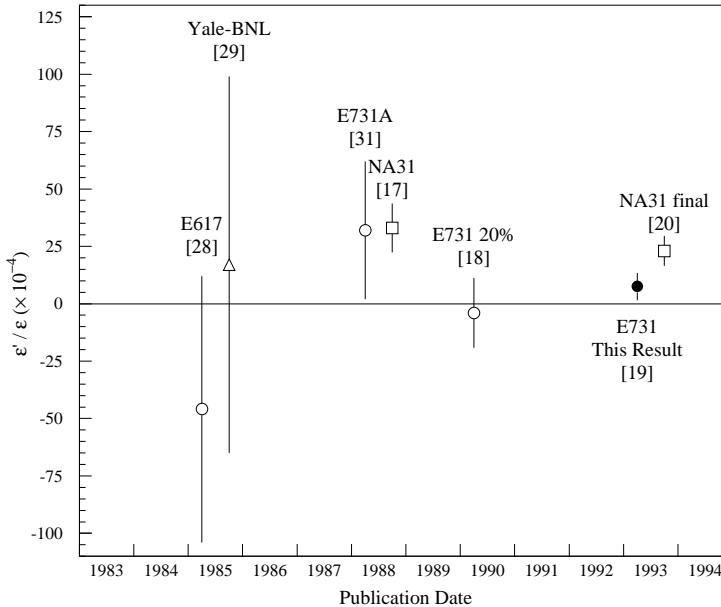
FIG. 115. The publication history of $Re(\varepsilon'/\varepsilon)$ measurements.

top quark masses, the electroweak penguin diagram could provide a significant cancellation of the effect of the strong penguin. New evidence for the top quark ($m_t = 176 \pm 13$ GeV/c^2 from CDF [63] and $m_t = 199 \pm 30$ GeV/c^2 from D0 [64]) implies that this cancellation could be quite important. For top masses above 200 GeV/c^2, the cancellation could be nearly complete, making $Re(\varepsilon'/\varepsilon)$ unable to distinguish between the superweak models and the Standard Model.

In spite of the difficulties, two groups have recently finished calculations at the next–to–leading order in QCD; a Rome group which used lattice methods [65,66], and a Munich group using renormalization techniques [67]. It is very heartening that the two groups obtain fairly compatible results using different techniques. A recent summary of both of these new calculations was presented by Peccei [68], who makes a "representative prediction" of

$$\frac{\varepsilon'}{\varepsilon} = \begin{cases} (11\pm4) \times 10^{-4} A^2\eta & (m_t = 140 \text{ GeV}/c^2), \\ (3\pm4) \times 10^{-4} A^2\eta & (m_t = 200 \text{ GeV}/c^2), \end{cases} \tag{100}$$

where A and η are parameters of the CKM matrix. From the information on η and A that we have from $|\varepsilon|$, $B^0 - \bar{B}^0$ mixing, and recent $|V_{ub}|/|V_{cb}|$ measurements, it would appear that these calculations favor values for $Re(\varepsilon'/\varepsilon)$ of order several times 10^{-4}.

The Rome group has calculated the allowed range of $Re(\varepsilon'/\varepsilon)$ versus $\cos\delta$, where δ is the CP violating phase in the CKM matrix. The central values and range for $Re(\varepsilon'/\varepsilon)$ do not change greatly as $|V_{ub}|$ decreases, but the allowed regions in $\cos\delta$ (or ρ) tend to coalesce and favor the first quadrant. The top quark mass assumed in [66] was 174 ± 17 GeV/c^2. The Munich results are for a top mass of $m_t = 130$ GeV/c^2, presented as a function of $\Lambda_{\overline{MS}}$. Both of these results are very compatible with our new measurement, and somewhat lower than the NA31 results. As the top quark mass varies, both predictions are consistent

with our result. The NA31 result, on the other hand, prefers a much lower value for m_t. Unfortunately, current measurements do not have the sensitivity needed to limit the range of values allowed for parameters like $\Lambda_{\overline{MS}}$ and m_t. If the theoretical uncertainty continues to diminish, the next experimental efforts may well be able to provide a test of the CKM paradigm. Note that the importance of *establishing* an unambiguous signal for direct CP violation should not be diminished even if the theoretical uncertainties remain at their current level.

2. The Future for $Re(\varepsilon'/\varepsilon)$

The technique we have employed to measure $Re(\varepsilon'/\varepsilon)$ still holds much promise for future refinements in precision. Our current result is statistically limited, and many of the dominant contributions to the systematic uncertainty are addressable in the design of a new detector in a straightforward fashion. Our group will run a new experiment (FNAL E832) at Fermilab, again using the double beam technique, with a much improved beam and detector. The heart of the new detector will be a new pure Cesium Iodide (CsI) electromagnetic calorimeter that will replace the current lead glass calorimeter. Compared to our current lead glass calorimeter, the new calorimeter is expected to have much better electron and photon resolutions (of order 1%), much smaller nonlinearities, better light yields, faster timing, and (since the crystals are 27 radiation lengths long) little difference in response to electrons and photons. With this new calorimeter, it should be straightfoward to reduce the contribution of the systematic uncertainty on $Re(\varepsilon'/\varepsilon)$ from the $2\pi^0$ energy scale, which is the largest systematic contribution in our current measurement.

Many other areas of the experiment are also being improved. The regenerator will be fully active and hence will be able to suppress the inelastic backgrounds further. Such a regenerator has already been used successfully by this group in an experiment (FNAL E773) dedicated to measuring $\Delta\phi$. In addition, the $3\pi^0$ background will be highly suppressed by an improved photon veto system and the finer granularity of the CsI calorimeter. All four $\pi\pi$ decay modes will be detected simultaneously in this experiment, as they were in the 20% subsample used for our first result [18]. While collecting all four modes simultaneously allows some convenient cross checks, it is not crucial for the success of the double beam technique.

The new experiment, slated to run in 1996, hopes to collect several million $K_L \to \pi^0\pi^0$ and $K_L \to \pi^+\pi^-$ decays, and reach an ultimate precision of order 10^{-4} on $Re(\varepsilon'/\varepsilon)$.

The CERN NA31 experiment [69] also has a new experiment (CERN NA48), and they too are now using a double beam method. Rather than use a regenerator to produce the K_S decays, however, the CERN group will be employing two separate targets. They are also switching from a calorimetry-based charged mode detection system to a magnetic spectrometer. They hope to achieve a sensitivity approaching 10^{-4} on $Re(\varepsilon'/\varepsilon)$ as well.

B. Other Kaon Parameters

1. Δm, τ_S, and the Superweak Phase

With the systematic contributions to the Δm and τ_S now estimated, we can compare the results from the $\pi^+\pi^-$ and $2\pi^0$ modes, and combine the results from the two modes to compare to the current world averages. The results for τ_S are

$$\tau_S = \begin{cases} (0.8952 \pm 0.0015 \pm 0.0020) \times 10^{-10} \ s & (\pi^+\pi^-) \\ (0.8912 \pm 0.0017 \pm 0.0012) \times 10^{-10} \ s & (\pi^0\pi^0) \end{cases} \tag{101}$$

Combining the systematic and statistical errors in quadrature gives

$$\tau_S = \begin{cases} (0.8952 \pm 0.0025) \times 10^{-10} \ s & (\pi^+\pi^-) \\ (0.8912 \pm 0.0021) \times 10^{-10} \ s & (\pi^0\pi^0) \end{cases} \tag{102}$$

These numbers are in agreement, with the difference at the level of 1.2 standard deviations. We therefore combine these two results, and our new measurement of τ_S becomes [28]

$$\tau_S = (0.8929 \pm 0.0016) \times 10^{-10} \ s, \tag{103}$$

which is in good agreement with previous measurements of τ_S and the PDG92 average of $(0.8922 \pm 0.0020) \times 10^{10} \ \hbar s^{-1}$ [27]. This was a 25% improvement in precision over the world average at that time.

For Δm, the results from the two modes are

$$\Delta m = \begin{cases} (0.5311 \pm 0.0044 \pm 0.0020) \times 10^{10} \ \hbar s^{-1} & (\pi^+\pi^-) \\ (0.5274 \pm 0.0030 \pm 0.0017) \times 10^{10} \ \hbar s^{-1} & (\pi^0\pi^0) \end{cases}, \tag{104}$$

and combining the errors in quadrature gives

$$\Delta m = \begin{cases} (0.5311 \pm 0.0048) \times 10^{10} \ \hbar s^{-1} & (\pi^+\pi^-) \\ (0.5274 \pm 0.0034) \times 10^{10} \ \hbar s^{-1} & (\pi^0\pi^0) \end{cases}. \tag{105}$$

These two results are also in agreement. The consistency both of the Δm and of the τ_S measurements, which depend on the shape of the decay distributions and hence are sensitive to biases in the acceptance, in the two different decay modes makes a powerful crosscheck for our $Re(\varepsilon'/\varepsilon)$ measurement. When we combine the Δm results from the two decay modes, our final result for Δm is

$$\Delta m = (0.5286 \pm 0.0028) \times 10^{10} \ \hbar s^{-1}. \tag{106}$$

Note that this value of Δm is the first new measure of this quantity in almost 20 years. While our result is in reasonable agreement with the previous two measurements, it is inconsistent with earliest measurements used in calculating the PDG92 average [27]. As a result, our new value is two standard deviations lower than the PDG92 average of $(0.5351 \pm 0.0024) \times 10^{10} \ \hbar s^{-1}$. Our precision is comparable to that of the PDG92 world average.

The systematic errors common to both the charged and the neutral mode (Section XI) have been included in the total errors for both Δm and τ_S. Even though our Δm result is

shifted lower than the PDG92 average, the value for the superweak phase we obtain using our new Δm and τ_s results does not change significantly. We find

$$\phi_\varepsilon = \tan^{-1}(2\Delta m/[\Gamma_S - \Gamma_L]) = 43.4° \pm 0.1°. \tag{107}$$

Recall that the Δm value was obtained assuming the superweak phase for ϕ_{+-}. The dependence of Δm to ϕ_{+-} is $0.0031 \times (\phi_{+-} - 43.3)\hbar s^{-1}$.

With ϕ_{+-} floating, we get $\Delta m = (0.5257 \pm 0.0049) \times 10^{10}~\hbar s^{-1}$ (see Sections IX B and IX C). This is still significantly lower than previous values although with larger error. Note that the latest PDG94 average [10] has included this result.

C. The $\Delta\phi$ and ϕ_{+-} Measurements

1. Testing CPT Symmetry

The first test of CPT symmetry rests on the direct comparison of the phases ϕ_{+-} and ϕ_{00} of the CP violating parameters η_{+-} and η_{00}. We have found

$$\Delta\phi = -1.6° \pm 1.0° \pm 0.7°, \tag{108}$$

and when the statistical and systematic errors are combined in quadrature the result becomes

$$\Delta\phi = -1.6° \pm 1.2°. \tag{109}$$

The accuracy of our final result is a substantial improvement over that of the PDG92 average. Note that the PDG92 average for $\Delta\phi$ includes our previous result based on 20% of the data sample included in this analysis. The 95% confidence level limit obtained from our result is $|\Delta\phi| < 3.6°$.

Let us consider the case where we have CPT violation directly in $K \to \pi\pi$ decays. Following Barmin $et~al.$ [4], this can be accomplished by explicitly incorporating manifestly CPT–violating terms B_I into the $I = 0$ and $I = 2$ decay amplitudes,

$$\langle I| \mathbf{H}_{eff} |K^0\rangle = (A_I + B_I)e^{i\delta_I}, \tag{110}$$

$$\langle I| \mathbf{H}_{eff} |\bar{K}^0\rangle = (A_I^* - B_I^*)e^{i\delta_I}. \tag{111}$$

After making the same isospin decomposition as in Section 1, the definition of ε' in Eq. (16) is slightly modified,

$$\varepsilon' \to \frac{i}{\sqrt{2}}e^{i(\delta_2-\delta_0)}\frac{ImA_2 - iReB_2}{A_0}. \tag{112}$$

In this expression, we have assumed that $|ImB_0| \ll A_0$, since A_0 determines the rate for the dominant $K_S \to \pi\pi$ ($I = 0$) decay rate, and it is very unlikely that a CPT–violating rate is this large. The CPT violating component adds a term that is 90° degrees out of phase with the previous CP–violating but CPT–conserving term. Since the final state $\pi\pi$ phase shifts place ε' so close to parallel with ε and since $\Delta\phi$ is so small, we can use the above expression in conjunction with Eqs. (17) and (18) to give

186

$$\frac{ReB_2}{ReA_2} = \frac{1}{|\omega|}\frac{ReB_2}{A_0} \approx \frac{\sqrt{2}}{3}\frac{|\varepsilon|}{|\omega|}(\phi_{+-} - \phi_{00}), \tag{113}$$

where $\omega \approx 1/22$ is the measured violation of the $\Delta I = 1/2$ rule. Using the PDG92 value [27] for $|\eta_{+-}|$ as the value of $|\varepsilon|$ and our new result for $\Delta\phi$ we get

$$\frac{ReB_2}{ReA_2} = (6.5 \pm 4.9) \times 10^{-4}. \tag{114}$$

With some reasonable assumptions about isospin, Barmin et $al.$ [4] relate the K^+ and K^- lifetime difference to the above ratio:

$$\frac{\tau^+ - \tau^-}{\tau^+} \approx -0.84\frac{ReB_2}{ReA_2}. \tag{115}$$

This allows us to compare the strength of the CPT test based on this result relative to the direct comparison of the lifetimes, and place the $\Delta\phi$ CPT test in a more intuitive framework:

$$\frac{\tau^+ - \tau^-}{\tau^+} = \begin{cases} (-5\pm4) \times 10^{-4} & \text{(our } \Delta\phi) \\ (11\pm9) \times 10^{-4} & \text{(from PDG [27])} \end{cases}.$$

The first result was obtained from our $\Delta\phi$ measurement, and the second from the experimental measurements of the charged kaon lifetimes. In this framework, we see that the current $\Delta\phi$ measurement places stronger bounds on possible CPT violation than those placed by the direct lifetime measurements.

2. ϕ_{+-} Measurement

The final measurement we have made is the measurement of ϕ_{+-} itself, and we have found

$$\phi_{+-} = 42.2° \pm 1.3° \pm 0.7°, \tag{116}$$

where, as usual, the first error is statistical and the second error is systematic. Combining the errors in quadrature, we have

$$\phi_{+-} = 42.2° \pm 1.5°. \tag{117}$$

This is in excellent agreement with the superweak phase $\phi_\varepsilon = 43.4°$ (43.7°) found using our (PDG92) values for Δm and τ_s. On the other hand, this result disagrees with the previous PDG92 average [27] for ϕ_{+-} of $46.5° \pm 1.2°$ at slightly over the 2 standard deviation level. The value for ϕ_{+-} extracted from each of the previous experiments, however, depends on the value of Δm assumed (the PDG92 average, in this case).

Since our Δm result is lower than the previous measurements, it is interesting to compare results of different phase experiments after correcting the experiments using our value of Δm. The results of the individual corrections to ϕ_{+-} are listed in Table XXXI, and the previous measurements agree very well with our own. When we now average the previous results with our own, we obtain a new world average of

TABLE XXXI. Our result for and previous best measurements of ϕ_{+-}. We have corrected the previously reported value of ϕ_{+-} for the change in the assumed Δm to our current result for Δm using the reported experimental dependences.

Experiment	ϕ_{+-} (degrees)	Internal Error (degrees)	Assumed Δm ($\times 10^{10}\ \hbar s^{-1}$)	$\Delta\phi_{+-}$ for $+1\%\ \delta\Delta m$ (degrees)	ϕ_{+-} (our Δm) (degrees)
C. Geweniger et al. [25]	45.6	1.0	0.5338	3.05	43.0
W.C.Carithers et al. [26]	45.5	2.8	0.5348	1.20	44.1
R.Carosi et al. [24]	46.9	1.6	0.5351	3.10	43.4
This experiment [28]	42.2	1.4	floated^a	—	42.2

----

^{a}See Section IX C

$$\phi_{+-} = 42.8° \pm 1.1°, \qquad (118)$$

which agrees very well with the superweak phase.

Note that no conclusions of this argument are significantly altered when we use the value of Δm which we obtained with ϕ_{+-} floating.

We can again try to relate this measurement to other physical parameters of the kaon. Of particular interest is the difference between the masses of the K^0 and $\bar{K}^0$, which should be equal if CPT is a good symmetry of nature. Let us consider for the CPT violating quantity $\bar{\varepsilon}$ defined similarly to Eq. (5) as

$$\bar{\varepsilon} = \frac{\imath(M_{11} - M_{22}) + \frac{1}{2}(\Gamma_{11} - \Gamma_{22})}{2(\imath\Delta m - \frac{1}{2}(\Gamma_S - \Gamma_L))}$$

$$= -e^{\imath\phi_\varepsilon} \frac{\imath(M_{11} - M_{22}) + \frac{1}{2}(\Gamma_{11} - \Gamma_{22})}{2\kappa\sqrt{2}\Delta m}, \qquad (119)$$

where $\kappa \equiv (1 + 1/(2\Delta m \tau_S)^2)^{\frac{1}{2}}/\sqrt{2} = 1.03$. Since we assumed $\mathbf{M}$ and $\mathbf{\Gamma}$ were hermitian, M_{11} and M_{22} are real, and if their difference is non-zero (that is, if the K^0 and $\bar{K}^0$ masses are not equal) then $\bar{\varepsilon}$ adds a term common to both η_{+-} and η_{00} that is 90° out of phase with the contribution from ε. If we suppose that the $I = 0$ $\pi\pi$ decays saturate $\mathbf{\Gamma}$ [68,70], then applying our current results for $|\eta_{00}/\eta_{+-}| \approx (1 - 3Re(\varepsilon'/\varepsilon))$ and for $\Delta\phi$ to the argument in Barmin et al. [4] implies one would not expect the second term to change the component of η parallel to ε beyond a limit of roughly 5%. For our purposes here, we therefore simply ignore this possible CPT-violating contribution.

Since the CPT-violating term from $\bar{\varepsilon}$ that arises from the mixing matrix is perpendicular to the CP-violating term, they form a right triangle with η along the hypotenuse, and we therefore have

$$\tan(\phi_{+-} - \phi_\varepsilon) = \frac{1}{\varepsilon} \frac{m_{K^0} - m_{\bar{K}^0}}{2\sqrt{2}\kappa\Delta m}. \qquad (120)$$

With our adjusted world average for ϕ_{+-} and our new value of the superweak phase, $\tan(\phi_{+-} - \phi_\varepsilon) = -0.010 \pm 0.019$. Combining this result with the world average of $|\eta_{+-}|$

for $|\varepsilon|$, the world average value of the neutral kaon mass, and our new value for Δm of $(3.479 \pm 0.018) \times 10^{-12}$ MeV/c^2, we can limit

$$\left| \frac{m_{K^0} - m_{\overline{K}^0}}{m_{K^0}} \right| < 2.0 \times 10^{-18} \tag{121}$$

at the 95% confidence level. This limit is about a factor of 2 better than the limit based on the PDG92 average value of ϕ_{+-} [27], with the improvement coming mainly from the shift in ϕ_{+-} towards the superweak phase.

In all, the combination of our new Δm, $\Delta\phi$ and ϕ_{+-} measurements further improve the limits on CPT violation.

D. Other Recent Measurements

Since the initial publication of these results [28], two experiments have published results concerning Δm, τ_S, ϕ_{+-} and $\Delta\phi$. The measurements of FNAL E773 [71], were made using essentially the same equipment described here, and a detailed article on E773 is in preparation [72]. They find $\tau_S = (0.8941 \pm 0.0014 \pm 0.0009) \times 10^{-10}$s, $\Delta m = (0.5297 \pm 0.0030 \pm 0.0022) \times 10^{10}\hbar\text{s}^{-1}$, $\phi_{+-} = 43.53° \pm 0.58° \pm 0.49°$, and $\Delta\phi = 0.62° \pm 0.71° \pm 0.75°$, where the first error quoted is statistical, and the second systematic. The CERN CPLEAR experiment has measured Δm using semileptonic neutral K decays, which frees this measurement of the correlation with ϕ_{+-} that one has with this measument in the $\pi\pi$ decay mode. They find [73] $\Delta m = (0.5274 \pm 0.0029 \pm 0.0005) \times 10^{10}\hbar\text{s}^{-1}$. They have also measured ϕ_{+-}, finding $\phi_{+-} = 42.7° \pm 0.9° \pm 0.6° \pm 0.9°$, where again the first and second errors are statistical and systematic, and the third error is from the uncertainty in their Δm measurement.

These measurements are consistent with the findings of E731. In particular, they confirm the supposition put forward in [28] that the disagreement between ϕ_{+-} and ϕ_ε arose simply because of the bias in the ϕ_{+-} resulting from too high an experimental value for Δm. Note that the E731 results are competitive with these later results, even though the experiment was not optimized for these particular measurements. The good agreement between these experiments and the E731 results for neutral K parameters lends additional credence to the reliability of the ε'/ε measurement presented here.

E. Summary Remarks

Experiment E731 was designed to measure $Re(\varepsilon'/\varepsilon)$. The final error quoted is a factor 10 improvement over the best result prior to this effort – E617 from our own group. In addition, the phase difference $\Delta\phi$ has been improved from an error of 6° to one of 1.2°, and the best values of τ_S and ϕ_{+-} have been reported. The first measurment of Δm made in 20 years has also been made, and correcting previous determination of ϕ_{+-} for this new value brings all experiments into agreement with each other and with CPT symmetry. Additional rare decay modes have been studied with this data set. The question of direct CP-violation remains open.

ACKNOWLEDGMENTS

[1] L.K. Gibbons, PhD thesis (The University of Chicago, August, 1993, unpublished).

[2] T.D. Lee and C.S. Wu, *Ann. Rev. Nuc. Sci.* **16**, 511 (1966).

[3] L. Wolfenstein, *Nuovo Cim.* **63 A**, 269 (1969).

[4] V.V. Barmin *et al.*, *Nucl. Phys.* **B247**, 293 (1984); *ibid.* **B254**, 747 (1984).

[5] J.W. Cronin, *Acta Phys. Pol. B* **15**, 419 (1984).

[6] R.G. Sachs, *The Physics of Time Reversal*, The University of Chicago Press, Chicago, 1987.

[7] K. Kleinknecht, in *CP Violation*, edited by C. Jarlskog, (World Scientific, Singapore, 1989), page 41.

[8] B. Winstein and L. Wolfenstein, *Rev. of Mod. Phys.* **65**, 1113 (1993).

[9] T.T. Wu and C.N. Yang, *Phys. Rev. Lett.* **13**, 380 (1964).

[10] Particle Data Group, L. Montanet, *et al.*, *Phys. Rev. D* **50**, 1173 (1994).

[11] L.K. Gibbons *et al.*, *Phys. Rev. Lett.* **61**, 2661 (1988).

[12] V. Papadimitriou *et al.*, *Phys. Rev. Lett.* **63**, 28 (1989).

[13] A.R. Barker *et al.*, *Phys. Rev. D* **41**, 3546 (1990).

[14] V. Papadimitriou *et al.*, *Phys. Rev. D* **44**, R573 (1991).

[15] G.E. Graham *et al.*, *Phys. Lett.* **B295**, 169 (1992).

[16] W. Ochs, Munich Preprint MPI-Ph/Ph91-35, πN Newsletter, No. 3, 25 (1991).

[17] H. Burkhardt *et al.*, *Phys. Lett.* **B206**, 169 (1988).

[18] J.R. Patterson *et al.*, *Phys. Rev. Lett.* **64**, 1491 (1990).

[19] L.K. Gibbons *et al.*, *Phys. Rev. Lett.* **70**, 1203 (1993).

[20] G.D. Barr *et al.*, *Phys. Lett.* **B317**, 233 (1993).

[21] M. Kobayashi and A.I. Sanda, *Phys. Rev. Lett.* **69**, 3139 (1992).

[22] V.A. Kostelecký and Robertus Potting, Preprint IUHET 236, Indiana University, 1992.

[23] M. Karlsson *et al.*, *Phys. Rev. Lett.* **64**, 2976 (1990).

[24] R. Carosi *et al.*, *Phys. Lett.* **B237**, 303 (1990).

[25] S. Gjesdal *et al.*, *Phys. Lett.* **52B**, 119 (1974).

[26] W.C. Carithers *et al.*, *Phys. Rev. Lett.* **34**, 1244 (1975).

[27] Particle Data Group, K. Hikasa, *et al.*, *Phys. Rev. D* **45**, 1 (1992).

[28] L.K. Gibbons *et al.*, *Phys. Rev. Lett.* **70**, 1199 (1993).

[29] J.K. Black *et al.*, *Phys. Rev. Lett.* **54**, 1628 (1985).

[30] R.H. Bernstein *et al.*, *Phys. Rev. Lett.* **54**, 1631 (1985).

[31] M. Woods *et al.*, *Phys. Rev. Lett.* **60**, 1695 (1988).

[32] W.R. Mozlon *et al.*, *Phys. Rev. Lett.* **41**, 1213 (1978).

[33] J. Ellis, M.K. Gaillard, and D.V. Nanopoulos, *Nucl. Phys.* **B109**, 213 (1976).

[34] Frederick J. Gilman, *Phys. Rev.* **171**, 1453 (1968).

[35] Roy A. Briere and Bruce Winstein, *Phys. Rev. Lett.* **75**, 402 (1995; *ibid.* **75**, 2070 (1995).

[36] K. Kleinknecht and S. Luitz, *Phys. Lett.* **B336**, 581 (1994).

[37] J.R. Patterson, PhD thesis (The University of Chicago, December, 1990, unpublished).

[38] V. Papadimitriou, PhD thesis (The University of Chicago, December, 1990, unpublished).

[39] M. Karlsson, PhD thesis (Princeton University, August, 1990, unpublished).

[40] M.B.Woods, PhD thesis (The University of Chicago, June, 1988, unpublished).

[41] A.M. Eisner R.J. Morrison, J. Cumalat and C. Lauer, *Nucl. Instr. and Meth.* **143**, 311 (1977).

[42] M. Asner *et al.*, *Nucl. Instr. and Meth.* **A291**, 577 (1990).

[43] E. Longo and I. Sestili, *Nucl. Instr. and Meth.* **128**, 283 (1987).

[44] W.R. Nelson, H. Hirayama, and W.O. Rogers, The EGS4 code system, Preprint SLAC-Report-265, Stanford Linear Accelerator Center, 1985.

[45] A. Carroll *et al.*, *Phys. Rev. Lett.* **44**, 529 (1980).

[46] E.J. Ramberg *et al.*, *Phys. Rev. Lett.* **70**, 2525 (1993).

[47] W.R. Molzon, PhD thesis (The University of Chicago, March, 1979, unpublished).

[48] J. Roehrig *et al.*, *Phys. Rev. Lett.* **38**, 1116 (1977).

[49] G.J. Bock *et al.*, *Phys. Rev. Lett.* **42**, 350 (1979).

[50] A. Gsponer *et al.*, *Phys. Rev. Lett.* **42**, 13 (1979).

[51] A.J. Malensek, Preprint FN-341, Fermi National Accelerator Laboratory, October 1981.

[52] R.A. Briere, PhD thesis (The University of Chicago, June, 1995, unpublished).

[53] A. Schiz *et al.*, *Phys. Rev. D* **21**, 3010 (1980).

[54] J.H. Hubbell, H.A. Gimm, and I. Øverbø, *J. Phys. Chem. Ref. Data* **9**, 1023 (1980).

[55] B. Rossi, *High Energy Particles*, Prentice-Hall, Inc., Englewood Cliffs, NJ, 1952.

[56] A. Gsponer *et al.*, *Phys. Rev. Lett.* **42**, 9 (1979).

[57] T.D. Lee and C.S. Wu, *Ann. Rev. Nuc. Sci.* **16**, 511 (1966).

[58] J. Roehrig, PhD thesis (The University of Chicago, December, 1977, unpublished).

[59] E.C. Swallow, in *The Vancouver Meeting, Particles and Fields '91*, edited by D. Axen, D. Bryman, and M. Comyn, (World Scientific, Singapore, 1992), page 581.

[60] B. Schwingenheuer, PhD thesis (The University of Chicago, June, 1995, unpublished).

[61] D'Huart Industrie S.A., Certificat d'analyse chimique, Coulee No. 873, 1976.

[62] J.M. Flynn and L. Randall, *Phys. Lett.* **224B**, 221 (1989).

[63] F. Abe *et al.*, *Phys. Rev. Lett.* **74**, 2626 (1995).

[64] S. Abachi *et al.*, *Phys. Rev. Lett.* **74**, 2632 (1995).

[65] M. Ciuchini, E. Franco, G. Martinelli, and L. Reina, *Phys. Lett.* **301B**, 263 (1993).

[66] M. Ciuchini, E. Franco, G. Martinelli, L. Reina, and L. Silvestrini, CERN-TH.7514/94, (Rome Preprint 94/1024), 1994.

[67] A.J. Buras, M. Jamin, and M.E. Lautenbacher, *Nucl. Phys.* **B408**, 209 (1993).

[68] R.D. Peccei, Preprint UCLA/93/TEP/19, University of California, Los Angeles, 1993.

[69] H. Burkhardt, *Nucl. Instr. and Meth.* **A268**, 116 (1988).

[70] J.W. Cronin, *Rev. Mod. Phys.* **53**, 373 (1981).

[71] B. Schwingenheuer *et al.*, *Phys. Rev. Lett.* **74**, 4376 (1995).

[72] R.A. Briere, B. Schwingenheuer, *et al.*, in preparation.

[73] R. Adler *et al.*, CERN-PPE/95-103 (1995). Submitted to Phys. Lett. B.

[74] R. Adler *et al.*, CERN-PPE/95-107 (1995). Submitted to Phys. Lett. B.